Chemical vapor deposition of Al, Fe and of the Al13Fe4 approximant intermetallic phase : experiments and multiscale simulations

Ioannis Aviziotis

THÈSE

En vue de l'obtention du

DOCTORAT DE L'UNIVERSITÉ DE TOULOUSE

Délivré par :

Institut National Polytechnique de Toulouse (INP Toulouse)

Discipline ou spécialité :

Science et Génie des Matériaux

Présentée et soutenue par :

M. IOANNIS AVIZIOTIS

le mardi 15 novembre 2016

Titre :

Chemical vapor deposition of Al, Fe and of the Al13Fe4 approximant intermetallic phase: Experiments and multiscale simulations

---

Ecole doctorale :

Sciences de la Matière (SDM)

Unité de recherche :

Centre Interuniversitaire de Recherche et d'Ingénierie des Matériaux (C.I.R.I.M.A.T.)

Directeur(s) de Thèse :

M. CONSTANTIN VAHLAS

M. ANDREAS BOUDOUVIS

Rapporteurs :

M. DIMITRIS DAVAZOGLOU, NCSR DEMOKRITOS

M. GÉRARD VIGNOLES, UNIVERSITE BORDEAUX 1

Membre(s) du jury :

M. EVANGELINA PAVLATOU, NATIONAL TECHNICAL UNIVERSITY ATHENES, Président

M. ANDREAS BOUDOUVIS, NATIONAL TECHNICAL UNIVERSITY ATHENES, Membre

M. CONSTANTINOS SIETTOS, NATIONAL TECHNICAL UNIVERSITY ATHENES, Membre

M. CONSTANTIN VAHLAS, INP TOULOUSE, Membre

M. FRÉDÉRIC SCHUSTER, CEA SACLAY, Membre

M. THOMAS DUGUET, INP TOULOUSE, Membre

To my father – A mon père

Acknowledgements

This thesis work was carried out in the framework of a bilateral agreement ("Cotutelle") between the National Technical University of Athens (NTUA) and the Institut National Polytechnique de Toulouse (INPT).

I would like to express my deepest appreciation to my supervisors, Prof. Andreas G. Boudouvis of NTUA and Dr. Constantin Vahlas and Dr. Thomas Duguet of INPT/ Centre Inter-universitaire de Recherche et d'Ingénierie des Matériaux (CIRIMAT), for introducing me to the worlds of computational analysis and material science. I am grateful to them for teaching me the value of the combination of theoretical with experimental knowledge. I appreciate the liberty they gave me to carry out this research with much of my own 'scientific intuition'. I am also grateful to them for the understanding and confidence they showed regarding the deadlines of this thesis.

Concerning the computational work of the thesis, I'd like to thank Dr. Nikolaos Cheimarios and Dr. Michail E. Kavousanakis for supplying valuable technical support, a large part of which was by introducing me to multiscale modeling. I'd like also to thank Dr. Anthony N. Spyropoulos for his support in parallel processing in the computational cluster.

I also wish to thank all the members of the group at NTUA and especially, Dr. Eleni Koronaki and Dr. George Pashos for providing advice and sharing their experience with me, Dr. George Kokkoris for our discussions in the difficult topic of kinetics and Nikolaos T. Chamakos, soon to become Dr., for being a good friend and a fellow traveller all these years.

Concerning the experimental work, I'd like to thank Daniel Sadowski for his constant and kind technical support and Diane Samélor for her help in the characterization of thin films.

I wish to thank all the members of the French team "SURF" and especially, Fouzi Addou, Dr. Pierre-Luc Etchepare, Andreas Gavrielides and Khaled Soussi for being good friends during the years of my thesis work.

I'd like to acknowledge the help from people with expertise on characterization methods: Djar Oquab and Yannick Thebault for the SEM, François Senocq for the XRD, Claudie Josse for the FIB/SEM, Philippe De Parseval for EPMA, Marie-Christine Lafont for TEM, Marc Heggen for STEM and Sofia Gaiaschi of HORIBA Jobin Yvon SAS for GDOES.

I thank the reviewers Dr. Dimitris Davazoglou and Prof. Gérard L. Vignoles for accepting to review my thesis manuscript and for respecting the time frames. Also, I would like to thank the members of the examination committee, Prof. Evangelia Pavlatou, Dr. Frédéric Schuster and Prof. Constantinos Siettos for accepting to participate in the examination procedure.

I am thankful to my godfather Dr. Ioannis A. Bitsanis for introducing me to the chemical engineering science.

Last and most importantly, I'd like to thank my parents, George and Thaleia, my brother, Paris, and my life partner, Niki, for standing always by my side during the difficult moments of the thesis.

Funding for my thesis was provided by the National Scholarship Foundation of Greece (IKY-Siemens Program, Grant number:#SpnD/11160/13β). The experimental work of my thesis was supported by CIRIMAT through the Institut Français du Petrole et des Energies Nouvelles (IFPEN, contract #268821). Support was provided by the European Integrated Center for the Development of New Metallic Alloys and Compounds (CMAC) in terms of travel grants for participation in CMAC conferences.

Contents of the Thesis

Abstract

Films containing intermetallic compounds exhibit properties and combination of properties which are only partially explored. They provide multifunctionality to advanced materials required by industrial sectors, thus becoming a source of breakthrough and innovation. Metalorganic chemical vapor deposition (MOCVD) potentially allows conformal deposition on, and functionalization of complex surfaces, with high throughput and moderate cost. For this reason, it is necessary to control the complex chemical reactions and the transport mechanisms involved in a MOCVD process. In this perspective, computational modeling of the process, fed with experimental information from targeted deposition experiments, provides an integrated tool for the investigation and understanding of the phenomena occurring at different length scales, from the macro- to the nanoscale.

The MOCVD of Al-Fe intermetallic compounds is investigated in this thesis as a paradigm of implementation of such a combined, experimental and theoretical approach. Processing of the approximant phase $Al_{13}Fe_4$ is particularly targeted, due to its potential interest as low-cost and environmentally benign alternative to noble metal catalysts in the chemical industry.

The attainment of the targeted $Al_{13}Fe_4$ intermetallic phase passes through the investigation of the MOCVD of unary Al and Fe films. The MOCVD of Al from dimethylethylamine alane (DMEAA) in the range 139^{o}C-241^{o}C results in pure films. Increase of the deposition temperature yields higher film density and decreased roughness. The Al deposition rate increases to a maximum of 15.5 nm/min at 185^{o}C and then decreases. Macroscopic simulations of the process predict deposition rates in sutisfactory agreement with experimental measurements, especially in the range 139^{o}C-227^{o}C. At higher temperatures, competitive gas phase and surface phenomena cannot be captured by the applied model. Multiscale modeling of the process predicts the RMS roughness of the films accurately, thus allowing the control of properties, such as electrical resistivity, which depend on the microstructure.

The MOCVD of Fe from iron pentacarbonyl, $Fe(CO)_5$, is investigated in the range 130^{o}C-250^{o}C for the possibility to obtain fairly pure Fe films with low O and C contamination. The surface morphology depends strongly on the temperature and changes are observed above 200^{o}C. The Fe deposition rate increases up to 200^{o}C, to a maximum of 60 nm/min, and then decreases. Moreover, the deposition rate decreases sharply with increasing pressure. Computational predictions capture accurately the experimental behavior and they reveal that the decrease at higher temperatures and pressures is attributed to the high gas phase decomposition rate of the precursor and to inhibition of the surface from CO. The multiscale model calculates RMS roughness in good agreement with experimental data, especially at higher temperatures.

Upon investigation of the two processes, a series of Al-Fe co-depositions performed at 200^{o}C results in Al-rich films with a loose microstructure. They contain no intermetallic phases and they are O-contaminated due to the reaction of the Al with the carbonyl ligands. Sequential deposition of Al and Fe followed by *in situ* annealing at 575^{o}C for 1 h is applied to bypass the O-contamination. The process conditions of Fe are modified to 140^{o}C, 40 Torr and 10 min resulting in O-free films with Al:Fe atomic ratio close to the targeted 13:4 one. Characterization techniques including X-ray diffraction, TEM and STEM/EDX reveal a composition gradient along the thickness of the films, and the formation of the m-$Al_{13}Fe_4$ approximant phase together with secondary Al-Fe intermetallic phases.

It is demonstrated that MOCVD is a suitable method to obtain films composed of intermetallic alloys. Such films, conformally processed on complex surfaces can be considered for a variety of applications.

Χημική απόθεση από ατμό Al, Fe και της προσεγγιστικής διαμεταλλικής φάσης $Al_{13}Fe_4$: Πειράματα και προσομοιώσεις πολλαπλών χωρικών κλιμάκων

Ιωάννης Γ. Αβιζιώτης

Εκτενής Ελληνική περίληψη

Η παρούσα διατριβή πραγματεύεται τη συνδυασμένη πειραματική και υπολογιστική μελέτη διεργασιών Χημικής Απόθεσης από Ατμό (ΧΑΑ) με απώτερο στόχο την εφαρμογή της για τον σχηματισμό μεταλλικών συμπλόκων (*complex metallic alloys* – CMAs) και διαμεταλλικών ενώσεων (*intermetallic compounds*) αλουμινίου-σιδήρου (Al-Fe) πάνω σε επιφάνειες. Πιο συγκεκριμένα, μελετάται η δυνατότητα σχηματισμού της προσεγγιστικής φάσης $Al_{13}Fe_4$, η οποία προσδίδει πολυ-λειτουργικές ιδιότητες σε προηγμένα υλικά. Μεταξύ άλλων, παρέχει και καταλυτικές ιδιότητες για τη διεργασία ημι-υδρογόνωσης του ακετυλενίου προς αιθυλένιο στην παραγωγή πολύ-αιθυλενίου (Armbrüster *et al.*, 2012).

Μεταξύ των διαφόρων μεθόδων απόθεσης, η ΧΑΑ επιλέγεται λόγω της υψηλής της απόδοσης και της δυνατότητας που παρέχει για ομοιόμορφη επικάλυψη επιφανειών με περίπλοκη γεωμετρία. Στη ΧΑΑ τα αποτιθέμενα μέταλλα περιέχονται σε αρχικές μοριακές ενώσεις, τους προδρόμους (*precursors*). Ατμοί των πρόδρομων ενώσεων παράγονται και μεταφέρονται στον αντιδραστήρα και στην επιφάνεια ενός υποστρώματος, από ένα φέρον αέριο. Οι πρόδρομες ενώσεις συμμετέχουν σε αντιδράσεις αέριας φάσης και επιφανειακές. Η απόθεση των μεταλλικών υμενίων πραγματοποιείται όταν στο υπόστρωμα παρέχεται η κατάλληλη ποσότητα ενέργειας. Η ορθή εφαρμογή της ΧΑΑ βασίζεται στην επιλογή κατάλληλων προδρόμων ενώσεων, την παραγωγή ατμών τους και τη μεταφορά τους στον αντιδραστήρα, στον σχεδιασμό του αντιδραστήρα, και στον έλεγχο των μηχανισμών που υπεισέρχονται στη διεργασία. Το τελευταίο βήμα αποτελεί τη μεγαλύτερη δυσκολία στην αποτελεσματική εφαρμογή της ΧΑΑ, εξαιτίας της περίπλοκης σύζευξης της χημείας με τα φαινόμενα μεταφοράς.

Η μαθηματική προτυποποίηση και η υπολογιστική ανάλυση διεργασιών ΧΑΑ αποτελεί πολύτιμο εργαλείο για τη μελέτη τέτοιων περίπλοκων αλληλεπιδράσεων. Επιπλέον, η προτυποποίηση πολλαπλών χωρικών κλιμάκων παρέχει τη δυνατότητα διερεύνησης μηχανισμών που συμβαίνουν σε διαφορετικές χωρικές κλίμακες. Η προτυποποίηση σε μακροσκοπικό επίπεδο (μακρο-κλίμακα) διερευνά τους μηχανισμούς στον κύριο όγκο του αντιδραστήρα. Η εγκυρότητά της προϋποθέτει την ισχύ της υπόθεσης του συνεχούς μέσου για τη διατήρηση της μάζας, της ορμής και της ενέργειας, που περιγράφονται από ένα σύνολο μη-γραμμικών, μερικών διαφορικών εξισώσεων. Οι εξισώσεις αυτές επιλύονται προσεγγιστικά, με τη χρήση μεθόδων υπολογιστικής ρευστοδυναμικής, στον τριδιάστατο χώρο υπό χρονικά μεταβαλλόμενες συνθήκες ή συνθήκες μόνιμης κατάστασης. Η προτυποποίηση στη μακρο-κλίμακα περιλαμβάνει ομογενείς αντιδράσεις αέριας φάσης και ετερογενείς επιφανειακές αντιδράσεις που οδηγούν στην απόθεση του μεταλλικού υμενίου.

Οι θεωρητικές προβλέψεις, που προκύπτουν με τη χρήση των υπολογιστικών μεθόδων, αφορούν, μεταξύ άλλων, στην εξάρτηση του ρυθμού απόθεσης των υμενίων από τις λειτουργικές παραμέτρους του αντιδραστήρα. Παρέχουν γνώση για τους μηχανισμούς της ΧΑΑ, και έτσι συμβάλλουν στον καθορισμό προτιμητέων «παραθύρων» λειτουργίας, καθώς και στη βελτιστοποίηση και τον έλεγχο της διεργασίας. Η αξιοπιστία της υπολογιστικής ανάλυσης επιβεβαιώνεται από τη σύγκριση των αποτελεσμάτων με αντίστοιχα πειραματικά δεδομένα. Η προτυποποίηση στη μικρο- και νανο-κλίμακα είναι απαραίτητη για τη διερεύνηση επιφανειακών διεργασιών, όπως προσρόφηση, διάχυση και εκρόφηση μορίων ή ατόμων. Για τη σύνδεση των δύο κλιμάκων, το πρότυπο μακρο-κλίμακας τροφοδοτεί με υπολογιστική πληροφορία το πρότυπο νανο-κλίμακας για την πρόβλεψη της νανο-μορφολογίας. Το προκύπτον πρότυπο πολλαπλών χωρικών κλιμάκων επιτρέπει την προσομοίωση χαρακτηριστικών της επιφάνειας, όπως η τραχύτητα της επιφάνειας των υμενίων, που συνδέονται με τις τελικές ιδιότητες των υμενίων. Συνεπώς, η μαθηματική προτυποποίηση μιας διεργασίας ΧΑΑ, που περιλαμβάνει προσομοιώσεις στη μακρο-κλίμακα και προσομοιώσεις πολλαπλών χωρικών κλιμάκων παρέχει πληροφορίες για τη συνολική παραγωγή ενός υμενίου: από την εξάρτηση του ρυθμού απόθεσης και του πάχους από τις λειτουργικές συνθήκες έως τη μικρο-δομή και τις ιδιότητες του υμενίου.

Η ΧΑΑ υμενίων που περιέχουν διαμεταλλικές ενώσεις προϋποθέτει την αρχική διερεύνηση των διεργασιών απόθεσης (μονο)-μεταλλικών υμενίων. Η συμβατότητα (χημική, θερμική, μεταφοράς ατμών στον αντιδραστήρα) των ξεχωριστών διεργασιών μελετάται, ώστε να καταστεί πραγματοποιήσιμη η ταυτόχρονη (συναπόθεση) ή η διαδοχική απόθεση των μετάλλων. Σημαντικές πληροφορίες παρέχονται από τα λεγόμενα διαγράμματα Arrhenius, που περιγράφουν την εξάρτηση του ρυθμού απόθεσης από τη θερμοκρασία. Το διάγραμμα Arrhenius είναι το αποτέλεσμα της μαθηματικής προτυποποίησης επικυρωμένο από τις αντίστοιχες πειραματικές μετρήσεις. Απεικονίζει σχηματικά διαφορετικές θερμοκρασιακές περιοχές, που σχετίζονται με τον ελέγχοντα μηχανισμό της διεργασίας· σε χαμηλές θερμοκρασίες, όπου ο ρυθμός απόθεσης του υμενίου αυξάνεται με τη θερμοκρασία, η διεργασία ελέγχεται από την κινητική των επιφανειακών αντιδράσεων (*reaction-limited regime*). Σε υψηλότερες θερμοκρασίες, ο ρυθμός απόθεσης παραμένει σχετικά σταθερός και η διεργασία ελέγχεται από κοινού από τις χημικές αντιδράσεις και από φαινόμενα μεταφοράς. Περαιτέρω αύξηση της θερμοκρασίας οδηγεί σε μείωση του ρυθμού απόθεσης λόγω της επικράτησης των φαινομένων μεταφοράς (*diffusion-/ transport-limited regime*). Για τις διεργασίες συναπόθεσης και διαδοχικής απόθεσης, η συνδυασμένη χρήση των διαγραμμάτων Arrhenius του κάθε μεταλλικού συστατικού παρέχει πληροφορίες για τον καθορισμό ενός κοινού παραθύρου λειτουργικών συνθηκών. Η διεργασία της συναπόθεσης είναι προτιμότερο να πραγματοποιείται σε χαμηλές θερμοκρασίες, όπου ελέγχων μηχανισμός είναι η επιφανειακή αντίδραση. Σε αυτό το θερμοκρασιακό εύρος η επίδραση των αντιδράσεων αέριας φάσης στη διεργασία, οι οποίες ενδέχεται να οδηγήσουν σε υψηλούς ρυθμούς διάσπασης και σε αλληλεπιδράσεις μεταξύ των προδρόμων ενώσεων, είναι περιορισμένη. Συγκεκριμένες πρόδρομες ενώσεις, όμως, παρουσιάζουν υψηλούς ρυθμούς

αντιδράσεων αέριας φάσης και διάσπασης, σε όλο το εξεταζόμενο θερμοκρασιακό εύρος. Σε αυτή την περίπτωση, η συναπόθεση πραγματοποιείται σε συνθήκες που περιλαμβάνουν διαφορετικές θερμοκρασιακές περιοχές για την κάθε πρόδρομη ένωση. Συνεπώς, η ΧΑΑ του πρώτου μετάλλου μπορεί να ελέγχεται από την συγκέντρωση των χημικών συστατικών στην αέρια φάση του αντιδραστήρα, ενώ του δεύτερου μετάλλου από τη θερμοκρασία απόθεσης.

Σε αυτό το γενικό πλαίσιο μελετάται η ΧΑΑ υμενίων αλουμινίου (Al) και σιδήρου (Fe) και συνακόλουθα, η συναπόθεση και η διαδοχική απόθεση των δύο μετάλλων. Η μαθηματική προτυποποίηση της διεργασίας και οι υπολογιστικές προσομοιώσεις πραγματοποιούνται στη Σχολή Χημικών Μηχανικών του Εθνικού Μετσοβίου Πολυτεχνείου (ΕΜΠ), υπό την επίβλεψη του Καθ. Α.Γ. Μπουντουβή. Η πειραματική διαδικασία πραγματοποιείται στο εργαστήριο *Centre Interuniversitaire de Recherche et d'Ingénierie des Matériaux (CIRIMAT)* του *Institut National Polytechnique de Toulouse (INPT)* της Γαλλίας, υπό την επίβλεψη των Dr. C. Vahlas και Dr. T. Duguet.

Η πειραματική διάταξη περιλαμβάνει έναν κάθετο, κυλινδρικό αντιδραστήρα ΧΑΑ, με ατσάλινα τοιχώματα, που παρέχει τη δυνατότητα πραγματοποίησης πειραμάτων με θερμά ή ψυχρά τοιχώματα. Η ύπαρξη ενός φορέα στήριξης υποστρωμάτων στο εσωτερικό του αντιδραστήρα επιτρέπει την απόθεση σε περισσότερα από ένα υποστρώματα, το καθένα με τυπική επιφάνεια 1 cm^2. Επιπλέον, η ύπαρξη ενός καταιωνιστήρα (*shower plate*) απέναντι από τον φορέα υποστρωμάτων ενισχύει την ομοιογένεια της ροής του αερίου μείγματος αντιδρώντων. Η συγκεκριμένη πειραματική διάταξη έχει επιτυχώς δοκιμαστεί για την παραγωγή μεταλλικών και διαμεταλλικών υμενίων (Aloui *et al*., 2012; Krisyuk *et al*., 2011; Xenidou *et al*., 2007; Xenidou *et al*., 2010).

Για τη μαθηματική προτυποποίηση της ΧΑΑ σε μακροσκοπικό επίπεδο, το πρότυπο που αναπτύσσεται περιλαμβάνει το μοντέλο του πειραματικού αντιδραστήρα που διακριτοποιείται σε ένα πλέγμα στοιχειωδών κελιών. Κάθε κελί αναπαριστά έναν πεπερασμένο όγκο μέσα στον οποίο οι τιμές των μεταβλητών που υπολογίζονται θεωρούνται σταθερές. Οι μερικές διαφορικές εξισώσεις διατήρησης της μάζας, της ορμής και της ενέργειας επιλύονται αριθμητικά σε κάθε κελί του πλέγματος με τη μέθοδο των πεπερασμένων όγκων (Boudouvis, 2010; Thompson *et al*., 1985; Versteeg and Malalasekera, 2007) και με τη χρήση του εμπορικού λογισμικού Fluent (Ansys 12.1/Fluent Documentation, 2009).

Το πρότυπο νανο-κλίμακας είναι στοχαστικό και βασίζεται σε έναν αλγόριθμο kinetic Monte Carlo (kMC) που αναπτύχθηκε από τους Lam and Vlachos (2001). Οι προσομοιώσεις στη νανο-κλίμακα γίνονται από κώδικα σε γλώσσα C/C++, ο οποίος διαχειρίζεται τριών ειδών επιφανειακές διεργασίες: προσρόφηση, διάχυση και εκρόφηση. Για την περιγραφή των επιφανειακών διεργασιών κατά την απόθεση εφαρμόζεται η προσέγγιση «στερεού σε στερεό» (*solid-on-solid approximation*) και θεωρούμε ότι οι αλληλεπιδράσεις των ατόμων στην επιφάνεια γίνονται μεταξύ των εγγύτερων γειτόνων τους (*first-nearest neighbor interactions* – Gilmer and Benema, 1972). Ως πρώτη προσέγγιση στα πειραματικά δεδομένα,

επιλέγεται ένα απλό κυβικό πλέγμα (*simple cubic lattice*), παρά τη διαφορετική, *fcc* και *bcc* δομή πλέγματος και τον προσανατολισμό των υμενίων Al και Fe ((111) και (100), αντίστοιχα). Η επιλογή αυτή του πλέγματος οδηγεί στην ανάπτυξη ενός αδρομερούς προτύπου νανο-κλίμακας που συμβάλλει στη μείωση του υπολογιστικού κόστους.

Η σύνδεση των δύο κλιμάκων βασίζεται στην υπόθεση ότι ο ρυθμός απόθεσης παραμένει σταθερός, ανεξάρτητα από την κλίμακα στην οποία προσομοιώνεται (Masi *et al*., 2000). Μετά την επίλυση του υπολογιστικού προβλήματος σε μακροσκοπικό επίπεδο, τα κλάσματα μάζας των συστατικών που συμμετέχουν στην απόθεση των μετάλλων, τροφοδοτούνται στο πρότυπο kMC για την προσομοίωση της νανο-δομής των υμενίων.

Για τη ΧΑΑ υμενίων Al επιλέγεται η πρόδρομη ένωση dimethylethylamine alane (DMEAA). Η επιλογή του συγκεκριμένου προδρόμου βασίζεται στη σχετικά υψηλή τάση ατμών του σε θερμοκρασία δωματίου και στη δυνατότητα που παρέχει για απόθεση υμενίων σε σχετικά χαμηλές θερμοκρασίες. Η πειραματική και υπολογιστική ανάλυση της διεργασίας στοχεύει στη διερεύνηση της εξάρτησης του ρυθμού απόθεσης και της μικρο-δομής των υμενίων από τη θερμοκρασία στο θερμοκρασιακό εύρος 139^{o}C – 241^{o}C.

Η ΧΑΑ του Al από το DMEAA έχει ως αποτέλεσμα την απόθεση καθαρών υμενίων χωρίς προσμίξεις άνθρακα ή αζώτου. Η μικρο-δομή των υμενίων παρατηρείται στο ηλεκτρονικό μικροσκόπιο σάρωσης (SEM). Μικρογραφίες της επιφάνειας και τομών των υμενίων παρουσιάζονται στο Σχ. Π-1 για θερμοκρασίες που αντιστοιχούν στους 139^{o}C, 198^{o}C and 227^{o}C (Aviziotis *et al*., 2015). Οι παρατηρήσεις των αποτιθέμενων υμενίων στη χαμηλότερη θερμοκρασία (Σχ. Π-1α και β) δείχνουν διάσπαρτους κρυστάλλους Al στην επιφάνεια που συμβάλλουν στη διαμόρφωση ασυνεχών υμενίων, με μικρή ομοιομορφία και τραχιά μορφολογία. Αντίθετα, η αύξηση της θερμοκρασίας συμβάλλει στην αύξηση της πυκνότητας του υμενίου λόγω συνένωσης των κρυστάλλων (Σχ. Π-1γ και δ, και μετά ε και στ). Η εκτίμηση του πάχους των υμενίων μέσω μετρήσεων της αύξησης της μάζας τους μετά την απόθεση δίνει τιμές 907 nm (±90 nm) και 833 nm (±90 nm) για τις θερμοκρασίες 198^{o}C and 227^{o}C, αντίστοιχα. Η μέτρηση του πάχους στο SEM δίνει αντίστοιχα τιμές ίσες με 873 nm (±50 nm) και 804 nm (±50 nm). Η σύγκριση μεταξύ των τιμών για τα πάχη των υμενίων δείχνει ότι τα αποτελέσματα είναι παρόμοια για τους δύο διαφορετικούς τρόπους μέτρησης. Αυτό είναι αποτέλεσμα της περιορισμένης πορώδους δομής, παρά την ύπαρξη τραχύτητας.

Για τη μακροσκοπική προτυποποίηση της διεργασίας, το σχήμα χημείας που εξετάζεται για την απόθεση Al από το DMEAA, περιλαμβάνει μια αέρια και μια επιφανειακή αντίδραση διάσπασης του προδρόμου, που οδηγεί τελικά στην απόθεση υμενίων Al (Han *et al*., 1994; Kim *et al*., 1996; Xenidou *et al*., 2010; Yun *et al*., 1998b). Για τις δύο αυτές αντιδράσεις χρησιμοποιούνται κινητικές Arrhenius πρώτης τάξης. Η ενέργεια ενεργοποίησης της αέριας αντίδρασης παρέχεται από τη βιβλιογραφία (Yun *et al*., 1998b), ενώ για την επιφανειακή αντίδραση υπολογίζεται από την κλίση του πειραματικού διαγράμματος Arrhenius, στην περιοχή όπου ελέγχων μηχανισμός είναι αυτή η αντίδραση. Οι προεκθετικοί συντελεστές προσαρμόζονται στα πειραματικά δεδομένα. Οι συνοριακές συνθήκες που

εφαρμόζονται στο πρότυπο μακρο-κλίμακας βασίζονται στις πειραματικές συνθήκες λειτουργίας του αντιδραστήρα: Θερμοκρασία εισόδου, $T_{εισ.}$=100^{o}C, θερμοκρασία τοιχωμάτων, $T_{τοιχ.}$=75^{o}C, θερμοκρασία απόθεσης, T_s=139^{o}C – 241^{o}C, πίεση, P=10 Torr και ροή εισόδου του DMEAA στον αντιδραστήρα, $Q_{prec} = 2$ sccm.

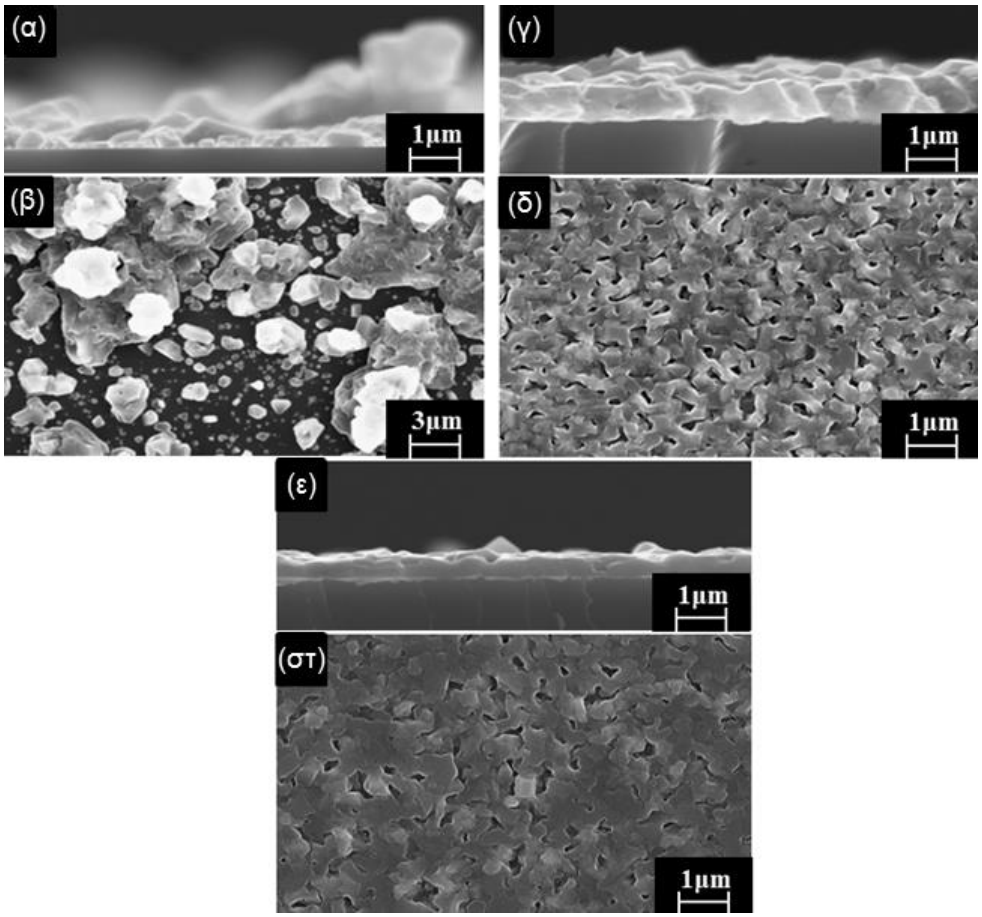

Σχ. Π-1: Μικρογραφίες SEM επιφανειών και τομών υμενίων Al που αποτέθηκαν σε θερμοκρασίες 139^{o}C (α,β), 198^{o}C (γ,δ) and 227^{o}C (ε,στ).

Το διάγραμμα Arrhenius της διεργασίας παρουσιάζεται στο Σχ. Π-2, όπου τα μαύρα τετράγωνα συμβολίζουν τις πειραματικές μετρήσεις και οι δύο καμπύλες τα αποτελέσματα των υπολογιστικών προσομοιώσεων. Μολονότι ο διαχωρισμός μεταξύ των διαφορετικών θερμοκρασιακών περιοχών είναι δύσκολος (Jang *et al*., 1998), η αύξηση του ρυθμού απόθεσης μέχρι τους 185^{o}C φανερώνει ότι σε αυτή την περιοχή ελέγχων μηχανισμός είναι η αντίδραση. Ο καθορισμός των ορίων μεταξύ των δύο περιοχών είναι κοντά στο εύρος που παρουσιάζεται σε προηγούμενες εργασίες, όπου οι μέγιστοι ρυθμοί απόθεσης μετρούνται σε θερμοκρασίες 150^{o}C-160^{o}C (Kim *et al*., 1996; Yang *et al*., 1998; Yun *et al*., 1998a). Η διαφορά των 20^{o}C-30^{o}C μπορεί να αποδοθεί στη διαφορετική πειραματική διάταξη και τις λειτουργικές συνθήκες που εφαρμόζονται στις εργασίες αυτές. Άνω των 185^{o}C, ο ρυθμός απόθεσης παρουσιάζει μια μικρή πτώση. Περαιτέρω αύξηση της θερμοκρασίας στους 240^{o}C οδηγεί στην απότομη πτώση του ρυθμού απόθεσης.

Σε ότι αφορά στα αποτελέσματα της υπολογιστικής ανάλυσης, παρουσιάζονται για δύο διαφορετικές ροές εισόδου της πρόδρομης ένωσης στον αντιδραστήρα, 2 sccm (μαύρη γραμμή) και 1.85 sccm (διακεκομμένη γραμμή). Η πρώτη τιμή υπολογίζεται υποθέτοντας ότι η εξάτμιση της πρόδρομης ένωσης στον εξατμιστήρα πραγματοποιείται σε κατάσταση θερμοδυναμικής ισορροπίας και ότι η αγωγιμότητα των σωληνώσεων που συνδέουν τον εξατμιστήρα με τη ζώνη απόθεσης είναι «άπειρη». Για αυτό η τιμή των 2 sccm αντιστοιχεί στο ανώτατο όριο ροής της πρόδρομης ένωσης στην είσοδο του αντιδραστήρα. Τα αποτελέσματα της υπολογιστικής ανάλυσης με αυτή την τιμή ροής εισόδου οδηγούν σε υπερεκτίμηση του ρυθμού απόθεσης στην περιοχή όπου ελέγχων μηχανισμός είναι η αντίδραση.

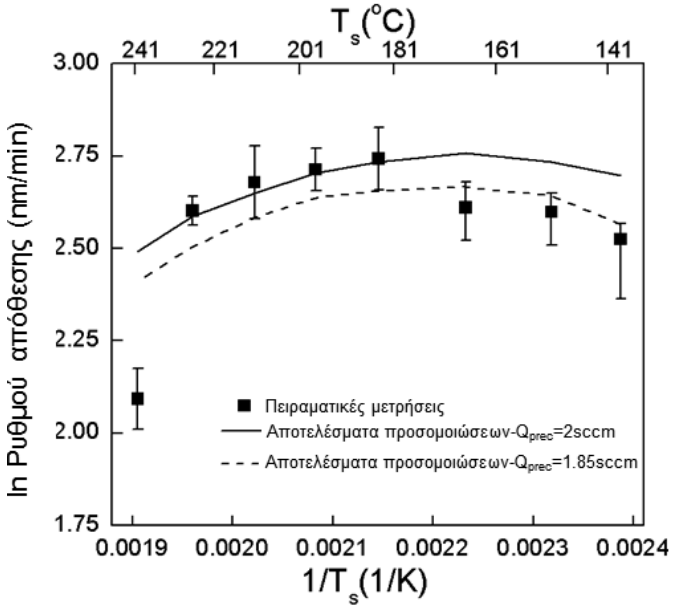

Σχ. Π-2: Το διάγραμμα Arrhenius της ΧΑΑ του Al από το DMEAA. Παρουσιάζονται οι πειραματικές μετρήσεις (μαύρα τετράγωνα) και αποτελέσματα της υπολογιστικής ανάλυσης (γραμμές) για δύο διαφορετικές ροές εισόδου της πρόδρομης ένωσης.

Για τον λόγο αυτό, εξετάζονται χαμηλότερες τιμές ροής εισόδου της πρόδρομης ένωσης στον αντιδραστήρα, στο εύρος 1.5 sccm – 1.95 sccm. Η καλύτερη εγγύτητα μεταξύ πειραματικών δεδομένων και υπολογιστικών αποτελεσμάτων προκύπτει για ροή εισόδου 1.85 sccm. Όπως φαίνεται στο Σχ. Π-2, οι υπολογιστικές προβλέψεις με αυτή τη ροή εισόδου βελτιώνουν τη σύγκριση με τα πειραματικά δεδομένα στις χαμηλές θερμοκρασίες, χωρίς να την επηρεάζουν σημαντικά στις υψηλότερες θερμοκρασίες (Aviziotis *et al*., 2015).

Η αλλαγή της ροής εισόδου του DMEAA σχετίζεται με την ποσότητα του που φτάνει στα υποστρώματα και είναι διαθέσιμη για την επιφανειακή αντίδραση. Είναι γενικά αποδεκτό ότι στην περιοχή χαμηλών θερμοκρασιών ο ρυθμός απόθεσης ελέγχεται από την επιφανειακή αντίδραση, ανεξάρτητα από την ποσότητα της πρόδρομης ένωσης που φτάνει στην επιφάνεια και με την προϋπόθεση ότι ο ρυθμός τροφοδοσίας είναι μεγαλύτερος από τον ρυθμό κατανάλωσης. Θα αναμενόταν, λοιπόν, στην εξεταζόμενη περίπτωση, ότι η μείωση

της ροής εισόδου της πρόδρομης ένωσης στον αντιδραστήρα θα επηρέαζε περισσότερο τη διεργασία στις υψηλότερες θερμοκρασίες.

Παρόλα αυτά, δεν πρέπει να παραγνωρίζεται το γεγονός ότι η διεργασία απόθεσης περιλαμβάνει και μια αντίδραση αέριας φάσης, η οποία μπορεί να καταναλώνει σημαντική ποσότητα της πρόδρομης ένωσης ακόμα και στην περιοχή χαμηλών θερμοκρασιών. Στο Σχ. Π-3, παρουσιάζεται το θερμοκρασιακό πεδίο στον αντιδραστήρα (Σχ. Π-3α) και ο ρυθμός της αντίδρασης αέριας φάσης (Σχ. Π-3β), όταν η θερμοκρασία του υποστρώματος είναι 151^{o}C. Από το σχήμα αυτό φαίνεται ότι η αντίδραση αέριας φάσης του DMEAA πραγματοποιείται όχι μόνο κοντά στο υπόστρωμα, όπου η θερμοκρασία είναι 151^{o}C αλλά και κοντά στην είσοδο του αντιδραστήρα, στους 100^{o}C. Συμπεραίνεται ότι ο ρυθμός της αντίδρασης αέριας φάσης είναι τέτοιος που καταναλώνει την πρόδρομη ένωση στην αέρια φάση, εμποδίζοντάς την να φτάσει στο υπόστρωμα και να συμμετάσχει στην επιφανειακή αντίδραση.

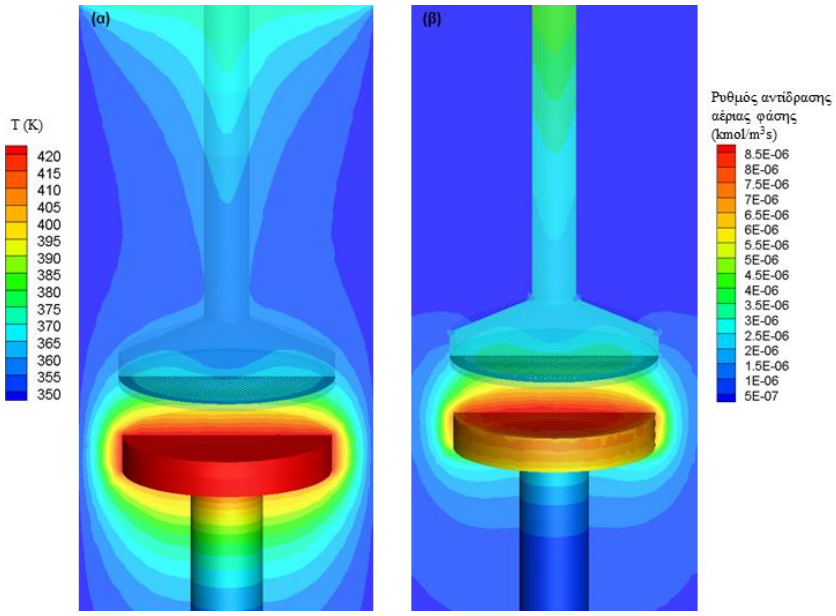

Σχ. Π-3: (α) Το θερμοκρασιακό πεδίο του αντιδραστήρα και (β) ο ρυθμός της αντίδρασης αέριας φάσης, όταν η θερμοκρασία του υποστρώματος είναι 151^{o}C.

Οι προβλέψεις των υπολογιστικών προσομοιώσεων παρουσιάζουν ικανοποιητική συμφωνία με τις πειραματικές μετρήσεις στο θερμοκρασιακό εύρος 139^{o}C – 227^{o}C. Ωστόσο, σε υψηλότερες θερμοκρασίες, το πρότυπο μακρο-κλίμακας αποτυγχάνει να προβλέψει τον πειραματικά μετρούμενο ρυθμό απόθεσης. Το γενικευμένο σχήμα αντιδράσεων που ενσωματώνεται στο μακροσκοπικό πρότυπο και οι κινητικές Arrhenius πρώτης τάξης που περιγράφουν τις αντιδράσεις, δεν λαμβάνουν υπόψη τους πρόσθετα φαινόμενα, όπως ο σχηματισμός ενδιάμεσων χημικών ειδών, με αποτέλεσμα την αποτυχία πρόβλεψης της απότομης μείωσης του ρυθμού απόθεσης. Ωστόσο, το παρόν πρότυπο μακρο-κλίμακας είναι έγκυρο στο θερμοκρασιακό εύρος 139^{o}C – 227^{o}C, όπου μπορούν να καθοριστούν κοινές συνθήκες λειτουργίας για τη διεργασία της συναπόθεσης με το Fe.

Οι μακροσκοπικοί υπολογισμοί παρέχουν τα κλάσματα μάζας του DMEAA στην επιφάνεια του υποστρώματος, τα οποία τροφοδοτούνται στο πρότυπο kMC για την πραγματοποίηση προσομοιώσεων πολλαπλών χωρικών κλιμάκων της επιφάνειας υμενίων Al και τον υπολογισμό της τραχύτητάς τους. Η πληροφορία για τις επιφανειακές χημικές αντιδράσεις του DMEAA σε επίπεδο νανο-κλίμακας ενσωματώνεται στον συντελεστή προσκόλλησης (*sticking coefficient*), s_0. Η ενσωμάτωση αυτή γίνεται μέσω πολυωνυμικής προσαρμογής του s_0 στα πειραματικά δεδομένα για τον ρυθμό απόθεσης στις διάφορες θερμοκρασίες.

Στο Σχ. Π-4, παρουσιάζεται η ρίζα μέσης τετραγωνικής απόκλισης (*root mean square*, RMS) της τραχύτητας των υμενίων Al που αντιστοιχεί σε πειραματικές μετρήσεις (μαύρα τετράγωνα) και θεωρητικές προβλέψεις με το πρότυπο πολλαπλών χωρικών κλιμάκων (Aviziotis *et al*., 2016). Οι πειραματικές μετρήσεις πραγματοποιήθηκαν με τη μέθοδο της συμβολομετρίας (*interferometry*). Η τραχύτητα RMS των υμενίων Al που αποτίθενται στη χαμηλότερη θερμοκρασία (139^{o}C) είναι υψηλή (0.6 μm). Μειώνεται καθώς αυξάνεται η θερμοκρασία και φτάνει στην ελάχιστη τιμή της, 0.15 μm, στους 198^{o}C. Περαιτέρω αύξηση της θερμοκρασίας δεν επιφέρει μεταβολές στην τραχύτητα. Η τραχύτητα σχετίζεται στενά με την αλλαγή της μικρο-δομής των υμενίων. Σε θερμοκρασίες μικρότερες των 150^{o}C, τα αποτιθέμενα υμένια δεν είναι συνεχή και αποτελούνται από διάσπαρτους κόκκους ανομοιόμορφους ως προς το μέγεθός τους, με αποτέλεσμα η τραχύτητα να είναι υψηλή. Αντίθετα, η αύξηση της θερμοκρασίας ενισχύει την ομοιομορφία της μορφολογίας της επιφάνειας και τη μείωση της τραχύτητας.

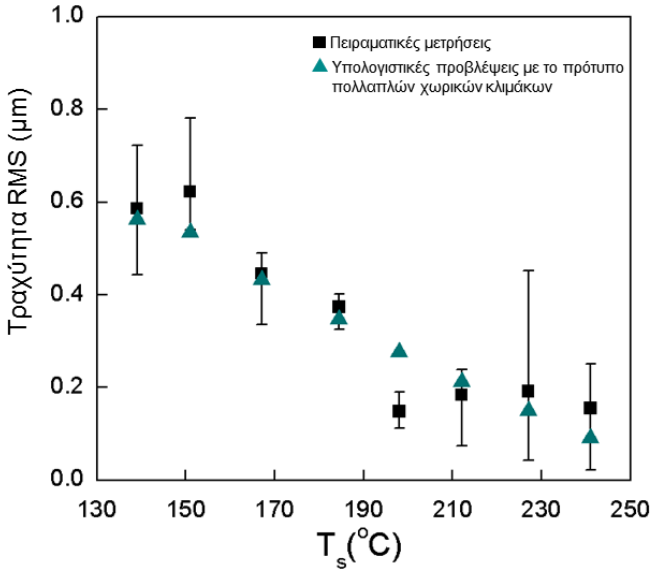

Σχ. Π-4: Εξέλιξη της τραχύτητας (RMS) υμενίων Al με τη θερμοκρασία απόθεσης, T_s. Τα αποτελέσματα αντιστοιχούν σε πειραματικές μετρήσεις (μαύρα τετράγωνα) και θεωρητικές προβλέψεις (πράσινα τρίγωνα).

Τα αποτελέσματα των προσομοιώσεων με το πρότυπο πολλαπλών χωρικών κλιμάκων προσεγγίζουν ικανοποιητικά τα πειραματικά δεδομένα. Λιγότερο ικανοποιητικές προβλέψεις προκύπτουν σε υψηλότερες θερμοκρασίες, όπου η τραχύτητα σταθεροποιείται. Αυτή η

αποτυχία πρόβλεψης μπορεί να οφείλεται στο αδρομερές μοντέλο που χρησιμοποιείται, καθώς και στην έμμεση ενσωμάτωση της χημείας στον συντελεστή προσκόλλησης. Η ανάπτυξη ενός προτύπου που θα λαμβάνει υπόψη του την ακριβή κρυσταλλική δομή του Al και θα ενσωματώνει πιθανές χημικές αντιδράσεις στην επιφάνεια σε επίπεδο νανο-κλίμακας ενδέχεται να διορθώσει την απόκλιση από τα πειραματικά δεδομένα και να επιτρέψει την προσομοίωση περισσότερων επιφανειακών χαρακτηριστικών, όπως ο σχηματισμός τριδιάστατων δομών Al στην επιφάνεια.

Ωστόσο, το παρόν πρότυπο συμβάλλει στην ικανοποιητική προσέγγιση της επιφανειακής τραχύτητας και αυτό μπορεί να επιτρέψει τον έλεγχο των τελικών ιδιοτήτων του υμενίου. Στο Σχ. Π-5 παρουσιάζεται η ηλεκτρική αντίσταση, όπως μετρήθηκε πειραματικά (κόκκινες σφαίρες) και εκτιμήθηκε υπολογιστικά με τη χρήση του μοντέλου Fuchs-Sondheimer (μαύρες σφαίρες) (FS model – Timalshina *et al.*, 2015), στο οποίο εισάγεται η τραχύτητα που υπολογίζεται από το πρότυπο πολλαπλών χωρικών κλιμάκων. Το βέλος στο επίπεδο (x,y) δείχνει την κατεύθυνση αύξησης της τραχύτητας. Τα μαύρα και κόκκινα σημεία στο επίπεδο (y,z) και η μπλε καμπύλη δείχνουν την εξέλιξη της ηλεκτρικής αντίστασης με την αύξηση της τραχύτητας. Όπως φαίνεται, η αντίσταση αυξάνεται με αύξηση της RMS από 10 μΩ.cm για RMS 0.15 μm σε 80 μΩ.cm για RMS 0.6 μm. Η παρατηρούμενη τάση της ηλεκτρικής αντίστασης οφείλεται στην αυξημένη διασπορά των ηλεκτρονίων σε τραχιές επιφάνειες, που οδηγεί σε σημαντική μείωση της αγωγιμότητας (Machlin, 2006).

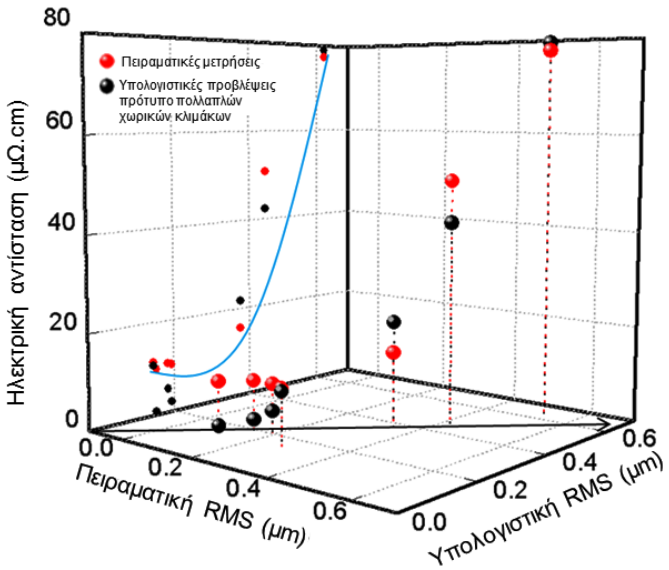

Σχ. Π-5: Η ηλεκτρική αγωγιμότητα υμενίων Al όπως μετρήθηκε πειραματικά (κόκκινες) σφαίρες και εκτιμήθηκε υπολογιστικά με το πρότυπο πολλαπλών χωρικών κλιμάκων (μαύρες σφαίρες), ως συνάρτηση της πειραματικής και υπολογιστικής τραχύτητας.

Η εκτίμηση της ηλεκτρικής αντίστασης με τη χρήση του προτύπου πολλαπλών χωρικών κλιμάκων και του μοντέλου FS φαίνεται να προσεγγίζει ικανοποιητικά την πειραματική τάση και τα πειραματικά δεδομένα σε απόλυτες τιμές. Καθώς η τραχύτητα μειώνεται, η διαφορά μεταξύ πειραματικών μετρήσεων και θεωρητικών προβλέψεων

αυξάνεται επειδή το μοντέλο FS δεν ενσωματώνει πληροφορίες για χαρακτηριστικά της επιφάνειας που ενδέχεται να επηρεάζουν την αγωγιμότητα, πέραν της τραχύτητας. Τα αποτελέσματα της ηλεκτρικής αντίστασης καταδεικνύουν τη σημασία του ακριβούς υπολογισμού και ελέγχου της τραχύτητας ενός υμενίου, καθώς μέσω αυτής μπορούν να ελεγχθούν οι τελικές ιδιότητές του.

Για τη ΧΑΑ υμενίων Fe επιλέγεται η πρόδρομη ένωση iron pentacarbonyl ($Fe(CO)_5$). Η επιλογή του συγκεκριμένου προδρόμου βασίζεται στην πολύ υψηλή τάση ατμών του σε θερμοκρασία δωματίου και στη δυνατότητα που παρέχει για απόθεση στο ίδιο θερμοκρασιακό εύρος που αποτίθενται υμένια Al. Η πειραματική και υπολογιστική ανάλυση της διεργασίας στοχεύει στη διερεύνηση της εξάρτησης του ρυθμού απόθεσης και της μικροδομής των υμενίων από τη θερμοκρασία στο θερμοκρασιακό εύρος 130^{o}C – 250^{o}C. Επιπροσθέτως, μελετάται η συμπεριφορά του ρυθμού απόθεσης συναρτήσει της πίεσης του αντιδραστήρα, για εύρος πιέσεων 10 – 40 Torr.

Η ΧΑΑ από το $Fe(CO)_5$ έχει ως αποτέλεσμα την απόθεση υμενίων Fe που μπορεί να περιέχουν και τη φάση Fe_3C ως δευτερεύουσα, κυρίως σε υψηλότερες θερμοκρασίες. Τα υμένια παρουσιάζουν σχετική καθαρότητα, με μικρές προσμίξεις άνθρακα και οξυγόνου. Η μορφολογία των υμενίων, όπως παρατηρήθηκε στο SEM, παρουσιάζεται στο Σχ. Π-6. Παρατηρείται ότι στη χαμηλότερη θερμοκρασία (Σχ. Π-6α) αποτίθενται ασυνεχή και ανομοιόμορφα υμένια.

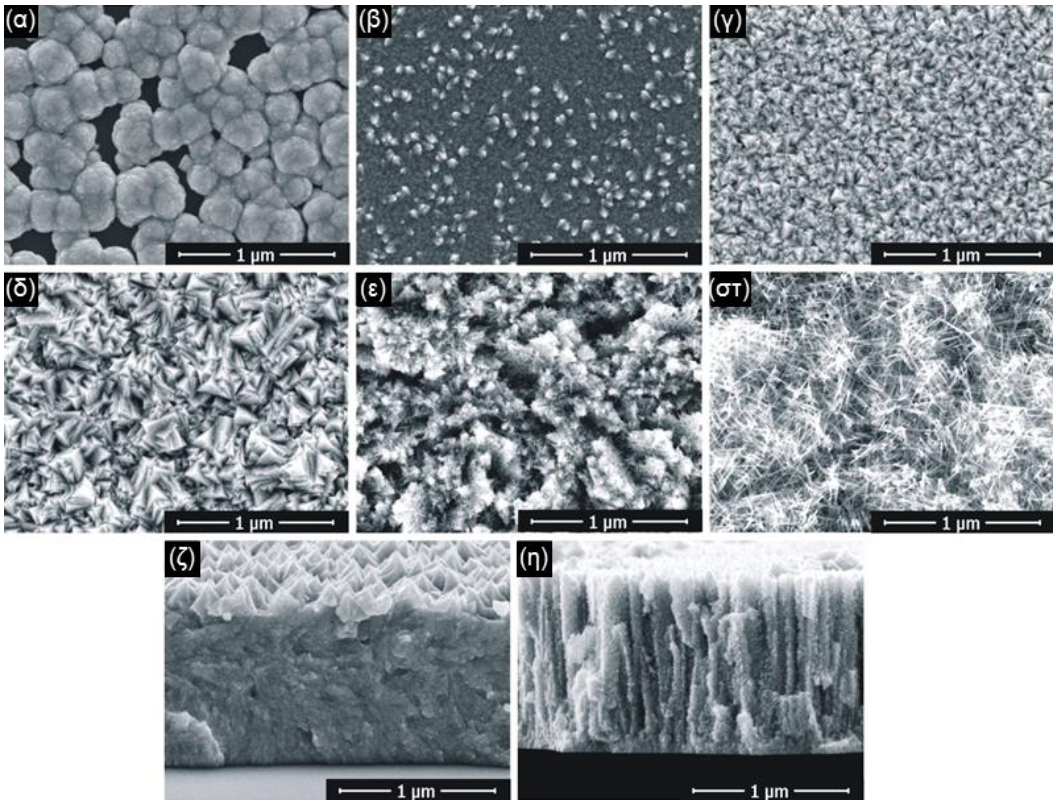

Σχ. Π-6: Μικρογραφίες της επιφάνειας υμενίων Fe, όπως παρατηρήθηκαν στο SEM, για θερμοκρασίες απόθεσης (α) 130^{o}C, (β) 150^{o}C, (γ) 170^{o}C, (δ) 190^{o}C, (ε) 200^{o}C και (στ) 240^{o}C. Επιπλέον, παρουσιάζονται τομές των υμενίων για θερμοκρασίες απόθεσης (ζ) 190^{o}C και (η) 200^{o}C.

Αύξηση της θερμοκρασίας στους 150°C (Σχ. Π-6β) οδηγεί στην αύξηση της πυκνότητας των υμενίων. Σε αυτή τη θερμοκρασία, το μέγεθος των κρυστάλλων παρουσιάζει ανομοιογένεια όπως φαίνεται στο Σχ. Π-6β, όπου οι μεγαλύτεροι κρύσταλλοι ξεχωρίζουν στο SEM μέσω φωτεινότερης αντίθεσης. Καθώς η θερμοκρασία αυξάνεται μέχρι τους 190°C (Σχ. Π-6γ και δ), παράγονται σχηματοποιημένοι, γωνιώδεις κρύσταλλοι, το μέγεθος των οποίων γίνεται ομοιόμορφο. Η πυκνότητα των υμενίων και η απουσία πορώδους δομής επιβεβαιώνονται από την τομή του Σχ. Π-6ζ. Ωστόσο, στους 200°C (Σχ. Π-6ε) η δομή αυτή των κρυστάλλων χάνεται σταδιακά και αντικαθίσταται από μία βελονοειδή, τυχαία μορφολογία, που γίνεται εντονότερη σε υψηλότερες θερμοκρασίες (240°C – Σχ. Π-6στ). Η μορφολογία αυτή, που επιβεβαιώνεται και στην τομή του Σχ. Π-6η, μπορεί να συνδέεται με την αύξηση της πορώδους δομής των υμενίων.

Για τη μακροσκοπική προτυποποίηση της διεργασίας, το πρότυπο χημείας που εξετάζεται για την απόθεση Fe από το $Fe(CO)_5$, περιλαμβάνει 7 αντιδράσεις αέριας φάσης και 3 επιφανειακές. Οι πρώτες περιγράφουν τη σταδιακή απώλεια μονοξειδίου του άνθρακα (CO) από το μόριο της πρόδρομης ένωσης για το σχηματισμό ενδιάμεσων συμπλόκων (για παράδειγμα, το $Fe(CO)_4$ σχηματίζεται όταν χάνεται ένα CO από το $Fe(CO)_5$). Επιπλέον, λαμβάνουν υπόψη το συνδυασμό των ενδιάμεσων ειδών με το $CO^{\cdot}$ για παράδειγμα, ο συνδυασμός του $Fe(CO)_4$ με ένα μόριο CO οδηγεί στον σχηματισμό του $Fe(CO)_5$. Για τις αντιδράσεις αυτές χρησιμοποιούνται κινητικές Arrhenius, η τάξη των οποίων υπαγορεύεται από τη στοιχειομετρία της αντίδρασης. Οι επιφανειακές αντιδράσεις περιγράφουν την απόθεση υμενίων Fe, στην οποία συνεισφέρουν το $Fe(CO)_5$, το $Fe(CO)_3$ και το Fe(CO) (Dateo *et al*., 2002; Jackman and Foord, 1989; Xu and Zaera, 1994). Για τις επιφανειακές αντιδράσεις χρησιμοποιούνται κινητικές τύπου Langmuir-Hinshelwood, για την παρεμπόδιση της απόθεσης από την παρουσία του CO. Οι ενέργειες ενεργοποίησης των αντιδράσεων παρέχονται από βιβλιογραφικά δεδομένα (Dateo *et al*., 2002; Gonzáles-Blanco and Branchadell, 1999; Lewis *et al*., 1984; Seder *et al*., 1986; Xu and Zaera, 1994), ενώ οι προεκθετικοί συντελεστές προσαρμόζονται στα πειραματικά δεδομένα. Οι συνοριακές συνθήκες που εφαρμόζονται στο πρότυπο μακρο-κλίμακας βασίζονται στις πειραματικές συνθήκες λειτουργίας του αντιδραστήρα: Θερμοκρασία εισόδου, $T_{εισ.}$=25°C, θερμοκρασία τοιχωμάτων, $T_{τοιχ.}$=25°C, θερμοκρασία απόθεσης, T_s=130°C – 250°C, πίεση, P=10 – 40 Torr και ροή εισόδου του $Fe(CO)_5$ στον αντιδραστήρα, $Q_{prec} = 0.7\,\text{sccm}$.

Το Σχ. Π-7 είναι το διάγραμμα Arrhenius της διεργασίας, όπου με μαύρα τετράγωνα συμβολίζονται οι πειραματικές μετρήσεις, ενώ η συνεχής καμπύλη αντιστοιχεί στις θεωρητικές προβλέψεις. Ο ρυθμός απόθεσης του Fe αυξάνεται με αύξηση της θερμοκρασίας, μέχρι τους T_s=180°C$^{\cdot}$ πρόκειται για την περιοχή όπου ελέγχων μηχανισμός είναι οι επιφανειακές αντιδράσεις. Μια μεταβατική περιοχή παρατηρείται στο εύρος 180°C – 200°C, όπου η διεργασία απόθεσης επηρεάζεται εξίσου από τις επιφανειακές αντιδράσεις και από τα φαινόμενα μεταφοράς. Σε αυτή την περιοχή ο ρυθμός απόθεσης φτάνει στη μέγιστη τιμή του, 60 nm/min, στους 200°C. Σε υψηλότερες θερμοκρασίες η διεργασία ελέγχεται από τα

φαινόμενα μεταφοράς και ο ρυθμός απόθεσης μειώνεται απότομα. Τα πειραματικά αποτελέσματα είναι σε συμφωνία με αποτελέσματα που έχουν καταγραφεί στη βιβλιογραφία (Carlton and Oxley, 1965; Lane and Wright, 1999; Lane *et al*., 1997; Senocq *et al*., 2006; Zhang *et al*., 2016).

Οι θεωρητικές προβλέψεις με το πρότυπο μακρο-κλίμακας βρίσκονται σε πολύ καλή συμφωνία με τα πειραματικά δεδομένα, σε όλο το θερμοκρασιακό εύρος που εξετάζεται. Συνεπώς, μπορούμε να χρησιμοποιήσουμε την υπολογιστική ανάλυση για να διερευνήσουμε τα αίτια της πτώσης του ρυθμού απόθεσης σε θερμοκρασίες μεγαλύτερες των 200°C – 215°C.

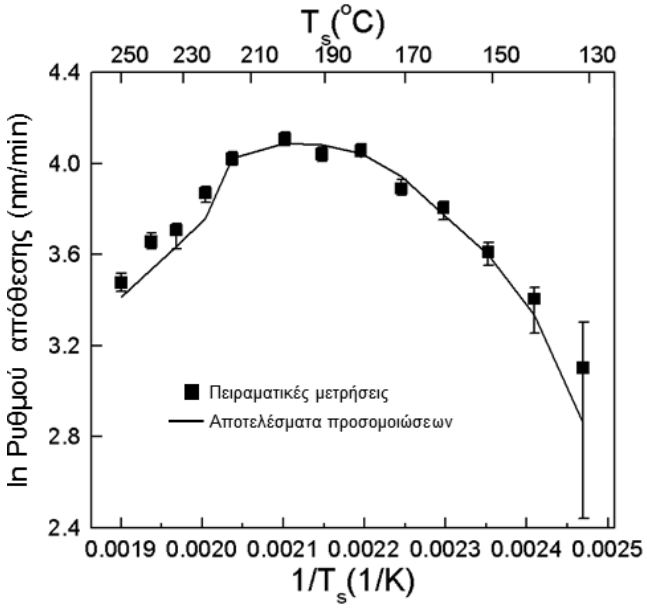

Σχ. Π-7: Το διάγραμμα Arrhenius της ΧΑΑ του Fe από το $Fe(CO)_5$. Παρουσιάζονται οι πειραματικές μετρήσεις (μαύρα τετράγωνα) και αποτελέσματα της υπολογιστικής ανάλυσης (γραμμές).

Το Σχ. Π-8 παρουσιάζει τους ρυθμούς αντιδράσεων αέριας φάσης, όταν η θερμοκρασία απόθεσης είναι 223°C και 215°C (Σχ. Π8α και β, αντίστοιχα), κατά μήκος μιας οριζόντιας γραμμής μήκους ίσου με της ακτίνας του υποστρώματος και σε απόσταση 1 mm πάνω από το υπόστρωμα. Οι αντιδράσεις που φαίνονται στα διαγράμματα αντιστοιχούν στη διάσπαση των $Fe(CO)_5$, $Fe(CO)_4$ και $Fe(CO)_3$ προς $Fe(CO)_4$, $Fe(CO)_3$ και $Fe(CO)_2$, αντίστοιχα, καθώς και στον συνδυασμό του $Fe(CO)_2$ με ένα CO για τον σχηματισμό του $Fe(CO)_3$. Οι υπόλοιπες αντιδράσεις αέριας φάσης έχουν μηδενικούς ρυθμούς. Παρατηρείται ότι στην υψηλότερη θερμοκρασία οι ρυθμοί διάσπασης της πρόδρομης ένωσης και των ενδιάμεσων συμπλόκων είναι υψηλότεροι από τους αντίστοιχους ρυθμούς σε θερμοκρασία 215°C. Συνεπώς, μειώνεται το κλάσμα μάζας του $Fe(CO)_5$ (Σχ. Π-8γ) που είναι διαθέσιμο για την επιφανειακή αντίδραση. Αντίθετα, το κλάσμα μάζας του $Fe(CO)_3$ αυξάνεται στους 223°C, ως αποτέλεσμα του υψηλότερου ρυθμού διάσπασης του $Fe(CO)_5$ στην αέρια φάση. Αυτή η τάση γίνεται εντονότερη καθώς το αέριο μείγμα προσεγγίζει το υπόστρωμα, όπου οι θερμοκρασίες είναι υψηλότερες, και τελικά οδηγεί στη μείωση του ρυθμού απόθεσης. Το κλάσμα μάζας του CO, το οποίο παράγεται από τις διασπάσεις της πρόδρομης ένωσης και

των ενδιάμεσων συμπλόκων της, παρουσιάζεται στο Σχ. Π-8δ. Φαίνεται ότι στην υψηλότερη θερμοκρασία, παράγεται περισσότερο CO κάτι το οποίο συμβάλλει στον κορεσμό της επιφάνειας του υποστρώματος και στην παρεμπόδιση της διεργασίας απόθεσης. Αντιδράσεις αέριας φάσης συμβαίνουν με χαμηλότερους ρυθμούς ακόμα και στην περιοχή όπου ελέγχων μηχανισμός είναι οι επιφανειακές αντιδράσεις.

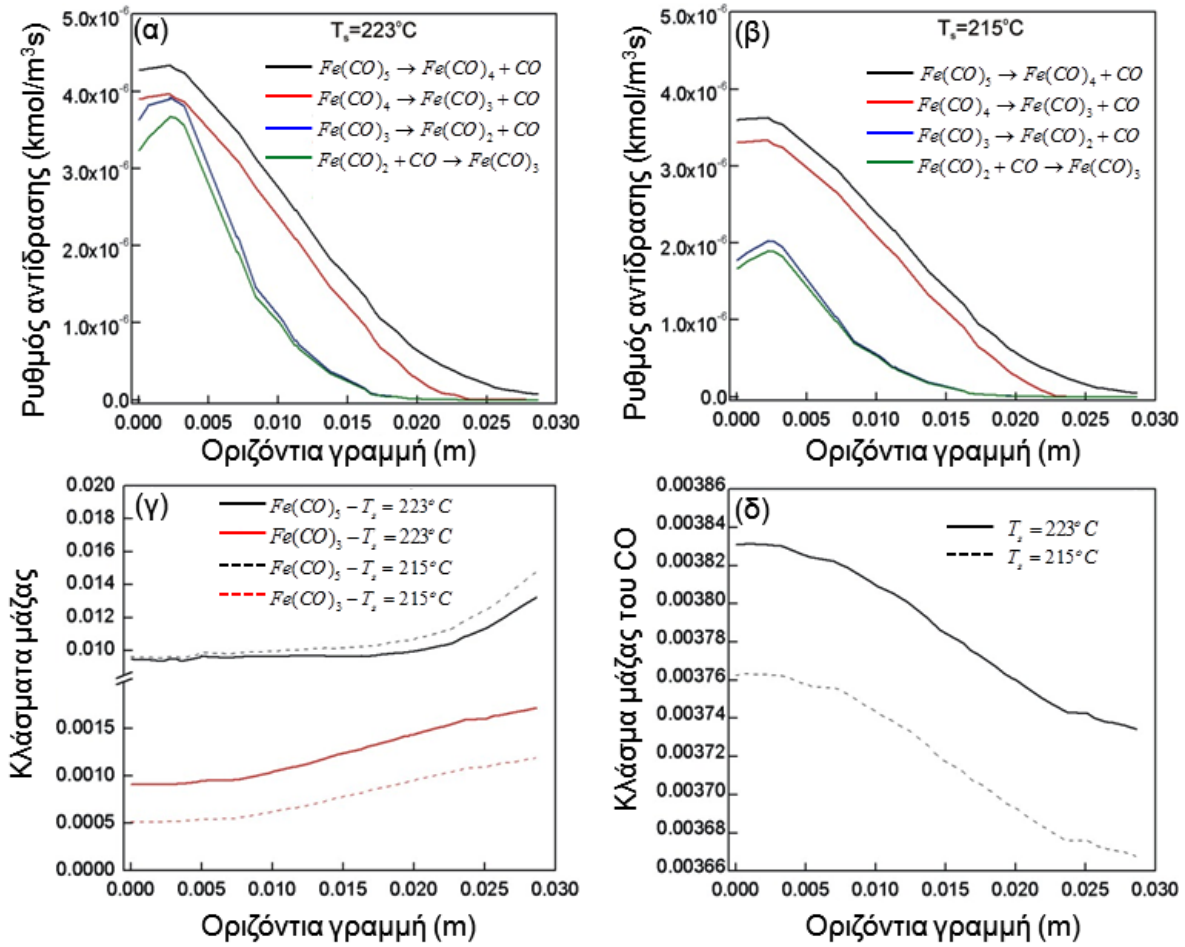

Σχ. Π-8: Οι ρυθμοί των αντιδράσεων αέριας φάσης όταν η θερμοκρασία απόθεσης είναι (α) T_s=223°C και (β) T_s=215°C. Παρουσιάζονται οι ρυθμοί διάσπασης του $Fe(CO)_5$ (μαύρες γραμμές), του $Fe(CO)_4$ (κόκκινες γραμμές), του $Fe(CO)_3$ (μπλε γραμμές) και ο ρυθμός της αντίδρασης $Fe(CO)_2$+CO (πράσινες γραμμές). (γ) Τα κλάσματα μάζας του $Fe(CO)_5$ (μαύρες γραμμές) και του $Fe(CO)_3$ (κόκκινες γραμμές) σε θερμοκρασίες απόθεσης T_s=223°C (συνεχείς γραμμές) και T_s=215°C (διακεκομμένες γραμμές). (δ) Το κλάσμα μάζας του CO σε T_s=223°C (συνεχείς γραμμές) και T_s=215°C (διακεκομμένες γραμμές).

Στη συνέχεια, διερευνάται η εξάρτηση του ρυθμού απόθεσης από την πίεση του αντιδραστήρα. Για τη διερεύνηση αυτή, η πίεση μεταβάλλεται σε ένα σχετικά περιορισμένο εύρος 10 – 40 Torr και η θερμοκρασία διατηρείται σταθερή στους 180°C. Τα αποτελέσματα παρουσιάζονται στο Σχ. Π-9, με μαύρα τετράγωνα για τις πειραματικές μετρήσεις και πράσινα τρίγωνα για τις θεωρητικές προβλέψεις. Παρατηρείται ότι ο ρυθμός απόθεσης μειώνεται από 58 nm/min σε 7 nm/min με αύξηση της πίεσης από 10 Torr σε 40 Torr. Η αλλαγή του ρυθμού απόθεσης συναρτήσει της πίεσης προβλέπεται με ακρίβεια από το πρότυπο μακρο-κλίμακας.

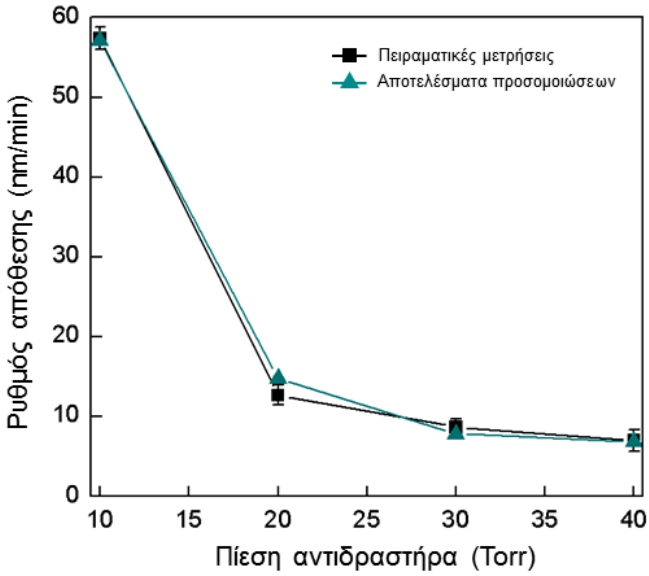

Σχ. Π-9: Εξάρτηση του ρυθμού απόθεσης από την πίεση του αντιδραστήρα. Τα αποτελέσματα αντιστοιχούν σε πειραματικές μετρήσεις (μαύρα τετράγωνα) και υπολογιστικές προβλέψεις (πράσινα τρίγωνα).

Στο Σχ. Π-10, παρουσιάζονται οι ρυθμοί διάσπασης του $Fe(CO)_5$ και του $Fe(CO)_3$ (Σχ. Π-10α) καθώς και ο συντελεστής διάχυσης αυτών των δύο στοιχείων (Σχ. Π-10β), για τις δύο παραπάνω πιέσεις. Οι παράμετροι αυτές υπολογίζονται κατά μήκος μιας οριζόντιας γραμμής μήκους ίσου με της ακτίνας του υποστρώματος και σε απόσταση 1 mm πάνω από το υπόστρωμα. Παρατηρείται ότι ο ρυθμός διάσπασης του $Fe(CO)_5$ και του $Fe(CO)_3$ αυξάνεται με την αύξηση της πίεσης, με συνέπεια την πτώση του ρυθμού απόθεσης. Επιπλέον, στο Σχ. Π-10β φαίνεται ότι η αύξηση της πίεσης οδηγεί στη μείωση του συντελεστή διάχυσης των συστατικών $Fe(CO)_5$ και $Fe(CO)_3$. Συνεπώς, η συγκέντρωση των στοιχείων αυτών στο υπόστρωμα είναι μικρότερη, με αποτέλεσμα ο ρυθμός απόθεσης να μειώνεται σε υψηλότερες πιέσεις.

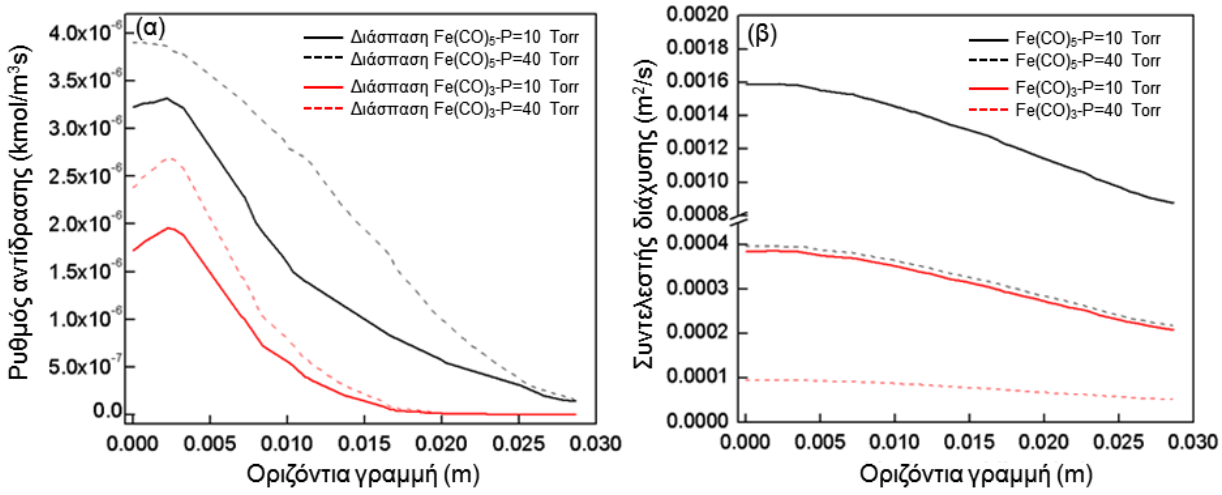

Σχ. Π-10: (α) Οι ρυθμοί διάσπασης του $Fe(CO)_5$ (μαύρες γραμμές) και του $Fe(CO)_3$ (κόκκινες γραμμές) και (β) οι συντελεστές διάχυσης του $Fe(CO)_5$ (μαύρες γραμμές) και του $Fe(CO)_3$ (κόκκινες γραμμές), για πιέσεις P=10 Torr (συνεχείς γραμμές) και P=40 Torr (διακεκομμένες γραμμές). Η θερμοκρασία είναι σταθερή στους 180°C.

Το πρότυπο μακρο-κλίμακας προβλέπει με ακρίβεια την εξάρτηση του ρυθμού απόθεσης από τη θερμοκρασία στο εύρος 130°C – 250°C. Η υπολογιστική ανάλυση καταδεικνύει ότι ο ρυθμός απόθεσης σε θερμοκρασίες μεγαλύτερες των 200°C μειώνεται λόγω του αυξημένου ρυθμού διάσπασης του $Fe(CO)_5$ στην αέρια φάση και λόγω κορεσμού της επιφάνειας των υποστρωμάτων, που παρεμποδίζεται από το CO. Σε ότι αφορά την εξάρτηση του ρυθμού απόθεσης από την πίεση, τα θεωρητικά αποτελέσματα βρίσκονται σε συμφωνία με τις πειραματικές μετρήσεις. Η πτώση του ρυθμού απόθεσης με την αύξηση της πίεσης οφείλεται στην αυξημένη αέρια διάσπαση των $Fe(CO)_5$ και $Fe(CO)_3$ καθώς και στη μείωση του μαζικού συντελεστή διάχυσής τους, όπως αποδείχθηκε μέσω της υπολογιστικής ανάλυσης. Οι λόγοι που οδηγούν στη μείωση του ρυθμού απόθεσης με την αύξηση της πίεσης και της θερμοκρασίας βρίσκονται σε συμφωνία με προηγούμενες εργασίες στη βιβλιογραφία (Fau-Canillac and Maury, 1994; Lane *et al*., 1997; Zhang *et al*., 2016).

Τα κλάσματα μάζας του $Fe(CO)_5$ και του $Fe(CO)_3$ που υπολογίζονται από το πρότυπο μακρο-κλίμακας στο επίπεδο της επιφάνειας των υποστρωμάτων, τροφοδοτούνται στο πρότυπο kMC για την πραγματοποίηση προσομοιώσεων πολλαπλών χωρικών κλιμάκων. Η πληροφορία που χρειάζεται για την περιγραφή της επιφανειακής χημείας στο επίπεδο της νανο-κλίμακας ενσωματώνεται στον συντελεστή προσκόλλησης, όπως συνέβη και στην περίπτωση του αλουμινίου. Οι θεωρητικές προβλέψεις (πράσινα τρίγωνα) και οι πειραματικές μετρήσεις (μαύρα τετράγωνα) για την τραχύτητα των υμενίων Fe συναρτήσει της θερμοκρασίας παρουσιάζονται στο Σχ. Π-11. Πειραματικά, η τραχύτητα αυξάνεται με αύξηση της θερμοκρασίας μέχρι τους 150°C από 0.67 μm σε 0.75 μm και στη συνέχεια μειώνεται μονότονα (0.48 μm) μέχρι τους 190°C. Περαιτέρω αύξηση της θερμοκρασίας οδηγεί σε απότομη μείωση της τραχύτητας (0.34 μm), καθώς η μορφολογία του υμενίου διαφοροποιείται (βλ. Σχ. Π-6). Σε υψηλότερες θερμοκρασίες η τραχύτητα μειώνεται σταδιακά και τελικά σταθεροποιείται (0.16 μm) στο εύρος 230°C – 250°C.

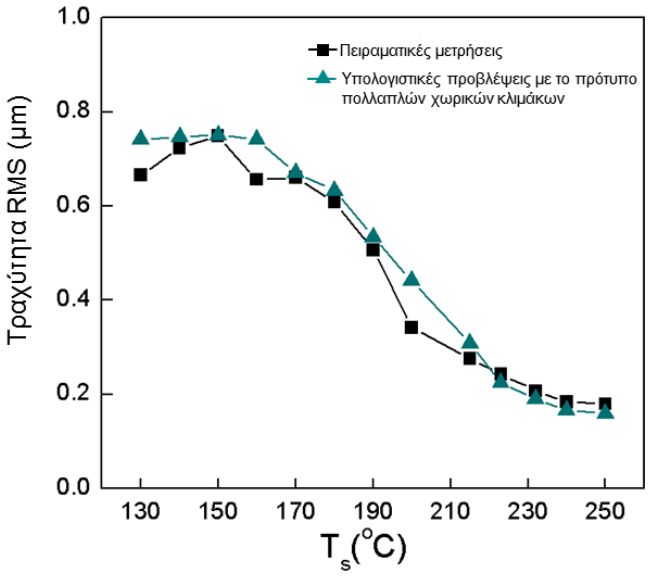

Σχ. Π-11: Εξέλιξη της τραχύτητας, RMS, υμενίων Fe με τη θερμοκρασία απόθεσης, T_s. Τα αποτελέσματα αντιστοιχούν σε πειραματικές μετρήσεις (μαύρα τετράγωνα) και θεωρητικές προβλέψεις (πράσινα τρίγωνα).

Οι θεωρητικές προβλέψεις του προτύπου πολλαπλών χωρικών κλιμάκων βρίσκονται σε ικανοποιητική συμφωνία με τα πειραματικά δεδομένα. Ωστόσο, στο εύρος 190^{o}C – 200^{o}C οι προβλέψεις είναι λιγότερο ακριβείς, λόγω του ότι η αλλαγή της νανο-μορφολογίας των υμενίων που παρατηρείται πειραματικά δε λαμβάνεται υπόψη στο πρότυπο πολλαπλών χωρικών κλιμάκων. Σε υψηλότερες θερμοκρασίες, η σταθεροποίηση της RMS προβλέπεται υπολογιστικά, καθώς σε αυτή την περιοχή οι διακυμάνσεις των γεγονότων διάχυσης που συμβάλλουν στην εξομάλυνση της επιφάνειας, είναι μικρές. Το πρότυπο πολλαπλών χωρικών κλιμάκων για την προσομοίωση επιφανειών υμενίων Fe επιδέχεται βελτιώσεων, ώστε να λαμβάνει υπόψη την ακριβή κρυσταλλογραφική δομή τους. Βελτιώσεις τέτοιου τύπου ενδέχεται να οδηγήσουν στη μεγαλύτερη ακρίβεια των θεωρητικών προβλέψεων και στην προσομοίωση περισσότερων επιφανειακών χαρακτηριστικών, όπως ο σχηματισμός συσσωματωμάτων.

Με βάση τη διερεύνηση των ΧΑΑ για απόθεση υμενίων Al και Fe, εφαρμόζεται μια διεργασία συναπόθεσης των δύο μετάλλων. Για την παραγωγή της προσεγγιστικής (approximant) φάσης $Al_{13}Fe_4$, οι συγκεντρώσεις των δύο μετάλλων στο υμένιο πρέπει να προσεγγίζουν τον λόγο 13:4. Η θερμοκρασία συναπόθεσης ορίζεται στους 200^{o}C, όπου για το μεν Al η ΧΑΑ ελέγχεται από τα φαινόμενα μεταφοράς, για το δε Fe η διεργασία βρίσκεται στη μεταβατική περιοχή, στην οποία οι επιφανειακές αντιδράσεις και τα φαινόμενα μεταφοράς είναι εξίσου σημαντικές για τη ΧΑΑ. Όπως έχει αναφερθεί παραπάνω, και στις δύο διεργασίες πραγματοποιούνται αντιδράσεις αέριας φάσεις σε όλο το εξεταζόμενο θερμοκρασιακό εύρος. Η επιλογή των 200^{o}C για τη διεργασία συναπόθεσης στοχεύει στον περιορισμό των αντιδράσεων αέριας φάσης, που μπορούν να οδηγήσουν σε ανεπιθύμητες αλληλεπιδράσεις μεταξύ των πρόδρομων ενώσεων. Στη συγκεκριμένη θερμοκρασία, τα υμενία Al παρουσιάζουν υψηλό ρυθμό απόθεσης, χαμηλή τραχύτητα και ικανοποιητική κάλυψη της επιφάνειας του υποστρώματος. Αντίθετα, η μορφολογία των υμενίων Fe είναι βελονοειδής και πορώδης.

Κατά τη συναπόθεση, υδρογόνο (H_2) προστίθεται στο αέριο μείγμα εισόδου στον αντιδραστήρα. Σκοπός είναι η μερική αναγωγή των οξειδομένων ενώσεων και κυρίως η αναχαίτιση της οξείδωσης του Al από το οξυγόνο (O) που παράγεται από τη διάσπαση του $Fe(CO)_5$. Το Σχ. Π-12 παρουσιάζει τη στοιχειακή ανάλυση του υμενίου σε ατομικό επίπεδο συναρτήσει της ροής H_2 στο μείγμα εισόδου. Η στοιχειακή ανάλυση πραγματοποιείται με τη μέθοδο της μικροανάλυσης ηλεκτρονίων (EPMA) για τον προσδιορισμό των στοιχείων Al, Fe, O και C. Παρατηρείται ότι στην περίπτωση που δεν χρησιμοποιείται H_2 στο αέριο μείγμα εισόδου στον αντιδραστήρα, η σύσταση των δύο μετάλλων στα αποτιθέμενα υμένια αντιστοιχεί σε έναν υποθετικό λόγο 13:1.3, που αποκλίνει σημαντικά από το επιθυμητό 13:4. Επιπλέον, τα υμένια αυτά περιέχουν υψηλή συγκέντρωση O (25%), η οποία ευνοεί τον σχηματισμό οξειδίων και εμποδίζει τον σχηματισμό διαμεταλλικών φάσεων. Η προσθήκη H_2 δεν έχει μεγάλη επίδραση στον περιορισμό του O καθώς το τελευταίο μειώνεται ελαφρώς στο 18% στην καλύτερη περίπτωση. Ωστόσο, επιδρά σημαντικά στον λόγο Al:Fe. Σε ότι

αφορά στη ΧΑΑ του Al, το H_2 μετατοπίζει την ισορροπία της επιφανειακής αντίδρασης του Al προς κατεύθυνση αντίθετη από την απόθεση. Ταυτόχρονα, φαίνεται να ευνοεί την απόθεση του Fe, πιθανώς λόγω σχηματισμού υδρογονανθράκων που αποσπούν τα μόρια CO από την επιφάνεια. Συνεπώς, με τη μείωση της συγκέντρωσης του Al και την αύξηση της συγκέντρωσης του Fe, ο λόγος των δύο μετάλλων βελτιώνεται σε 13:2.5, που όμως εξακολουθεί να αποκλίνει από το επιθυμητό 13:4.

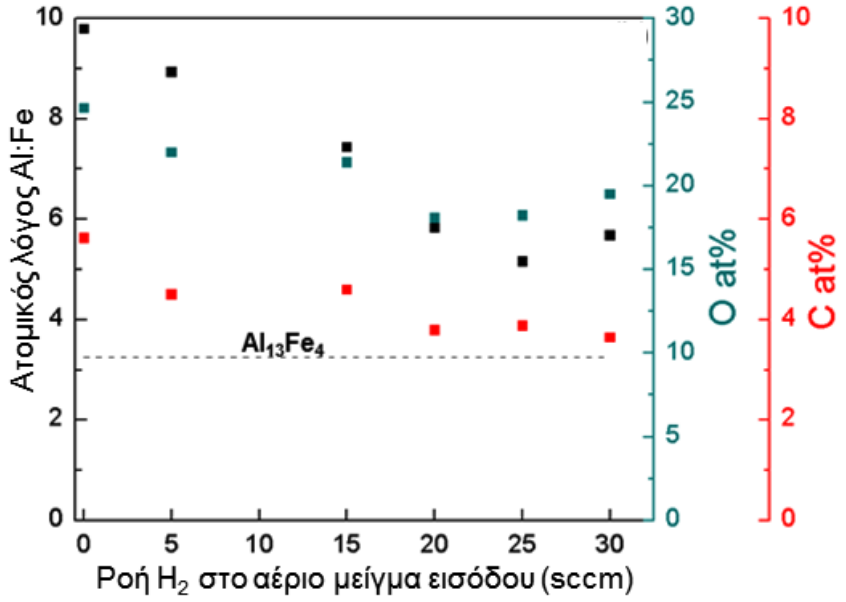

Σχ. Π-12: Στοιχειακή ανάλυση σε ατομικό επίπεδο συναρτήσει της ροής H_2 στο αέριο μείγμα εισόδου στον αντιδραστήρα.

Τα συναποτιθέμενα υμένια αποτελούνται από μεταλλικό Al, Fe και άμορφα οξείδια, ενώ δεν εντοπίζονται φάσεις διαμεταλλικών ενώσεων. Οι υψηλές συγκεντρώσεις O καθιστούν την περαιτέρω διερεύνηση της συναπόθεσης σε αυτές τις συνθήκες δύσκολη. Μελλοντικά, θα μπορούσε να μελετηθεί η συναπόθεση σε χαμηλότερες θερμοκρασίες και σε συνδυασμό με τη θερμική κατεργασία των υμενίων. Η προτυποποίηση της διεργασίας θα μπορούσε να βοηθήσει αυτή τη διερεύνηση.

Παρόλα αυτά, παρέχεται η εναλλακτική διεργασία της διαδοχικής απόθεσης των δύο μετάλλων. Κατά τη διάρκεια της διαδοχικής απόθεσης, οι πρόδρομες ενώσεις δεν έρχονται σε άμεση επαφή μεταξύ τους και συνεπώς μειώνονται οι πιθανότητες απόθεσης υμενίων με υψηλές συγκεντρώσεις O. Η ΧΑΑ του Al πραγματοποιείται σε θερμοκρασία 180°C και πίεση 10 Torr. Η ΧΑΑ του Fe πραγματοποιείται σε θερμοκρασία 140°C και πίεση 40 Torr. Η επιλογή των συγκεκριμένων συνθηκών γίνεται με βάση την πειραματική και υπολογιστική ανάλυση που προαναφέρθηκε και στοχεύει στη δημιουργία υμενίων με υψηλές συγκεντρώσεις Al, όπως απαιτείται από τη σύσταση της φάσης $Al_{13}Fe_4$. Πειράματα διαδοχικής απόθεσης πραγματοποιούνται σε υποστρώματα γυαλιού και διοξειδίου του πυριτίου (SiO_2). Αποφεύγεται η χρήση υποστρωμάτων πυριτίου, διότι μπορεί να οδηγήσει στην ανάπτυξη πυριτιδίων (silicides) του σιδήρου. Η διαδοχική απόθεση ακολουθείται από θερμική κατεργασία των υμενίων για την ενίσχυση της αντιδραστικότητας μεταξύ των δύο

μετάλλων που μπορεί να υποβοηθήσει τον σχηματισμό διαμεταλλικών ενώσεων. Συγκεκριμένα, η θερμική κατεργασία πραγματοποιείται στους 575^{o}C, όπου έχει παρατηρηθεί ο σχηματισμός της φάσης $Al_{13}Fe_4$ (Haidara *et al*., 2012).

Η φασματοσκοπία φωτοηλεκτρονίων με ακτίνες X (XPS) χρησιμοποιείται για τον χαρακτηρισμό της επιφάνειας των υμενίων Al-Fe και για τον ποσοτικό προσδιορισμό της στοιχειακής σύστασης στο επίπεδο της επιφάνειας. Με βάση αυτές τις μετρήσεις, ο λόγος Al:Fe ισούται με 13:4.3, τιμή που είναι κοντά στον στόχο του 13:4. Το Σχ. Π-13 απεικονίζει τα XPS φάσματα του Fe 2p και του Al 2p στην επιφάνεια ενός υμενίου Al-Fe, που αναπτύχθηκε με τη διεργασία της διαδοχικής απόθεσης στις παραπάνω συνθήκες. Το φάσμα Fe 2p (Π-13α) περιέχει μόνο μία κορυφή με μικρή μετατόπιση ως προς το φάσμα αναφοράς που αποδίδεται σε σύμπλοκο Al-Fe. Στο φάσμα Al 2p (Π-13b), η κορυφή στα 72.2 eV αντιστοιχεί σε μεταλλικό Al, ενώ στα 74.6 eV σε οξείδιο του Al. Για αυτό υποθέτουμε ότι στην επιφάνεια αυτών των υμενίων υπάρχει ένα λεπτό στρώμα οξειδίου του Al, το οποίο όμως δεν επεκτείνεται στο υπόλοιπο υμένιο και δεν επηρεάζει το σχηματισμό διαμεταλλικών φάσεων Al-Fe.

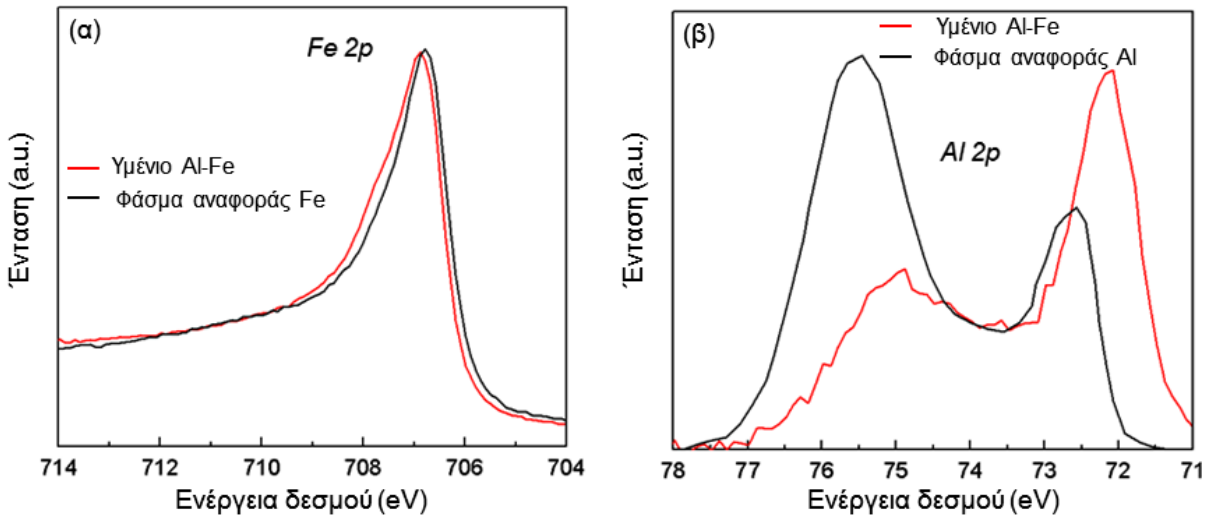

Σχ. Π-13: Το XPS φάσμα ενός υμενίου Al-Fe. (α) Το φάσμα Fe 2p σε σύγκριση με το φάσμα αναφοράς του Fe. (β) Το φάσμα Al 2p σε σύγκριση με το φάσμα αναφοράς του Al.

Το Σχ. Π-14 παρουσιάζει το φάσμα διάθλασης ακτινών X (XRD) ενός υμενίου Al-Fe για τις ίδιες συνθήκες απόθεσης. Το φάσμα συγκρίνεται με το πρότυπο φάσμα του $Al_{13}Fe_4$ που παρέχεται από τη βιβλιογραφία (Ellner, 1995; Grin *et al*., 1994). Παρατηρείται ότι το παρόν φάσμα παρουσιάζει ικανοποιητική συμφωνία με το πρότυπο της βιβλιογραφίας. Συγκεκριμένα, οι κορυφές σε χαμηλές γωνίες 2θ, μεταξύ 20°-30°, μαζί με τις κορυφές μεγάλης έντασης στις 40°-50° και κάποιες κορυφές μικρότερης έντασης σε μεγαλύτερες 2θ γωνίες, είναι χαρακτηριστικές της προσεγγιστικής φάσης m-$Al_{13}Fe_4$. Παρατηρούνται, όμως, και άλλες κορυφές, όπως για παράδειγμα σε γωνίες 38°-39° και 50° που αποδίδονται στη φάση Al_5Fe_2 καθώς και σε μεταλλικό Al. Από την ύπαρξη διαφορετικών φάσεων συμπεραίνεται ότι η χημική σύσταση στο υμένιο δεν είναι ομοιόμορφη. Για τον προσδιορισμό αυτής της ομοιομορφίας χρησιμοποιείται η μέθοδος της ηλεκτρονικής

μικροσκοπίας σταθερής δέσμης διέλευσης (STEM) συνδυασμένη με τη φασματοσκοπία ενεργειακής διασποράς (EDX).

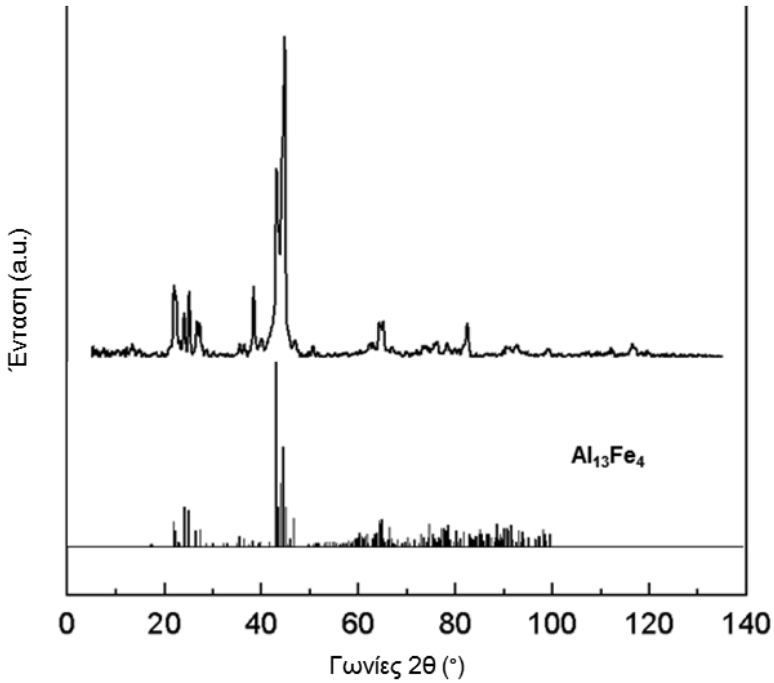

Σχ. Π-14: Το XRD φάσμα ενός υμενίου Al-Fe, που αποτέθηκε στις συνθήκες που περιγράφονται παραπάνω. Το πρότυπο φάσμα στο κάτω μέρος του σχήματος παρέχεται από τη βιβλιογραφία (Ellner, 1995; Grin *et al*., 1994).

Οι παρατηρήσεις με τη μέθοδο STEM παρουσιάζονται στο Σχ. Π-15. Η μικρογραφία του Σχ. Π-15α αποκαλύπτει ένα πορώδες υμένιο, στο οποίο η ανάμειξη των δύο μετάλλων είναι πλήρης. Ωστόσο, επιβεβαιώνεται ότι η στοιχειακή σύσταση είναι ανομοιόμορφη κατά μήκος του υμενίου. Για παράδειγμα, στην εικόνα Π-15β φαίνεται ότι περισσότερο από το 50% κατ'όγκο του κάτω μέρους του υμενίου (bottom) αποτελείται από κρυστάλλους πλούσιους σε Fe (Al(25)Fe(75) ή Al(15)Fe(85) όπως μετρήθηκε από το STEM/EDX). Στο πάνω μέρος του υμενίου (top), ο Fe μειώνεται σταδιακά μέχρις ότου η σύσταση γίνεται ομοιόμορφη. Η εικόνα Π-15γ παρουσιάζει τη στοιχειακή χαρτογράφηση στο πάνω μέρος του υμενίου. Παρατηρούμε ότι υπάρχει η ομοιόμορφη κατανομή κρυστάλλων Al(75)Fe(25), που αντιστοιχεί στη σύσταση του $Al_{13}Fe_4$. Η εικόνα Π-15δ παρουσιάζει τη χαρτογράφηση στο μαύρο τετράγωνο της Π-15γ, σε υψηλότερη ανάλυση. Κοντά στους πόρους του υμενίου μετράται υψηλότερη συγκέντρωση Al, που σχετίζεται με την παρουσία του O σε αυτά τα σημεία. Η οξείδωση του Al είναι συνηθισμένη στα κράματά του με τα μέταλλα μετάπτωσης και βρίσκεται σε συμφωνία με τις μετρήσεις XPS, όπου παρατηρήθηκε ένα επιφανειακό στρώμα οξειδίου του Al. Κατά τη διάρκεια της θερμικής κατεργασίας των υμενίων, υποθέτουμε ότι οι διαμεταλλικές Al-Fe φάσεις σχηματίζονται πρώτα στη διεπιφάνεια με το υπόστρωμα. Η υπόθεση αυτή επιβεβαιώνεται από τις παρατηρήσεις με την τεχνική STEM/EDX, όπου φαίνεται ότι οι εμπλουτισμένοι με Fe κρύσταλλοι συγκεντρώνονται στη διεπιφάνεια με το υπόστρωμα.

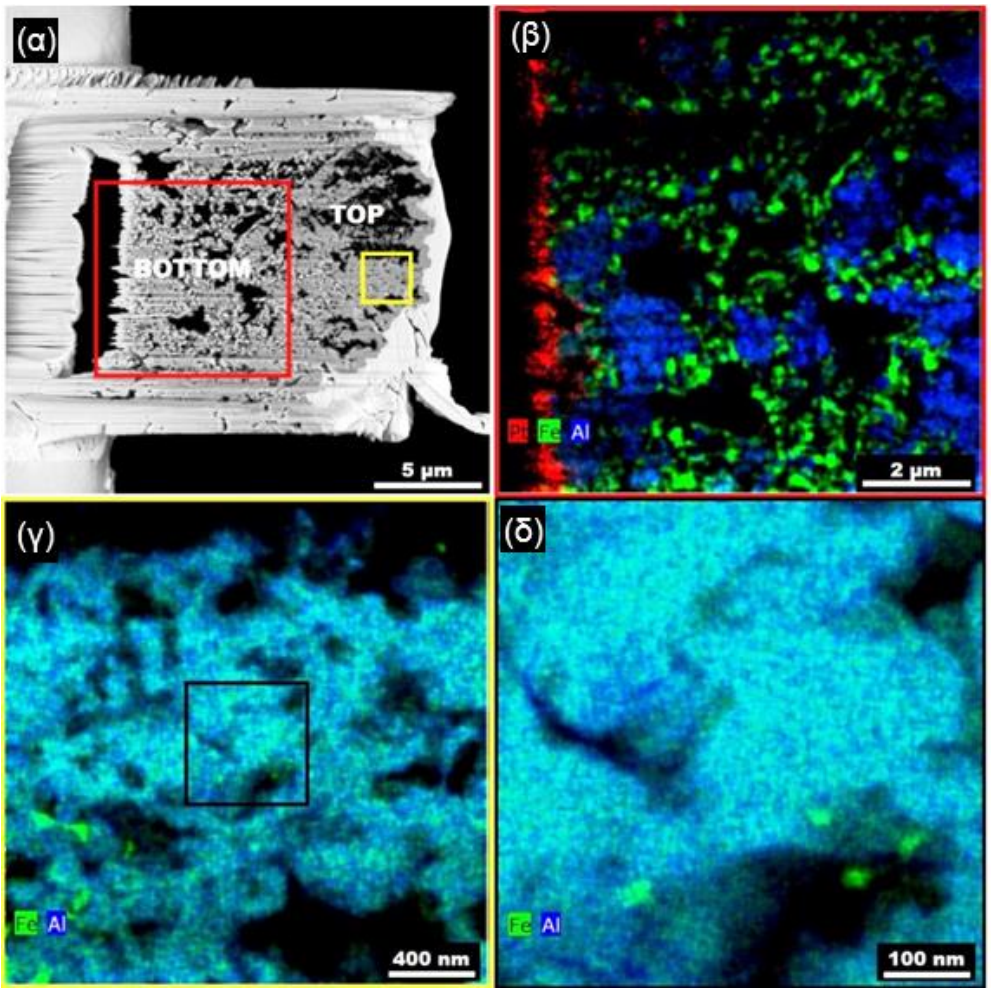

Σχ. Π-15: (α) Μικρογραφία του υμενίου Al-Fe. Χαρτογράφηση STEM/EDX (β) στο κάτω μέρος (κόκκινο τετράγωνο) και (γ) στο πάνω μέρος του υμενίου (κίτρινο τετράγωνο). (δ) STEM/EDX υψηλότερης ανάλυσης στο μαύρο τετράγωνο του γ.

Το Σχ. Π-16 παρουσιάζει την ανάλυση ηλεκτρονικής μικροσκοπίας διέλευσης (TEM) ενός υμενίου Al-Fe. Στο κάτω μισό του υμενίου τα δύο μέταλλα είναι πλήρως αναμειγμένα, ενώ στο πάνω μισό εντοπίζονται εναλλασσόμενες περιοχές Al και Al-Fe, κάθετες στο υπόστρωμα (Σχ. Π-16α). Η μεγέθυνση της διεπιφάνειας μεταξύ των περιοχών Al και Al-Fe (άσπρος κύκλος στο Σχ. Π-16α) παρουσιάζεται στο Σχ. Π-16β. Παρατηρείται ένας ορθογώνιος κρύσταλλος Al-Fe πάχους 180 nm, που έχει αναπτυχθεί πλευρικά στην περιοχή Al. Η υψηλή ανάλυση του κρυστάλλου αυτού παρουσιάζεται στο Σχ. Π-16γ. Μέσω του μετασχηματισμού αυτής της εικόνας με τη μέθοδο FFT (*fast Fourier transform*) επιβεβαιώνεται ο σχηματισμός της φάσης m-$Al_{13}Fe_4$ και προσδιορίζονται οι κρυσταλλογραφικοί παράμετροι a=15.49Å, b=8.08Å, c=12.48Å, β=107.75°, που βρίσκονται σε συμφωνία με αντίστοιχα αποτελέσματα της βιβλιογραφίας (Ellner, 1994; Grin *et al*., 1995).

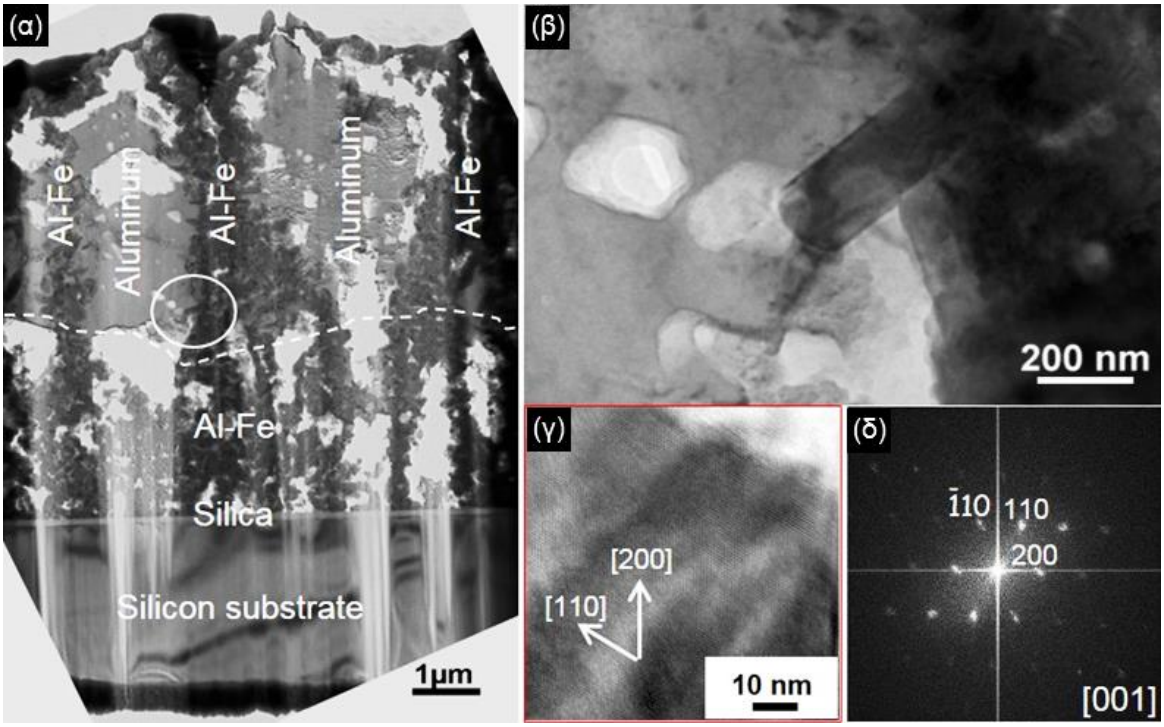

Σχ. Π-16: (α) Τομή TEM ενός υμενίου Al-Fe. (β) Μεγέθυνση στην περιοχή που καθορίζεται από τον άσπρο κύκλο στο α. (γ) Εικόνα υψηλής ανάλυσης του νανο-κρυστάλλου Al-Fe που απεικονίζεται στο β. (δ) Μετασχηματισμός Fourier της εικόνας γ, ο οποίος επιβεβαιώνει το σχηματισμό της φάσης m-$Al_{13}Fe_4$ κατά μήκος του άξονα [001].

Στη συνέχεια, τα υμένια που περιέχουν την προσεγγιστική φάση m-$Al_{13}Fe_4$ δοκιμάζονται για τις καταλυτικές τους ιδιότητες στη διεργασία της ημι-υδρογόνωσης του ακετυλενίου. Τα καταλυτικά πειράματα πραγματοποιούνται στο εξειδικευμένο Ινστιτούτο IRCELYON, στη Γαλλία. Οι αρχικές μετρήσεις καταδεικνύουν ότι η δραστικότητα των υμενίων είναι περιορισμένη· σε όλες τις περιπτώσεις που δοκιμάζονται, η μετατροπή του ακετυλενίου σε αιθυλένιο είναι πολύ μικρή. Η κακή απόδοση των υμενίων μπορεί να αποδοθεί στην οξείδωσή τους, καθώς και στην ανομοιομορφία της σύστασής τους, όπως αυτή παρατηρήθηκε παραπάνω. Για τη βελτίωση της ομοιομορφίας στη σύσταση, ο χρόνος της θερμικής κατεργασίας των υμενίων πρέπει να αυξηθεί. Επιπλέον, η βελτίωση της πορώδους δομής των υμενίων μπορεί να καταστήσει την οξείδωσή τους δυσκολότερη. Η υπολογιστική ανάλυση πολλαπλών χωρικών κλιμάκων μπορεί να βοηθήσει προς αυτήν την κατεύθυνση, μέσω της διερεύνησης της πορώδους δομής των αποτιθέμενων υμενίων σε συνάρτηση με τις λειτουργικές συνθήκες.

Dépôt chimique en phase vapeur d'Al, Fe et de la phase approximante $Al_{13}Fe_4$: Expériences et simulations multi-échelles

Ioannis G. Aviziotis

Résumé étendu en Français

La thèse présente une étude combinée expérimentale et théorique du procédé de dépôt chimique en phase vapeur (CVD). Le but ultime est sa mise en œuvre pour la formation d'alliages complexes métalliques (complex metallic alloys – CMAs) et des composés intermétalliques d'aluminium-fer (Al-Fe) sur des surfaces. En particulier, la possibilité de la formation de la phase approximante $Al_{13}Fe_4$ est examinée, ce qui fournit des propriétés multifonctionnelles à des matériaux avancés. Entre autres, $Al_{13}Fe_4$ possède des propriétés catalytiques pour la semi-hydrogénation de l'acétylène en éthylène dans la production de polyéthylène (Armbrüster *et al.*, 2012).

Parmi une gamme de techniques, le dépôt chimique en phase vapeur à partir de précurseurs métallo-organiques (MOCVD) permet un dépôt conforme sur, et la fonctionnalisation de, surfaces complexes, avec un temps de traitement court. Les métaux déposés sont contenus dans des composés moléculaires nommés précurseurs. Les vapeurs des précurseurs sont produites et transportées par un gaz vecteur dans la chambre réactionnelle et à la surface d'un substrat. Les précurseurs participent à des réactions dans la phase gazeuse et à la surface. Le dépôt d'un film métallique se produit lorsque la quantité appropriée d'énergie est fournie au substrat. La mise en œuvre réussie d'un procédé MOCVD est basée sur la sélection de précurseurs appropriés, la production de leurs vapeurs et leur transfert dans le réacteur, le design du réacteur, et le contrôle des mécanismes impliqués dans le procédé. Ceux-ci sont associés à l'inconvénient principal du procédé, à savoir le couplage complexe entrela chimie et le transport.

La modélisation mathématique et informatique d'un procédé MOCVD est un outil précieux pour l'étude de ces interactions complexes. De plus, la modélisation multi-échelle permet l'étude des mécanismes qui se produisent à des échelles spatiales différentes. La modélisation au niveau macroscopique (échelle macro) étudie les mécanismes au niveau du réacteur. La validité est assurée par l'hypothèse de continuum pour la conservation de la masse, de la quantité de mouvement et de l'énergie, décrit par un ensemble d'équations différentielles et non-linéaires. Ces équations sont résolues numériquement, en utilisant des méthodes de calcul de dynamique des fluides, dans l'espace à trois dimensions dans des conditions de régime transitoire ou permanent. La modélisation à l'échelle macro inclut des réactions homogènes dans la phase gazeuse et des réactions hétérogènes qui conduisent au dépôt du film métallique. Les prédictions théoriques obtenues avec l'utilisation de méthodes de calcul sont associés à la dépendance de la vitesse de croissance des films sur les paramètres opérationnels du réacteur et ils fournissent des connaissances sur les mécanismes

du dépôt MOCVD. Ainsi, ils contribuent à la détermination de "fenêtres" opérationnelles préférentielles et à l'optimisation et au contrôle du processus. La fiabilité d'un modèle est assurée par une validation approfondie avec des mesures expérimentales. La modélisation à l'échelle micro- ou nano- est nécessaire pour l'étude des processus de surface telles que l'adsorption, la désorption et la diffusion des molécules ou des atomes. La liaison entre les deux échelles, macro- et nano-, à savoir le développement d'un modèle multi-échelle, est effectuée par l'alimentation du modèle nano avec des informations calculées macroscopiquement. Il permet le calcul des caractéristiques de surface, telles que la rugosité qui est associée aux propriétés finales des films. Dans ce cadre, les simulations macroscopiques et multi-échelles fournissent un ensemble d'informations qui couvre la totalité de la production du film, de la dépendance de la vitesse de dépôt et de l'épaisseur du film sur les conditions opérationnels, à la microstructure du film et ses propriétés.

La mise au point du dépôt de la phase $Al_{13}Fe_4$ est subordonnée à l'étude des procédés MOCVD des films unaires. Si une compatibilité globale (chimique, thermique, de transport) est trouvée, le dépôt simultané (co-dépôt) ou le dépôt séquentiel des constituants métalliques peuvent être réalisées. Des informations sont fournies par le diagramme Arrhenius du procédé MOCVD de chaque métal qui montre la dépendance de la vitesse de croissance avec la température. Le diagramme Arrhenius est le résultat des prédictions théoriques, validées par des mesures expérimentales correspondant. Il permet de distinguer schématiquement des régimes différents, chacun associé à un mécanisme de contrôle du processus de dépôt, que ce soit la cinétique des réactions chimiques de surface (reaction-limited regime) à basse température, ou le transport (diffusion-/mass transport-limited regime) à des températures élevées, ou à des régimes intermédiaires. Pour les processus de co-dépôt ou de dépôt séquentiel, la superposition des deux diagrammes d'Arrhénius de chaque métal à déposer contribue à la détermination d'une "fenêtre" opérationnel commune. Pour le co-dépôt, il est généralement préférable d'opérer dans le régime cinétique. Dans ce régime, les mécanismes qui prévalent sont attribués principalement à des réactions de surface. L'effet des réactions homogènes, qui peut conduire à des vitesses de décomposition élevées et des interactions entre les précurseurs, est limitée. Cependant, pour certains précurseurs la réalisation de réactions en phase gazeuse est inévitable dans toute la gamme des températures étudiée. Ainsi, un processus commun peut être effectué dans une fenêtre de températures contenant des régimes différents pour chaque précurseur. D'une telle manière, le dépôt du premier élément peut être contrôlé par la concentration de la phase gazeuse réactive et le dépôt de la deuxième par la température de dépôt.

Dans ce contexte général, nous étudions la MOCVD de films d'aluminium (Al) et de fer (Fe) et par la suite, le co-dépôt et le dépôt séquentiel des deux métaux. La modélisation mathématique du procédé et les calculs sont réalisées à la *School of Chemical Engineering, National Technical University of Athens (NTUA)* en Grèce, sous la supervision du Prof. A.G. Boudouvis. La contrepartie expérimentale est effectuée dans le laboratoire Centre

Interuniversitaire de Recherche et d'Ingénierie des Matériaux (CIRIMAT) de l'Institut National Polytechnique de Toulouse (INPT), sous la supervision des Drs. C. Vahlas et T. Duguet.

Le dispositif expérimental est composé d'un réacteur MOCVD vertical et cylindrique, avec des parois en acier inoxydable, qui offre la possibilité de fonctionner en mode parois froides ou chaudes. La présence d'un grand porte-substrat à l'intérieur du réacteur permet le dépôt sur plusieurs substrats de surface 1 cm^2. De plus, l'existence d'une douchette qui fait face au porte-substrat améliore l'homogénéisation de l'écoulement des gaz. Le dispositif expérimental présenté a été testé avec succès pour la production de films unaires et intermétalliques (Aloui *et al*., 2012; Krisyuk *et al*., 2011; Xenidou *et al*., 2007; Xenidou *et al*., 2010).

Pour la modélisation mathématique d'un procédé CVD au niveau macroscopique, le modèle mis au point comprend la mise en place expérimentale du réacteur qui est discrétisé en un maillage de cellules élémentaires. Chaque cellule représente un volume fini, dans lequel les valeurs des variables calculées sont considérées stables. Les équations aux dérivées partielles de la conservation de la masse, de la quantité de mouvement et d'énergie sont résolues numériquement dans chaque cellule du maillage avec la méthode des volumes finis (Boudouvis, 2010; Thompson *et al*., 1985; Versteeg et Malalasekera, 2007) et en utilisant le logiciel commercial Fluent (Ansys 12.1 / Documentation Courant 2009).

Le modèle nano est stochastique. Il est basé sur un algorithme de Monte Carlo cinétique (kMC) développé par Lam et Vlachos (2001). Les simulations à l'échelle nanométrique sont effectuées par un code qui est écrit en C / C ++ et il gère trois types de processus de surface: l'adsorption, la migration (diffusion) et la désorption. Pour la description des processus de surface pendant le dépôt l'approximation «solide sur solide» (*solid-on-solid approximation*) est appliquée. Dans le modèle, les interactions entre les atomes de surface ne concernent que les premiers plus proches voisins (*first-nearest neighbors interactions* – Gilmer et Benema, 1972). En première approche, un réseau cubique simple est sélectionné, sans ignorer les structures *fcc* et *bcc* et la texturation de l'Al et du Fe ((111) et (100), respectivement), expérimentalement.

La mise en relation des deux échelles est basée sur l'hypothèse que la vitesse de croissance reste inchangée, quelle que soit l'échelle à laquelle elle est simulée (Masi *et al*., 2000). Les fractions massiques des espèces contribuant au dépôt provenant du calcul macroscopique sont introduites dans le modèle kMC pour la simulation nano.

Pour la CVD de l'Al, le diméthyléthylamine alane (DMEAA) est sélectionné en tant que précurseur. Le choix du précurseur est dicté par une pression de vapeur relativement élevée à température ambiante et la possibilité de dépser des couches minces à des températures relativement basses. Les expériences et l'analyse informatique du processus vise

à étudier la dépendance de la vitesse de croissance et de la microstructure des films sur la température dans la gamme 139°C – 241°C.

La CVD d'Al à partir de DMEAA conduit à des films purs sans contamination au carbone ou à l'azote. La microstructure du film est observée par microscopie électronique à balayage (MEB). Des micrographies de surface et en coupe transverse des films sont présentés sur la Fig. S-1, pour des températures correspondant à 139°C, 198°C et 227°C (Aviziotis *et al*., 2015). Le dépôt à la température la plus basse (Fig. S-1a et b) montre des grains dispersés sur la surface qui forment des morphologies rugueuses avec une mauvaise uniformité et pas de continuité. Contrairement à ce cas, en augmentant la température (Fig. S-1c et d, puis e et f) la densité du film augmente parce que les grains ont coalescé. La mesure du gain de masse, en supposant la masse volumique de l'Al massique, donne une estimation de l'épaisseur de 907 nm (± 90 nm) et 833 nm (± 90 nm) pour 198°C et 227°C, respectivement, à comparer avec des mesures MEB de 873 nm (± 50 nm) et 804 nm (± 50 nm), respectivement. La comparaison des épaisseurs de film estimées par différence de masse et mesurées sur MEB révèle que, sauf pour les basses températures, les résultats sont similaires parce que les films présentent une faible porosité, en dépit de la rugosité de la surface observée.

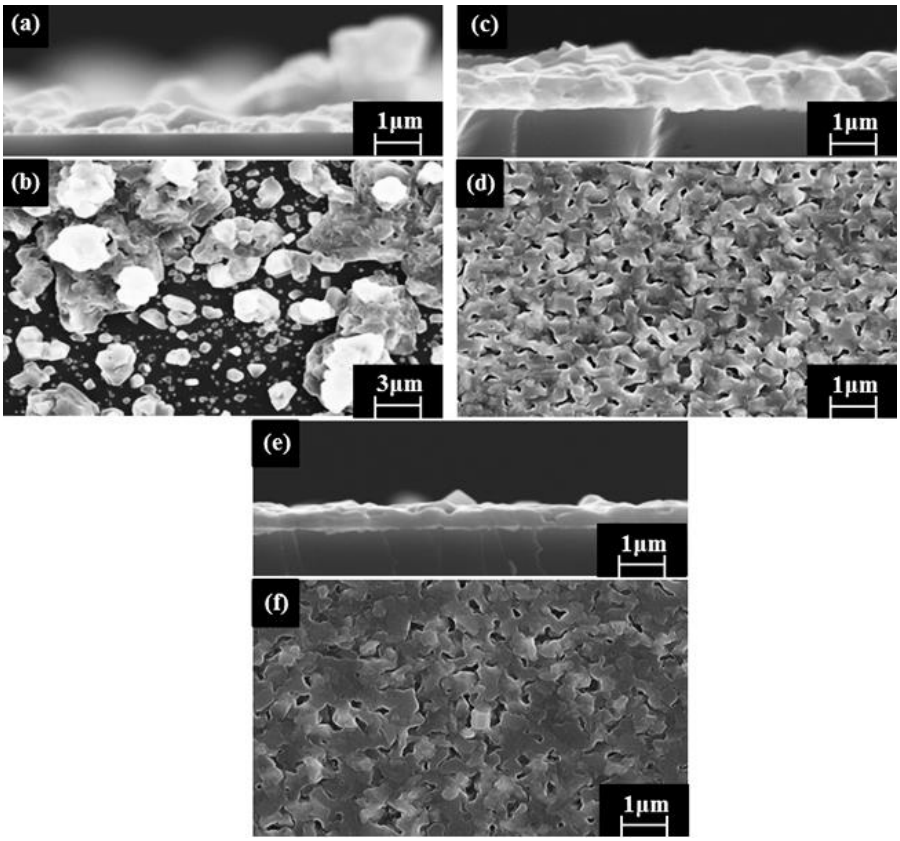

Fig. S-1: Micrographies MEB de surface et en coupe transverse des films d'Al déposés à 139°C (a,b), 198°C (c,d) and 227°C (e,f).

Pour la modélisation macroscopique, le dépôt d'Al à partir de DMEAA comprend une réaction en phase gazeuse et une réaction en surface pour la décomposition du précurseur.

(Han *et al*., 1994; Kim *et al*., 1996; Xenidou *et al*., 2010; Yun *et al*., 1998b). Des cinétiques Arrhenius de premier ordre sont appliquées pour ces réactions. L'énergie d'activation de la réaction en phase gazeuse est fournie par la littérature (Yun *et al*., 1998b), tandis que celle pour la réaction de surface est calculée à partir de la pente de la courbe d'Arrhénius expérimentale, dans le régime cinétique. Les facteurs pré-exponentiels sont basés sur des données expérimentales. Les conditions aux limites appliquées au modèle macroscopique sont basées sur les conditions opérationnelles expérimentales: température d'entrée, T_{en}=100^{o}C, température de la paroi, T_{par}=75^{o}C, température de dépôt, T_s=139^{o}C – 241^{o}C, pression, P=10 Torr et débit de DMEAA à l'entrée du réacteur DMEAA, $Q_{prec} = 2$ sccm.

Le diagramme d'Arrhenius du processus est présenté sur la figure S-2, où les carrés noirs représentent les mesures expérimentales et les deux courbes les résultats de simulations informatiques. Bien que la séparation entre les différentes zones de température est difficile (Jang *et al*., 1998), une augmentation de la vitesse de croissance jusqu'à 185^{o}C montre que, dans ce régime le mécanisme dominant est la cinétique. La détermination des frontières entre les deux régions dans la gamme représentée est similaire aux travaux précédents, où les vitesses de croissance maximales ont été mesurées à des températures de 150^{o}C-160^{o}C (Kim *et al*., 1996; Yang *et al*., 1998; Yun *et al*., 1998a). La différence de 20^{o}C-30^{o}C peut être attribuée aux configurations géométriques et aux conditions expérimentales différentes. Au-dessus de 185^{o}C, la vitesse de croissance montre une légère baisse. À un dépôt au-delà de 240^{o}C conduit à la forte baisse de la vitesse de croissance.

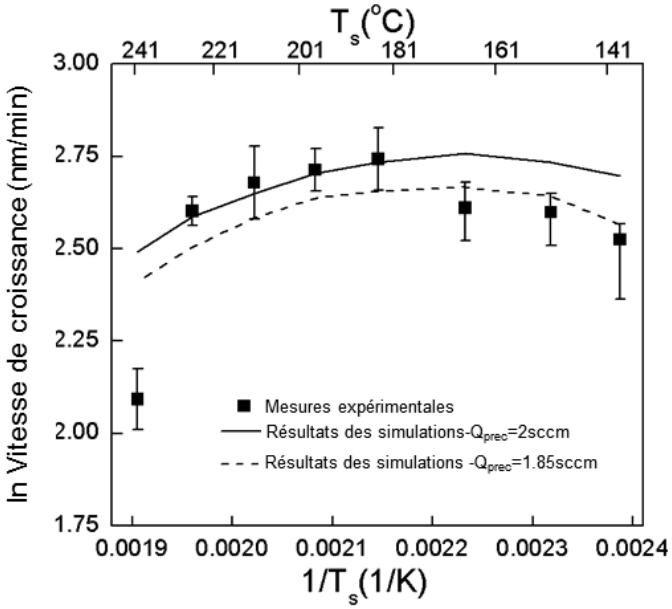

Fig. S-2: Le diagramme d'Arrhenius de la CVD d'Al à partir de DMEAA. Le diagramme montre des mesures expérimentales (carrés noirs) et des résultats des calculs (courbes) pour deux flux de DMEAA différents.

En ce qui concerne les résultats calculés, deux flux de DMEAA différents sont présentées, 2 sccm (ligne noire) et 1.85 sccm (ligne pointillée). La première valeur est calculée en supposant que l'évaporation du précurseur dans le bulleur est réalisée à l'état

d'équilibre thermodynamique, et que la conductivité de la canalisation reliant le bulleur vers la zone de dépôt est infinie. Pour cela, la valeur de 2 sccm correspond à la limite maximale d'écoulement du précurseur à l'entrée du réacteur. Ce débit conduit à une surestimation de la vitesse de croissance dans le régime cinétique.

Par conséquent, plusieurs débits d'entrée du précurseur sont considérés dans la gamme de 1.5 sccm – 1.95 sccm. La meilleure comparaison entre les données expérimentales et les résultats des calculs est obtenue pour un débit de 1.85 sccm. Comme on le voit sur la Fig. S-2, les prédictions théoriques avec cette valeur améliorent la comparaison avec les mesures expérimentales à des température basses avec un petit effet à des températures plus élevées (Aviziotis *et al*., 2015). La modification du débit d'entrée de DMEAA est associée à sa dégradation avant d'atteindre les substrats, le rendant indisponible pour la réaction de surface. Il est généralement admis que, dans le régime des basses températures, la vitesse de dépôt est contrôlée par la réaction de surface, à condition que la vitesse d'alimentation soit supérieure à la vitesse de consommation. Par suite, on pourrait s'attendre à ce que la réduction de l'écoulement du précurseur dans le réacteur aurait eu un effet plus important à des températures élevées.

Cependant, il ne faut pas oublier que le procédé de dépôt implique une réaction en phase gazeuse, qui peut consommer une quantité de précurseur significative, même à basses températures. La Fig. S-3 présente le champ de température dans le réacteur (Fig. S-3a) et la vitesse de réaction en phase gazeuse (Fig. S-3b), lorsque la température du substrat est de 151^{o}C. Il apparaît que la réaction en phase gazeuse de DMEAA se produit non seulement à proximité du substrat, où la température est élevée, mais aussi près de l'entrée du réacteur, à 100^{o}C. On en conclut que la vitesse de la réaction en phase gazeuse est telle qu'elle consomme le précurseur et l'empêche d'atteindre le substrat, diminuant ainsi la quantité disponible pour la réaction de surface.

Les prédictions théoriques sont en bon accord avec les mesures expérimentales dans la gamme 139^{o}C – 227^{o}C. Cependant, à des températures plus élevées, le modèle macroscopique ne parvient pas à prédire les vitesses de croissance mesurées expérimentalement. Le schéma réactionnel généralisé qui est incorporé dans le modèle et les cinétiques Arrhenius de premier ordre ne prennent pas en compte les effets supplémentaires, tels que la formation d'espèces chimiques intermédiaires. Ainsi, le modèle ne peut pas prévoir la réduction abrupte de la vitesse de dépôt. Cependant, le modèle est valide dans la gamme 139^{o}C – 227^{o}C, où les conditions opérationnelles communes peuvent être déterminées pour le procédé de co-dépôt avec le Fe.

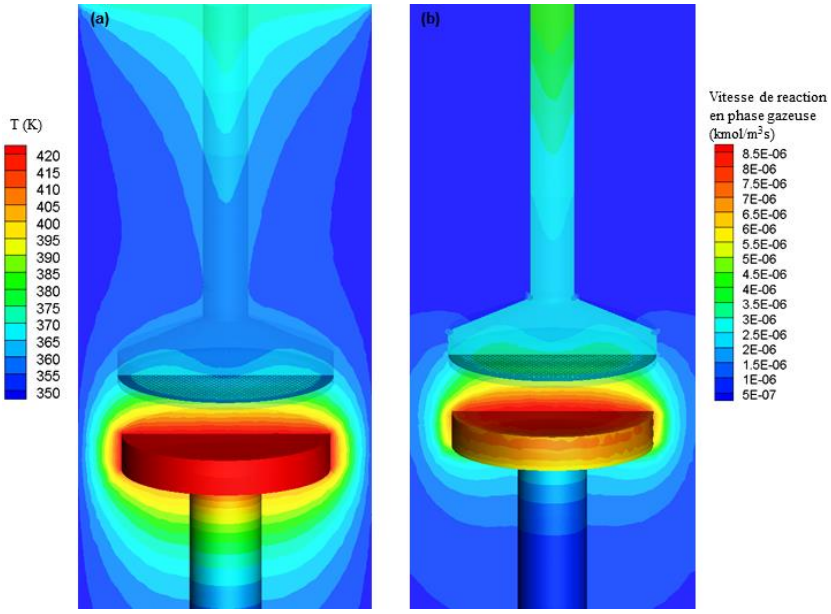

Fig. S-3: (a) Le profil des températures du réacteur et (b) la vitesse de réaction en phase gazeuse, lorsque la température du substrat est de 151°C.

Les calculs macroscopiques fournissent les fractions massiques de DMEAA à la surface du substrat. Ces fractions massiques sont ensuite fournies à l'algorithme kMC pour effectuer des simulations multi-échelles et calculer la rugosité de surface. Les informations pour les réactions chimiques de surface de DMEAA au niveau nano sont incorporées dans le coefficient de collage, s_0. Cette incorporation est réalisée par une régression polynomiale de s_0 des mesures expérimentales de la vitesse de croissance en fonction de la température.

La figure. S-4 montre la rugosité quadratique (*root mean square*, RMS) des films d'Al pour les mesures expérimentales (carrés noirs) et les prédictions théoriques avec le modèle multi-échelle (triangles cyans) (Aviziotis *et al*., 2016). Des mesures expérimentales ont été réalisées par interférométrie optique. Les films d'Al déposés à la plus basse température (139°C) présentent une rugosité élevée (0.6 μm). Elle diminue lorsque la température augmente et atteint sa valeur minimale de 0.15 μm, à 198°C. L'augmentation de la température conduit à la stabilisation de la rugosité. La rugosité RMS est étroitement liée à la variation de la microstructure des films. À des températures inférieures à 150°C, les films déposés ne sont pas continués et sont constituée de grains dispersés de tailles inégales, et la rugosité est élevée. Au contraire, l'augmentation de la température améliore l'uniformité des films et la rugosité diminue.

Les résultats des simulations multi-échelles sont en bon accord avec les mesures expérimentales. L'accord est moins bon à des températures plus élevées, où la rugosité se stabilise. Cette défaillance peut être due à l'application d'un modèle grossier (*coarse-grain*) et sur l'incorporation de l'information chimique dans le coefficient de collage. Le développement d'un modèle qui représentera la structure cristallographique exacte de l'Al et inclura explicitement des réactions chimiques en surface au niveau nano peut améliorer

l'accord modèle-expériences. Il pourrait aussi permettre la simulation de plusieurs caractéristiques de surface, telles que la formation de structures 3D d'Al sur la surface.

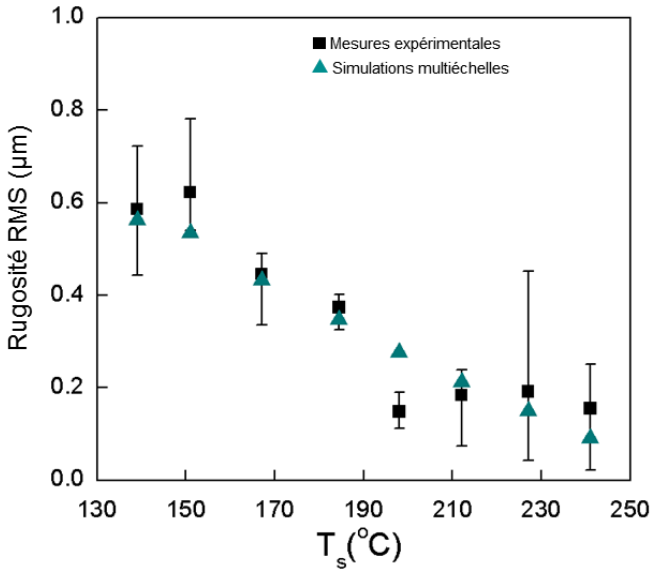

Fig. S-4: La rugosité (RMS) de films d'Al en fonction de la température, T_s. Les carrés noirs correspondent à des mesures expérimentales et les triangles cyans à des prédictions théoriques.

Cependant, le modèle présenté se rapproche bien de la rugosité de surface. Donc, il peut permettre le contrôle des propriétés finales du film. La Figure. S-5 présente la résistivité électrique mesurée expérimentalement (sphères rouges) et évaluées par des calculs en utilisant le modèle Fuchs-Sondheimer (sphères noirs) (modèle FS -. Timalshina *et al.*, 2015), dans lequel la rugosité requise est calculée par le modèle multi-échelle. La flèche dans le plan (x,y) indique la direction d'augmentation de la rugosité. Les points noirs et rouges dans le plan (y,z) et la courbe bleue montre l'évolution de la résistivité électrique en augmentant la rugosité. Comme on le voit, la résistivité est augmentée en augmentant la RMS de 10 μΩ.cm à 0.15 μm à 80 μΩ.cm à 0.6 μm. La tendance observée de la résistivité électrique est attribuée à la diffusion des électrons dans une microstructure associée à une surface rugueuse; ce qui conduit à une réduction significative de la conductivité (Machlin, 2006).

L'estimation de la résistivité électrique avec l'utilisation du modèle multi-échelle et le modèle FS semble être en accord satisfaisant avec les mesures expérimentales. Comme la rugosité diminue, la différence entre les mesures expérimentales et les prédictions théoriques est augmenté parce que le modèle FS, sauf pour la rugosité, ne comporte pas d'informations sur les caractéristiques des films qui peuvent affecter la conductivité. Les résultats de la résistivité électrique démontrent l'importance du calcul précis de la rugosité, puisque grâce à son contrôle les propriétés finales du film peuvent être pilotées.

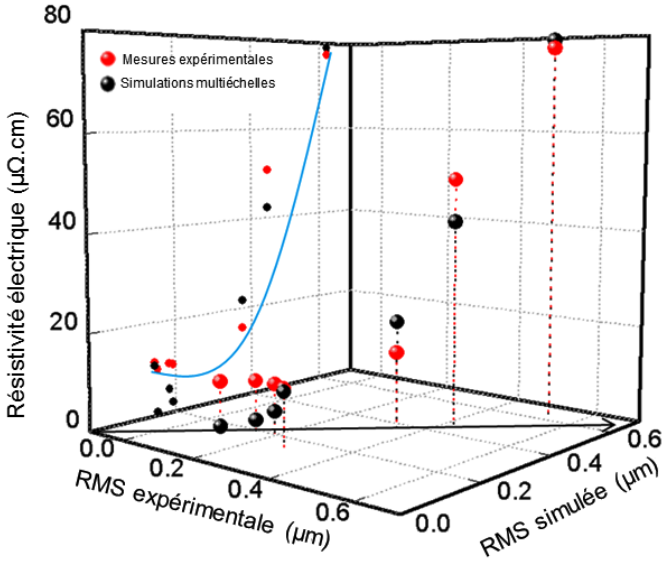

Fig. S-5: La résistivité électrique d'Al expérimentale (sphères rouges) et théorique (sphères noirs) en fonction de la rugosité.

Pour la CVD du Fe, le fer pentacarbonyle ($Fe(CO)_5$) est sélectionné en tant que précurseur. Le choix est basé sur sa pression de vapeur qui est très élevée à la température ambiante et la possibilité d'effectuer des dépôts dans la même gamme de température que l'Al. Les expériences et la simulation du process vise à étudier la dépendance de la vitesse de croissance et de la microstructure des films sur la température dans la gamme 130°C – 250°C. De plus, le comportement de la vitesse de croissance en fonction de la pression est étudié dans la gamme 10 – 40 Torr.

La CVD à partir de $Fe(CO)_5$ conduit à des films de Fe qui peuvent contenir Fe_3C comme phase secondaire, le plus souvent à des températures plus élevées. Les films sont relativement purs, avec une faible contamination par le carbone et l'oxygène. La morphologie des films, comme on l'observe au MEB, est présentée dans la Fig. S-6. On observe que, à la température la plus basse (Fig. S-6a) des films discontinus avec une mauvaise uniformité sont déposées. L'augmentation de la température à 150°C (Fig. S-6b) entraîne une augmentation de la densité des films. A cette température, la taille des grains n'est pas homogène comme le montre la Fig. S-6b, où émergent des grains plus gros (contraste lumineux). Lorsque la température augmente jusqu'à 190°C (Fig. S-6c et d), des grains anguleux et facettés sont formés avec une taille apparemment homogène. La densité des films s'améliore, et l'absence de porosité est confirmée sur la coupe transverse de la Fig. S-6g. Cependant, à 200°C (Fig. S-6F) la morphologie des grains anguleux et facettés est atténuée. Elle est progressivement remplacée par une morphologie aciculaire jusqu'à 240°C (Fig. S-6f). Cette morphologie est confirmée par la coupe transverse de la Fig. S-6h. Il peut en résulter une augmentation de la porosité des films.

Pour la modélisation macroscopique du procédé, le modèle chimique inclut 7 réactions en phase gazeuse et 3 réactions de surface. Les premières décrivent la perte successive de monoxyde de carbone (CO) par la molécule de $Fe(CO)_5$ pour former des

espèces intermédiaires (par exemple, $Fe(CO)_4$ est formé lorsqu'un carbonyle est perdu par le $Fe(CO)_5$). De plus, les réactions en phase gazeuse sont responsables de la recombinaison des espèces intermédiaires avec du CO; par exemple, l'association de $Fe(CO)_4$ avec une molécule de CO conduit à la formation de $Fe(CO)_5$. Pour ces réactions, la cinétique d'Arrhenius est appliquée, dont l'ordre est déterminé par la stœchiométrie de la réaction. Les réactions de surface décrivent le dépôt de films Fe, dans lequel $Fe(CO)_5$, Fe(CO)3 et Fe(CO) contribuent (Dateo *et al*., 2002; Jackman et Foord, 1989; Xu et Zaera, 1994). Une cinétique de type Langmuir-Hinshelwood est appliquée pour les réactions de surface en considérant l'inhibition du dépôt par la contamination de surface par les CO_{ads}. Les énergies d'activation sont fournis par la littérature (Dateo *et al*., 2002;. Gonzáles-Blanco et Branchadell, 1999; Lewis *et al*., 1984; Seder *et al*., 1986; Xu et Zaera, 1994), tandis que les coefficients pré-exponentielle sont ajustés aux données expérimentales. Les conditions aux limites appliquées au modèle macroscopique sont basées sur les conditions de fonctionnement du réacteur expérimental : température d'entrée, T_{en}=25^{o}C, température de parois, T_{par}=25^{o}C, température de dépôt, T_s=130^{o}C – 250^{o}C, pression, P=10-40 Torr, et débit d'entrée de $Fe(CO)_5$, $Q_{prec} = 0.7$ sccm.

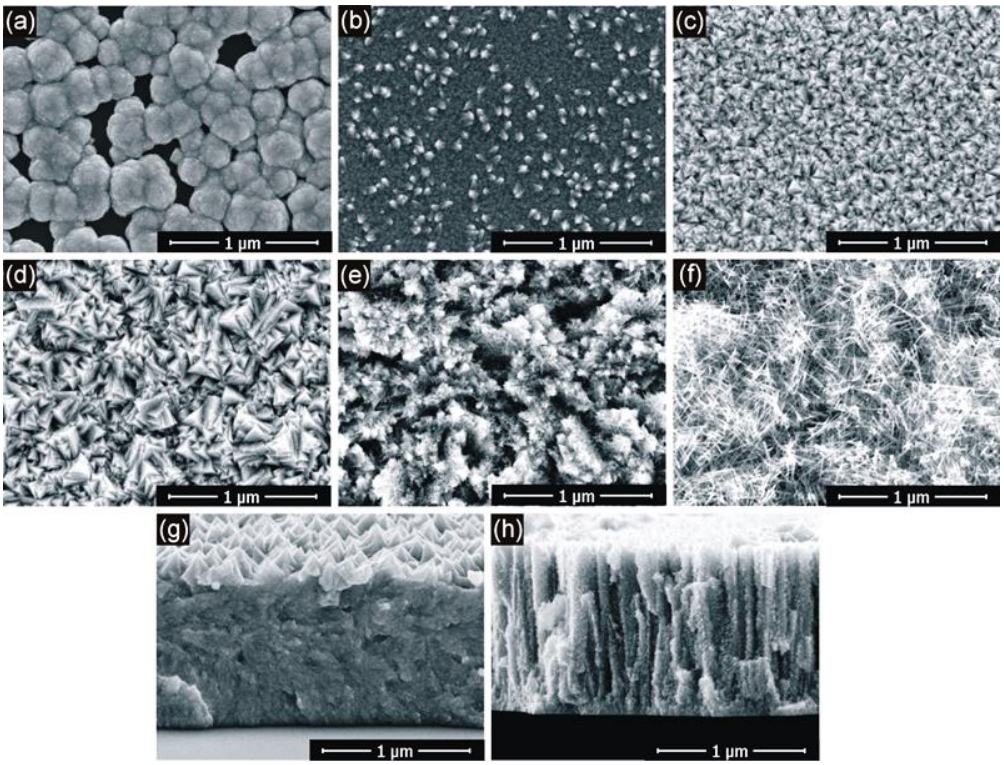

Fig. S-6: Micrographies MEB de la surface de films de Fe déposés à (a) 130^{o}C, (b) 150^{o}C, (c) 170^{o}C, (d) 190^{o}C, (e) 200^{o}C et (f) 240^{o}C. Deux coupes transverse de Fe déposé à (g) 190^{o}C et (h) 200^{o}C.

La Fig. S-7 est le diagramme d'Arrhenius du procédé, où les carrés noirs représentent les résultats expérimentaux et la courbe solide correspond aux prédictions théoriques. La vitesse de croissance de Fe augmente lorsque la température augmente, jusqu'à T_s=180^{o}C; c'est le régime où les cinétiques des réactions de surface contrôlent le processus global. Un régime de transition est observé dans la gamme 180^{o}C – 200^{o}C, où le processus de dépôt est

affecté également par des réactions de surface et les phénomènes de transport. Dans ce domaine, la vitesse de croissance atteint sa valeur maximale, 60 nm/min, à 200°C. À des températures plus élevées, le procédé de dépôt est contrôlé par les phénomènes de transport et la vitesse de croissance diminue fortement. Les résultats expérimentaux sont en accord avec les résultats rapportés dans la littérature (Carlton et Oxley, 1965; Lane et Wright, 1999; Lane *et al*., 1997; Senocq *et al*., 2006; Zhang *et al*., 2016).

Les prédictions théoriques avec le modèle macroscopique sont en très bon accord avec les mesures expérimentales dans toute la gamme de températures. Par conséquent, on peut appliquer nos calculs pour étudier la diminution de la vitesse de croissance à des températures supérieures à 200°C – 215°C.

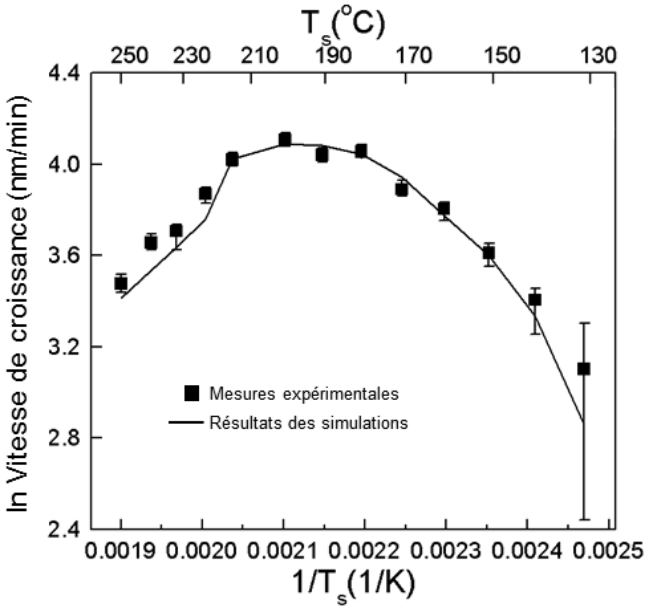

Fig. S-7: Le diagramme d'Arrhenius du dépôt CVD de Fe à partir de $Fe(CO)_5$. Le diagramme montre les mesures expérimentales (carrés noirs) et les résultats des calculs (courbe solide).

La Fig. S-8 montre les vitesses des réactions en phase gazeuse lorsque la température de dépôt est de 223°C et 215°C (Fig. S-8a et b, respectivement). Les vitesses sont calculées sur une ligne horizontale égale au rayon du porte substrat et situé à 1 mm au-dessus. Les réactions montrées dans les schémas correspondent à la décomposition de $Fe(CO)_5$, Fe(CO)4 et $Fe(CO)_3$ pour la formation de $Fe(CO)_4$, $Fe(CO)_3$ et $Fe(CO)_2$, respectivement, et à la combinaison de $Fe(CO)_2$ avec une molécule de CO pour former $Fe(CO)_3$. Les autres réactions en phase gazeuse ont des vitesses négligeables. On observe que, à la température la plus élevée, les vitesses de décomposition du précurseur et des complexes intermédiaires sont plus élevées que les vitesses correspondantes à 215°C. Par conséquence, la fraction massique de $Fe(CO)_5$, qui est disponible pour la réaction de surface, diminue (Fig. S-8c). Au contraire, la fraction massique de $Fe(CO)_3$ augmente à 223°C, à cause de la vitesse de décomposition élevée de $Fe(CO)_5$ à cette température. Cette tendance devient plus prononcée que le mélange gazeux se rapproche du porte-substrat, où les températures sont élevées, et finalement conduit à la réduction de la vitesse de dépôt. La fraction massique de CO, qui est produite par les

décompositions du précurseur et ses complexes intermédiaires, est présentée sur la Fig. S-8d. Il apparaît qu'à des températures plus élevées, plus de CO est produit, ce qui contribue à la saturation de la surface du substrat et inhibe le processus de dépôt. Les réactions en phase gazeuse se produisent aussi dans le régime cinétique avec des vitesses inférieures.

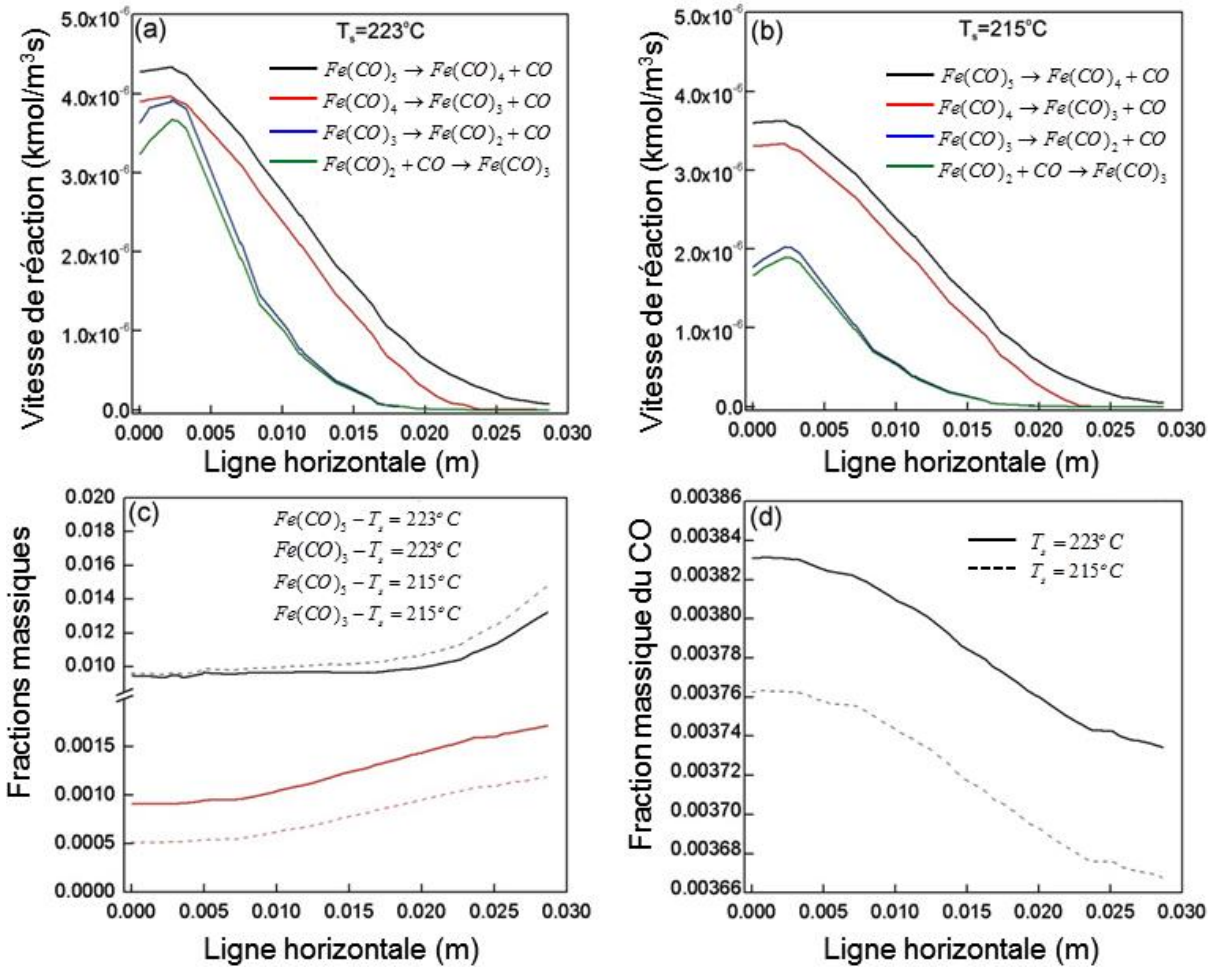

Fig. S-8: Les vitesses des réactions en phase gazeuse lorsque la température de dépôt est (a) 223°C et (b) 215°C. La décomposition de $Fe(CO)_5$ est notée avec les courbes noirs, de $Fe(CO)_4$ avec les courbes rouges, de $Fe(CO)_3$ avec les courbes bleues et l'association de $Fe(CO)_2$+CO avec les courbes vertes. (c) Les fractions massiques de $Fe(CO)_5$ (courbes noirs) et de $Fe(CO)_3$ (courbes rouges) à T_s=223°C (courbes solides) et T_s=215°C (courbes en pointillés). (d) La fraction massique du CO à T_s=223°C (courbes solides) et T_s=215°C (courbes en pointillés).

On étudie maintenant, la dépendance de la vitesse de croissance de Fe avec la pression du réacteur. Pour cette étude, la pression varie dans une gamme relativement étroite de 10 à 40 Torr, et la température est maintenue à 180°C. Les résultats sont présentés sur la Fig. S-9, où les carrés noirs correspondent à des mesures expérimentales et les triangles cyans à des prédictions théoriques. On observe que la vitesse de croissance diminue de 58 nm/min à 7 nm/min en augmentant la pression de 10 Torr à 40 Torr. La variation de la vitesse de croissance en fonction de la pression est prévue avec précision par le modèle macroscopique.

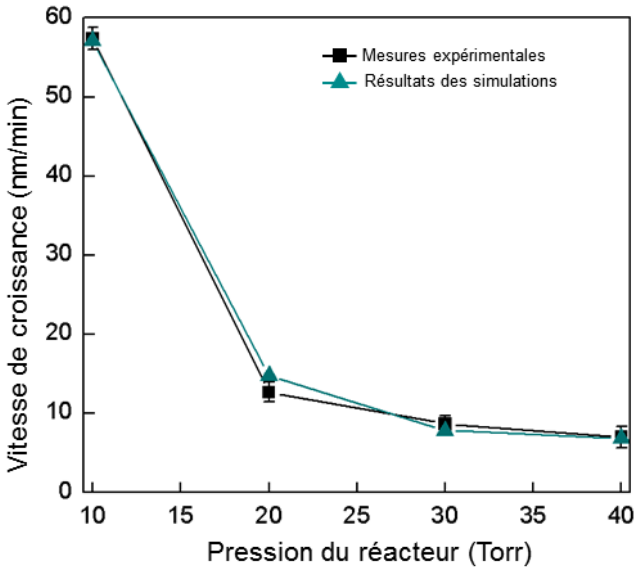

Fig. S-9: La dépendance de la vitesse de croissance sur la pression du réacteur. Les résultats correspondent à des mesures expérimentales (carrés noirs) et à des prédictions théoriques (triangles cyans).

La Fig. S-10 présente les vitesses de décomposition du $Fe(CO)_5$ et du $Fe(CO)_3$ (Fig. S-10a) et les coefficients de diffusion de ces deux espèces (Fig. S-10b) pour les pressions de 10 et 40 Torr. Ces paramètres sont calculés sur une ligne horizontale égale au rayon du porte substrat et situé à 1 mm au-dessus. On observe que les vitesses de décomposition du $Fe(CO)_5$ et du $Fe(CO)_3$ augmentent lorsque la pression augmente, avec une diminution ultérieure de la vitesse de croissance. De plus, la Fig. S-10b montre que l'augmentation de la pression conduit à la réduction des coefficients de diffusion des espèces $Fe(CO)_5$ et $Fe(CO)_3$. Par conséquent, la concentration de ces éléments à la surface du substrat est plus faible, et la vitesse de croissance diminue à des pressions supérieures.

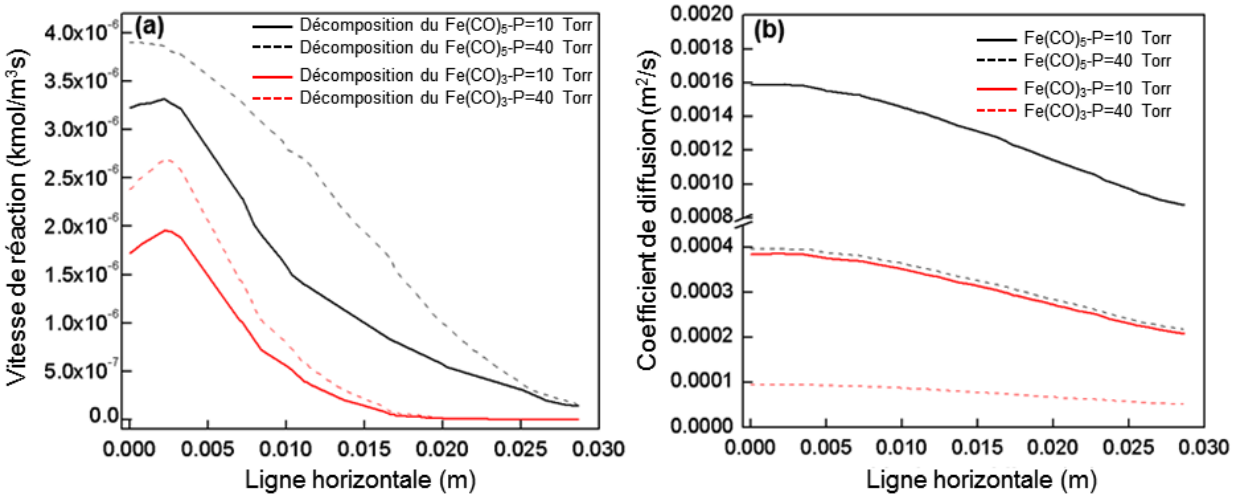

Fig. S-10: (a) Les vitesses des décompositions du Fe(CO)5 (courbes noirs) et du Fe(CO)3 (courbes rouges) et (b) les coefficients de diffusion du Fe(CO)5 (courbes noirs) et du Fe(CO)3 (courbes rouges) à des pressions de P=10 Torr (courbes solides) et P=40 Torr (courbes en pointillés). La temperature est maintenue à T_s=180°C.

Le modèle macroscopique prédit avec précision la dépendance de la vitesse de croissance dans la gamme de température 130°C – 250°C. L'analyse des résultats des calculs

indique que la vitesse diminue à des températures supérieures de 200°C en raison de la vitesse de décomposition augmentée de $Fe(CO)_5$ en phase gazeuse et à cause de la saturation de la surface du substrat qui est inhibée par le CO_{ads}. Pour la dépendance de la vitesse de croissance avec la pression, les prédictions théoriques sont en accord avec les mesures expérimentales. La diminution de la vitesse à des pressions élevées est attribuée à l'augmentation de la décomposition en phase gazeuse de $Fe(CO)_5$ et de $Fe(CO)_3$ et à la réduction de leur coefficients de diffusion. Les causes de la réduction de la vitesse de croissance à des pressions et des températures élevées démontrées ici sont similaires aux résultats de publications antérieures (Fau-Canillac et Maury, 1994; Lane *et al*., 1997; Zhang *et al*., 2016).

Les fractions massiques de $Fe(CO)_5$ et de $Fe(CO)_3$, qui sont calculées macroscopiquement à la surface du substrat, sont introduits dans l'algorithme kMC pour effectuer des simulations multi-échelles. La chimie de surface à l'échelle nanométrique, est incorporée dans le coefficient de collage, comme pour le cas de l'Al. Les prédictions théoriques (triangles cyans) et les mesures expérimentales (carrés noirs) de la rugosité des films de Fe en fonction de la température, sont présentées sur la Fig. S-11. Expérimentalement, la rugosité augmente avec la température jusqu'à 150°C, de 0.67 μm à 0.75 μm. Ensuite, elle diminue de façon monotone (0.48 μm) jusqu'à 190°C. Au-delà, on observe une forte réduction de la rugosité (0.34 μm), car la microstructurechange (voir Fig. S-6). À des températures plus élevées, la rugosité diminue progressivement et se stabilise (0.16 μm) à 230°C – 250°C.

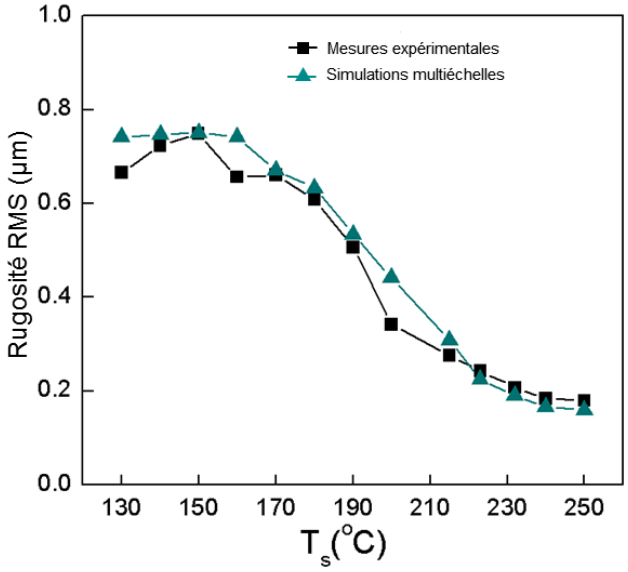

Fig. S-11: La rugosité (RMS) de films de Fe en fonction de la température, T_s. Les carrés noirs correspondent à des mesures expérimentales et les triangles cyans à des prédictions théoriques.

Les prédictions théoriques avec le modèle multi-échelle sont en bon accord avec les mesures expérimentales. Cependant, dans la gamme 190°C – 200°C les prédictions sont moins précises, parce que le changement de nano-morphologie des films, qui est observé

expérimentalement, ne peut pas être capturé par le modèle multi-échelle. À des températures plus élevées, la stabilisation de la rugosité RMS est prévue, étant donné que dans cette région, les fluctuations des événements de diffusion, qui contribuent au lissage de la surface, sont faibles. Le modèle multi-échelle pour les simulations des surfaces de Fe peut être améliorée afin de prendre en compte sa structure cristallographique exacte. Les améliorations de ce type peuvent conduire à une plus grande précision des prédictions théoriques; ils pourraient aussi permettre la simulation de plusieurs caractéristiques de surface, telles que la formation des grains.

Sur la base de l'étude des dépôts CVD de films unaires d'Al et de Fe, un procédé de co-dépôt des deux métaux est appliqué. Pour la production de la phase approximante $Al_{13}Fe_4$, les concentrations de ces deux métaux dans le film devrait approcher le rapport de 13:4. La température de co-dépôt est fixée à 200^{o}C, où la CVD d'Al est contrôlée par les phénomènes de transport et le procédé correspondant de Fe se situe dans le régime de transition. Comme il est mentionné ci-dessus, dans les deux procédés des réactions en phase gazeuse se produisent à toutes les températures. La sélection de 200^{o}C pour le processus de co-dépôt vise à limiter les vitesses des réactions en phase gazeuse, ce qui peut conduire à des interactions indésirables entre les deux précurseurs. A cette température particulière, les films d'Al montrent une vitesse de croissance élevée, une faible rugosité et une bonne couverture de la surface du substrat. Au contraire, la morphologie des films de Fe est aciculaire et poreux.

Au cours du co-dépôt, de l'hydrogène (H_2) est ajouté au mélange gazeux entrant dans le réacteur. L'objectif est la réduction partielle des composés oxygénés et plus particulièrement, la limitation de l'oxydation d'Al par l'oxygène (O) produit par la décomposition du $Fe(CO)_5$. La Fig. S-12 présente l'analyse élémentaire du film en fonction du flux de H_2 dans le mélange gazeuse. L'analyse élémentaire est réalisée grâce à une microsonde de Castaing (*Electron probe microanalyser*, EPMA) pour identifier et quantifier les éléments Al, Fe, O et C. On constate que, en l'absence d'H_2, la composition des deux métaux dans le film déposé correspond à un rapport hypothétique de 13:1.3, ce qui dévie de manière significative du rapport désiré de 13:4. De plus, ces films contiennent une forte concentration d'O (25%), ce qui favorise la formation des oxydes et empêche la formation de composés intermétalliques. L'ajout d'H_2 n'a pas d'effet significatif de réduction, puisque l'O ne diminue que légèrement : 18% dans le meilleur des cas. Cependant, il a une influence majeure dans le rapport Al:Fe. Lorsque la CVD d'Al est concerné, l'H_2 déplace l'équilibre de la réaction de surface d'Al dans une direction opposée au dépôt. Dans le même temps, l'ajout d'H_2 semble favoriser le dépôt de Fe. Par conséquence, en réduisant la concentration d'Al et en augmentant la concentration de Fe, le rapport des deux métaux est améliorée à 13:2.5, dans le meilleur des cas, mais encore, il diffère du rapport désiré de 13:4.

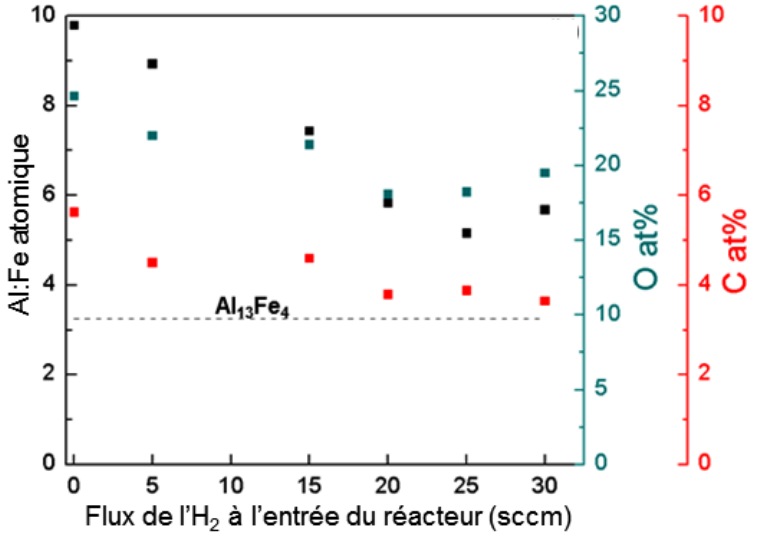

Fig. S-12: Des analyses atomiques EPMA en fonction du flux de l'H_2 à l'entrée du réacteur.

Les films obtenus par co-dépôt sont constitués d'Al et de Fe métalliques et d'oxydes amorphes, et aucune phase intermétallique n'est identifiée. La grande quantité d'O ne laisse aucun espace pour une étude plus approfondie de la formation de phases intermétalliques, par exemple par recuit post-dépôt approprié. Cependant, le processus de co-dépôt à des températures plus basses ainsi que le recuit thermique devrait être examinée comme une possibilité de former des phases intermétalliques Al-Fe. La modélisation macroscopique peut soutenir une telle étude.

Néanmoins, une solution existe avec le dépôt séquentiel des deux métaux. Au cours de ce processus, les précurseurs ne sont jamais en contact direct et donc la possibilité d'obtenir des films avec des concentrations élevés d'O, est réduite. Le dépôt CVD de la couche d'Al est réalisé à 180^{o}C et à 10 Torr. Le dépôt CVD de la couche de Fe est réalisé à 140^{o}C et à 40 Torr. Le choix de ces conditions est basé sur l'analyse expérimentale et numérique présentée précédemment et vise à créer des films avec des concentrations d'Al élevées, tel que requis par la phase approximante $Al_{13}Fe_4$. Les expériences de dépôt séquentiel sont réalisées sur des substrats de verre et de dioxyde de silicium (SiO_2). L'utilisation de substrats de silicium devrait être évitée, car elle peut conduire au développement de siliciures de fer. Le dépôt séquentiel est suivi d'un recuit thermique pour faciliter la réactivité entre les deux métaux et améliorer la formation de composés intermétalliques. En particulier, le recuit thermique est effectué à 575^{o}C, où la formation de la phase $Al_{13}Fe_4$ a été rapportée (Haidara *et al*., 2012).

La spectroscopie de photoélectron X (XPS) est utilisé pour analyser la surface des films Al-Fe, et pour quantifier la composition élémentaire au niveau de la surface. Sur la base de ces mesures, le rapport Al:Fe égale 13:4.3, une valeur qui est proche de l'objectif de 13:4. La Figure. S-13 montre les spectres XPS de Fe 2p et d'Al 2p à la surface d'un film Al-Fe, qui est formé dans les conditions ci-dessus. Le spectre de Fe 2p (S-13a) contient un seul pic avec un petit déplacement chimique par rapport au spectre de référence. Cette différence est

caractéristique de la structure électronique modifiée dans les composés intermétalliques de métaux de transition. Dans le spectre d'Al 2p (S-13b), le pic à 72.2 eV correspond à l'Al métallique, tandis qu'à 74.6 eV à un oxyde d'Al. Par conséquent, on suppose que la surface de ces couches inclut une couche mince d'oxyde d'Al, qui n'est pas présente dans le reste du film et ne provoque pas la dissolution de l'alliage Al-Fe au-dessous.

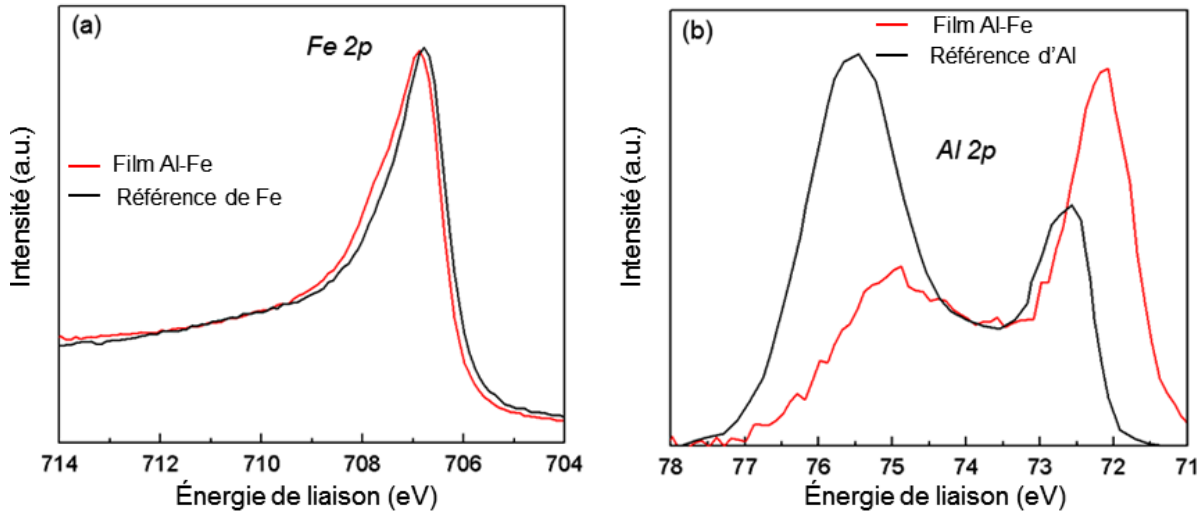

Fig. S-13: Le spectre XPS d'un film Al-Fe. (a) Le pic Fe 2p comparé avec une référence de Fe. (b) L'Al 2pcomparé à une référence d'Al.

La Fig. S-14 montre le diagramme de diffraction des rayons X (DRX) d'un film Al-Fe déposé dans les mêmes conditions. Le spectre est comparé avec ceux de la littérature sur $Al_{13}Fe_4$ (Ellner, 1995; Grin *et al.*, 1994).

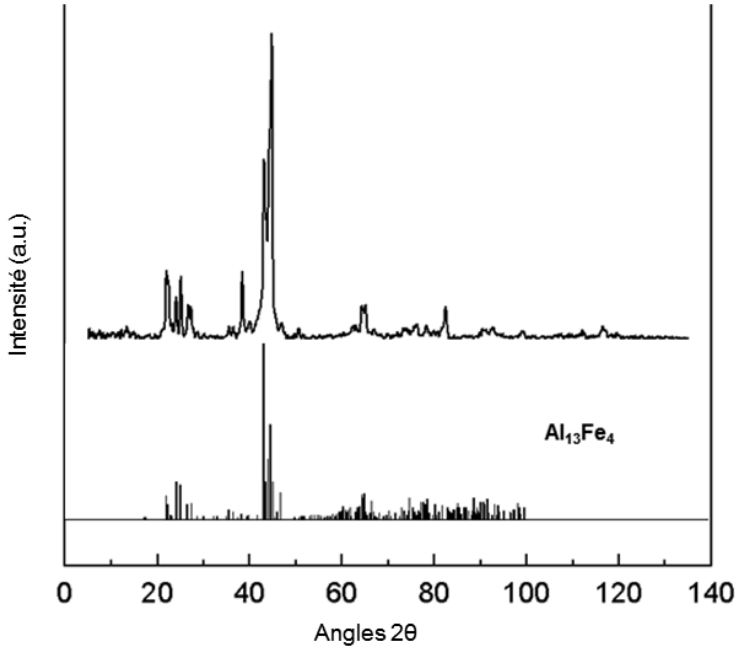

Fig. S-14: Le spectre DRX d'un film Al-Fe (haut) en comparaison avec ceux (bas) d'Ellner (1995) et de Grin *et al.*, (1994).

Une bonne correspondance entre le spectre de DRX et ceux de la littérature est observée, confirmant la formation de la structure intermétallique d'$Al_{13}Fe_4$. En particulier, les pics à bas angles 2θ, entre 20°-30°, ainsi que les pics de haute intensité à 40°-50° et des pics moins intenses à grands angles 2θ sont caractéristiques de la phase approximant m-$Al_{13}Fe_4$. Il y a, cependant, d'autres pics, par exemple à des angles de 38°-39° et 50° qui sont attribués à la phase Al_5Fe_2 et à l'Al métallique. Etant donné que des phases différentes coexistent dans le film, il est conclu que sa composition chimique n'est pas uniforme. Pour déterminer le gradient de composition la microscopie électronique à balayage entransmission est utilisé (STEM) et combinée avec l'analyse dispersive en énergie (STEM-EDX).

Les résultats STEM-EDX sont présentés sur la Fig. S-15. La micrographie de la Fig. S-15a révèle un film poreux, où l'interdiffusion des deux métaux semble complète. Cependant, il est confirmé que la composition élémentaire n'est pas uniforme dans le film. Par exemple, la Fig. S-15b montre que plus de 50% volumique de la partie inférieure du film (bottom) est constitué par des grains riches en Fe (Al(25)Fe(75), ou Al(15)Fe(85), tel que mesurée par STEM/EDX).

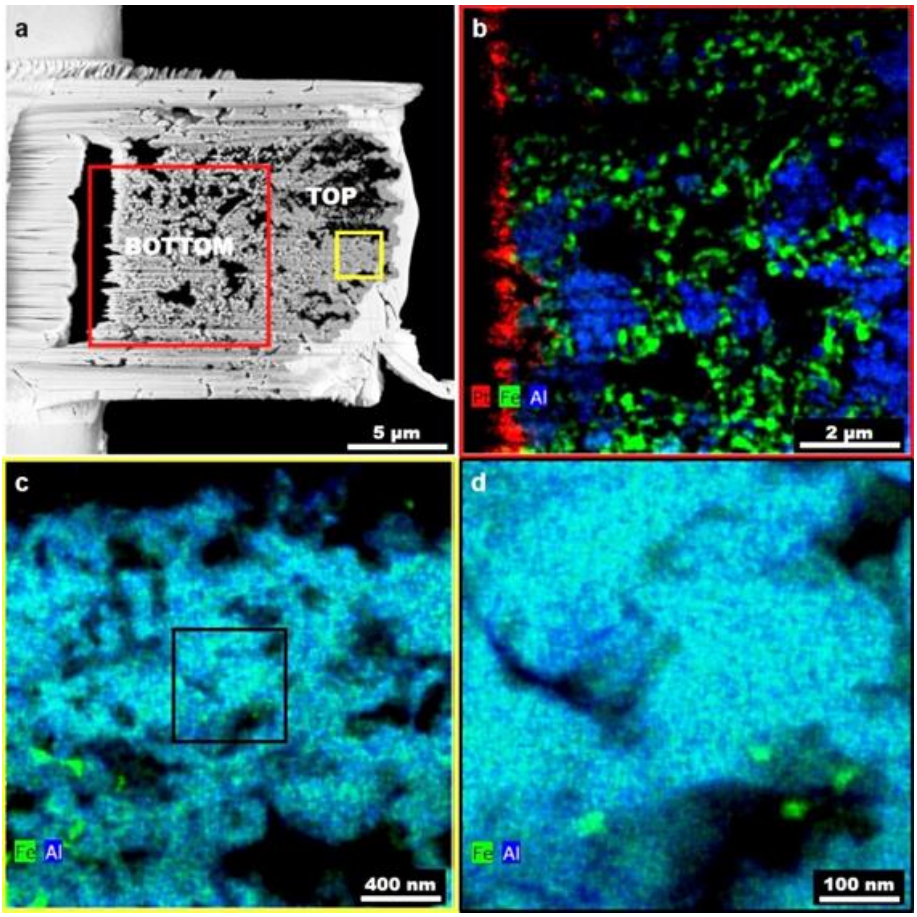

Fig. S-15: (a) Micrographie du film Al-Fe. Cartographie STEM/EDX du film (b) en bas (carré rouge) et (c) en haut (carré jaune). (d) STEM/EDX en résolution supérieure dans le carré noir de la figure c.

Dans la partie supérieure du film (top), la concentration en fer réduit progressivement jusqu'à une composition uniforme sur un épaisseur de 2-3 µm. La Fig. S-15c montre la

cartographie élémentaire de la partie supérieure du film. On observe qu'il y a une répartition uniforme des grains de type Al(75)Fe(25), qui correspond à la composition d'$Al_{13}Fe_4$. La Fig. S-15d montre la cartographie dans le carré noir de S-15c, à une résolution supérieure. À la proximité des pores des films, la concentration en Al est supérieure, et elle est associée à la présence d'O. L'oxydation préférentielle d'Al est commune sur les alliages d'Al avec des métaux transition et elle est en accord avec l'XPS, où une couche d'oxyde d'Al a été observée à la surface. Pendant le recuit thermique des films, on suppose que les phases intermétalliques Al-Fe sont d'abord formées à l'interface avec le substrat. Cette hypothèse est confirmée par les observations STEM/EDX qui montrent que les grains riches en Fe se concentrent à l'interface avec le substrat.

La Fig. S-16 montre l'analyse par microscopie électronique à transmission (MET) d'un film Al-Fe. Dans la moitié inférieure du film, les deux métaux sont complètement mélangés, tandis que dans la partie supérieure des régions d'Al-Fe et d'Al sont détectées en alternance (Fig. S-16a). Un zoom sur l'interface entre les zones d'Al et d'A l-Fe (cercle blanc sur la Fig. S-16a) est présenté sur la Fig. S-16b. Il y a un grain Al-Fe rectangulaire de 180 nm d'épaisseur, développée dans la région d'Al. L'image de haute résolution de ce cristal est montrée sur la Fig. S-16c. L'analyse de la transformée FFT (*fast Fourier transform*) démontre la formation de la phase approximante m-$Al_{13}Fe_4$; les paramètres cristallographiques déterminés sont a=15.49Å, b=8.08Å, c=12.48Å, β=107.75°. Ces valeurs sont en accord avec les résultats de la littérature correspondant (Ellner, 1994;. Grin *et al*., 1995).

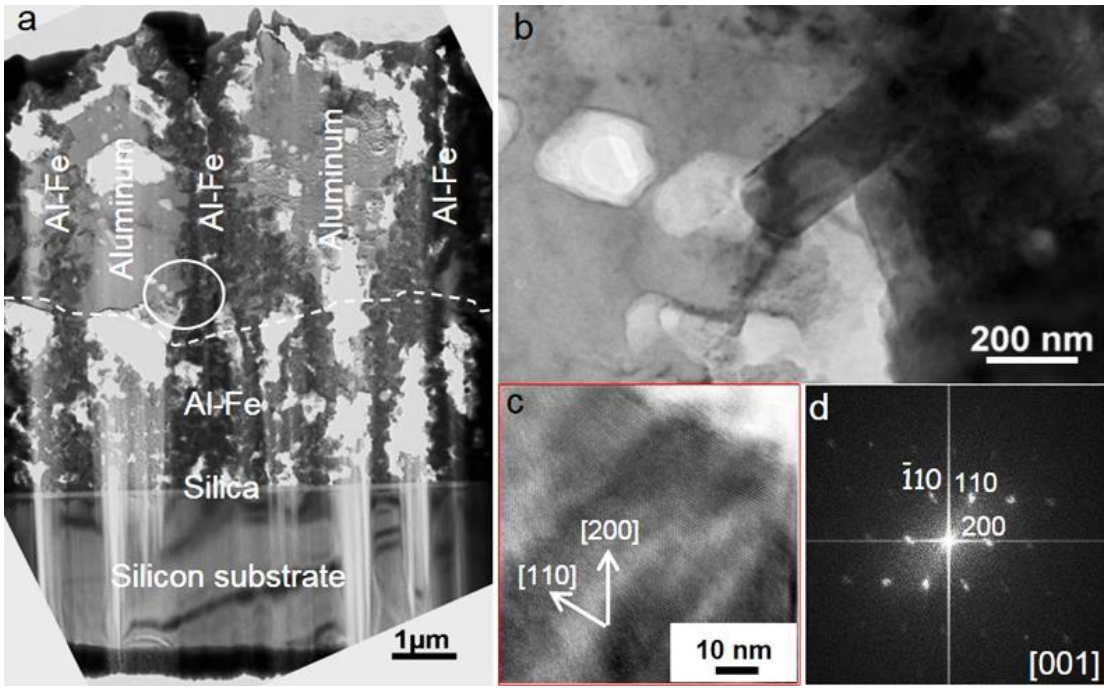

Fig. S-16: (a) Une coupe transverse d'un film Al-Fe. (b) La magnification dans la région du cercle blanc de la figure a. (c) Une image TEM en haute résolution du cristal observé sur b. (d) Transformée de Fourier de c, qui confirme la formation d'$Al_{13}Fe_4$ en axe de zone [001].

Enfin, les films contenant la phase approximant m-$Al_{13}Fe_4$ sont testés pour leurs propriétés catalytiques dans le procédé de semi-hydrogénation de l'acétylène. Les expériences catalytiques ont été réalisées à l'Institut spécialisé IRCELYON en France. Les mesures initiales montrent que l'activité du film est limitée; dans tous les cas, la conversion d'acétylène en éthylène est très faible. La mauvaise performance des films peut être attribuée à leur oxydation et au gradient de composition, comme s'observé au-dessus. Afin d'améliorer l'uniformité de la composition chimique, la durée du recuit thermique doit être augmentée. Par ailleurs, l'amélioration de la porosité des films peut limiter leur oxydation. En ce sens, l'analyse informatique avec un modèle multi-échelle peut explorer la dépendance de la porosité avec les conditions de fonctionnement.

General Introduction

Complex metallic alloys (CMAs) is a particular family of intermetallic phases which was recently defined in the frame of the "Complex Metallic Alloys" FP6 European Network of Excellence (Dubois, 2008). CMAs are characterized by large unit cells containing up to thousands of atoms, some disorder and the presence of highly coordinated clusters: another physical length in addition to their lattice parameters. CMAs provide materials with advantageous combined properties which are usually not found together in the same material. This is a consequence of their structural complexity from the crystallographic and the electronic structure point of view. At the top of this structural complexity, quasicrystals (QCs) and approximant phases can be found. QCs are well-ordered, non-periodic solids often associated with classically forbidden rotational symmetries. On the other hand, an approximant is a periodic crystalline material that is closely related to a QC in chemical composition and in atomic structure. Approximant phases often contain the same clusters as those embedded in QCs of related composition (Goldman and Kelton, 1993). Al-Fe intermetallic compounds such as AlFe and $AlFe_3$ are mostly preferred for high-temperature applications because of their excellent hot-gas corrosion resistance (Klöwer, 1996; Tortorelli and Natesan, 1998). Recently, the approximant phase $Al_{13}Fe_4$ has been identified as a promising catalyst for the semi-hydrogenation of acetylene to ethylene, a possible substitute of precious noble metals (Armbrüster *et al*., 2012).

The production of intermetallic compounds comprising approximant phases is limited almost exclusively to crystal growth methods such as Czochralski or Bridgman (Langsdorf and Assmus, 1999). These techniques are powerful in the production of high-purity single crystals and therefore, they are useful for the investigation of the crystallographic characteristics and the basic physical properties. Nevertheless, these bulk materials suffer a number of disadvantages amongst which fragility that limits their application. Thus, alternative techniques such as films deposition methods can be applied to ensure the properties of the formed phases, in terms of a supporting material, the robustness and the reproducibility of the formation process and its transferability to large scale, industrial production.

There is a wide variety of deposition processes, nevertheless few of them meet the required specifications for the production of an intermetallic approximant phase. Films and coatings deposited by physical techniques (physical vapor deposition, sputtering, beam epitaxy) suffer from poor conformality. Solution deposition methods (sol-gel deposition) are limited mainly by requirements originating from the solubility of precursors in a solvent and the sufficient wetting of the substrate from the solution without any chemical interactions between them. Atomic layer deposition techniques (ALD) yield very low throughput. Thus, for the formation of Al-Fe intermetallic phases and in particular of the $Al_{13}Fe_4$ approximant phase (Chapter 1), the chemical vapor deposition technique (CVD) is selected. It has the advantages of high throughput, while enabling conformal coverage of complex-in-shape surfaces. MOCVD precursors are molecules containing the metal to be deposited. They are

evaporated prior entering the reactor and their vapors are transported by a carrier gas to the surface of the substrate. Precursors may undergo gas phase or surface reactions. When the appropriate amount of energy is provided to the surface, it results in the deposition of a metallic film.

The key ingredients of a CVD process are the following three; first, the choice of appropriate precursor molecules and the formation and transport of their vapors in the reactor. The use of metalorganic precursors renders possible the low-temperature operation of MOCVD processes, thus extending the targeted applications spectrum so as to cover temperature-sensitive substrates, like polymeric surfaces. Second, the design of the reactor in terms of operating conditions (pressure, temperature, input feed rate), geometry, etc. (Chapter 2). Third, the mechanisms occurring during the process. The latter are associated with the main drawback of the process, namely, the complicated coupling of chemistry and transport. The gas phase and surface reactions, the transport phenomena and their interplay need to be understood and controlled in order to consolidate a process for the production and formation of films with controllable and reproducible thickness, microstructure and chemical composition.

The computational modeling of a CVD process provides an invaluable tool for the investigation of such complex mechanisms (Chapter 1). Furthermore, with multiscale modeling, mechanisms pertaining at different spatial scales are addressed. Macroscopic scale (macroscale) modeling is valid as long as the continuum hypothesis prevails. It lies on the mathematical statement of first principles, namely the conservation of mass, momentum and energy, which gives rise to a set of nonlinear partial differential equations (Chapter 3). The equations must be solved in three-dimensional and often geometrically complicated domains under transient or steady-state conditions. Macroscale models account for transport mechanisms in the bulk (volume) of the reactor. They incorporate homogeneous, gas phase chemical reactions as well as heterogeneous, surface reactions which yield the solid product, i.e., the deposited metallic film. With the exploitation of computing power, these models are meant to be predictive tools, enabling the illumination of mechanisms and, subsequently, process optimization and control. In practical terms, they can provide predictions of the dependence of the deposition rate of the film on the manipulated operating parameters of the reactor and determine preferred operating “windows”. The reliability of the model is ensured by thorough validation with experimental measurements. Micro- and nano-scopic scale (microscale and nanoscale) models are necessary for the treatment of surface processes, such as adsorption, migration and desorption of molecules or atoms. In this thesis, nanoscale models are applied, such as kinetic Monte Carlo (kMC) (Chapter 3). The linking between the two scales, macro- and nano-, i.e., the development of a multiscale framework, is performed through the feeding of information calculated macroscopically to the nanoscale model. It enables the calculation of surface features, such as roughness which is associated with the final properties of the films. Thus, a modeling framework including standalone macroscopic

and multiscale simulations of the CVD process provides a set of information which covers the entire film production, from the dependence of the deposition rate and the film thickness on operating conditions to the film microstructure and properties.

The formation of films containing intermetallic phases by CVD passes through the investigation of the deposition of unary metals. If an overall compatibility (chemical, thermal, transport) is found, then the simultaneous or the sequential deposition of the metallic constituents can be performed. A set of information is provided by the Arrhenius plot of the CVD of each metal which shows the dependence of the deposition rate on temperature. The Arrhenius plot is the outcome of theoretical predictions, validated by corresponding experimental measurements. It schematically maps out different regimes, each associated with a controlling mechanism of the deposition process, be it surface chemical reaction kinetics (reaction-limited regime) at low temperatures, or transport (diffusion-/transport-limited regime) at high temperatures or both at intermediate, transition, temperature regimes. For co-deposition or sequential deposition processes, the superposition of both Arrhenius plots of each metal to be deposited helps in the determination of a common operating window. For co-deposition, it is generally preferable to operate in the reaction-limited regime. In this regime, the prevailing mechanisms are attributed mainly to surface reactions and the effect of homogeneous reactions, which may lead to high decomposition rates and interactions between the precursors, is limited. However, for particular precursors systems the occurrence of gas phase reactions is inevitable in the entire temperature range of investigation. Thus, a common process should be carried out in a temperature window containing different temperature regimes for each precursor. In such a way, deposition of the first element can be controlled by the concentration of the reactive gas phase in the input gas and deposition of the second by the deposition temperature.

Following the above mentioned general framework, the CVD of unary Al and Fe films is investigated in Chapters 4 and 5, respectively. We determine the operating conditions for the combined processing of the two metals potentially leading to the formation of the $Al_{13}Fe_4$ approximant phase. For the CVD of Al, the dimethylethylamine alane (DMEAA) precursor is chosen (Chapter 1). Investigation of the process yields the corresponding Arrhenius plot and the evolution of the microstructure with temperature. Macroscopic simulations alone reveal that homogeneous reactions occur even at low temperatures. The predicted deposition rates are in fairly good agreement with experimental measurements in the investigated regime, except for higher temperatures, indicating that a more detailed chemical pathway needs to be applied. Multiscale simulations reveal the evolution of the film microstructure and, in particular, of the surface roughness with temperature; the microstructure is important for the feasibility of the subsequent co-deposition or sequential deposition. The CVD of Fe is performed by using the iron pentacarbonyl ($Fe(CO)_5$) precursor (Chapter 1). The investigation of the process includes the determination of the dependence of the deposition rate on temperature and pressure, modifications of the surface morphology

when temperature increases above a certain limit and the evolution of the surface roughness with temperature. As in the case of Al, macroscopic theoretical predictions are close enough to experimental measurements of the deposition rate versus temperature and pressure. They also reveal gas phase decomposition of the precursor and inhibition of the surface at high temperatures. The multiscale analysis reproduces the evolution of roughness with temperature.

CVD experiments and modeling of unary Al and Fe films yield the determination of the operating parameters for the co-deposition and the sequential deposition of the two metals, presented in Chapter 6. The possibility of obtaining Al-Fe intermetallic phases is first examined by the one-step, co-deposition process, which is actually in its infancy. The investigation of the unary processes provides evidences for the gas phase decompositions of the two precursors and consequently, for their potential interactions when fed simultaneously in the reactor. However, these interactions are not adequately known and they may lead to uncontrollable results including contamination and/or insufficient control of chemical composition. The two-step, sequential deposition becomes the process of choice in order to avoid interactions between precursors and to obtain pure metallic phases. However, depositions occur at rather low temperatures ($<200^{o}C$). Therefore annealing of the films is required to activate the formation of Al-Fe intermetallic phases. Identification of the phases is realized by a range of characterization techniques. Among them, high resolution TEM and STEM allow the determination of the compositional, structural and microstructural characteristics of the films.

The thesis project was carried out in the framework of a joint program – "co-tutelle" – which involves the cooperation between the School of Chemical Engineering of the National Technical University of Athens (NTUA) and the Centre Interuniversitaire de Recherche et d'Ingénierie des Matériaux (CIRIMAT) of the Institut National Polytechnique de Toulouse (INPT). In this framework, the modeling procedure including the development of algorithms and the computational simulations of the process were performed in the School of Chemical Engneering under the supervision of Prof. A.G. Boudouvis whereas the experimental work, including film characterization, were carried out at CIRIMAT, under the supervision of Dr. C. Vahlas and Dr. T. Duguet.

Chapter 1: Formation of unary films and complex intermetallic structures with CVD: motivation, materials and elaboration processes

In Chapter 1 are presented the aim of the thesis, the CVD technique and its principles with regard to the targeted co-deposition and sequential deposition processes. The criteria of precursors' choice are described and the selection of precursor for aluminium and iron deposition is justified along with potential reaction pathways of these molecular compounds. Furthermore, theoretical aspects in terms of modeling CVD processes are discussed. In this sense, a macro-, a nano- and a multiscale model are presented. Through modeling, chemistry and kinetics are coupled with transport and their interplay is investigated at different/multiple scales. Finally, as a case study, the intermetallic $Al_{13}Fe_4$ approximant is presented.

1.1. The aim of the thesis

The thesis presents a combined experimental and theoretical approach for the application of a Chemical Vapor Deposition (CVD) process to the formation of intermetallic compounds on surfaces. The compound of choice is an Al-Fe one, namely the $Al_{13}Fe_4$ approximant phase. Iron aluminides have been among the most studied intermetallics in the literature with respect to structural and functional applications (Stoloff, 1998), due to their excellent corrosion resistance under oxidizing, carburizing and sulfidizing atmospheres (Ehteman Haghighi *et al*., 2010), their relatively high electrical resistivity and low thermal conductivity (Krasnowski and Kulik, 2007), their good magnetization properties (Madurga *et al*., 2008), their good mechanical properties (Senderowski *et al*., 2010) and their low cost (Senderowski *et al*., 2010). Among the six $AlFe_3$, AlFe, Al_2Fe, Al_3Fe_2, Al_5Fe_2 and $Al_{13}Fe_4$ non-stoichiometric Al-Fe intermetallic compounds (Sundman *et al*., 2009), the latter one, also named Al_3Fe for convenience, is a complex metallic approximant phase which presents provides multifunctional properties useful to advanced materials, including catalytic applications such as the semi-hydrogenation of acetylene to ethylene feed for polyethylene production (Armbrüster *et al*., 2012). Single crystals of such intermetallic phases, useful for getting insight in the crystallographic characteristics of the fundamental physical properties, can be produced by crystal growth methods, e.g. the Czochralski technique. However, in order to ensure implementation of the formation of such phases in large scale industrial applications, alternative methods, such as CVD, are used providing functionalization of complex surfaces with high throughput.

There is a wide spectrum of materials that can be deposited by CVD, ranging from metals and oxides to carbides, nitrides, sulphides as well as polymers and intermetallic phases. CVD can address the limitations caused by physical deposition techniques (physical vapor deposition, molecular beam epitaxy or sputtering), such as poor conformality. Furthermore, in comparison with other chemical deposition techniques such as ALD, sol-gel deposition and electrochemical deposition, CVD by operating at relatively low to moderate temperatures (i.e., the reaction-limited regime, see hereafter) can meet the requirements for the deposition on complex, non-line-of sights surfaces with limited process time.

The main hard point which has to be tackled in CVD technique is the complexity of the involved chemical reactions and mechanisms. As opposed to other deposition techniques where no chemical reactions or only surface reactions occur, the evolution of transport phenomena, including homogeneous, gas phase reactions, may have a strong impact on the surface reaction and consequently, on the process and material (the final film and its interaction with the substrate) characteristic. In complement to a classical try and error experimental approach, it takes modeling and computational analysis to cope with these difficulties and to investigate and understand the phenomena occurring at different length scales. Macroscopically, transport phenomena and chemical reactions and kinetics which affect qualitatively and quantitatively the film, need to be understood for a better control and

optimization of the process. At the film surface level, additional phenomena occur with an important impact on the microstructure of the films. Thus, the theoretical approach of CVD processes carried out in this thesis is a precious tool for the investigation and understanding and, subsequently, control and optimization of the complex mechanisms occurring during the deposition of Al and Fe films. Modeling of the CVD process should not be considered alone. Indeed, it not only consolidates the investigated CVD processes but it also provides a "communication"/feedback with the experimental procedure towards attaining the targeted intermetallic material, in the present case the formation of the $Al_{13}Fe_4$ approximant phase.

The processing of the targeted $Al_{13}Fe_4$ intermetallic phase passes through the investigation of the CVD of unary Al and Fe films for the definition of the operating parameters of each deposition, to end up with a combined process, namely a co-deposition or a sequential deposition, for either the simultaneous or the successive deposition of the two metals, respectively. Through this investigation, the impact of the deposition temperatures, the operating pressures and of the mass flow rates of the initial gas mixture on the output of the CVD is experimentally and computationally examined. Furthermore, the experimentally supported computational modeling of the unary Al and Fe depositions allows fetching information concerning the chemical reactions and the microstructure of the films. This information is a valuable tool concerning the common Al and Fe processing since it reveals potential interactions in the gas phase and at the surface level. The overall objective of the thesis is to demonstrate that a combined experimental and theoretical approach leads to the conclusion that an appropriately set CVD process could be an advantageous method of choice for the growth of intermetallic films.

1.2. Chemical vapor deposition

1.2.1. General description

CVD is a technique applied for the formation of thin solid films and coatings on the surface of a substrate, by a surface chemical reaction. Therefore, it can be distinguished from physical vapor deposition (PVD) techniques, such as evaporation and sputtering which, in their majority, simply include the adsorption of atomic or molecular species on the substrate and with no chemical processes involved. Industrially CVD has played an important role in the microelectronics and the semiconductors engineering for the manufacturing of micro- and nanometric chips, interconnects and integrated circuits since the early days of the information and communication technology (Sherman, 1987). Nowadays, CVD has been recognized as a generic technology of major importance for the implementation of Key Enabling Technologies as explicitly illustrated in the ad hoc report[1]. It provides advanced high performance materials with advantageous properties for targeted applications as presented in

[1] see Figure 4 in
http://ec.europa.eu/DocsRoom/documents/11283/attachments/1/translations/en/renditions/native

Figure 1.1. This figure summarizes representative illustrations of such applications: Thin alumina (Al_2O_3) coatings are deposited by CVD at the inner surface of bottles due to their excellent barrier, anti-corrosion and high optical transmission properties for the protection of the content of the bottle (Figure 1a) (Etchepare *et al*., 2014). In cases where selective growth is demanded on different types of surfaces or on patterned surfaces, the application of CVD ensures the device integration, the high and conformal coverage of complex geometry and the scale-up of the process. Example are, the growth of gallium nitride (GaN) nanowires on $LiAlO_2$ and MgO surfaces, which provides various optical properties (Figure 1b) (Kuykendall *et al*., 2004) and the growth of zeolitic imidazolate (ZIF-8) framework thin films on surfaces with pillar geometry (Figure 1f) (Stassen *et al*., 2015).

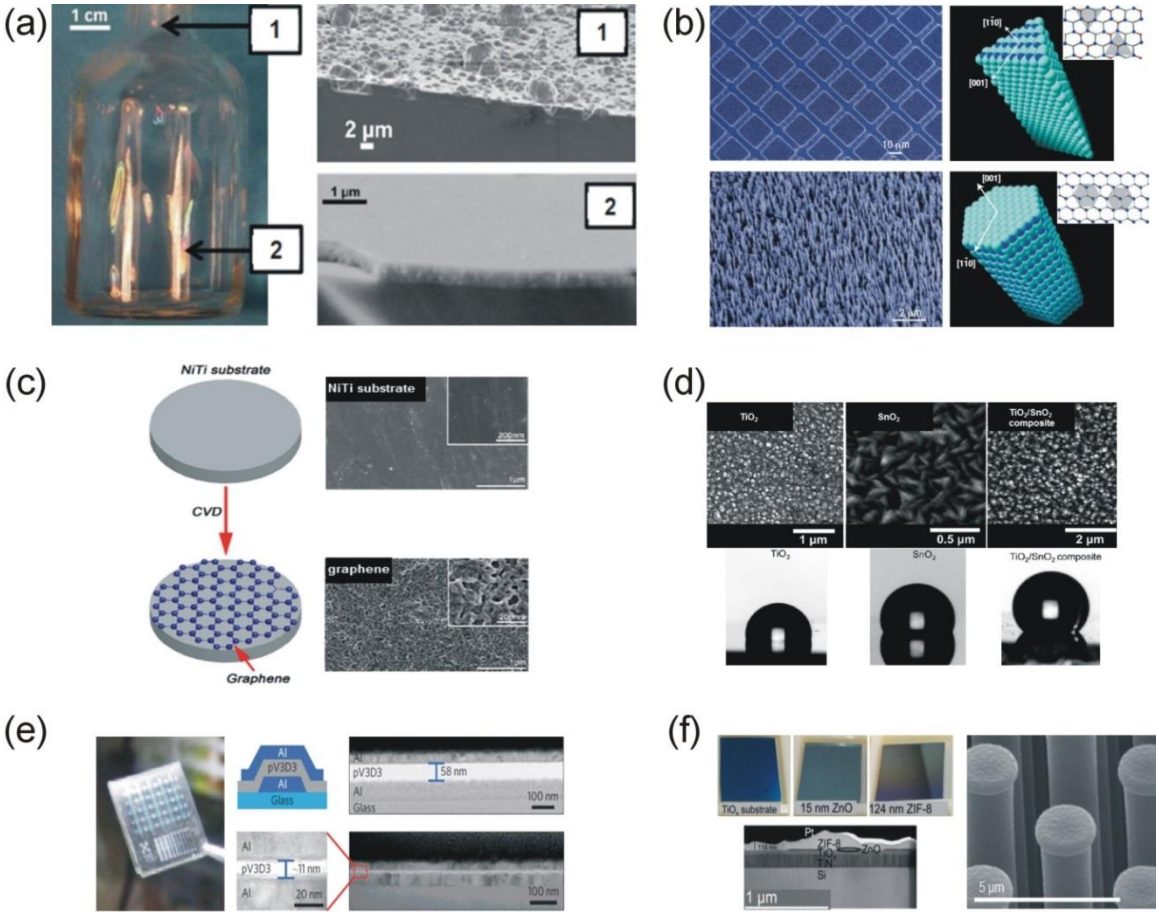

Figure 1.1: Materials produced by CVD techniques for targeted applications. (a) Thin Al_2O_3 coatings deposited by CVD at the inner part of a bottle (Etchepare *et al*., 2014); (b) CVD grown GaN nanowires on $LiAlO_2$ (top) and MgO surfaces (bottom) (Kuykendall *et al*., 2004); (c) CVD growth of graphene on NiTi substrates (Li *et al*., 2015); (d) Aerosol assisted CVD of composite TiO_2–SnO_2 films (Ponja *et al*., 2013); (e) Synthesis of polymer insulating layers by initiated CVD (Moon *et al*., 2015); (f) ZIF-8 thin films grown by CVD (Stassen *et al*., 2015).

Furthermore, CVD grown materials are used for functionalization such as increasing surface bioactivity or enhancing surface hydrophobicity and photocatalytic activity. Such cases are the CVD coated NiTi surface by graphene (Figure 1c) (Li *et al*., 2015) and the composite TiO_2–SnO_2 films (Figure 1d) (Ponja *et al*., 2013), respectively. Last but not least, there is an increased interest in the CVD of polymers, which provides ultrathin insulating

polymer layers for low-power soft electronics, among other desirable properties (Figure 1e) (Moon *et al*., 2015).

In CVD, the substrate to be covered is positioned in a zone of the reactor where energy (heat, radiation, electricity) is provided. An inert gas, called carrier gas, transports the reactive gas by convection in the reactor chamber to the surface of the substrate. The gas phase contains molecules – named precursors – with the elements to be deposited. Prior to entering the reactor, the precursors are evaporated. Alternatively, they already exist in their gas form. The energy provided enables the decomposition of the precursors in the bulk of the reactor and preferably on the surface of the substrate. It is this surface decomposition which leads to the production of the solid film and of volatile by-products which are removed from the reactor.

The principle of CVD is presented in Figure 1.2 where the different steps of the process are shown (Vahlas, 2010). Two distinct parts are illustrated: the precursors' scientific and technological management and the reactor zone. Within the latter, the different deposition mechanisms are depicted. First part refers to the design and the selection of the precursor based on the targeted application and the transport of the precursor's vapors in the reactor chamber. The selection of a precursor is an important stage since the characteristics and the required properties of the obtained thin films are inherently connected to the chemical structure and the reactivity of these molecular compounds.

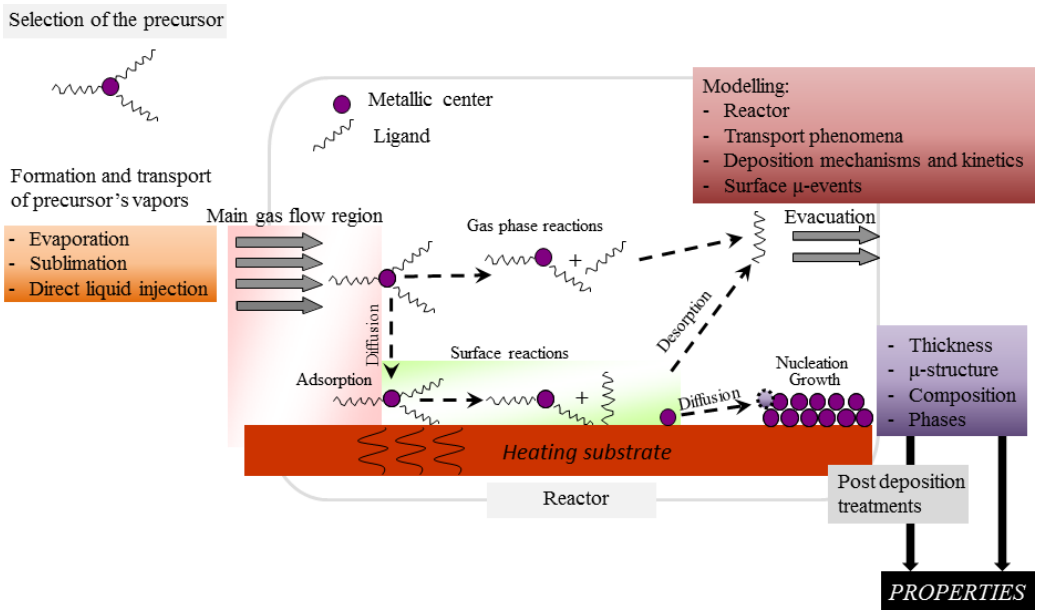

Figure 1.2: Schematic representation of the CVD process. The different pathways that the precursor and its products follow, indicate the involved steps and the complexity of the process.

The choice of a molecular precursor is adapted for each specific case or system to be investigated, however, it should fulfil specific prerequisites (Maury, 1995; Sovar, 2006):

- high purity;
- sufficient chemical stability to avoid degradation during storage;
- elevated vapor pressure at relatively low temperatures (room temperatures for liquid precursors, not more than 100^{o}C for solid precursors) for the complete and convenient transportation of its vapors in the reactor chamber;
- sufficiently high decomposition temperature to prevent as much as possible the premature gas phase reactions during transportation from the storage vessel to the process volume, but low enough to be able to process on temperature sensitive parts;
- clean decomposition with volatile by-products, avoiding the contamination of the resulting materials by heteroatoms such as oxygen, carbon, fluor or nitrogen;
- absence of dangers by its utilization, such as toxicity, pyrophoricity or explosiveness;
- affordable prices, regulations clearance and availability during its purchase.

Further constraints for the choice of precursors are added when a co-deposition process is applied and concern mainly the interactions among the different precursor molecules which may lead to unwanted results (see §1.2.3.). Last but not least, the efficient production of precursor's vapors and their transport to the reactor chamber are important issue that have to be tightly controlled in order to ensure controllable flow rates and consequently, contribute to the deposition of films with the targeted characteristics, and with satisfactory deposition rates (see §2.1.1.5.).

The second part of Figure 1.2 concerns the type of the process and the corresponding design and configuration of the reactor, namely the operating conditions which should be applied for the desired result. Among several classifications of CVD, metal-organic chemical vapor deposition (MOCVD) utilizes organometallic[2] precursors and results in thin films and coatings with targeted specifications, in terms of film thickness and uniformity, of substrate shape and compatibility with elevated temperatures or environmental compatibility and sustainability. The high-purity precursors may contain a direct metal-carbon bond, such as those included in metal carbonyls or in metal alkyls and lead to the production of solid films of high thicknesses. The definition of MOCVD has been extended to include compounds containing metal-oxygen bonds such as metal-β-diketonates, metal-nitrogen bonds such as metal amidinates and metal hydrides such as alane precursors (trimethylamine alane, triethylamine alane) (Luo and Gladfelter, 2009).

The development of MOCVD enhances the advantages already provided by conventional CVD techniques such as the conformal coverage of complex-in-shape surfaces

[2] While the term organometallic refers in general to a compound where a metallic atom is linked to one or more organic ligands, the term metalorganic is a more restrictive one, referring to metal-containing compounds lacking direct metal-carbon bonds but which contain organic ligands.

and the high throughput. Furthermore it allows operating at low to moderate temperatures, thus extending the deposition application to sensitive substrates (e.g. composite or polymeric surfaces), due to the existence of weak chemical bonds between the elements to be deposited and the other atoms (oxygen, carbon, nitrogen) or groups of atoms (ligands) to be removed from the reactor chamber.

In the case presented in this thesis, thermally activated MOCVD is preferable over the photo-assisted MOCVD or the plasma-enhanced MOCVD, where additional energy sources such as higher frequency radiation and electrical energy are applied to initiate and maintain the process. Such kind of sources may be intrusive to the involved sensitive chemistries; especially, they may impact in a differential way the two unary processes resulting in a tedious control of the process-structure relation.

MOCVD reactors are divided in two categories. The first are hot wall reactors, where the heat source to the substrates is the walls of the reactor themselves. The latter are often heated by a resistive coil gyred around them. Inside the reactor, there is a relatively homogeneous temperature distribution rather than a temperature gradient and the gas phase is heated yielding homogeneous, volumetric reactions and decompositions of the precursor molecule. As a result, the precursor undergoes gas phase consumption which prevents it reaching the substrate and may even result in powder formation due to homogeneous nucleation. These competitive phenomena imply a lower yield and the reactor must be serviced at a regular basis to be kept in clean conditions. It will be shown in the next chapters that, in the investigated combined process of Al and Fe, the gas phase and the surface reactions coexist over the entire temperature range and the operation in an environment which enhances the gas phase reaction rates renders the co-deposition more complex. However, due to the large heated volume involved, hot wall reactors are used in the industry when high throughput is requested.

The second category includes cold-wall reactors for which the substrate is heated directly inside the reactor chamber. Due to the difference in temperature between the main body of the reactor and the deposition surface, sharp temperature gradients exist which prevent in some cases the intense gas phase decomposition of the precursor and ensure consumption of the latter close to the surface. Thus, cold-wall reactors are more appropriate for the investigation of the mechanisms of the process.

Regarding operating pressure, MOCVD processes can take place at low pressures (LPCVD) as the cases presented in the following chapters, at ultra-high vacuum (UHV-CVD), as for the deposition of epitaxial silicon (Si) and germanium silicide (GeSi) layers (Adam, 2010) or at high pressures and more often under atmospheric pressures (APCVD) as for the cases of graphene (Vlassiouk *et al.*, 2013) or of Al_2O_3 coatings (Etchepare *et al.*, 2015). The LPCVD has limited impact on the behavior of the precursor molecules compared with UHV-CVD and APCVD where the vacuum or high pressure conditions may lead to the

increased desorption from the surface or to high decomposition rates of the precursor in the gas phase.

The different phenomena occurring during the process depicted in Figure 1.2, are gas phase (volumetric) and surface reactions, adsorption, desorption and diffusion of molecules or atoms on the surface and also the growth process per se; these phenomena are a matter of investigation of modeling and computational analysis and will be thoroughly analyzed in Chapter 3 of the thesis. The combination of the chemical, physical and technical options of each of the described parts have a significant impact on the final outcome of the process such as the thickness of the obtained material, its microstructure, its elemental composition and the formed phases.

As it is illustrated in Figure 1.2, the CVD technique can be schematically shown as a sequence of more than one steps. In particular, the precursor decomposes in the gas phase or it diffuses to the surface where it can undergo adsorption, decomposition or other reactions and migration. These mechanisms often depend on several operating conditions, such as the temperature, the pressure and the concentration of the precursor in the input gas mixture. In CVD processes, there always exists a limiting step which dominates and controls the whole process, in terms of deposition rate. Thus, different regimes of a deposition process can be defined, based on the corresponding limiting step (Jones and Hitchman, 2009; Pierson, 1999). The discrete regimes are shown in Figure 1.3, where a general Arrhenius plot is presented, i.e., the natural logarithm of the deposition rate of the film as a function of the inverse temperature in degrees Kelvin.

At low temperatures (regime I), the deposition rate is controlled by surface reaction kinetics (reaction-limited regime). In the reaction-limited regime, the amount of precursor which is available at the growing surface is in excess with regard to the quantity required for the resulting deposition rate; i.e., increase of the precursor feeding rate has no impact on the deposition rate. The deposition reaction occurs slowly and it strongly depends on the surface temperature, that is, the higher the temperature, the higher the rate of the deposition reaction and, thus, the deposition rate of the film. In the general form of an Arrhenius plot, the curve in regime I is linear, with a slope corresponding to the activation energy, E_a, of the deposition reaction. E_a, is the energy required to overcome the barrier of the transition from the state of the reactants (X) to the state of the products (Y), i.e., from the CVD precursors and other reactive gases to the solid film and the gaseous by-products (inset of Figure 1.3).

Further increase of the temperature above a certain limit, leads the deposition reaction to be performed so fast that the process is limited by the transport phenomena (regime II). In this case (transport or diffusion-limited regime), the diffusion rate of the reactants through the mass transfer boundary layer and the diffusion rate of the gaseous by-products out of this layer are the dominating mechanisms over the deposition reaction and control the overall deposition process. In the diffusion-limited regime, increase of temperature has limited impact on deposition rate. This is illustrated by the regime II of the Arrhenius plot where the

deposition rate is saturated. Indeed, temperature impacts the diffusivity of the species but it has limited influence on the deposition rate and the concentration of the reactants is high close to the surface. Therefore, in the diffusion-limited regime, the increase of the initial concentration of the precursor in the initial gaseous mixture yields higher deposition rates.

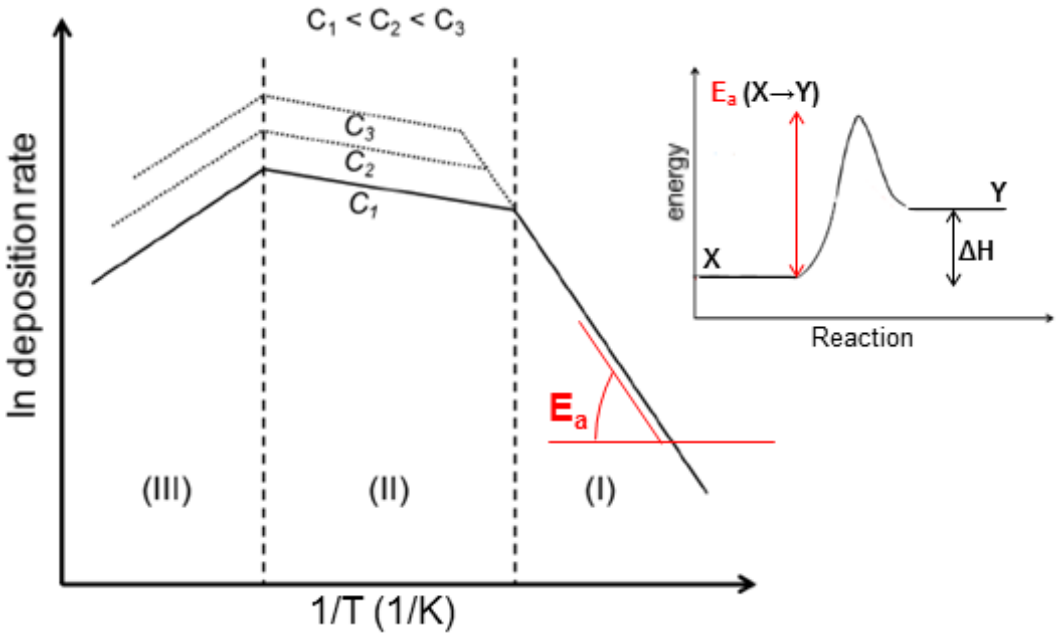

Figure 1.3: Arrhenius plot for a CVD process; evolution of the logarithm of the deposition rate as a function of the inverse surface temperature. The definition of the activation energy, E_a, for the initiation of the surface reaction is shown. The inset schematically depicts the physical meaning of E_a which is the energy required to pass from the state of reactants, X, to the CVD reaction products, Y.

At even higher temperatures (regime III), a significant decrease of the deposition rate is observed. In this region, various competitive phenomena may occur against the surface reaction. Most commonly, high temperature is a source of energy for the activation of the homogeneous gas phase reactions which occur with high reaction rates leading to the gaseous decomposition of the precursor molecule or to gas phase particle nucleation prior the diffusion of the reactants at the vicinity of the surface. The consequence of these side phenomena is the reduced availability of precursor molecules for the surface reaction leading to the targeted film, thus resulting in the decrease of the deposition rate. Moreover, processing films in this regime may lead to their contamination by heteroatoms or to the deposition of powders. Indeed, the provided heat in these conditions is high enough and may induce inappropriate decomposition of the initial molecular compounds and subsequent incorporation of ligands or part of ligands in the films as inhibition factors to the deposition, thus decreasing the deposition rate. The inappropriate decomposition of the precursor may also lead to the production of unwanted secondary materials that act as etching species (Choy, 2003). Finally, precursor's or other reactants' molecules which are adsorbed on the surface and are responsible for the deposition may undergo desorption with high rates, under the high temperature conditions, resulting in reduced deposition rates and thickness (Choy, 2003).

The operating pressure is another parameter of importance for a CVD process, as it also impacts the deposition rate of the film. For example, when the precursor molecule is stable enough, the increase of the total pressure strengthens the partial pressure of reactants (for the same molar fraction) and thus, leads to an *a priori* higher deposition rate (Pierson, 1999). On the other hand, by increasing the total pressure the mean free path of the precursor's molecules decreases and the collisions between the molecules increase, thus promoting homogeneous, gas phase reactions. This in turn, causes a high consumption rate of the precursor in the gas phase, lowers the available amounts on the surface and consequently lowers deposition rates. Furthermore, an increase of the pressure for a CVD process occurring in the diffusion-limited regime results in the lower diffusion of reactive species to the surface (the diffusivity of a gas phase species is inversely proportional to the pressure) and therefore, in reduced deposition rates.

The Arrhenius plot is a convenient basis for the optimization of a MOCVD process. For example, it allows defining the reaction-limited regime which gives the process ability of conformal coverage of complex-in-shape surfaces. However, the low deposition rates corresponding to the conditions in this regime render the performance of the process more convenient at temperatures between the limit of the reaction-limited regime and the diffusion-limited regime (transition temperatures). Hence, it is important to determine the limits of each regime at the Arrhenius plot, either experimentally or computationally, in order to be able to choose the appropriate operating conditions ("windows").

The effects of process temperature, pressure and initial precursor concentration on the deposition rate of Al and Fe films are experimentally and computationally investigated in Chapters 4 and 5. It will be shown that although the Arrhenius plot is a useful tool for the investigation and the understanding of the process, it is an oversimplification of a complex situation with various co-existing phenomena and mechanisms, and the different temperature regimes simply distinguish domains where a mechanism may prevail over the others. For example, as opposed to the schematic of Figure 1.3, a change in the precursor's concentration in the reaction-limited regime may have a strong effect on the deposition rate due to the co-existence of the surface reaction with a homogeneous reaction which consumes the precursor. Moreover, it has been shown in Aviziotis *et al*. (2013), that an alteration of the surface reaction rate affects not only the extend of the reaction-limited regime but also the diffusion-limited regime.

A global, simplified reaction scheme may describe sufficiently the behavior of the film deposition while neglecting any intermediate species. The absence of intermediate reaction steps may lead to the loss of important information for the explanation of a steep change in the deposition rate. The chemistry pathways involved in a CVD process is a difficult aspect of the overall investigation, due to the unavailability of extended chemistry libraries. The exploration of this complex part can be performed experimentally by techniques such as mass spectrometry or temperature programmed desorption, if available.

Alternatively, computational modeling of a CVD process can be applied for this investigation, by using already explored schemes, enhanced with further information such as an additional intermediate reaction or a different kinetic expression taking into account the inhibition effects of a by-product on the surface (see Chapter 5 for the CVD of Fe).

Additional complexities of an Arrhenius plot are revealed when a combined process such as the co-deposition, for the simultaneous processing of two or more metals, is concerned. These issues are addressed in details in the next section.

1.2.2. The co-deposition process of two or more materials

We refer to co-deposition as the one-step MOCVD process involving the simultaneous deposition of two or more metals for the production of intermetallic coatings. The application of co-deposition for the formation of complex metallic alloys (CMAs) is in its infancy and limited works can be found in the literature. Indicatively, it is referred the work of Prud'homme *et al*. (2013) where Al and Cu are co-deposited for the formation of the γ-Al_4Cu_9 approximant phase; the formed phase found to present surface wettability similar to that of equivalent bulk crystals. Another example is the co-deposition of Al with Pt on Ti surfaces for the formation of various phases, such as $AlPt_3$, $AlPt_2$, $Al_{21}Pt_6$ which strengthen the thermal properties of Ti6242 (Delmas, 2005; Delmas *et al*., 2005).

Additional constraints concerning the choice of precursors arise in the case of co-deposition. The process strongly depends on the availability of these molecular compounds (Vahlas, 2010):

- Similar transport behavior; similar thermal regulation of precursors is convenient and avoids subjecting thermally sensitive compounds to high thermal stresses. Moreover, precursors' flows have to be mixed at the entrance of the reactor chamber.
- Absence of heteroatoms in the ligands which may react with the other metal. This constraint is required even more when Al-based intermetallic compounds are concerned. In this case, the use of oxygen-containing ligands in the precursor molecule of the second metal results in the formation of aluminium oxide in the films.
- Compatible decomposition schemes. The dissociation of each precursor in the gas phase and on the deposited surface should remain unaffected by the presence of the other precursors. In a first approach, competitive phenomena among the precursors, such as inhibition of the growing surface by a decomposition by-product, should be avoided since it may cause a shift in the elemental composition of the film with regard to that of the input gas.
- Precursors from a common family of molecular compounds (e.g. amidinates) are preferable in the MOCVD of intermetallic compounds. In this way, the process is simplified and up-scaling is facilitated.

A co-deposition process implies the combined reading of two Arrhenius plots. As explained in the previous section, it is generally preferable to work in the reaction-limited regime to prevent gas phase interactions. However, for the particular Al and Fe systems chosen, gas phase reactions are inevitable over the entire investigated temperature range. Moreover, the cross linked reactivity between the two metals in terms of thermochemistry (oxidation of Al from the CO ligands) and of surface reaction[3] may pose additional problems in the determination of the appropriate operating conditions. Therefore, an additional degree of freedom is provided by the possibility to operate in a temperature window containing the early diffusion-limited regime for one element and the late reaction-limited or even the transition one, for the other. In such a way, the degree of incorporation of each element can be controlled by the concentration in the input gas of the precursor (diffusion-limited regime) and by the deposition temperature (reaction-limited regime).

1.2.3. The sequential deposition process of two or more materials

Incompatibilities between precursors may cause difficulties in the co-deposition process. Interactions and other competitive phenomena may result, in the selected operating conditions, in films whose compositions is shifted with regard to the targeted one or contaminated by heteroatoms. In order to circumvent these complications, sequential deposition in the form of bi- or multi-layers can be carried out. In this way, the involved precursors are never in contact in the deposition chamber. Furthermore, to avoid potential surface interactions caused by residues of the precursor used in a previous step, the reaction chamber is evacuated between the successive steps.

Sequential deposition bypasses the requirement of working at the same operating conditions for all the precursors. Optimum conditions for each precursor and the targeted intermetallic phase can be applied, instead. Sequential deposition is usually followed by an appropriately tuned annealing which leads to the formation of the targeted phases. The process has been widely applied for the formation of intermetallic phases. Indicatively, sequential deposition process has been performed for the formation of films containing the θ-Al_2Cu, η-AlCu and γ-Al_4Cu_9 phases (Aloui *et al*., 2012) and the formation of Al-Pt coatings on Ti alloy substrates (Delmas *et al*., 2005).

1.3. Computational modeling of CVD processes

1.3.1. Why modeling CVD?

Modeling accompanied by computational analysis of CVD processes aims at the understanding of the prevailing mechanisms occurring during the process. It further helps in defining the optimum operating conditions for the deposition of films with the desired

[3] It will be shown in the next chapters that non-optimized co-deposition results in films with low Fe content with regard to the targeted $Al_{13}Fe_4$ composition.

properties, and assists in the efficient upscaling of the process and its implementation in production lines. Through a computational model the validity of the chemistry scheme can be investigated and alternative schemes and mechanisms can be proposed and examined in connection with experimental observations and measurements. The modeling procedure is of high importance when co-deposition or sequential deposition are concerned, since it can provide an insight on unavailable in the literature chemical aspects which cannot be understood from simple experimental observations. In any case, experiments are driving and feeding the models and the theoretical predictions obtained from the latter could orient further experiments. That's how progress is made towards illuminating the important mechanisms of the process with further consequences, such as process control and optimization.

Furthermore, through modeling and computational analysis of a CVD process the preferred "operating windows" are determined, that is the values of key operational and physical parameters yielding the desired outcome of the process, in terms of overall efficiency and final product quality. Indicative parameters are the feed rate of the reactants, and the temperature and pressure in the reactor. The quality is usually determined by the thickness of the film and its uniformity, the elemental composition and the presence of heteroatoms and the surface microstructure, including crystallinity, grains and grain boundaries, porosity and surface roughness. The determination of preferred operating windows is even more important for co-deposition and sequential deposition where the combination of individual CVD processes requires the *a priori* knowledge of the key operating conditions and a consolidated process.

However, the mechanisms and phenomena involved in a CVD process may simultaneously occur at multiple length scales, in the bulk phase of the reactor and/or on the films' surface. Multiple length scales cover the macroscopic scale (macroscale) of the reactor, which is of the order of m to cm, down to the nanomorphology of the deposited film, of the order of nm to few μm, as it is schematically presented in Figure 1.4. Thus, with regard to the phenomena under investigation, a holistic study at all scales is required.

For these reasons and by considering that the occurrence of the nanoscale phenomena passes through the macroscale, the development of multiscale modeling frameworks is important (Braatz *et al.*, 2006; Rodgers and Jensen 1997; Vlachos 2005). It allows the investigation of phenomena occurring at the macroscopic level such as the chemical reactions and kinetics during a CVD process and at the same time it enables defining the impact of the macroscopic operating conditions to the nanomorphology of the films. The latter cannot be cast within the context of a single scale, since the nanoscale model requires macroscopic information for the surface simulations (see Chapter 3).

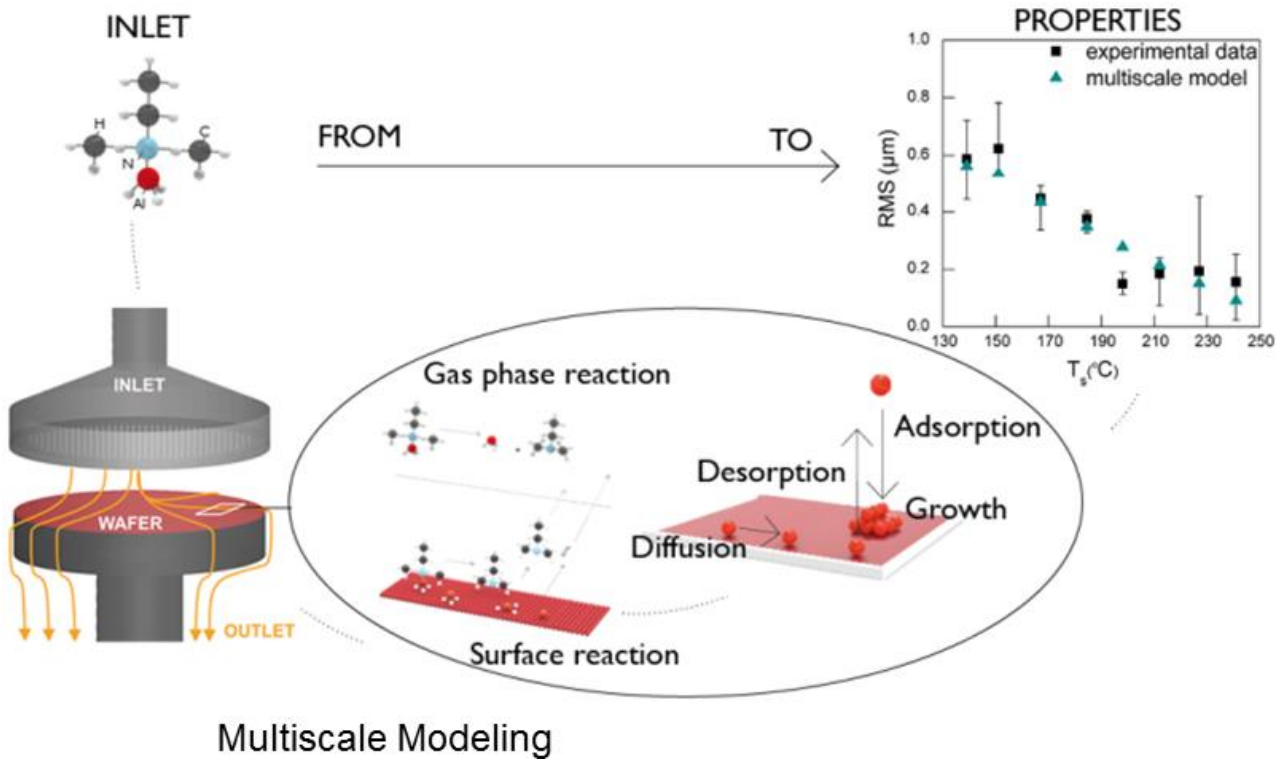

Figure 1.4: From the reactor scale to the calculation of the final film properties. Starting from the inlet and simulating the process macroscopically including the involved chemistry (gas phase and surface reactions), nanoscale simulations can be performed, by using computed quantities from the macroscale, which enable the calculation of the film growth and its roughness. The illustration depicts the link between the deposition mechanisms of Al from dimethylethylamine alane and the resulting surface roughness (see Chapter 4).

The two cases analyzed with multiscale modeling are the MOCVD processes of Al and Fe. The analysis aims at determining the chemical pathways and kinetics involved in the processes at the macroscopic level, simulating the surface evolution of the films at the nanoscale, and calculating the film surface roughness. In both cases, the analysis provides useful information for the impact of the operating conditions on the final quality of the film. Most importantly, it leads to the selection of the proper operating windows for the co-deposition and the sequential deposition of the two metals which is the ultimate goal. Two different models, one for the macroscale and one for the nanoscale are required for the description of the different simulated scales and the bridging between them is performed through the macroscopic species concentrations calculated at the computational surface.

1.3.2. Macroscopic modeling in CVD processes

The macroscopic mathematical model is composed of the partial differential equations describing the transport phenomena in the MOCVD reactor. The basic equations are those of the conservation of mass, momentum and energy and have to be solved numerically for the unknowns which are the velocity field, the distribution of pressure, temperature and species concentrations. The basic equations are augmented with necessary constitutive equations and they incorporate the kinetics of the chemical reactions both in the bulk (volume of the reactor) and on the deposition surface. The approximate solution of the equations is most

usually done with commercial software, i.e., Computational Fluid Dynamics (CFD) codes, using various discretization schemes, most often based on the finite element and finite volume methods. In the cases presented here, the commercial CFD software Ansys 12/ Fluent (Fluent hereafter) (Ansys 12.1/Fluent Documentation, 2009) is used which implements the finite volume discretization scheme (Thompson, 1985; Versteeg and Malalaskera, 2007).

1.3.3. Nanoscale modeling in CVD processes

For the description of surface processes and the evolution of the surface nanomorphology during the deposition of a film, stochastic growth equations (Barabasi and Stanley 1995; Voight 2004) as well as the grain-continuum approach (Bloomfield and Cale, 2004; Bloomfield *et al*., 2003) have been applied. In the present thesis, the widely used kinetic Monte Carlo (kMC) stochastic modeling is employed for calculating the surface evolution. Stochastic modeling is extensively used in deposition process simulation (Barabasi and Stanley 1995; Barbato *et al*., 2007; Battaile and Srolovitz 2002; Cavallotti *et al*., 2004; Chatterjee and Vlachos 2007; Kajikawa 2008; Lam and Vlachos 2001; Smy *et al*., 2001); also, in the related etching processes (Drotar *et al*., 2000; Kokkoris *et al*., 2007). The stochastic kMC algorithm accounts for three surface events, namely adsorption, desorption and migration (or diffusion), and the parameters required for the computation of these events may be obtained from experimental data or from molecular dynamics simulations (Frenkel and Smith 2002; Rapaport 2004).

1.3.4. Multiscale modeling in CVD processes

Microstructural characteristics depend on process conditions (temperature, pressure, etc.). In turn, they affect the targeted, desired properties such as electrical resistivity (Timalshina *et al*., 2015), hydrophobicity of the surface (Bormashenko *et al*., 2006; *Bravo et al*., 2007) or adsorption of proteins (Rechendorff *et al*., 2006; Zhdanov 2008). Consequently, the technological implementation of such processes with regard to targeted specifications requires the establishment of a robust relation between process parameters and films microstructure which, among others is characterized by the surface roughness. This can be met through the multiscale modeling of a CVD process with the roughness as an output.

For CVD processes, transport phenomena are modeled as briefly described above. However, the continuum description, through partial differential equations, breaks down as the length scale approaches that relevant to the surface level. Modeling the surface characteristics, e.g. roughness, at the same length scale used to model the bulk phase of the reactor leads to the loss of any structural information of the evolving surface (Barbato *et al*., 2007). The limitation of the use of the continuum models for the description of surface processes and the evolution of the surface nanomorphology during the film growth has led to the development of the above mentioned stochastic modeling and further, to multiscale

modeling (Cheimarios *et al*., 2011; Christofides *et al*., 2008; Crose *et al*., 2015; Lam and Vlachos 2001; Rodgers and Jensen 1998; Zhang *et al*., 2010).

In multiscale models, the reactor scale is linked to the surface level through the feeding of computational information. Among the first efforts for the one-way linking of deterministic macroscopic models with stochastic kMC models are those which refer to the CVD of diamond (Battaile *et al*., 1998; Battaile and Srolovitz, 2002; Srolovitz *et al*., 1997), while efforts for the bi-directional coupling of the two different scales are reported for CVD processes taking place in a vertical reactor without using any specific chemical system (Raimondeau and Vlachos, 2000). In the latter, due to the low concentration of the precursor, the continuum equations are solved decoupled. At the macroscopic level, the partial differential equations are reduced to one-dimensional, whereas only one "communication" node in the macroscopic computational domain is used for passing the necessary information to the nanoscale simulations.

A multiscale framework for the CVD of Si is reported in Masi *et al*. (2000). In this case, only the species transport equations are solved at the macroscopic level and the kMC model does not account for the formation of dimers, which is a characteristic of Si surfaces. The linking between the two scales is performed through the deposition rate, by assuming that it remains unchanged regardless the scale of simulation. The same assumption has also been used in a work for the CVD of diamond (Grujicic and Lai, 2000). These studies confirmed that, process conditions such as deposition temperature and molar fractions of the reactants in the inlet gas mixture have significant effect on the deposition rate and on the surface roughness of the films (Lam and Vlachos, 2001).

More recently, the coupling of different scales has been attempted for the multiscale modeling of the Si deposition process (Barbato *et al*., 2007; Cavallotti *et al*., 2004; Cavallotti *et al*., 2005). There the kMC model takes into account the adsorption of multiple molecules and the formation of dimer structures. Finally, multiscale frameworks are also developed for plasma-enhanced CVD; indicatively, the formation of Si thin films for solar cells (Crose *et al*., 2015) involves a macroscopic model that consists of the 2D conservation equations and a hybrid kMC model which accounts for additional events on the surface, such as hydrogen abstraction (Tsalikis *et al*., 2013).

In this thesis, the multiscale computational framework is based on the assumption that the deposition rate remains unchanged regardless the scale at which it is calculated. At the macroscopic level, steady-state, 3D simulations are performed for the solution of the conservation equations and the computational information which is fed to the nanoscale is the mass fraction of the reactants, containing the solid metal, at the surface level. The derived kMC algorithm for the description of the nanomorphology state is developed based on an existing model (Lam and Vlachos, 2001). Through this framework, the MOCVD processes of Al and Fe films are investigated by focusing on the involved kinetics and the deposition rate (macroscale) and the surface roughness (nanoscale). The two latter are compared with

experimental data obtained in similar conditions for the determination of operating conditions with regard to the co-deposition and the sequential deposition of the two metals.

1.4. The MOCVD of aluminum thin films

1.4.1. Precursors for Al deposition

The precursor for the MOCVD of Al, should fulfil the majority of the criteria described above. Various precursors have been reported in the literature between years 1980 and 2000 for the MOCVD of Al films. Among them, the triisobutylaluminum (TIBA), the dimethylaluminum hydride (DMAH), the trimethylaluminum (TMA), the trimethylamine alane (TMAA), the triethylamine alane (TEAA) and the dimehtylethylamine alane (DMEAA) are the most widespread used.

TIBA has been extensively studied as a precursor for deposition of Al films in the temperature range 200^{o}C – 400^{o}C (Bent *et al*., 1989; Green *et al*., 1984; Kobayashi *et al*., 1988; Sekiguchi *et al*., 1988). The rate-determining step in the deposition of Al involves cleavage of the Al-C bond by a β-hydrogen elimination, but a competitive β-methyl elimination becomes significant at temperatures around 300^{o}C yielding C-contaminated films (Bent *et al*., 1989). The deposition of Al from TMA suffers also from C-contamination of the films, since the direct Al-C bond in the precursor molecule is sufficiently strong to render simple bond homolysis ineffective as a mechanism leading to metallic Al (Luo and Gladfelter, 2009). The DMAH has been used to deposit high purity Al films (Amazawa, 1998; Kondoh and Ohta, 1995; Naik *et al*., 1998; Tsubouchi *et al*., 1990; Zhu *et al*., 1992). Depositions occur at elevated temperatures that is, greater than 270^{o}C for blanket coverage of various substrates and between 230^{o}C – 270^{o}C for selective deposition (Tsubouchi and Masu, 1992). In addition, above 350^{o}C, carbon incorporation into the film becomes significant. Beside these problems, the handling of the precursor per se is difficult, since DMAH undergoes a polymerization at the liquid state and at room temperature thus, increasing its viscosity at high levels (close to that of honey) (Lee *et al*., 1999).

Interest in amine alanes such as TMAA, TEAA and DMEAA is motivated by the requirement of producing C-free films, since these molecular compounds contain only a weak Al-N and three Al-H bonds. Tertiary amine groups do not bind strongly at the surface, the hydride ligand undergo facile elimination through the H_2 desorption from the surface and high crystalline Al films are obtained (Beach *et al*., 1989; Gladfelter *et al*., 1989; Simmonds *et al*., 1991; Simmonds *et al*., 1994). Due to the presence of weak bonds, deposition temperatures are significantly lower than for other precursors, at about 100^{o}C (Simmonds *et al*., 1994). Among the amine alanes, DMEAA is preferred due to its liquid state comparing to the solid state of TMAA which facilitates its evaporation and transport (Frigo *et al*., 1994; Simmonds *et al*., 1991), the easier dissociation of the Al-N bond comparing to the TEAA

(Frigo *et al*., 1994), the lower pyrophorocity compared to other alkyl aluminium precursors and its relatively high vapor pressure (Yun and Rhee, 1998).

1.4.2. The DMEAA precursor

The physical and chemical properties of DMEAA are presented in Table 1.1. DMEAA meets most of the selection criteria for an MOCVD precursor. Although it can be stored easily in a refrigerator at temperatures below 5^{o}C (freezing point), it requires careful handling due to its pyrophoricity and it is of relatively high cost. Its vapor pressure is given by the following relation (Frigo *et al*., 1994):

$$\log\left[P\left(Torr\right)\right] = 10.85 - 3080 / T\left(K\right). \quad (1.1)$$

This relation corresponds to relatively high vapor pressures for DMEAA, e.g. 0.7 Torr at 7^{o}C. DMEAA is maintained permanently at 3^{o}C with a cryostatic regulator and during the deposition process it is regulated at 7^{o}C, to achieve the targeted vapor pressure. The evaporation and the transport of the precursor are described in detail in Chapter 2 (see §2.1.1.5.).

Table 1.1: Physicochemical characteristics of DMEAA.

Identification	Name	Dimethylethylamine alane			
	CAS Number	124330-23-0			
	Appearance	Colourless liquid			
Chemical characteristics	Chemical formula	$(CH_3)_2(C_2H_5)N{\cdot}AlH_3{=}C_4H_{14}NAl$			
	Molecular structure	Tertiary amine ligand			
	Composition	C	H	N	Al
		46.58%	13.68%	13.58%	26.16%
	Molecular weight	103.14			
	Chemical stability	Degradation in normal conditions of P and T			
	Decomposition products	Dimethylethylamine (DMEA), alane (AlH_3), solid aluminium (Al) and molecular hydrogen (H_2)			
Physical characteristics	Density	0.78 g/cm^3			
	T_m	5^{o}C			
	T_b	-			
	Solubility	Violent reaction with air and water			
Security	Toxicity	Material is extremely destructive to tissue of the mucous membranes and upper respiratory tract, eyes, and skin.			
	Pyrophoricity	Auto-ignition with air contact, explosive with water contact			

The DMEAA molecule, which is shown in Figure 1.5, consists of an alane group (AlH_3) and an amine group where the nitrogen is connected with two methyl- (CH_3) and an ethyl- group (C_2H_5). DMEAA belongs to the tertiary amine family and its structure, with an Al-N bond between the AlH_3 and the amine group, is similar to trimethylamine alane (TMAA) and to triethylamine alane (TEAA). The weakness of the Al-N bond in the

precursor molecule results in the facile decomposition of the precursor, thus significantly lowering the Al deposition temperature.

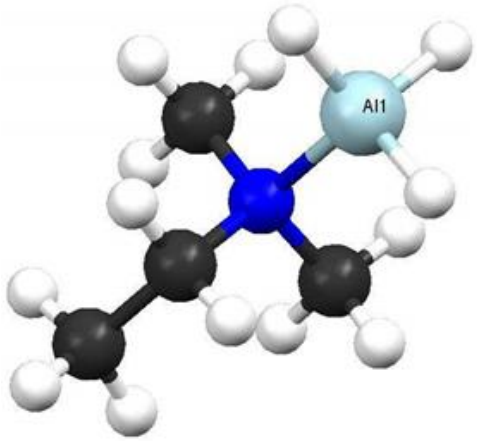

Figure 1.5: The molecule of DMEAA: the Al atom is coloured in light blue, the N atom in blue, the C atoms in black and the H atoms in white.

Due to the absence of direct bonds between Al and C, DMEAA produces C-free Al films, which was the critical problem leading to wire breakages in USLI circuits (Nakajima *et al*., 2003). Moreover, the weak bond between the AlH_3 group and the alkyl amine ($(CH_3)(C_2H_5)N$ – DMEA) is dissociated easily at temperatures as low as $\approx 100^oC$ with the organic by-product, DMEA, being inactive (Neo *et al*., 1999). However, the precursor is thermally unstable above its melting point and it undergoes degradation when it is stored for long periods even below its melting point. Thus, during the thesis three loads of 50 g of the precursor are used, for each series involving Al deposition.

1.4.3. Decomposition schemes of DMEAA

The behavior of DMEAA during the CVD of Al has been extensively studied and reported in the literature and several pathways of the gas phase and the surface decomposition of the precursor have been proposed to explain certain experimental observations (Han *et al*., 1994; Jang *et al*., 1998; Kim *et al*., 1996; Nakajima *et al*., 2003; Simmonds *et al*., 1994; Xenidou *et al*., 2010; Yun *et al*., 1998b). Among them, the most commonly used is schematically described in Figure 1.6 and it follows the similar decomposition schemes of TMAA (Dubois *et al*., 1990) and TEAA (Dubois *et al*., 1991).

The precursor can be decomposed in the gas phase for the production of AlH_3 and DMEA. This reaction has been confirmed by performing Fourier Transform Infrared (FTIR) analysis (Yun *et al*., 1998b). AlH_3 gas may undergo a polymerization which includes the formation of monomer, dimer and trimer intermediates and produces Al particles in the gas phase (not shown in the cartoon of Figure 1.6) (Yun *et al*., 1998b). The non-decomposed precursor is adsorbed on the surface by presenting the basis of the tetrahedron corresponding to the AlH_3 part. It is then separated from the amine and momentarily adsorbed on the surface

prior desorption. The AlH_3 lose the three hydrogen atoms which migrate on the surface and combine with each other to form molecular hydrogen desorbed from the surface. The rate limiting step of this process is either the decomposition of DMEAA on the surface (rate determining step of TMAA) or the desorption of molecular hydrogen from the surface (rate determining step of TEAA) or a combination of these two surface steps.

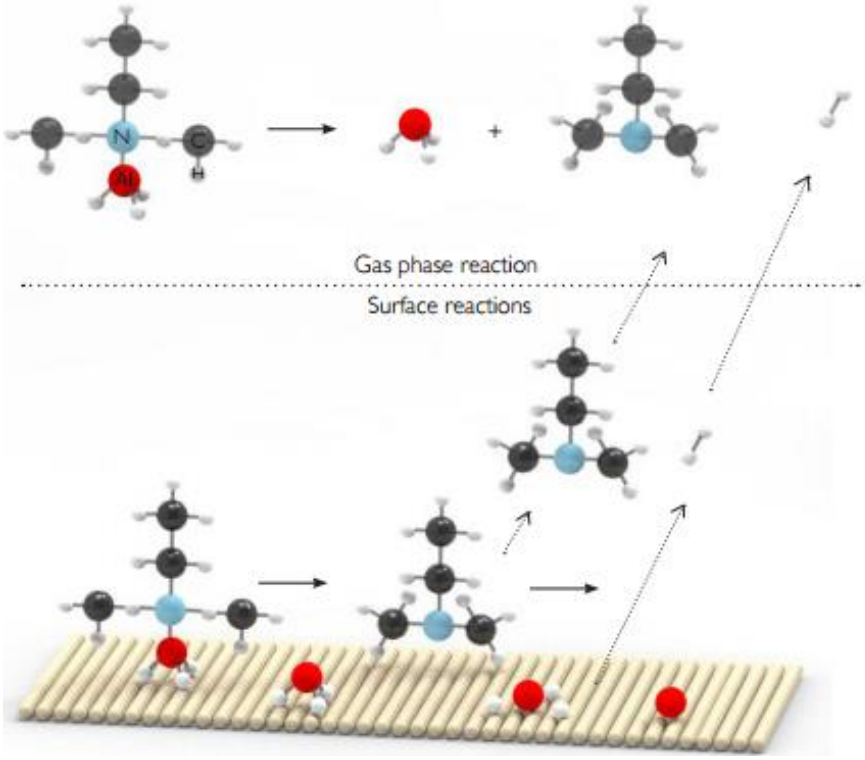

Figure 1.6: Decomposition pathway of DMEAA (Simmonds *et al*., 1994).

A different decomposition mechanism is proposed in Nakajima *et al*. (2003) including successive dehydrogenation steps of the AlH_3 until the deposition of Al. In this thesis, the decomposition mechanism described above is examined for the prediction of the behavior of the Al deposition rate in the investigated temperature range. The decomposition paths of the MOCVD of Al from DMEAA as well as the kinetics describing these mechanisms are investigated in terms of macroscopic modeling in Chapter 4.

1.5. The MOCVD of iron thin films

1.5.1. Precursors for Fe deposition

Various Fe metalorganic precursors have been studied for the deposition of Fe films. The ferrocene ($FeCP_2$, Cp:cyclopentadienyl) and the $Fe(COT)(CO)_3$ (COT: cyclooctatetraen) have been tested for the production of Fe-C:H films and not for pure Fe films (Luithardt and Benndorf, 1996). The binuclear compound bis(μ-tetracarbonyl-η-cyclopentadienyl) iron ($Fe_2Cp_2(CO)_4$) is a solid state precursor which requires high sublimation temperature (80°C–120°C) and high deposition temperatures (280°C–300°C) for the deposition of fairly pure (≈

97%) Fe films (Feurer *et al*., 1988). The Fe bis(trimethyl)sylylamido molecular compound $(Fe[N(SiMe_3)_2])_3$ also requires high temperatures for sublimation and deposition and the resulting Fe films are less pure than previously (Baxter *et al*., 1995). Thus, both $Fe_2Cp_2(CO)_4$ and $Fe[N(SiMe_3)_2]_3$ operate at higher deposition temperatures than those admitted for the MOCVD of Al from DMEAA; a compatibility problem for co-deposition.

More recently, a limited investigation of Fe(II) dihydrides and [(arene)(diene)Fe(0)] compounds as MOCVD precursors for Fe deposition has been reported. The $H_2Fe[P(OCH_3)_3]_4$ and the $H_2Fe[P(CH_3)_3]_4$ of the dihydrides family, have been found to result in either $Fe+Fe_3O_4$ or pure Fe films, respectively, within the temperature range 230°C–280°C (Park *et al*., 2006). Precursors such as [(1,3-cyclohexadiene)(toluene)Fe(0)] of the [(arene)(diene)Fe(0)] category deposit films in lower to moderate temperatures. Yet, the films consist mostly in iron oxides and the deposition duration is in the range of 4 h – 8 h to a measurable thickness (Michkova *et al*., 2010). MOCVD processes of iron amidinate precursors such as $[Fe_2(\mu\text{-}^{i}PrMeAMD)_2(\eta^2\text{-}^{i}PrMeAMD)_2]$ or $[Fe(^{t}Bu\text{-}MeAMD)_2]$ (AMD:acetamidinate) yield Fe carbide or Fe nitride films (Krisyuk *et al*., 2010), although their application in ALD processes results in pure Fe films (Lim *et al*., 2003). Moreover, the Fe(II) amidinate precursors are extremely sensitive to air and light (Gottlieb-Schoenmeyer *et al*., 2010) and thus, a careful and difficult handling is required.

Iron pentacarbonyl ($Fe(CO)_5$) is a widely studied molecular compound which provides high vapor pressure at room temperature (Lane *et al*., 1999) thus, facilitating its transport into the reactor chamber. Furthermore, its deposition temperature is compatible with that of DMEAA. Despite the existence of Fe-C bonds, $Fe(CO)_5$ leads to pure Fe films with C and O contaminants at the level of a few at% (Jackman and Foord, 1989).

1.5.2. The $Fe(CO)_5$ precursor

The physical and chemical properties of $Fe(CO)_5$ are presented in Table 1.2. $Fe(CO)_5$ meets most of the selection criteria for a MOCVD precursor as well as the additional constraints set by its co-deposition with DMEAA. The main drawback is that it contains C and O heteroatoms which may lead to undesired contamination of the film and to oxidation of Al. Also, its storage is difficult since it requires very low temperatures (ideally, lower than -20°C which is its freezing point). However, it can be stored in a refrigerator, at 0°C, where the lower vapor pressure limits the high degradation rate of the precursor sufficiently. The weakness of the Fe-CO bond has an impact on the thermal stability of the precursor and renders it unstable; it yields a high vapor pressure of 22 Torr, at 20°C, as calculated by the following formula (Gilbert and Sulzmann, 1974):

$$\log\left[P(Torr)\right] = 8.4959 - 2096.7 / T(K). \quad (1.2)$$

When evaporated from a bubbler (see §1.4.3.), $Fe(CO)_5$ is maintained permanently at -18°C with a cryostatic regulator. However, even at this low temperature the precursor has a

relatively high vapor pressure (1.88 Torr – see §2.1.1.5.). The evaporation and the transport of the precursor are described in detail in Chapter 2 (see §2.1.1.5.). The precursor is also light sensible and it degrades when it is stored for long. Thus, additionally to low temperature conditions, its contact with light should be prevented during storage.

Table 1.2: Physicochemical characteristics of $Fe(CO)_5$.

Identification	Name	Iron pentacarbonyl
	CAS Number	13463-40-6
	Appearance	Yellow to dark red liquid
Chemical characteristics	Chemical formula	C_5FeO_5 or $Fe(CO)_5$
	Molecular structure	trigonal bipyramidal
	Composition	C: 30.66%, O: 40.84%, Fe: 28.50%
	Molecular weight	195.9
	Chemical stability	Unstable at room temperature
	Decomposition products	CO, $Fe(CO)_4$, $Fe(CO)_3$, $Fe(CO)_2$, FeCO, solid iron (Fe)
Physical characteristics	Density	1.453 g/cm^3
	T_m	-21°C
	T_b	103°C
	Solubility	Degradation in the presence of air or moisture – Flammability/pyrophoricity danger.
Security	Toxicity	Highly toxic vapors; irritation of the upper respiratory tract, eyes, skin; injury of liver, kidneys, lungs; headache, dizziness, nausea.
	Pyrophoricity	Pyrophoric in air; dangerous fire risk; may be ignited by heat sparks or flames.

The $Fe(CO)_5$ molecular compound, which is shown in Figure 1.7, belongs to the general family of metal carbonyls. It has a slightly distorted trigonal-bipyramidal geometry and it consists of an Fe atom surrounded by five CO ligands, three in equatorial position and two axially bound, where each of the Fe-C-O linkage is linear.

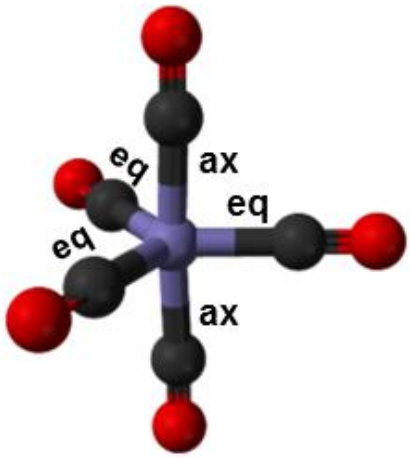

Figure 1.7: The $Fe(CO)_5$ molecule. The Fe atom is coloured in purple, the C atoms in black and the O atoms in red. The ax and eq notation stands for the equatorial and the axial position of the CO ligands.

Within the molecule, the Fe-CO bond is relatively weak and this low strength renders the compound volatile and facilitates the deposition process. This fact along with the symmetrical structure of the compound and its charge neutrality, renders $Fe(CO)_5$ highly volatile (Braga *et al*., 1993; Mathey, 2013).

1.5.3. Decomposition schemes of $Fe(CO)_5$

The behavior of $Fe(CO)_5$ during the CVD of Fe has been extensively investigated in the literature. Various pathways for the decomposition of the precursor in the gas phase and at the surface have been proposed to explain the experimental observations and the molecular structure of the $Fe(CO)_5$ compound and its intermediates (Carlton and Oxley, 1965; Jackman and Foord, 1989). The simplest mechanism involves the one-step surface dissociation of the precursor to metallic Fe and five adsorbed CO ligands (Carlton and Oxley, 1965). The kinetics applied for this simple mechanism includes a Langmuir-Hinshelwood type expression, where the precursor is adsorbed and dissociates on the surface under specific activation energies and the produced CO as well as the precursor which has not decomposed may inhibit the deposition surface.

However, this scheme seems unlikely to occur since the $Fe(CO)_5$ compound can be decomposed even at room temperature. More detailed reaction pathways include the successive decarbonylation steps of the precursor to the formation of metallic Fe (Barnes *et al*., 1991; Gonzáles-Blanco and Branchadell, 1999; Lewis *et al*., 1984; Seder *et al*., 1986; Xu and Zaera, 1994; Zaera, 1991). The $Fe(CO)_5$ starts decomposing in the reactor but close to the deposition surface, where the temperature is elevated, and the first step yields the formation of gaseous $Fe(CO)_4$ and CO (Gonzáles-Blanco and Branchadell, 1999; Xu and Zaera, 1994). The intermediate tetracarbonyl compound dissociates into $Fe(CO)_3$ and CO due to the high rate of this reaction (Dateo *et al*., 2002). Thus, $Fe(CO)_4$ is totally converted to the tricarbonyl compound. The $Fe(CO)_3$ loses one more CO group for the gas phase production of $Fe(CO)_2$ and CO and the same holds for the dicarbonyl compound which provides FeCO and CO (Barnes et al., 1991; Gonzáles-Blanco and Branchadell, 1999). The dicarbonyl, tricarbonyl and tetracarbonyl intermediate compounds can also undergo recombination reactions with the gaseous CO groups in a backward reaction scheme (Seder *et al*., 1986). The rates of the recombination reactions of $Fe(CO)_2$ and $Fe(CO)_3$ are much higher than that of the recombination reaction of $Fe(CO)_4$, since the latter is spin forbidden as reported in Seder *et al*. (1986). The FeCO compound has not been reported to recombine with CO for the formation of $Fe(CO)_2$.

The quantity of $Fe(CO)_5$ which is not converted to $Fe(CO)_4$ undergoes a surface decomposition to metallic Fe and 5 adsorbed CO groups which may saturate the surface (Carlton and Oxley, 1965; Jackman and Foord, 1989; Zhang *et al*., 2016). Moreover, the intermediate compound $Fe(CO)_3$ can decompose on the surface to metallic Fe and adsorbed CO (Xu and Zaera, 1994). The same occurs for FeCO (Dateo *et al*., 2002; Ricca, 2001). In all

these surface steps, the presence of the adsorbed CO group may act as an inhibitor to the deposition of pure Fe (Zhang *et al*., 2016). Due to the high energy barrier required for the gas phase dissociation of $Fe(CO)_2$ into FeCO and CO (Gonzáles-Blanco and Branchadell, 1999), the surface decomposition of FeCO is negligible.

The presented decomposition path of the MOCVD of Fe from $Fe(CO)_5$ along with the involved kinetics describing these mechanisms are used in the macroscopic modeling in Chapter 5.

1.6. Formation of $Al_{13}Fe_4$ intermetallic compounds by MOCVD

1.6.1. The $Al_{13}Fe_4$ intermetallic structure

It has been recently reported that the monoclinic, m-$Al_{13}Fe_4$ intermetallic structure, which follows the site-isolation concept, has advantageous catalytic properties that is, high activity and selectivity, for the semi-hydrogenation of acetylene to ethylene for polyethylene production (Armbrüster *et al*., 2012). This structure follows site-isolation concept: Fe atoms are isolated in highly-coordinated Al clusters. These smaller active sites allow only a limited number of adsorption configurations, which potentially leads to a smaller number of by-products and higher selectivity towards ethylene. In addition, as the majority of complex metallic alloys, $Al_{13}Fe_4$ is a structurally ordered metallic phase, which comprises covalent bonding making the structure more stable and reducing segregation. Its unit cell is composed of 102 atoms (78 Al and 24 Fe atoms) shared between 2 flat (17 Al/8 Fe atoms) and 2 puckered (22 Al/4 Fe atoms) layers stacked in the decagonal quasicrystal structure (Ledieu *et al*., 2013; Matilainen *et al*., 2015). In this sense, m-$Al_{13}Fe_4$ is an approximant of the decagonal quasicrystal. The Fe atoms in the flat layers form rhombi and two types of pentagons. The atomic structure of the puckered layers can be interpreted as composed of pentagons and additional, dubbed Al atoms which operate as glue atoms as shown in Figure 1.8a (Ledieu *et al*., 2013). The individual Al pentagons are paired to form a bipentagonal motif. The Fe atoms are located slightly below or above the mean plane of the pentagons. The individual Fe-centered, Al pentagon corresponds to either the bottom or the top cap of a "pentagonal bipyramid" clusters suggested by Black (1955) and Grin *et al*. (1994) for the geometrical description of the $Al_{13}Fe_4$ bulk structure.

Figure 1.8b shows a 3D view of the m-$Al_{13}Fe_4$ structure (Armbrüster *et al*., 2012), where the Fe atoms are either solely coordinated by Al or arranged in Fe-Al-Fe groups located in the cavities of the three dimensional Al framework (Grin *et al*., 1994). This results in a complete encapsulation of the potential active transition-metal sites by Al atoms, thus, following the site-isolation concept. Furthermore, segregation is significantly decreased by the covalent bonding presented in this particular phase of the intermetallic structure yielding a structural stability. In turn, the resulting structural stability can preserve the geometric

arrangement under reaction conditions and prevents the formation of hydrides, thus, leading to higher durability.

The m-$Al_{13}Fe_4$ intermetallic phase is preferable for the catalytic semi-hydrogenation of acetylene over conventional catalysts such as palladium (Pd). Pd is a highly active catalyst for this reaction, and is alloyed with silver on Al_2O_3 supports to decrease the size of the active sites (Konvir *et al*., 2007; Konvir *et al*., 2009; Osswald *et al*., 2008). However, the catalyst presents limited selectivity due to random arrangement of the atoms leading to a partial isolation of the active sites from each other and to segregation of the alloy. This results in the creation of larger active sites with time on stream and subsequently to the deactivation of the catalyst because of the formation of carbonaceous deposits. Moreover, comparing to other intermetallic structures, such as the palladium-gallium (Pd-Ga) system, the $Al_{13}Fe_4$ phase provides a cheap solution for the replacement of the precious, noble metals, without any potential health risks, as for example the nickel (Ni) structures.

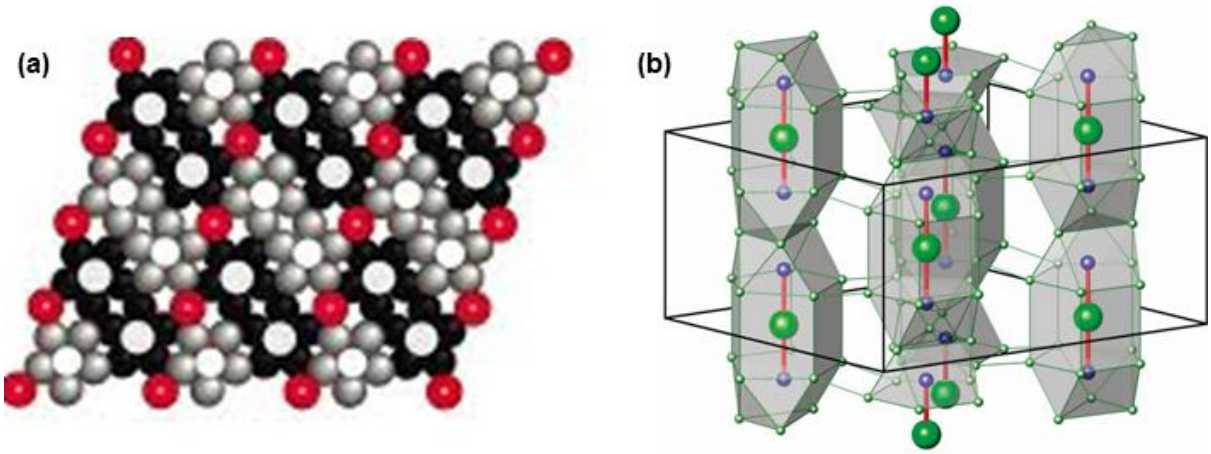

Figure 1.8: Representation of the structure of the m-$Al_{13}Fe_4$ crystal. (a) A puckered layer of the crystal (Ledieu *et al*., 2013). Black and light grey spheres correspond to Al atoms forming bipentagonal motifs. Red spheres stand for the Al operating as glue atoms. Fe atoms are located above (hatched circles) or below (empty circles) the mean plane position. (b) A 3D view of the $Al_{13}Fe_4$ unit cell (Armbrüster *et al*., 2012). Large and small green spheres represent the Al atoms and blue spheres the Fe atoms. The representation of the unit cell emphasizes the structurally isolated Fe-Al-Fe units.

1.6.2. Processing Al-Fe by MOCVD for $Al_{13}Fe_4$ supported catalysts

In the work of Armbrüster *et al*. (2012), the $Al_{13}Fe_4$ was synthesized from Al and Fe metals with a process described in Gille and Bauer, (2008) to form a single crystal. In contrast to the commercial Pd/Al_2O_3 supported catalyst which is optimized for the semi-hydrogenation of acetylene to ethylene, the $Al_{13}Fe_4$ used for the same application is a single crystal without any engineering optimization. It is expected that optimization of the complex intermetallic phase in terms of supporting the material may lead to an even better catalytic performance. The supporting $Al_{13}Fe_4$ phase will confer multifunctionalities to advanced materials required by industrial sectors and functionalization of complex surfaces. To ensure

the industrial prerequisites, an appropriate method should be selected for the formation of films containing the m-$Al_{13}Fe_4$ intermetallic phase.

Several studies are devoted the formation of intermetallic phases in the Al-Fe system (Csanády *et al*., 1988; Haidara *et al*., 2012; Teixeira *et al*., 1987; Teixeira *et al*., 1989). Various deposition techniques have been applied to obtain Al-Fe intermetallic coatings, including thermal spraying and magnetron sputtering (Haidara *et al*., 2012; Kumar *et al*., 2006; Yang *et al*., 2011), self-propagated high-temperature synthesis (SHS) (Azem *et al*., 2011; Godlewska *et al*., 2003), 3D laser cladding (Shishkovsky *et al*., 2013; Zhao *et al*., 2012), selective laser melting (SLM) (Dadbakhsh and Hao, 2012; Song *et al*., 2012), gas detonation spraying (Senderowski, 2014) and mechanical alloying (Canakci *et al*., 2013). Despite the effective production of Al-Fe intermetallics, these methods suffer a number of drawbacks, such as the creation of sponge-like structures because of rapid and violent phases transformations during the reaction synthesis, technical difficulties related to considerable differences in the physical properties of the substrate and the coating materials (e.g. their melting points and bonding properties), uncertainties about keeping the particles of the powder feedstock in the solid state while reaching a temperature at which they undergo softening and high connection strength due to difference in the temperature expansion coefficients of the coating and the base layer.

Furthermore, catalytic processes require high surface to volume ratio of the catalytic material and for this reason, processing of Al-Fe films on supports is even more desired. By operating at low to moderate temperatures, i.e., in the vicinity of the reaction-limited regime, MOCVD processes can meet the requirements for the processing of such coatings on complex, non-line-of-sights surfaces and powders.

At first, a trial for the direct, one-step co-deposition process is attempted. For the co-deposition, an operating window of the two involved precursors is identified. In particular, a deposition temperature and a reactor pressure are chosen in such a way that the deposition is performed in the reaction-limited regime. However, the lack of data concerning the interactions between the two precursors during the co-deposition is a major limitation and prevents the *a priori* foresight of the resulting structures. For these reasons, at a second step a two-step process is performed. That is a sequential deposition of Al and Fe in the form of layer by layer deposition, followed by an appropriate *in situ* thermal annealing. The sequential deposition is more easily tuned although it consists of more than one step.

Both processes and the resulted films are presented in detail in Chapter 6. Coatings deposited under various process conditions are characterized by several techniques for the determination of the elemental composition, the structure and microstructure, and to identify the formation of the desired m-$Al_{13}Fe_4$ complex intermetallic phase.

Summary-Conclusions

The purpose of this thesis is the implementation of a CVD technique for the processing of Al-Fe intermetallic films and specifically, for the deposition of the m-$Al_{13}Fe_4$ approximant phase which exhibits the multifunctionalities of intermetallic structures, including catalytic properties. To this direction, a co-deposition and a sequential deposition process are applied.

The pillars on which a successful CVD process is based are the proper selection of precursor molecular compounds, the proper design of the reactor and the insight in and control of the various phenomena occurring during deposition. All of these aspects are inherently connected with the outcome of the CVD and are summed up in the Arrhenius type plots. The latter is very important for a CVD process since it enables the determination of distinct regions where the surface reaction, the diffusion and other competitive phenomena dominate the process. CVD is an advantageous technique, since it provides relatively thick films at reasonable process time, conformally deposited on complex surfaces.

Before proceeding to co- or sequential deposition, the MOCVD of the unary films of each metal, Al and Fe, should be examined. To begin with, DMEAA and $Fe(CO)_5$ are selected among a large number of Al and Fe precursors, respectively, due to the fact they meet most criteria that molecular precursors should fulfill. Several pathways for the decomposition of the two precursors have been proposed in the literature and examined in this thesis.

This investigation is performed by modeling the MOCVD processes of the two metals. The modeling is carried out at different scales. Chemical mechanisms and their corresponding kinetics at the reactor scale are studied by macroscopic modeling, based on the continuum assumption and on the basic equations of the conservation of mass, momentum and energy. On the other hand, for the study of the surface nanomorphology, multiscale models are applied, which link the reactor scale with the nanoscale of the surface. Multiscale simulations enable the calculation of the evolution of the film surface and of surface properties such as roughness.

Chapter 2: Experimental materials and methods

Chapter 2 presents the setup of the MOCVD reactor where the depositions of unary and complex metallic films are performed. Experimental techniques such as the regulation of the temperature, the pressure are described in detail and the evaporation and the injection systems used for the transport of the precursors in the reactor, are thoroughly presented. Furthermore, the protocols applied for the preparation of the samples prior deposition, the MOCVD process per se and the procedures followed after the deposition are given in detail. The chapter finishes with the description of the techniques used for the analysis of the structure, the microstructure and chemical composition of the deposited films and the short presentation of the setup of the catalytic tests.

2.1. Experimental techniques

2.1.1. The concept of the reactor

The reactor is designed to meet the specifications and to better reproduce the MOCVD of unary and complex metallic films in static configuration. Figure 2.1 shows a 3D schematic of the MOCVD reactor designed with the commercial software CATIA®, on which the various modules of the reactor and the degrees of freedom are indicated. Each part of the system is removable in order to be cleaned as for the case of tubing or viewports of the reactor chamber, to be replaced if needed (e.g. a broken mass flow controller) and to be loaded with the appropriate precursor (bubbler for DMEAA and bubbler or DLI system for $Fe(CO)_5$). The MOCVD system has been successfully tested for the deposition of unary as well as binary metallic films (Aloui *et al*., 2012; Krisyuk *et al*., 2011; Xenidou *et al*., 2007; Xenidou *et al*., 2010). It has been modified to meet the requirements of the MOCVD processes presented in this thesis.

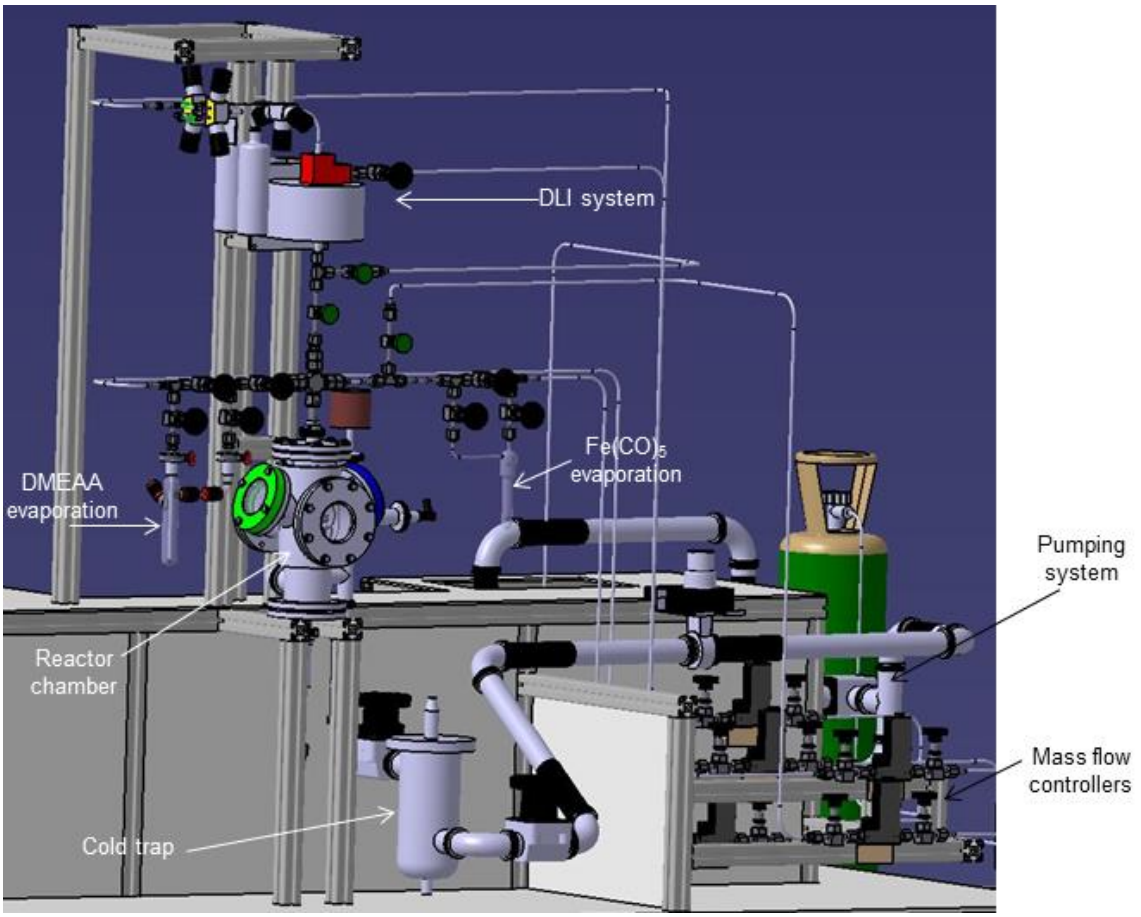

Figure 2.1: 3D design by CATIA software of the MOCVD reactor used for the deposition of unary and intermetallic films.

The flow chart of Figure 2.2. of the MOCVD system shows all the gas lines, the vacuum system, the evaporation and the DLI systems, the exact position of the valves and the control of pressure and temperature.

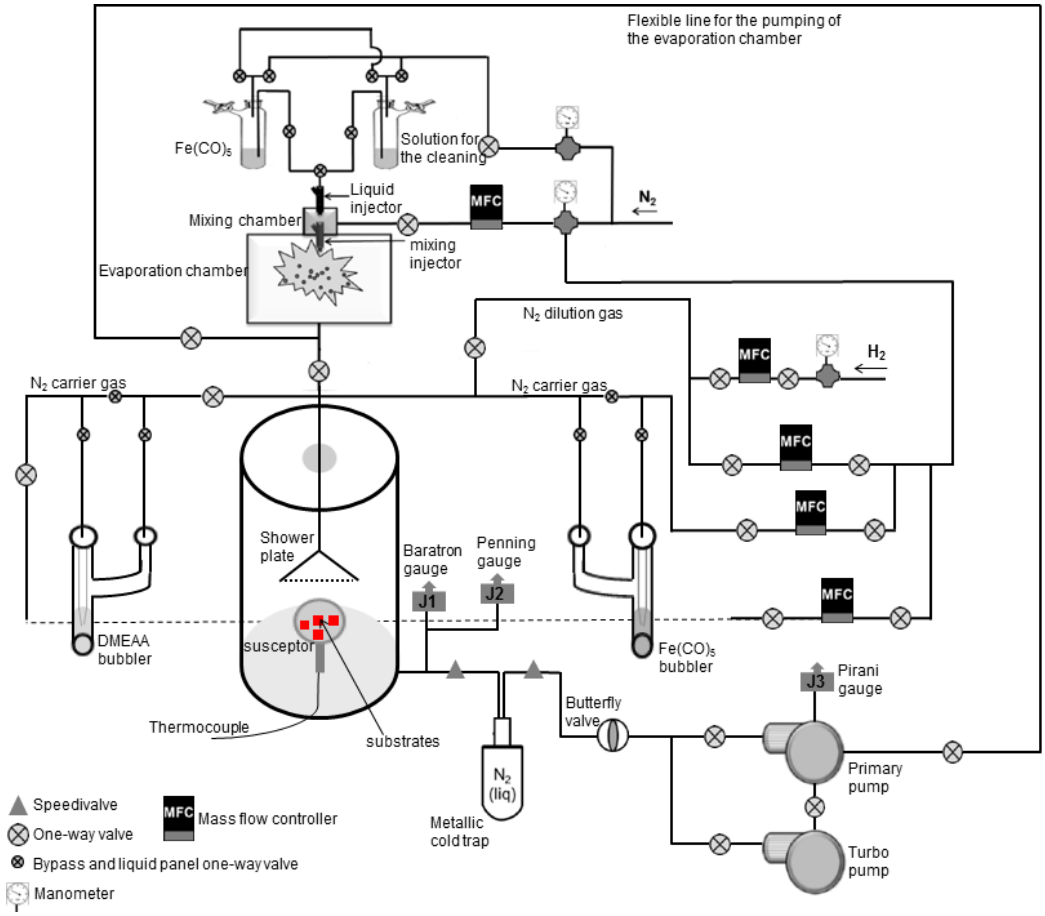

Figure 2.2: The detailed flow chart of the MOCVD system used for the deposition of Al and Fe unary films and Al-Fe intermetallic structures.

2.1.1.1. The main body of the reactor

A photograph of the reactor chamber is shown in Figure 2.3a. The chamber consists of a vertical cylinder with double stainless steel walls and three windows, two at the side walls and one at the front, allowing the operator to do several observations inside the reactor, such as the change of the color of the substrates during a deposition process or any possible problems occurring during the MOCVD process. The chamber was provided by the company MECA 2000 and the regulation of temperature is ensured by silica oil circulation (Fischer Scientific) thermostated by POLYSTAT 36. Thus, it is possible to work at cold, warm or hot walls with regard to the applied process and up to 205^{o}C where the silica oil degrades. Figure 2.3b depicts the gas flow of the input mixture (white arrows), entering the reactor from its upper part and coming out from an exit at the bottom part which allows the evacuation of the by-products and of the non-consumed reactive gas-phase by the pump.

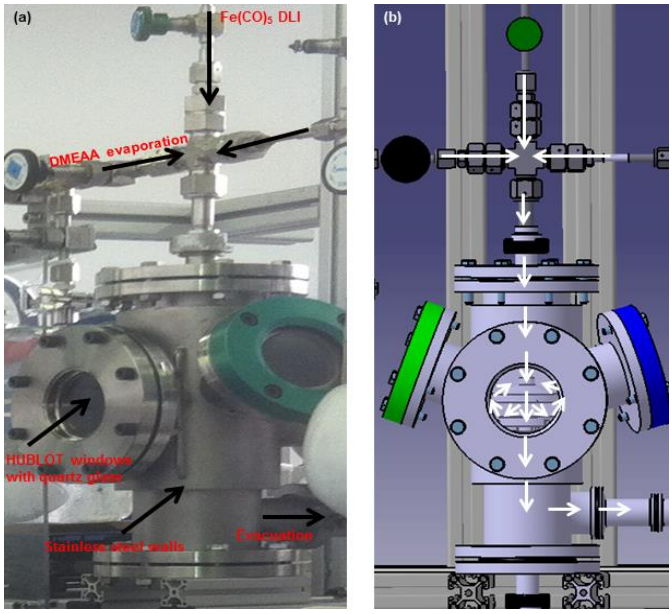

Figure 2.3: Photograph of the main body of the MOCVD reactor (a) and a 3D design (CATIA) of the reactor chamber (b). The white arrows show the flow of the gas mixture from the inlet of the reactor to its outlet.

Inside the reactor (Figure 2.4a), the substrates are placed on a 58 mm diameter metallic, substrate holder, susceptor hereafter, heated by a resistance coil gyred just below the surface. In the presence of a perforated shower plate which is facing the substrates, a homogeneous distribution is ensured; in contrast a large recirculation zone sets in when the shower plate is absent (Xenidou *et al*., 2010). The shower plate's diameter is 60 mm and its thickness 1mm; it is perforated by 1450 holes of 0.76 mm diameter each (Figure 2.4b). The optimum distance between the susceptor and the shower plate is fixed at 15 mm. It has been verified that at this position, the temperature of the susceptor is not influenced by the presence of the shower plate (Aloui, 2012). All the dimensions of the reactor are presented in detail in Chapter 3 (§3.1.1.).

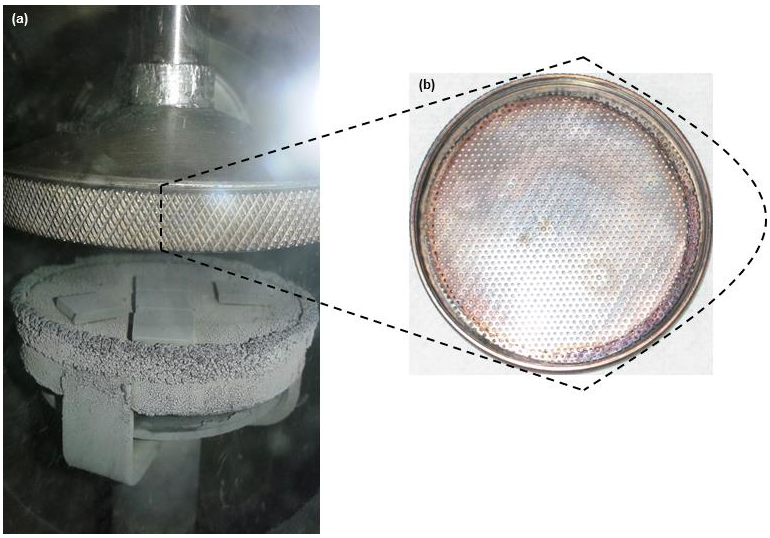

Figure 2.4: Inside the reactor chamber. (a) A photograph showing 5 substrates placed on the susceptor during Al/Fe sequential deposition and the shower plate facing them. (b) A photograph showing the shower plate with the holes which homogenize the flow.

2.1.1.2. Regulation of the temperature

Temperatures of the walls, of the lines (if needed) and of the susceptor are controlled by PID regulators. In particular, the deposition temperature is regulated by a thermocouple connected to a PID controller and attached to the down part of the susceptor. Due to the thickness of the susceptor and the thermal conductivity of the substrates, the imposed temperature is different than the actual one on the surface of the substrates. A calibration is, thus, required for a proper control of the deposition temperature during the process. The calibration is performed by attaching a second thermocouple on the surface of the substrates under temperature and flow conditions similar to those used for the desired MOCVD process and under atmospheric pressure, since the front window of the chamber is open to pass the second thermocouple. Figure 2.5 presents the calibrated temperature as a function of the set temperature, corresponding to three different substrates, namely silicon, Si (black line), glass (orange line) and thermally oxidized silicon, SiO_2 (green line). Additional measurements at the high temperatures are performed for glass and SiO_2 substrates since a post deposition thermal annealing process is adopted in some cases. The equations correspond to the plotted trendlines of each type of substrates and provide the actual deposition temperature for a set value of the regulator.

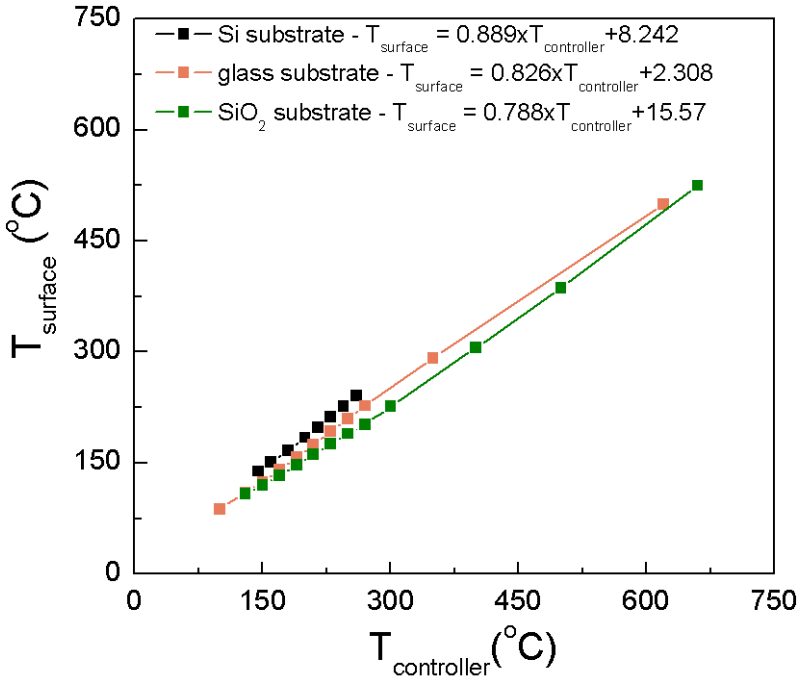

Figure 2.5: A plot showing the calibration of the deposition temperature, i.e., the actual $T_{surface}$ as a function of the $T_{controller}$. Calibration is performed for Si substrates (black line with symbols), glass substrates (orange line with symbols) and SiO_2 substrates (orange line with symbols). For the targeted $T_{surface}$ where the deposition will be performed, the equations corresponding to the trendline of each calibration are solved to define the $T_{controller}$.

It is observed that in all cases the actual temperature on the surface of the substrates is lower than the set one and especially in the case of the glass due to its thickness (2 mm compared to 1 mm for Si and SiO_2 substrates). As temperature increases the differences are

even higher, since the thermal conductivity is inversely proportional to the temperature (Barton and Guillemet, 2005; Glassbrenner and Slack, 1964). It is therefore straightforward that a non- or an inappropriate calibration of the deposition temperature may lead to misguided results.

Another important factor is the temperature of the gas phase in the reactor since it has a key role in the decomposition rate of the precursors and/or the interactions among them. However, the experimental calibration and the monitor of the gas phase temperature is not possible with the available tools and its definition is limited to the computational determination of the temperature gradient inside the MOCVD reactor (Chapter 4 and 5).

2.1.1.3. Pumping system - Regulation of the pressure

Pumping is ensured by a two-stage system composed of a turbomolecular pump and a primary backing pump in series. A Pirani gauge (pressure range 3.8 $x10^{-3}$ – 75 Torr) connected to its electronics indicates the primary vacuum. A Penning gauge (pressure range 10^{-10} – 6.8 x 10^{-3} Torr) enables the monitoring of the secondary vacuum. The pumping system allows a base pressure of 3.8 x 10^{-5} – 7.5 x 10^{-5} Torr before every deposition experiment, a value which ensures a clean reactor. After this step, the turbo pump is turned off. The working pressure of the reactor, $P_{reactor}$, during depositions is regulated by an MKS system consisting in a Baratron gauge (pressure range 1 – 760 Torr) connected to a butterfly valve at the upstream of the primary pump, through a pressure controller. The opening percentage of the butterfly valve varies with the set pressure, the gas flow rates in the reactor, the conductance of the system and the capacity of the pump. For example for a set $P_{reactor}$=10 Torr and by considering the gas flow rates during Al (Chapter 4) and Fe (Chapter 5) depositions and the properties of the system and the pump, the butterfly valve is 33% open. The Penning and the Baratron gauges are placed at the exit of the main reactor chamber while the Pirani gauge is located close to the primary pump (Figure 2.2).

At the outlet of the reactor chamber, the by-products of the precursors' decomposition and the remaining of the reactive gas-phase that is not consumed during the experiments are trapped in a stainless steel vessel with double walls containing liquid nitrogen, for the protection of the pumping system. The cold trap system includes two speedy valves at its inlet and its outlet allowing its isolation for cleaning after a series of depositions.

2.1.1.4. Regulation of the gas flows

The flow rates of the dilution gas, N_2, as well as of the carrier gas of DMEAA, N_2, and the gas reagent, H_2 (99.995% Air Products), are regulated using MKS mass flow controllers (range 0 – 500 sccm, 0 – 50 and 0 – 50 sccm, respectively) connected to a computer where values are set. The carrier gas, N_2, flowing through the $Fe(CO)_5$ precursor is controlled by a 4^{th} MKS controller connected to the computer, with mass flow rate range of 0 – 25 sccm, since less quantity of the Fe precursor is required to be sent in the reactor. The

three N_2 lines are fed by the same cylinder (99.9992% Air Products) and split into three independent lines at the entrance of the reactor chamber, while the H_2 line is directly connected to the dilution N_2 line.

2.1.1.5. Evaporation and injection systems

A. DMEAA

The selection of the evaporation and the transport system is of crucial importance, especially for precursors sensitive to air and moisture, such as DMEAA. There exist several systems to evaporate liquid precursors and transport them by the carrier gas within the reactor chamber, which are summarized in a recent review. Among them, the evaporation and the transport of DMEAA by a bubbler is applied (Vahlas *et al*., 2015).

DMEAA is disposed within a double-wall glass container, equipped with a 3-valve bypass system (Figure 1.6) which allows observing the state of the precursor and prevents its degradation, as opposed to the case of stainless steel containers. The glass bubbler includes also a flexible branch made of PTFE, in order to stand mechanical stretching caused by thermal heating without breaking.

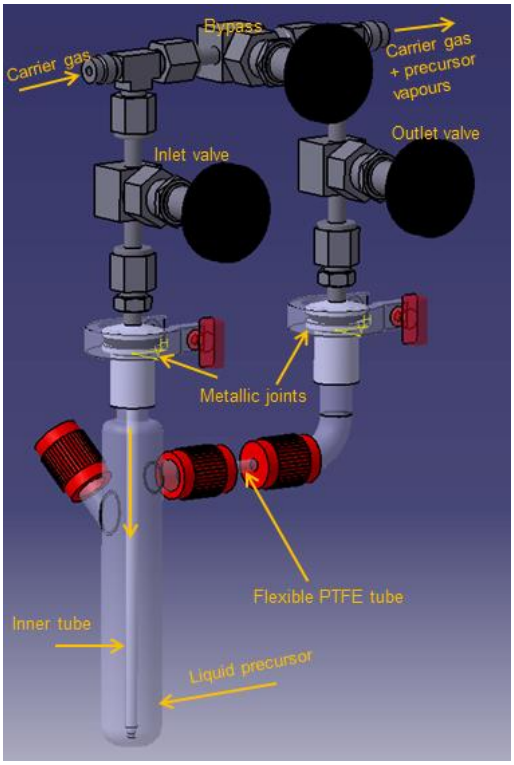

Figure 2.6: A design of the glass bubbler applied for the evaporation and the transport of DMEAA, with the CATIA software.

With the use of the bypass system, the carrier gas is introduced under pressure through the inner tube of the bubbler which is immersed in the precursor. The carrier gas is loaded with precursor's vapors and when it becomes saturated, the reactive gas phase is

transported to the reactor chamber through the lines of the system. The regulation of the bubbler's temperature along with the pressure and the flow rate of the carrier gas allow controlling the quantity of the precursor in the gas mixture which enters the reactor.

The bubbler system presents some specific drawbacks such as the weakness of controlling optimally the quantity of the precursor that enters the rector, the flow stability, since high flow rates of the carrier gas may lead to the creation of turbulence in the bubbler and eventually, the reproducibility of the evaporation process. However, by considering that bubbler is the only way to evaporate and transport DMEAA and that the system has been previously utilized and optimized for the production of pure Al films, the bubbling process is sufficient for the MOCVD of from DMEAA.

For the evaporation of the Al precursor, the DMEAA is stored in the glass bubbler at 3^oC permanently in order to avoid its degradation. During deposition of Al the temperature of the precursor is increased at 7^oC where according to Eq. 1.1, the saturated pressure of DMEAA equals 0.7 Torr.

The maximum mass flow rate of two precursors is calculated through the formula proposed by Hersee and Ballingal (1990):

$$Q_{prec} = Q_{N_2,carrier} \frac{P_{sat}(T_{prec})}{P_{reactor} - P_{sat}(T_{prec})}, \quad (2.1)$$

where Q_{prec} is the precursor flow rate, $Q_{N_2,carrier}$ is the flow rate of the carrier gas, N_2 and $P_{sat}(T_{prec})$ is the saturated vapour pressure at the evaporation temperature of the precursor, T_{prec}. The maximum value of the precursors' flow rates is obtained under the assumption that by assuming that vaporization of the precursor in the bubbler proceeds at thermodynamic equilibrium and that the conductance of the lines connecting the bubbler to the deposition chamber is infinite. As we present in Chapter 4, the applied pressure and gas flow conditions result in an upper limit of 2 sccm for DMEAA flow rate.

B. $Fe(CO)_5$

During the MOCVD of unary Fe films, the evaporation and the transport of $Fe(CO)_5$ in the reactor chamber is realised with the use of the bubbler previously described (Figure 2.6). The $Fe(CO)_5$ is placed in the glass bubbler and it is maintained permanently; i.e., both during operation and storage, at -18^oC. At this temperature the vapor pressure of the Fe precursor is 1.88 Torr (Eq. 1.2). By using the above Eq. 2.1, the upper limit of the $Fe(CO)_5$ flow rate equals to 0.69 sccm (see Chapter 5). The rational for the chosen $Fe(CO)_5$ flow rate with regard to DMEAA flow rate is dictated by the targeted 13:4 ratio of the Al-Fe stoichiometry in the final film, mainly during the co-deposition process (see Chapter 6).

Direct liquid injection (DLI) is applied to the MOCVD of Fe during the as processing with Al, due to the fact that this system provides a more controllable mass inflow rate and a smaller quantity of precursor in the reactor chamber, with regard to the targeted intermetallic

phase. A Vapbox 500 provided by Kemstream® is used for the DLI of $Fe(CO)_5$ and it is presented in Figure 2.7. The principle of the DLI is to inject fine droplets of the liquid precursor into an evaporation chamber, where the droplets are instantaneously evaporate due to their size.

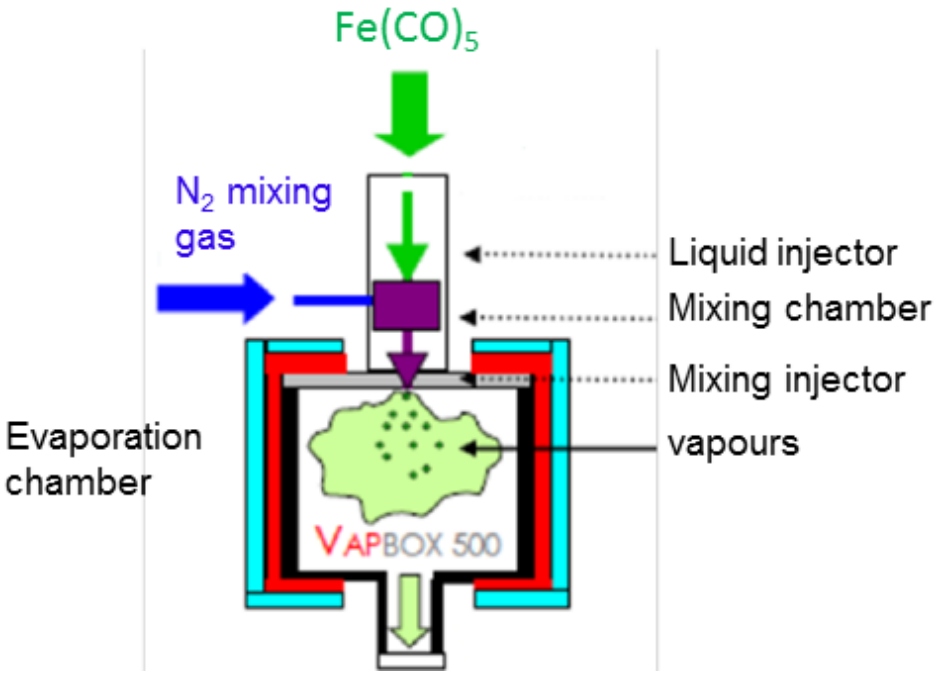

Figure 2.7: Schematic representation of the DLI system (Vapbox, Kemstream®) used for the evaporation and the transport of $Fe(CO)_5$.

During the deposition of Fe, 5 ml of pure $Fe(CO)_5$ are filled in a glass vessel, the schlenk, where the carrier gas is introduced under a pressure of 3.5 bar. A second schlenk containing only a solvent is used in order to rinse the injection system after each deposition. The two reservoirs are mounted on a panel and they are isolated by valves. The panel is connected to the DLI system through a Teflon™ tube. The precursor is atomised that is, fine precursor droplets are created by a modified automobile technology injector which is called liquid injector and it is composed of 8 holes of 6 μm diameter each. The liquid injector functions in an open loop and it is controlled by the injection frequency and the opening time. The gas which is formed is introduced by pulses in a very low volume chamber where it is mixed with the dilution, mixing gas, N_2 pressurized at 1.5 bar.

The flow of the mixing gas is measured by a mass flow meter (MKS, N_2: 0-20000 sccm) and it is controlled by the computer system of the DLI by imposing a frequency for the opening of the mixing injector. The difference between the pressures imposed at the liquid and gas lines is 2 bar in order to force the liquid precursor to move from its schlenk to the evaporation chamber. Then, the binary phase composed of precursor droplets and the mixing gas is atomised by a second injector, the mixing injector, in the evaporation chamber. The evaporation chamber is a stainless steel vessel surrounded by a heating mantle for the

regulation of the temperature. In the case of $Fe(CO)_5$ no heat is needed since the precursor is instantaneously evaporated. In this chamber, the small size droplets (of the order of 10 μm for the diameter according to Froger (2012) are directly evaporate allowing the generation of important flow rates of the reactive gas phase. During deposition the two injectors are always out of phase, to prevent liquid enter the gas line. The operating parameters of the liquid and mixing injectors are not necessarily identical among the deposition but they have to be optimized in order to ensure the reproducibility of the process.

The mass flow rate, $Q_{injection}$, is determined by calibration of the liquid injector before a given experimental series. For this reason the Teflon™ tube is scaled allowing the direct measurement of volume per unit time that is, volumetric flow rate. For instance, when the frequency is set at 1 Hz and the opening time at 2 ms $Q_{injection}$ equals 0.02 ml/min.

The lines and the chambers of the DLI system can be cleaned directly after the deposition by injecting and evaporating the solvent from the second schlenk under a stream of dilution gas. The solvent should be chosen so as to dissolve and transport the residues of the pentacarbonyl precursor which is may deposit in the walls of the system. Hexane or heptane are used as solvents in this case, since they dissolve $Fe(CO)_5$.For a more thorough maintenance of the system, the Vapbox should be opened after a deposition series and its metallic spare parts should be cleaned in a H_2SO_4/H_2O solution.

DLI has many advantages comparing to the simple evaporation system by bubbling, such as the optimal control of the injected, evaporated and consequently transported precursor flow rate in the reactor chamber, the possibility of delivering high/low quantities of the reactive gas phase favorable to high/low thicknesses and the possibility of short depositions with small quantities of a highly unstable molecular compound, as the $Fe(CO)_5$, without any temperature regulation requirements, since all of the precursor is consumed in each deposition.

2.1.2. MOCVD protocols

This paragraph presents the various protocols applied for deposition. Therefore, we describe the cleaning procedure of the substrates used for the MOCVD of Al and Fe and their co-deposition and sequential deposition processes, the filling of the glass schlenk with Fe(CO)5 when the DLI is used, the deposition experiments *per se*, the cleaning of the reactor after deposition and the neutralization of the unused or degraded precursors.

Three types of substrates are used during the investigated MOCVD processes, namely silicon, Si, glass and thermally oxidized silicon, SiO_2 for purposes explained in Chapter 6. All types of substrates are treated in the same way before deposition. They are cleaned in an ultrasonic bath with acetone and ethanol, they are dried under argon flux and baked in a furnace at 60^oC for 30 min to cast off humidity. The substrates are weighted before and after

deposition in order to determine the deposition rate. Three independent weight measurements are carried out for each substrate before and after the experiment and an average value is calculated. The maximum (minimum) deviation from this average value is estimated by the difference between the minimum (maximum) measured value before experiment and the corresponding maximum (minimum) value after the experiment.

Upon the placement of the substrates on the susceptor, primary vacuum is applied at first, down to 3.8×10^{-2} Torr, followed by secondary vacuum to help desorbing compounds, mainly organic, that are adsorbed on the internal surfaces during the opening of the reactor. Once the desired vacuum is reached ($6.8 \times 10^{-5} - 9 \times 10^{-4}$ Torr) the deposition protocol is initiated. For the MOCVD with evaporation of the precursors, the two precursors are permanently maintained in their bubblers at temperature conditions where degradation is limited. Proper temperatures are applied at the lines of the carrier and the dilution gas, and at the walls of the reactor and the precursors' temperatures are regulated to the desired levels for deposition. Then, the carrier and the dilution gases start to flow at their set mass flow rates and the pressure is set to the desired value. The deposition temperature is set to the susceptor. 10 min are required for its stabilization. To start the deposition, first the outlet valve of the bubbler and then its inlet valve are opened and the bypass is closed to start passing the carrier gas through the precursor. This order of the opening of the two valves of the bubbler should be followed in order for the precursor not to be sucked by the pump.

During deposition experiments the cold trap is filled with liquid nitrogen for the entrapment of the by-products. To finish the deposition the bypass is opened and the valves of the bubbler are closed in the opposite order; i.e., first the inlet valve and then the outlet valve. Precursors' temperatures are regulated to the storing conditions and the heating of the susceptor is turned off. The flowing of the N_2 continues for 10 more min to better evacuate the reactor from the by-products and the unconsumed reactive gas phase. When the reactor cools down, at a temperature below 50^oC, it can be opened to collect the samples. Each one of the samples is stored in identified plastic bags with code (the code corresponds to the number of experiment and the place of the sample on the susceptor) and the plastic bags are placed in a desiccator under vacuum. The same protocol is followed also in the case of the co-deposition of the two metals where the two precursors are sent simultaneously in the reactor.

For the MOCVD of Fe with the DLI system, the process differs concerning the treatment of the precursor and the flow conditions. A new $Fe(CO)_5$ batch is filled in the schlenk for each experiment. The filling of the precursor is performed carefully in a vacuum/argon line, shown in Figure 2.8, under hood, due to the toxicity, pyrophoricity and sensitivity of the precursor. The filled schlenk is then mounted to the liquid panel. Finally, the DLI system is purged by three successive cycles of vacuum and N_2 pressurization. The mixing chamber and the line between the liquid injector and the liquid panel are set under vacuum by setting maximum conditions at the two injectors ($f = 10Hz$ and $t_{on} = 50ms$) in

order to remove any water traces. Then, the desired temperature, pressure and mass flow conditions are set and a deposition experiment is performed. At the end of deposition, the reactor is isolated from the DLI system and the evaporation and the mixing chambers are purged under primary vacuum and N_2 flux to consume the remaining precursor's quantity. Then, the DLI system is rinsed by injection and evaporation of a solvent such as hexane or heptane and dried by a N_2 flow stream. The cleaning and the drying of the DLI are carried out in the same injection conditions used for the deposition experiment for 20 min. Again, we wait for the cooling of the reactor for opening and taking the samples. The latter are stored as described before.

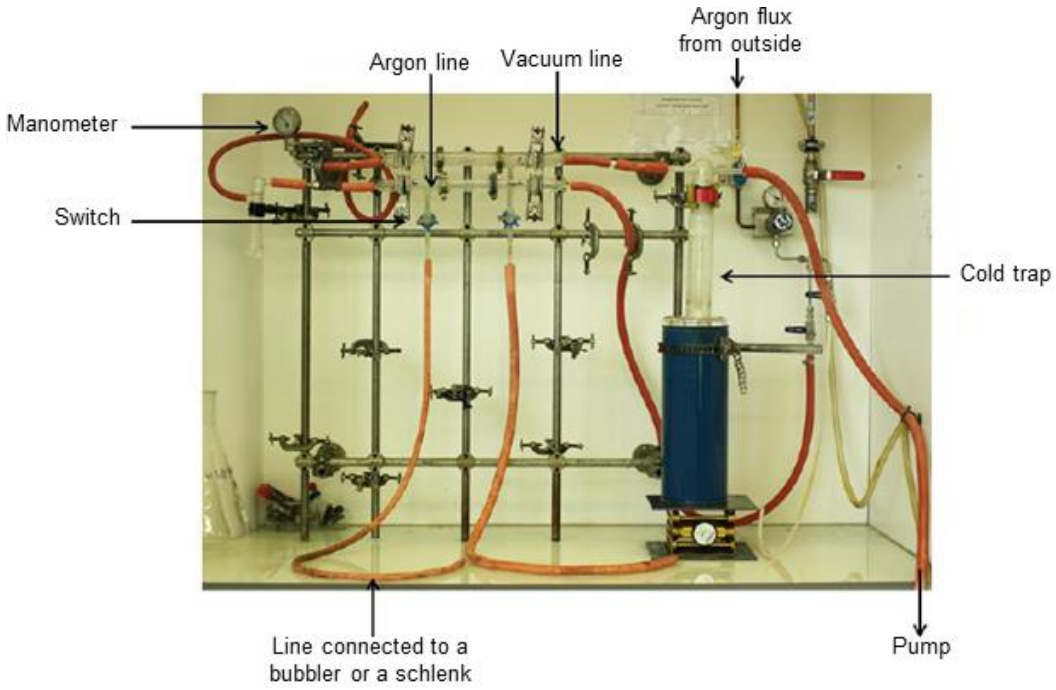

Figure 2.8: Photograph of the vacuum/argon line used to fill the $Fe(CO)_5$ in the glass schlenk and for the neutrilization of the $Fe(CO)_5$ and DMEAA precursors.

Sequential deposition is performed in two steps; first, by the MOCVD of Al by evaporation and second, by the MOCVD of Fe by DLI, as described above. At the end of the deposition of the Fe layer an *in situ* thermal annealing is applied. Without removing the substrates from the reactor, the temperature of the susceptor is increased and it is regulated to the desired value for 60 min and under rough vacuum conditions (7.5×10^{-2} Torr). At the end of annealing, the reactor cools down prior opening.

The neutralization of an unused or decomposed $Fe(CO)_5$ quantity is performed on the vacuum/argon line for safety reasons. The precursor quantity is diluted in hexane under mechanical stirring and commercial household bleach is slowly added to release the toxic CO and to form the solid $Fe(OH)_3$. The neutralization of DMEAA is more complicated due to its high reactivity originating from the AlH_3 part of the compound. The remaining precursor is diluted in toluene under stirring and ice cooling. Then, the reactivity is decreased by adding alcohols, starting from heavier and finishing with methanol in a series of substitution

reactions. At first, droplets of tert-butanol and of iso-propanol are added successively in the diluted precursor. These first two steps should be performed slowly and carefully and stopped when a lower reactivity of the solution is observed by the less violent bubbling of the solution. The iso-propanol step is followed by ethanol and methanol additions to finish with ionised water. The final solution appears as a jelly liquid $Al(OH)_3$ that we store in a plastic vessel.

The reactor system is thoroughly cleaned between different deposition experiments. For example, when an experimental series of Al deposition is completed and a new series of Fe deposition is to be performed, the reactor chamber, the Vapbox, the cold trap and the lines are dismounted and they are cleaned in acetone and ethanol baths. In some cases, when a more efficient cleaning is required, the stainless steel parts only are placed in a KOH bath.

2.2. Material and structural characterizations

2.2.1. Scanning electron microscopy – Energy dispersive X-ray spectroscopy – Focused ion beam

Scanning electron microscopy (SEM) is used to study the microstructure of the films on the different substrate types and to estimate their thickness. Observations are realized in a SEM LEO 435VP instrument and at a FEI Helios 600i station including a field emission gun and located at the Raimond Castaing Microcharacterisation center. Since the deposited metallic films are electrically conductive, no special preparation of the samples, such as metallization is required even with glass substrates.

Observations with the SEM LEO 435VP instrument are obtained at a voltage power of 15 keV, a probe current of 120 pA and a distance from the sample in the range 14 – 19 mm. The microstructure of the various films is studied in both surface and cross section micrographs and their thickness is estimated on cross section micrographs. Usually, the secondary electron mode is used to observe the characteristics of the films such as porosity, uniformity, faceting of the crystals and coalescence. But in the case of binary films the backscattered electrons mode is applied for the chemical contrast observation of Al and Fe. The observations performed at the FEI Helios 600i instrument are obtained at a voltage power of 5 keV, a probe current of 340 pA and a distance from the sample of 4 mm.

Both microscopes are equipped with energy dispersive X-ray spectrometer (EDX) allowing the qualitative elemental analysis of the obtained films and especially for the case of SEM Helios 600i FEI, the 3D mapping of the elemental composition. At LEO 435VP, the operating conditions for a qualitative chemical analysis of the films are a voltage power of 15 keV, a probe current of 1500 pA and a distance of 19 mm from the sample. At FEI Helios 600i the corresponding conditions are a voltage power of 5 keV, a probe current of 0.34 nA and a distance of 4 mm from the sample.

Furthermore, the SEM Helios 600i FEI is equipped with a focused ion beam (FIB) system for preparing cross sections and lamellas for TEM analysis. Before ion etching, a 50 x 30 x 0.2 μm^3 Pt layer is deposited (ion beam deposition) on the surface of the sample with a gas injection system (GIS) included in the apparatus in order to protect the top layer from oxidation. Then, the sample is tilted at an angle of 52^o and 60 x 15 x 0.3 μm^3 cross sections are formed with a 30 keV voltage power and a 65 nA probe current. For TEM lamellas, the latter cross sections are cut by successively applying 45 nA, 21 nA and 2.5 nA probe currents with the same voltage power. Finally, the 60 x 5 x 0.3 μm^3 too-thick rectangles are etched under 30 keV voltage power and 2.5 nA probe current until a transparent 60 x 5 x 0.08 μm^3 lamella is obtained.

2.2.2. X-ray diffraction

X-ray diffraction (XRD) is performed to study the crystalline structures of Fe unary films deposited on Si substrates and for Al-Fe complex structures deposited on Si, glass and SiO_2 substrates. XRD analyses are performed with a Seifert – 3000TT instrument composed of a Cu K_α (1.540598 Å) X-ray tube operating at 40 kV and 40 mA, a Ni filter and a solid-state Lynxeye detector. By considering that the thickness of the coatings varies from several tens of nanometers to some tens of micrometers, the 2θ configuration at fixed grazing incidence ($\omega=2^o$) is chosen. The 2θ angle varies from 5^o to 135^o.

2.2.3. X-ray photoelectron spectroscopy

X-ray photoelectron spectroscopy (XPS) consists of a monochromatic beam of X-rays with sufficiently high energy to create ionization of the atoms of the irradiated material. An electron from the core of the atom is thus ejected (photoelectric effect) and its kinetic energy is detected and measured. This implies that the latter photoelectron reaches vacuum, and therefore that the surface is at a distance shorter than the photoelectron inelastic mean free path. Thus, detected photoelectrons only originate from the extreme surface of the material that is, only from a few nm. The kinetic energy of a photoelectron is impacted by its environment (oxidation degree, bonding type, polarity, etc.) and by many other mechanisms activated during its travel to vacuum (core-hole screening, interaction with valence electrons, etc.). Fortunately, whereas the latter mechanisms require theoretical support to be understood, conventional XPS with proper standards and bibliography allow the determination of the atom environment, and semi-quantitative composition.

XPS measurements are performed on a Thermo Scientific K-Alpha instrument using monochromatic Al K_α (1486.6 eV). The base pressure in the XPS chamber equals to 10^{-9} Torr. Atomic concentrations of the Al-Fe films deposited on glass substrates (Chapter 6) are determined from photoelectron peak areas using the atomic sensitivity factors reported by Scofield, taking into account the transmission function of the analyzer. Before analysis an etching procedure in the XPS chamber is applied to remove the oxide layer formed upon

exposure to air. The ion etching rate (Ar^+, 2 kV) is *ca.* 0.08 nm/s. High resolution scans are obtained at constant pass energy of 30 eV with energy steps of 0.1 eV.

2.2.4. X-ray fluorescence

X-ray fluorescence (XRF) functions by exposing the sample to a beam of primary X-rays. The atoms of the sample adsorb energy from the X-rays, become temporarily excited and then emit secondary X-rays. Each chemical element emits X-rays at a unique energy. By measuring the characteristic energy and the intensity of the emitted X-rays, the XRF analysis can provide qualitative and quantitative data regarding the thickness and the composition of the investigated material.

XRF measurements are performed in an X-Strata920 instrument equipped with a tungsten anode tube (50 W, 50 kV and 1 mA) and a Xenon proportional counter detector. Before measurements the instrument is calibrated with Cu and Ag standards for a functional performance. Furthermore, a sample with known thickness (of Fe in this work) is used to create a thin film standard, and a bulk pure Fe piece is used to get an infinite standard. With this procedure and the algorithm included in the software, measurements are carried out with an accuracy of ± 5%. However, the apparatus cannot detect Al within the obtained films. Thus, in the frames of the thesis, only Fe film thickness is measured with the XRF technique.

2.2.5. Electron probe microscopy analysis

The quantitative chemical composition of the Al-Fe co-deposited or sequentially deposited films is determined by the electron probe microscopy analysis (EPMA). EPMA measurements allow the quantification of the Al:Fe ratio in the final film as well as the determination of the at% contamination of the films by the heteroatoms O and C. Measurements are performed in a Cameca SXFive instrument equipped with a field emission electron source (Schottky emitter) and a wavelength dispersive spectrometer (WDS) and located at the Raimond Castaing Microcharacterisation center. The apparatus operates at 15 keV and 20 nA. It is calibrated using high purity Al and Fe as well as SiC (Si:70.05% and C:29.95%) and F_2O_3 (Fe:69.94% and O:30.06%) standards.

2.2.6. Radio frequency glow discharge optical emission spectroscopy

Depth elementary profiles of the Al-Fe films (Chapter 6) are determined by radio frequency glow discharge optical emission spectroscopy (RF GD-OES) with a Horiba Scientific GD-Profiler2[1]. The RF GD-OES method applies a low pressure plasma for a rapid etching (few μm/min) of the sample and for the excitation of the sprayed atoms. Light emitted during their de-excitation is collected by a polychromator which detects from UV to IR (including elements such as H, O, C and N). The use of radio frequency eliminates the

[1] HORIBA Jobin Yvon SAS

limitation of using conducting substrates, thus glass substrates cam be readily characterized. Due to the absence of calibration curves in this work, only qualitative trends of the depth profiles are obtained.

2.2.7. Transmission electron microscopy – Scanning transmission electron microscopy

Transition electron microscopy (TEM) is used for a more detailed observation of the microstructure. TEM is a technique in which a beam of electrons is transmitted through an ultra-thin specimen and interacts with it. This interaction causes the creation of an image of the electrons transmitted through the specimen and the image is magnified and depicted from an imaging device. A great advantage of TEM over other microscopic techniques is its ability to switch operation between the imaging and diffraction modes very easily, thereby investigating the crystallographic structure of a specific material by the analysis of the image.

TEM coupled with EDX measurements is performed on the Al-Fe films sequentially deposited on SIO_2 substrates (Chapter 6) in order to extract high resolution images with crystallographic information of the Al-Fe phase. The measurements are performed on a JEOL JEM 2100F high resolution microscope operating at 200 kV and equipped with a BRUKER EDX spectrometer for chemical analysis. The apparatus is located at the Raimond Castaing Microcharacterization center. The quantitative chemical analysis performed at the level of the lamella, obtained by FIB, provides local values of the Al:Fe atomic ratio at different points of the sample; it also allows to observe the enrichment in Al and Fe or the O contamination at the various regions of the lamella. TEM and high resolution TEM analysis is followed by a fast Fourier transformation of an atomically resolved image in order to identify crystallographic orientations and eventually, to define the phase.

In scanning transmission electron microscopy (STEM), an electron beam focused to a small surface area (100 nm – 2 μm) is raster scanned in parallel across the sample surface and the detector collects the signal arising from the interaction of the electrons with the solid material. The signal intensity is used to construct 2D maps of the material properties in each pixel. The advantage of STEM is that it does not need imaging lenses which have chromatic aberration and limit the resolution of TEM images. Further, high-angle annular dark field STEM (HAADF-STEM) allows the observation of STEM images with higher resolution and compositional information.

STEM is performed on the Al-Fe sequentially deposited films on glass substrates (Chapter 6) using a FEI Titan 80-200 (“ChemiSTEM”) electron microscope (Kovács *et al*., 2016) operating at 200 kV, equipped with a spherical-aberration (C_s) probe corrector (CEOS GmbH), and a HAADF detector. A probe semi-angle of 25 mrad and an inner collection semi-angle of the detector of 88 mrad are used. Compositional maps are obtained with EDX using four large-solid angle symmetrical Si drift detectors. For EDX analysis, Fe K and Al K peaks are used. The instrument is located in Juelich, at the Ernst Ruska-Centre (ER-C) for

Microscopy and Spectroscopy with Electrons German national facility and the Peter Grünberg Institute, under the supervision of Dr. Marc Heggen.

2.2.8. Interferometry and mechanical profilometry

The surface roughness of Al films observed during SEM analyses is quantified by performing optical interferometry measurements with a Zygo MetroPro™, New View 100 instrument. The apparatus uses a Mirau interferometer which consists of a semi-reflecting sample placed in front of a long-range target. A light beam is sent on the sample surface through a microscope objective. The incident beam is split and the two obtained beams separate according to two distinct geometrical paths, one of which is directed towards the surface to be observed and the second functions as the reference radiation. The phase shift between the beams is due to the topography of the surface of the observed material. The commercial software MetroPro translates the signal caused by the interference and provides results concerning the RMS and Ra roughness among others. A 1.4 x 1.4 mm^2 surface is analyzed with a lateral resolution of 1 μm. The analyzed depth can reach 100 μm with a vertical resolution of 1 nm. For each sample, we perform 3 measurements at different regions in order to acquire statistical information on the roughness. It is presented as an average value plus deviations (uncertainties).

When the reflectance of the surface is limited as for the Fe films, no interference can be detected from light interferometry. Thus, a mechanical profilometer is used which is compatible with all types of material surfaces. Mechanical or stylus profilometry is a destructive technique based on a tip (stylus) touching and moving across the surface of the sample, thus providing the profile of the surface. The measurements are performed at a KLA Tencor P16+ mechanical profilometer located at the Laboratoire d'Analyse et d'Architecture des Systèmes (LAAS) in Toulouse. The tip has a 2 μm curvature and it is attached to the surface with an angle of 45^o and a force of 2.5 kPa. The RMS roughness of Fe films is determined across a 1 mm surface line with a lateral resolution of 0.5 μm.

2.2.9. Electrical resistivity

Electrical resistivity is determined following the theory of Smits (1958). Measurements of the sheet resistance are performed with a proprietary resistivity apparatus based on the four-point probe method (Samélor *et al.*, 2010). Two external pins supplying current (I) are aligned with two internal pins measuring voltage (V). Thin films resistivity (ρ_s) is given by the formula:

$$\rho_s = \frac{V}{I} \times C \times t, \tag{2.3}$$

where ρ_s is the electrical resistivity in [μΩ.cm], V is the voltage in [mV], I is the current intensity in [mA], C is a constant correction factor depending on the dimensions of the

surface and *t* is the thickness of the film in [nm]. The tip apex of the apparatus equals 40 μm in diameter and the constant spacing between the pins is 1.5 mm. Signal acquisition and treatment are driven by a computer program. Measurements are performed on a 20 x 10 mm^2 surface area at room temperature, by applying a current I=50 mA. The thickness of the Al films varies from 600 nm to 1 μm (Chapter 4) and the constant C=4.5324 which represents a general correction.

2.2.10. The catalytic procedure

Catalytic tests are performed at IRCELYON by a collaborating group. They are carried out at atmospheric pressure in a continuous flow fixed-bed reactor. It is consisted of a 16 mm diameter cylindrical glass tube and it is equipped with a sintered glass filter in order to hold the catalyst. The reactor is placed in a ceramic furnace whose temperature is controlled via a thermocouple. The reactant gases (C_2H_2:H_2:He) are mixed using mass-flow controllers (Brooks and Vögtlin Instruments) and they are flowed through the reactor at a total rate of 50 mL/min. The effluent gases are analyzed online using a Shimadzu GC-2014 gas chromatograph equipped with a Supelco alumina sulfate plot fused silica capillary column and a FID detector. Acetylene semi-hydrogenation reactions are conducted by using 25 mg of $Al_{13}Fe_4$ films, in two different conditions:

a) C_2H_2:H_2:He = 2:10:88 at 50ml/min at 200°C.
b) C_2H_2:H_2:He = 0.5:5:94.5 at 50ml/min at 200°C.

The first catalytic experiment is performed without pretreatment of the catalyst surface, and the other tests are preceded by a treatment at 200°C under H_2 (40 mL/min) or air (50 mL/min) in order to regenerate the catalyst. After the reductive treatments of $Al_{13}Fe_4$ films, the reactive mixture is immediately introduced in the reactor. On the contrary, after the oxidative treatment under air, the reactor is flushed with He before switching to the reactive mixture.

Summary-Conclusions

A MOCVD reactor system is designed and mounted for the deposition of Al and Fe unary and binary films. The reactor chamber is a cylindrical, vertical one with stainless steel walls which allow processing in hot as well as cold wall modes. Within the chamber, a 58 mm diameter substrate holder (susceptor) allows the deposition on more than one substrates of 1 cm^2 typical surface area. Also, the presence of a shower plate which faces the susceptor ensures homogenized flow. The transport of the DMEAA in the reactor chamber is performed by evaporation, while for the $Fe(CO)_5$ both evaporation and DLI methods are used. DLI ensures a better control of the transport of the Fe precursor and avoid its regulation at very low temperatures.

Several qualitative and quantitative characterization techniques are used to analyze the elemental composition, the structure, the microstructure and the properties of the films. Qualitative methods, although not providing specific values, give useful information, especially when the chemical composition is concerned. For the Al-Fe complex films particularly, the high-resolution TEM and STEM analysis allows defining the size of the crystals, the distances between them and the phase of the intermetallic structure as well as coating homogeneity through the entire layer.

Chapter 3: Modeling of processes: methods and computational simulations

This chapter presents the models developed for the study of the physical/chemical phenomena occurring at the different scales, macroscale and nanoscale, during MOCVD processes. The macroscale refers to the bulk of the MOCVD reactor and it is of order of cm or mm. The phenomena occurring at the macroscopic level are governed by the fundamental conservation equations (mass, momentum and energy) combined with the kinetics of the Al and Fe gas phase and surface chemical reactions. The nanoscale refers to the surface level and the nanomorphology of the film and it is of order of nm. At this scale, a stochastic kinetic Monte Carlo (kMC) model is developed for the simulation of the nano-processes at the surface. The linking of the two scales results in a multiscale framework which simulates the surface evolution and calculates the surface roughness of Al and Fe films.

3.1. Modeling and computations at the macroscale

A MOCVD process comprises simultaneous transport phenomena and chemical reactions occurring in the gas phase and at the surface of the substrate. The corresponding mathematical model is set in a domain defined by the geometry of the experimental MOCVD reactor. The partial differential equations (PDEs) are discretized and solved in the domain by employing the commercial computational fluid dynamics (CFD) software Ansys/Fluent (Ansys 12.1/Fluent Documentation, 2009).

3.1.1. The computational domain

The computational domain is determined by the geometry of the reactor which is presented in Chapter 2. The domain is drawn with the commercial software Gambit (Gambit Documentation, 2006) and it is depicted in Figure 3.1. Figure 3.1a shows the 3D geometry model configuration. The reactive gas mixture enters the reactor from the inlet, flows through the shower plate and the shower plate towards the susceptor, where the solid product of the chemical reactions is deposited and the film is grown, and the gaseous by-products leave the reactor at the outlet. The actual dimensions of the experimental MOCVD reactor, including the shower plate and the plate with its holes, are used for sizing the 3D model and they are depicted in Figures 3.1c and d. The experimental reactor is axially symmetric as indicated by the rectangular area defined by the red dashed line. Thus, a 2D model of the reactor is also built (Figure 3.1b) which contains an axisymmetric half slice of the 3D domain. However, the geometry of the holes of the shower plate is not captured by the 2D geometry; actually, a hole in 3D could only be "approximated", in an axisymmetric setup, by a circular ring. The blue line in Figure 3.1b represents the shower plate without holes. The 2D model of the reactor is computationally less expensive than the 3D (see §3.1.2.) and it is used in preliminary calculations for getting estimates of the parameters entering the kinetic equations (see §3.1.4.).

3.1.2. Discretization

Upon building the geometry of the reactor model, the computational domain is discretized into a mosaic of elementary cells called mesh. Each cell represents a finite volume within which the values of the calculated variables are considered constant; that is, within each ("infinitesimal") cell, there is no spatial variation of the variables. Cells are delineated by boundaries defined by the mesh. The set of PDEs is solved at each cell of the mesh. At the end, an interpolation from the discrete solution of the PDEs at each cell yields a solution on the entire domain.

Meshing is an important step of the computational process since it is connected with the reliability of the simulations. The mesh density and quality influences the convergence of the solution procedure, the accuracy of the obtained solution and the associated

computational effort. The main mesh quality criteria are two (Ansys 12.1/Fluent Documentation, 2009): (a) the aspect ratio, which for a quadrilateral cell corresponds to the length ratio of the longest edge to the smallest and (b) the distortion of each cell, expressed by the ratio between the maximum and minimum angles between the edges. Cells with indicated aspect ratio and distortion are shown in Figure 3.2a and b, respectively.

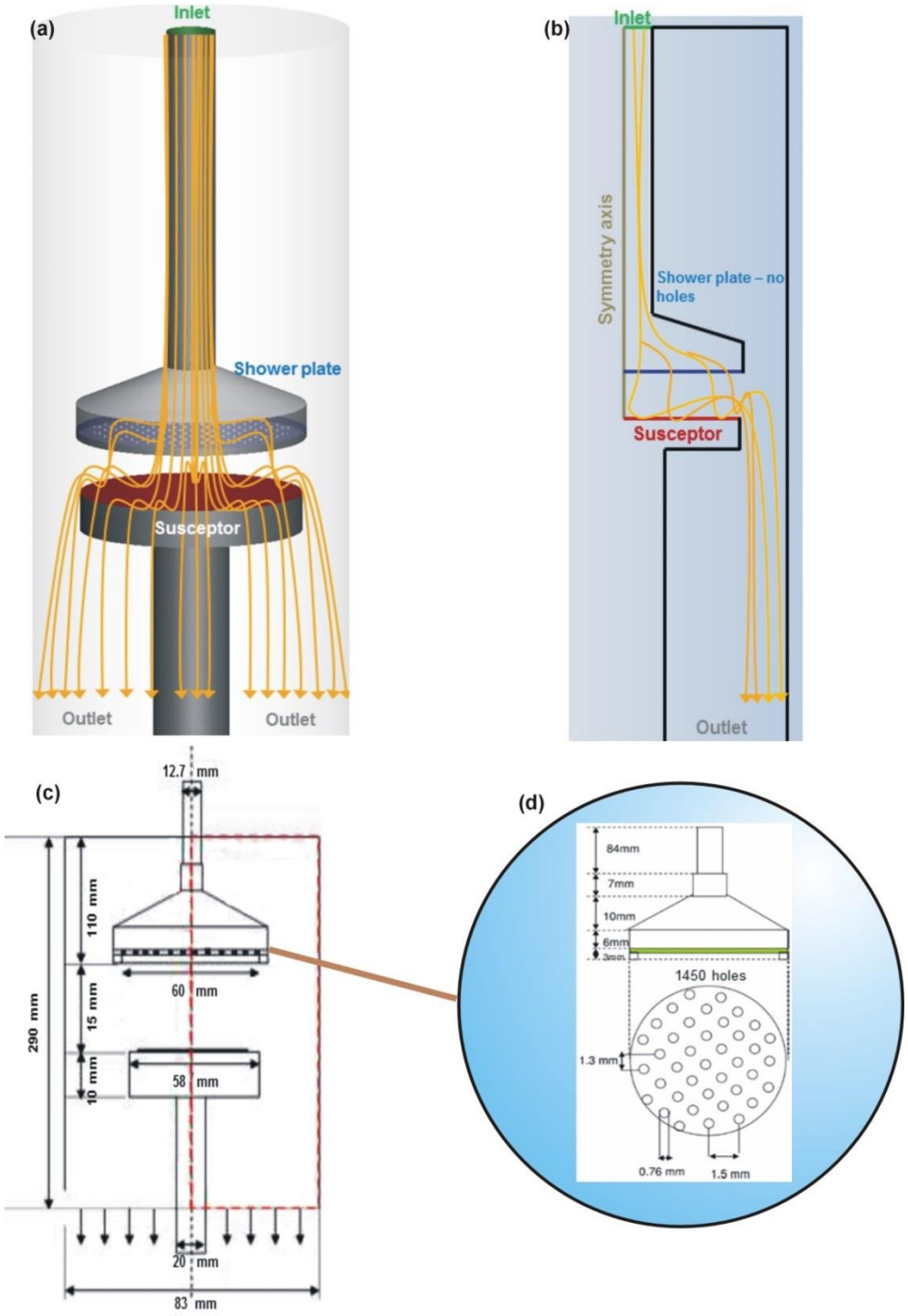

Figure 3.1: A 3D (a) and a 2D (b) model of the experimental MOCVD reactor which is used for the solution of the set of PDEs. The two models are designed based on the exact dimensions of the experimental setup (c). The 3D model includes the holes at the shower plate (d) while the 2D model does not.

Based on the shape of the cells, meshes are distinguished into two categories: structured meshes (Figure 3.2c – left) comprised by rectangular/quadrilateral (2D) or hexahedral elements (3D) following a uniform pattern; unstructured meshes (Figure 3.2c – right) composed by triangular (2D) or pyramidal (3D) elements that are not following any pattern and they are randomly arranged in space. A structured mesh is often preferred over an unstructured since it reduces computational cost and allows for better control of the density and the arrangement of cells. On the other hand, an unstructured mesh offers flexibility in dealing with complex geometries and/or locally selective refinement or coarsening.

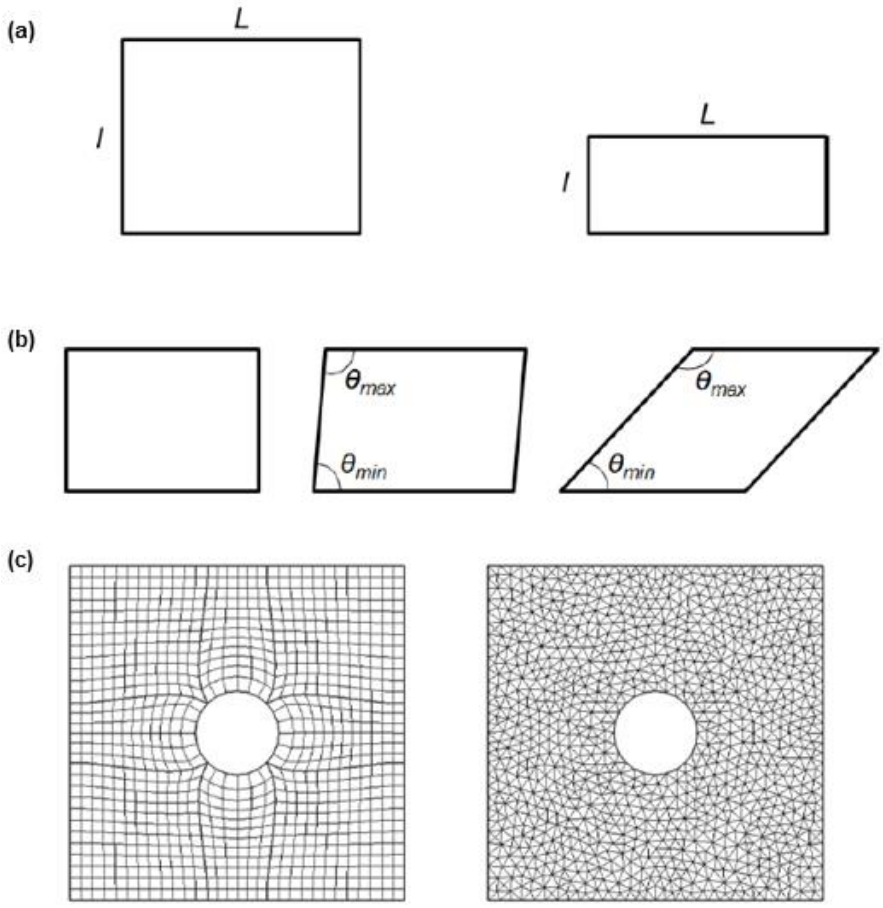

Figure 3.2: Representation of two rectangular 2D elements (a) with a low aspect ratio (left) and a high aspect ratio (right). Representation of three quadrilateral 2D elements (b) without distortion (left), with a slight distortion (middle) and with a strong distortion (right). Spatial discretization of the same geometry (c) with a structured (left) and an unstructured mesh (right).

An example of the discretization of the computational domain of the MOCVD reactor is shown in Figure 3.3. A mesh is created for both the 3D (Figure 3.3a) and 2D (Figure 3.3b) models with the use of the commercial software Gambit (Gambit Documentation, 2006). The mesh of the 3D model is unstructured while the mesh of the 2D model is structured in the bulk of the reactor and unstructured in the area from the inlet up to the shower plate. Inset figures are magnifications of the inlet, shower plate and susceptor areas.

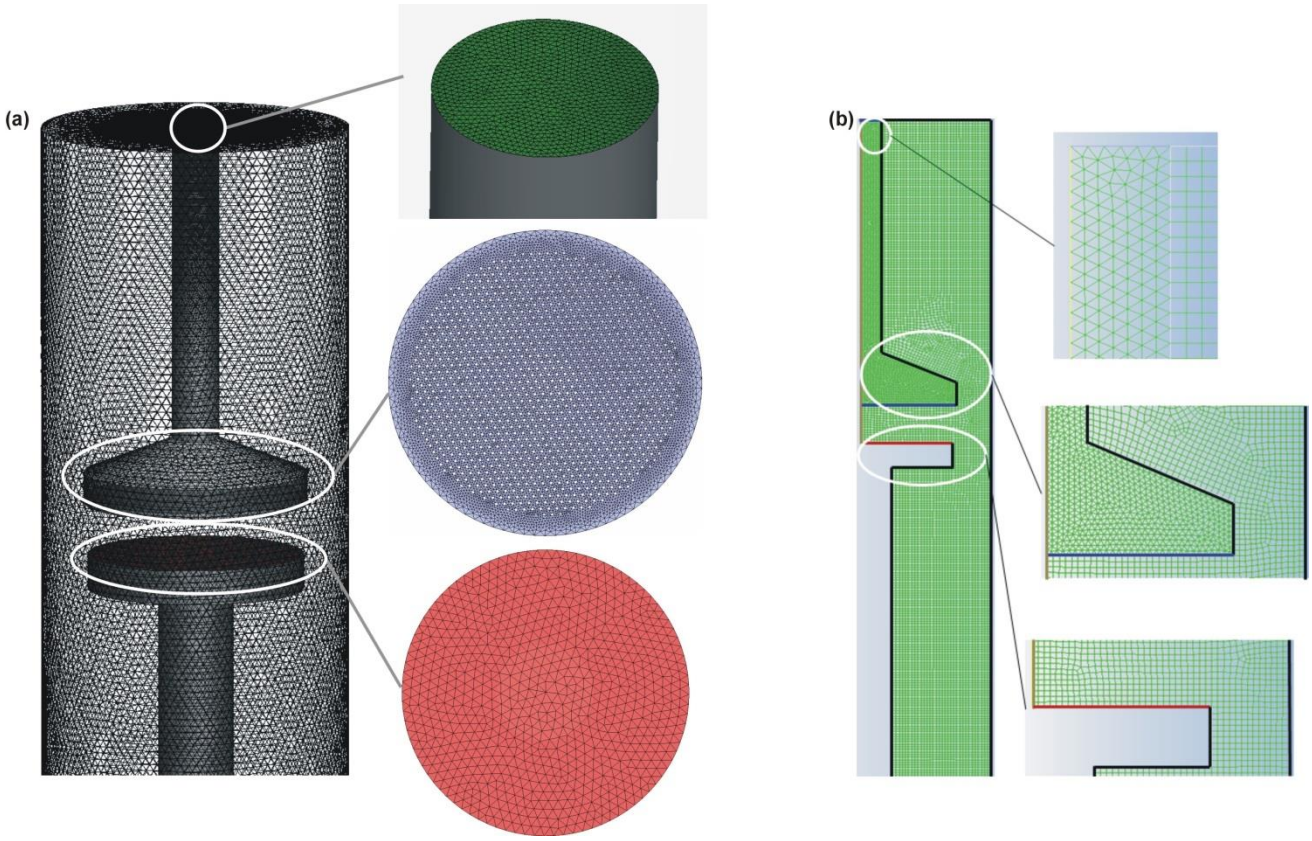

Figure 3.3: (a) An unstructured mesh is created for the 3D model. (b) A hybrid mesh containing both triangular and square elements is built for the 2D model. The insets are magnifications of the inlet, the shower plate and the susceptor where the mesh is finer.

Finer mesh is required in these areas so as to accommodate anticipated steep changes (gradients) of the computed solutions.

The density (fineness) of the mesh should be sufficiently high for obtaining solutions with high enough accuracy. However, mesh refinement should be done with care, since unnecessarily too fine discretization could be harmful, in terms of required computer memory and time. To establish solution reliability requires its mesh independence verification. This is performed by systematically monitoring the dependence of the values of chosen variables on mesh density. The variable of choice here is the mass fraction of the precursor. The mesh independence study is presented for a particular configuration of the 2D model but it is carried out for every, 2D and 3D, case.

The density of the mesh is increased successively, starting from the initial mesh, A, presented in Figure 3.3b. The generic mesh A has been created by default in Gambit. The first refinement is performed for the whole volume of the reactor model while the second is performed selectively, in the area between the shower plate and the susceptor since this area is a particular “action zone” in terms of surface reactions and species concentration gradients and associated transport. Figure 3.4a shows the refinement of the initial mesh A (11625 cells) to the mesh B (36700 cells) and C (50862 cells).

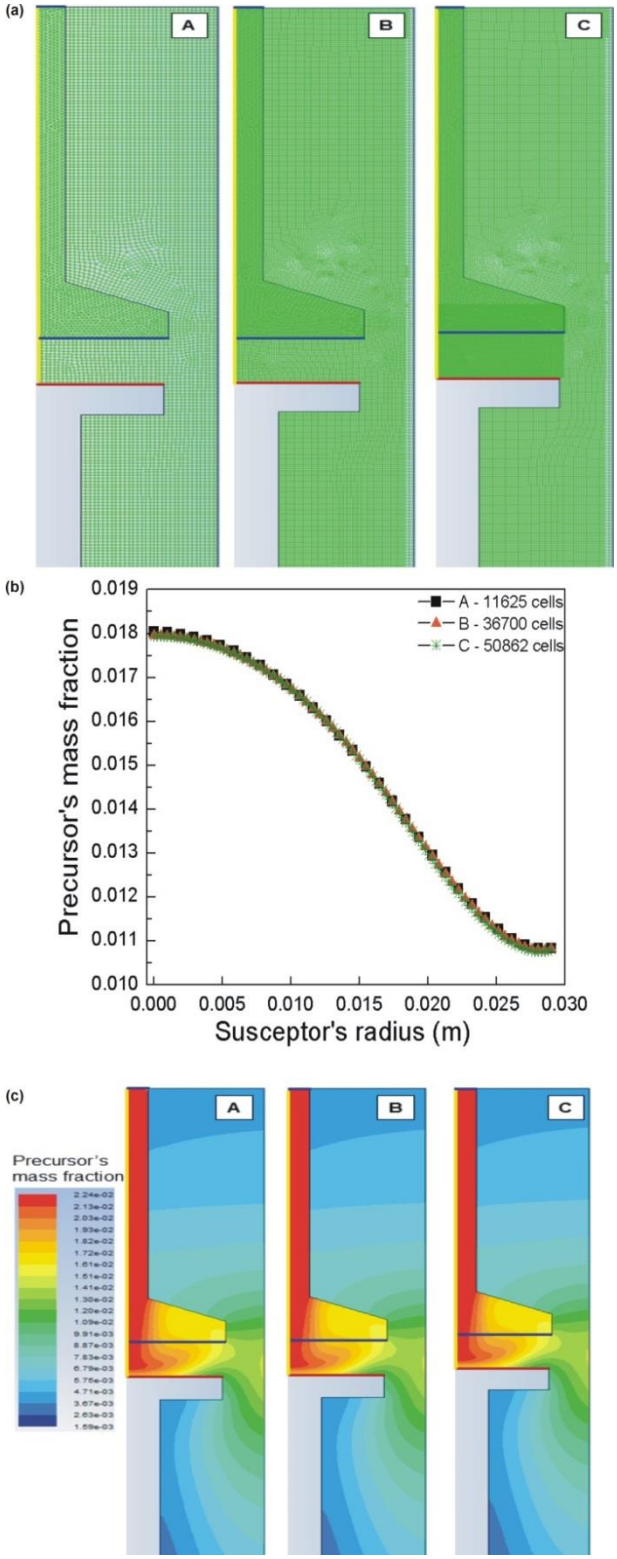

Figure 3.4: (a) Mesh refinement for the whole reactor and in specific areas. (b) Evolution of the mass fraction of the precursor along the susceptor (b) and (c) in the reactor for the different meshes.

Figure 3.4b and c present, respectively, the mass fraction of the precursor along the susceptor and in the MOCVD reactor for the three meshes density, A, B and C. It can be observed that the differences are negligible; actually, the difference is less than 0.6%, even between the coarse mesh A and the denser mesh C. It can be deduced that the mesh A suffices for

obtaining accurate 2D solutions. Furthermore, the computational time required to obtain solution with mesh A is less than 10 min, compared to 20 and 30 min, required for meshes B and C, respectively. The CPU memory required for the 2D simulations varies between 160 – 220 MB depending on the density of the mesh. A similar mesh independence study was carried out for the 3D model; a mesh with as many as 1.232.468 cells comes out to be an appropriate one. Due to the size of the resulting computational problem, parallel processing in computer clusters is indispensable. The CPU time and memory required for the solution of a 3D problem are 4 h and 2 GB, respectively.

3.1.3. The fundamental transport equations at steady state

The gas mixture in the MOCVD reactor is treated as a continuum ideal gas, since the Knudsen number (Bird, 1994) expressing the ratio of the free path of molecules to a characteristic length in the problem under study is much less than unity (Kn<<1). The flow is taken laminar, as dictated by a typical value of the Reynolds number. More specifically, with the following typical values of the involved quantities:

Density of gas mixture=$1.22\text{x}10^{-2}$ kg/m^3, viscosity of gas mixture=$2.1\text{x}10^{-5}$ kg/m.s, reactor diameter=$8.3\text{x}10^{-2}$ m, velocity of gas mixture at the inlet=4.2 m/s, mean free path=$1.59\text{x}10^{-6}$ m (calculated at P=10 Torr and T=100^{o}C), typical values of the dimensionless numbers are Kn=$1.92\text{x}10^{-5}$ and Re=202.52.

The CVD process is analyzed at steady state. The fundamental equations describing the transport phenomena at the macroscale and at steady state are the conservation (or balance) equations of mass and species, momentum and energy (Bird *et al*., 2002; Deen, 1998):

- *Mass conservation*:

$$\nabla\cdot\left(\rho\mathbf{u}\right)=0, \tag{3.1}$$

where ρ is the density of the mixture and $\mathbf{u}$ the velocity vector.

- *Momentum conservation*:

$$\nabla\cdot\left(\rho\mathbf{u}\mathbf{u}\right)=-\nabla P+\nabla\left[\mu\left(\nabla\mathbf{u}+\nabla\mathbf{u}^{\mathrm{T}}\right)-\mu\frac{2}{3}\left(\nabla\cdot\mathbf{u}\right)\mathbf{I}\right]+\rho\mathbf{g}, \tag{3.2}$$

where P is the pressure, μ the dynamic viscosity, $\mathbf{I}$ the unit dyadic and $\mathbf{g}$ the gravitational acceleration.

- *Energy conservation*:

$$C_p\nabla\cdot\left(\rho\mathbf{u}T\right)=\nabla\cdot\left(\lambda\nabla T\right)-\sum_{i=1}^{N}\mathbf{j}_i\cdot\frac{\nabla H_i}{M_i}-\sum_{i=1}^{N}\sum_{k=1}^{N_{gas}}H_iR_{k,gas}, \tag{3.3}$$

where C_p is the specific heat capacity under constant pressure, T the temperature, λ the thermal conductivity, $\mathbf{j}_i$ the diffusion rate of the species i, H_i the enthalpy of formation of the species i, M_i the molecular weight of the species i, N the number of the chemical species, N_{gas} the number of the gas phase chemical species and $R_{k,gas}$ the net rate of the gas phase reaction k.

- *Species conservation*:

$$\nabla \cdot \left(\rho \mathbf{u} \omega_i \right) = -\nabla \cdot \mathbf{j}_i + M_i \sum_{k=1}^{N_{gas}} R_{k,gas}, i = 1, \ldots, N-1, \tag{3.4}$$

with ω_i expressing the dimensionless mass fraction of the species i of the gas mixture composed of N-constituents, which sum up to unity.

In CVD processes the diffusion rate, $\mathbf{j}_i$, is calculated by the full multicomponent diffusion model (Ansys 12.1/Fluent Documentation, 2009). For multicomponent mixtures, the derivation of explicit relations for the diffusion fluxes containing the gradient of only one component, as it is required by Fick's law, is not feasible. Thus, for the computation of the diffusion rate the Stephan-Maxwell equations are applied, which are expressed in the following form for ideal gases:

$$\sum_{\substack{j=1 \\ j \neq i}}^{N} \frac{f_i f_j}{D_{ij,m}} \left(\frac{\mathbf{j}_j}{\rho_j} - \frac{\mathbf{j}_i}{\rho_i} \right) = \nabla f_i - \frac{\nabla T}{T} \sum_{\substack{j=1 \\ j \neq i}}^{N} \frac{f_i f_j}{D_{ij,m}} \left(\frac{D_{T,j}}{\rho_j} - \frac{D_{T,i}}{\rho_i} \right), \tag{3.5}$$

where f_i, f_j are the molar fractions of the chemical species i,j, $D_{ij,m}$ is the binary mass diffusion coefficient of component i in component j and $D_{T,i}, D_{T,\mathrm{j}}$ are the thermal diffusion coefficients of the chemical species i,j. The term $\mathbf{j}_i$, for the chemical species i, is then calculated by the equation:

$$\mathbf{j}_i = -\sum_{j=1}^{N-1} \rho D_{i,m} \nabla \omega_i - D_{T,i} \frac{\nabla T}{T}. \tag{3.6}$$

Eq. (3.6) is an alternative expression of the Fick's law, taking into consideration the Soret effect (Bird *et al*., 2002). The calculation of the binary mass diffusion coefficient, $D_{ij,m}$, is realized through the Chapman-Enskog equation:

$$D_{ij,m} = 0.00188 \frac{\left[T^3 \left(\frac{1}{M_i} + \frac{1}{M_j} \right) \right]^{0.5}}{P_{abs} \sigma_{ij}^2 \Omega_D}, \tag{3.7}$$

where P_{abs} is the absolute pressure, σ_{ij} the active diffusion collision diameter and Ω_D the diffusion collision integral. The latter is a measure of the molecular interaction and it is a function of the quantity T_D^*, where

$$T_D^* = \frac{T}{\left(\varepsilon / k_B\right)_{ij}}, \tag{3.8}$$

with $k_B = 1.3806 \times 10^{-23} \ \frac{m^2 kg}{s^2 K}$ being the Boltzmann constant and $\left(\varepsilon / k_B\right)_{ij}$ the energy parameter of the mixture which is computed by the geometric average:

$$\left(\varepsilon / k_B\right)_{ij} = \sqrt{\left(\varepsilon / k_B\right)_i \left(\varepsilon / k_B\right)_j}. \tag{3.9}$$

The active diffusion collision diameter, σ_{ij}, is calculated by the arithmetic average of the individual σ:

$$\sigma_{ij} = \frac{1}{2}\left(\sigma_i + \sigma_j\right). \tag{3.10}$$

The thermal diffusion coefficients are calculated through the following empirical equation which quantifies the Soret effect:

$$D_{T,i} = -2.59 \times 10^{-7} T^{0.659} \left[\frac{M_i^{0.511} f_i}{\sum_{i=1}^{N} M_i^{0.511} f_i} \right] \cdot \left[\frac{\sum_{i=1}^{N} M_i^{0.511} f_i}{\sum_{i=1}^{N} M_i^{0.489} f_i} \right]. \tag{3.11}$$

The last equation of the set is a constitutive one, namely the ideal gas law for the mixture, from which the density is calculated:

$$\rho = \frac{PM}{RT}, \tag{3.12}$$

where $R = 8314.34 \ \frac{J}{kmolK}$ is the universal gas constant and M the molecular weight of the mixture.

The transport equations are augmented with the appropriate boundary conditions (Chapter 4 & 5) which refer to the primary unknowns that are, velocity, pressure, temperature and species concentrations. In general, boundary conditions are of Dirichlet-type (prescribed values of the primary unknowns), Neumann-type (prescribed values of the derivatives of the primary unknowns) and Robin-type (linear combination of the values of the unknowns and their derivatives).

3.1.4. Gas phase and surface reactions

The control of the thickness and chemical composition of the film for the various operating conditions is of crucial importance in all CVD processes. Both of them are strongly affected by the reactions taking place in the gas phase and on the deposition surface as well as by the flow inside the reactor chamber. These chemical reactions are described by the following general equation:

$$\sum_{i=1}^{N_{gas}} \gamma'_{ik} G_i \overset{r_k / r_s}{\rightleftharpoons} \sum_{i=1}^{N_{gas}} \gamma''_{ik} G_i + \sum_{i=1}^{N_{sur}} \gamma''_{ik} S_i, \tag{3.13}$$

where G_i is the gas phase species *i*, S_i is the solid species *i*, N_{gas} is the number of the gas phase chemical components, N_{sur} is the number of the solid chemical components, γ'_{ik} is the stoichiometric coefficient of the reactant *i* in the k^{th} reaction, γ''_{ik} is the stoichiometric coefficient of the product *i* of the k^{th} reaction and r_k is the total reaction rate of the k^{th} reaction. Eq. (3.13) accounts for both reversible and non-reversible reactions. The summation terms appearing in Eq. (3.13) refer to the components of the chemical system but only species that participate as reactants or products have non-zero stoichiometric coefficients.

The rate of an elementary gas phase reaction $R_{k,gas}$ can be given by an Arrhenius type expression:

$$R_{k,gas} = k_{0,gas} T^b \exp\left(-\frac{E^k_{a,gas}}{R T_{gas}} \right) f(C_{1,gas}, \ldots C_{N_{gas}}), \tag{3.14}$$

where $k_{0,gas}$ is the pre-exponential factor of the reaction *k*, b is the temperature exponent, $E^k_{a,gas}$ is the activation energy of the reaction *k*, C the molar concentration of the reactants and f a function expressing the dependence of the rate from the species concentrations. Thus, the net consumption or production rate of the chemical species *i* in the gas phase for a total number of gas phase reactions, K_{gas}, is given by:

$$R_{k,gas} = \sum_{k=1}^{K_{gas}} \left(\gamma''_{ik} - \gamma'_{ik} \right) R_k, \;\; i = 1, \ldots, N_{gas}. \tag{3.15}$$

The left hand side of Eq. (3.15) appears in the third term of the right hand side of energy balance equation (Eq. 3.3) and in the second term of the right hand side in the species balance equation (Eq. 3.4).

At the surface, it is assumed that the mass flux of each species in the gas phase equals its consumption/production rate (Deen, 1998):

$$\rho_{sur} D_i \mathbf{n} \cdot \nabla \omega_{i,sur} = M_i \sum_{k=1}^{K_{sur}} R_{k,sur}, \;\; i = 1, \ldots, N_{gas}, \tag{3.16}$$

where ρ_{sur} is the density at the surface, D_i the diffusion coefficient of the chemical species *i*, $\omega_{i,sur}$ the mass fraction of the species *i* on the surface, **n** the outward pointing unit normal vector to the plane of the surface and K_{sur} the total number of the surface reactions in which the chemical species *i* participates. The net surface reaction rate, $R_{k,sur}$, is provided by the following equation:

$$R_{k,sur} = \sum_{k=1}^{K_{sur}} \left(\gamma''_{ik} - \gamma'_{ik}\right) R_{sur}, \;\; i = 1, \ldots, N_{sur}. \tag{3.17}$$

Here R_{sur} obeys the Arrhenius type Eq. (3.14) and the corresponding parameters (pre-exponential factor, activation energy, temperature and molar concentrations) being calculated at the surface.

The Fluent CFD code applies by default Eqs. (3.15) and (3.17) as well as the Arrhenius type expression of Eq. (3.14) for the calculation of the gas phase and surface reaction rates. However, the user has the possibility to import other expressions for reaction rates, such as Langmuir-Hinshelwood type expressions, by using external files with user defined functions (UDFs). The UDFs are linked to the software through dynamic libraries and extend the possibilities of the CFD code. Functions are written in C language and they are imported in the code with specific macro-definitions, for the gas phase and the surface reaction rates, respectively.

3.1.5. Solution of the equations – The finite volume method

The numerical (approximate) solution of the set of PDEs, described in the previous paragraphs, amounts to the integration of the PDEs over each elemental control volume (cell) of the computational domain. A generalized governing transport equation, at steady state, reads:

$$\nabla \cdot \left(\rho \mathbf{u} \Phi\right) = \nabla \cdot \left(\Gamma \nabla \Phi\right) + S_\Phi, \tag{3.18}$$

where Φ is the generalized variable, ρ is the density, $\mathbf{u}$ the velocity and Γ the diffusion coefficient. The term in the left hand side of Eq. (3.18) is the convective contribution of Φ. The terms in the right hand side account for the rate of change of Φ due to diffusion and to sources/sinks, respectively (Boudouvis, 2010). Upon integration, Eq. (3.18) yields:

$$\int_V \nabla \cdot \left(\rho \mathbf{u} \Phi\right) dV = \int_V \nabla \cdot \left(\Gamma_\Phi \nabla \Phi\right) dV + \int_V S_\Phi dV \tag{3.19}$$

and by virtue of the divergence theorem,

$$\int_A \mathbf{n} \cdot \mathbf{u} \rho \Phi dA = \int_A \mathbf{n} \cdot \left(\Gamma_\Phi \nabla \Phi\right) dA + \int_V S_\Phi dV, \tag{3.20}$$

where A is the boundary of the control volume, V. The quantities in Eq. (3.20) are calculated with the finite volume method (Thompson *et al.*, 1985; Versteeg and Malalasekera, 2007), schematically summarized in Figure 3.5. In Figure 3.5a, a control volume is depicted in a form of a triangular cell , where C_0 is the center of the cell, f is the center of the face KM, $\mathbf{r}_0$ is the vector from the center of the cell to f and $\mathbf{A}_f$ is the normal vector to the face KM with length equal to $|KM|$.

The Eq. (3.20) is approximated over a control volume, V as follows:

$$\sum_i \rho_{f_i} \Phi_{f_i} u_{f_i} \cdot A_{f_i} = \sum_i \Gamma_\Phi \nabla \Phi_{f_i} \cdot A_{f_i} + S_\Phi V, \tag{3.21}$$

where i runs over the faces enclosing the control volume, f_i denotes evaluation at the center, f, of the face i, and Φ_f is the value of Φ at f.

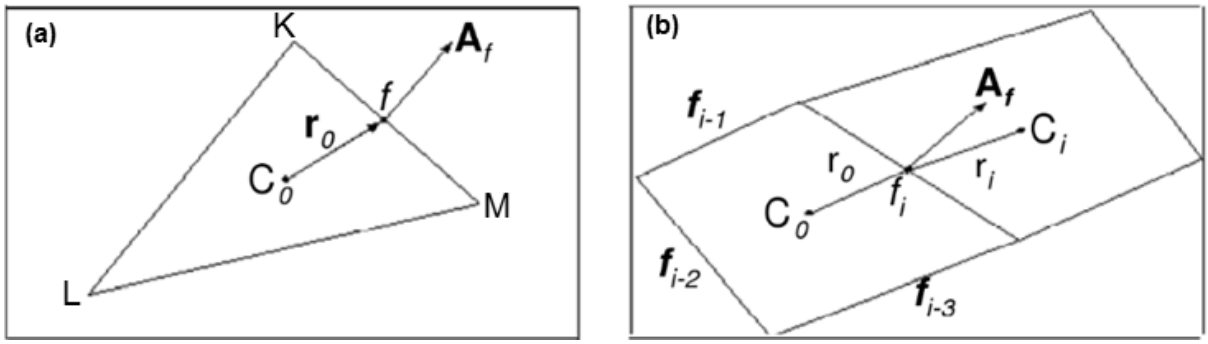

Figure 3.5: (a) A typical triangular cell used in the finite volume method. (b) Two quadrilateral neighboring cells.

The values of the unknown variables to be solved for are the values of Φ at the center of each cell, Φ_{C_0}. The values of Φ_f at the faces of each cell are calculated by using a second order upwind scheme:

$$\Phi_{f_i} = \Phi_{C_0} + \nabla \Phi_{C_0} \cdot \mathbf{r}_0 \tag{3.22}$$

$$\nabla \Phi_{C_0} = \frac{1}{V} \sum_i \tilde{\Phi}_{f_i} A_{f_i}, \tag{3.23}$$

with $\tilde{\Phi}_{f_i}$ being the average of the values at the neighboring cell centers (Figure 3.5b):

$$\tilde{\Phi}_{f_i} = \frac{\Phi_{C_0} + \Phi_{C_i}}{2}. \tag{3.24}$$

In Eq. (3.21), $\mathbf{r}_0$ is the displacement vector from the upstream cell center to the face center. Alternative schemes for the computation of Φ_f can be applied, such as first-order upwind and power-law schemes (Ansys 12.1/Fluent Documentation, 2009; Versteeg and Malalasekera, 2007). Eventually, $\nabla \Phi_{f_i}$ is computed by a central difference scheme:

$$\nabla\Phi_{f_i} = \frac{1}{2}\left[\left(\nabla\Phi_{C_0}\right) + \left(\nabla\Phi_{C_i}\right)\right]. \tag{3.25}$$

The substitution of Eqs. (3.21), (3.22) and (3.25) in Eq. (3.20) yields the system of algebraic equations to be solved for the unknown values of Φ at the center of each cell. At each cell, the corresponding algebraic equation becomes:

$$a_{C_0}\Phi_{C_0} = \sum_{neigh} a_{neigh}\Phi_{neigh} + S, \tag{3.26}$$

where a are the linearized coefficients at the neighboring cell centers (cf. Figure 3.5). The set of Eqs. (3.26) can be written in the more compact, matrix form:

$$\underline{\underline{A}}\,\underline{\Phi}_C = \underline{b}, \tag{3.27}$$

where $\underline{\underline{A}}$ is the matrix of coefficients, $\underline{\Phi}_C$ is the vector of the unknown variables and $\underline{b}$ is the vector of the source values. In our case, $\underline{\Phi}_C$ comprises the unknown values of the velocity, pressure, temperature and species mass fractions.

The finite volume solution algorithm is iterative in nature, and in a converged solution the so-called residuals – discrepancies in the conservation equations – are very small. There are no standard global metrics to be used as convergence criteria. The convergence criterion used by the Fluent CFD code requires that the residuals R_Φ,

$$R_\Phi = \frac{\sum_{C_0}\left|\sum_{neigh} a_{neigh}\Phi_{neigh} + S - a_{C_0}\Phi_{C_0}\right|}{\sum_{C_0}\left|a_{C_0}\Phi_{C_0}\right|}. \tag{3.28}$$

become lower than 10^{-3} for all equation (Ansys 12.1/Fluent Documentation, 2009). However, for the computations on CVD of Al and Fe in this thesis, a more strict convergence tolerance deemed necessary; it was set to 10^{-6}. This choice followed the careful monitoring of the residuals of the species equations along with the change of the corresponding mass fractions. For convergence acceleration, the so-called pressure-based coupled algorithm is chosen within the Fluent code, which in contrast to the so-called segregated algorithm, solves a coupled system of equations comprising the momentum equations and the continuity equation (Ansys 12.1/Fluent Documentation, 2009). However, the memory requirements increase by 1.5 - 2 times compared to the segregated algorithm. The required memory for the solution of the 3D problem with the coupled algorithm is 2 GB.

3.2. Modeling and computations at the nanoscale

The nanoscale model is stochastic and based on the kinetic Monte Carlo (kMC) algorithm (Battaile and Srolovitz, 2002; Cavallotti *et al*., 2004; Chaterjee and Vlachos, 2007; Gillespie, 1977, 2001). The Monte Carlo method (MC) has been used extensively to study the

equilibrium as well as the time evolution of spin lattice systems with nearest neighbor interactions (Binder and Stoll, 1973; Bortz *et al*., 1974; Fosdick, 1963). MC-type methods can also be used to study non-equilibrium and kinetic phenomena (kMC) for which the exploration of phase space must be performed along a Markov chain of states (Battaile and Srolovitz, 2002). A thermodynamic MC approach samples random system configurations in an attempt to lower energy, whereas a kMC algorithm tracks the temporal evolution of a system by stochastically choosing among the state-dependent sets of transitions available to the system (Battaile and Srolovitz, 2002). The two main ingredients of a kMC algorithm are the identification of the possible surface events and the determination of the rates at which these events can occur. In this thesis, the kMC algorithm can handle three major surface events: adsorption, desorption and migration. The algorithm is implemented in C/C++ language; the calculation related to the surface events are carried out on a computational lattice and incorporate C++ classes which allow the handling of multiple surface sites as groups, in a computationally cost effective way.

3.2.1. The computational lattice

For the description of surface mechanisms during MOCVD on an initially flat surface, a pseudo-3D kMC stochastic model is developed on a rectangular computational lattice, schematically shown in Figure 3.6a, by applying the solid-on-solid approximation. As a first approach to the experimental data and without ignoring the crystallinity and the structure of the obtained Al and Fe films, the model is chosen to be coarse-grained. Coarse-graining amounts to using a simple cubic structure as a computational lattice, despite the *fcc* and *bcc* structures and the (111) and (100) textures of the Al ad Fe films, respectively. The implementation of this approximation for the computational lattice reduces computational effort since the interactions between the surface atoms and consequently the order of the model are limited. By a fitting procedure of the sticking coefficient (see §3.2.3. and Chapters 4 & 5), the model reproduces accurately the experimental values of the roughness of the film surface.

Within the kMC model the interactions among the surface atoms extend only to the first-nearest neighbors (Gilmer and Bennema, 1972), which for the case of the simple cubic lattice are 5 – 12 and 8 for the *fcc* (111) and the *bcc* (100) structures of Al and Fe, respectively. The first-nearest neighbor approximation is schematically depicted in Figure 3.6b. The probability of an adatom reaching the surface (yellow sphere) to perform a nanoscopic event depends only on the neighboring atom of the bottom layer (green sphere) and the four neighboring atoms of the same layer (blue spheres) that surround the selected adatom.

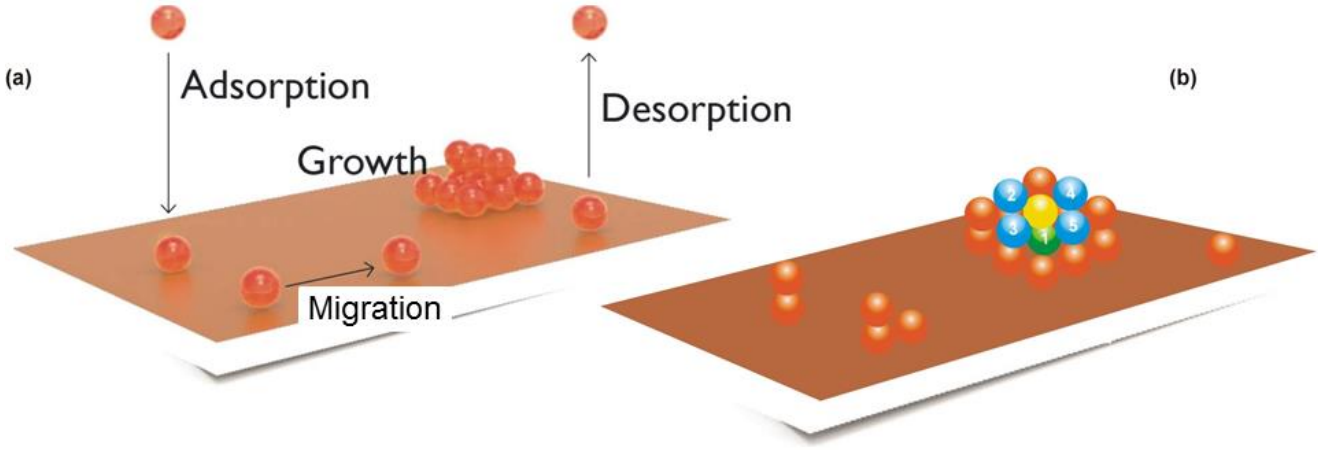

Figure 3.6: Schematic description of the stochastic kMC model. The algorithm accounts for adsorption, desorption and migration events occurring on an initially flat surface (a) of a simple cubic lattice where first-nearest neighbor interactions among 5 neighboring adatoms are considered. (b) The yellow sphere represents the selected atom to perform a surface event based on its 4 neighbors from the same layer (blue atoms) and the neighbor from the bottom layer (green atom). The numbering of the neighbors is random.

The implementation of such an approximation, results in a reduced number of interactions between the surface atoms and consequently in a reduced computational effort, without sacrificing accuracy. Indicatively, the CPU time required for kMC simulations of the Al (Aviziotis *et al*., 2016) and Fe surfaces is approximately 3 h; a similar to the presented kMC model applied in (Vlachos, 2008), requires 73 min of CPU time, for a 40x40 lattice and without incorporating migration events. Acceleration of the computations can be achieved – 1.8 min of CPU time, for the latter case – when appropriate methods, such as the τ-leap method, are applied (Gillespie, 2001; Vlachos, 2008). In contrast, at the nanoscale level, exact atomistic simulations instead of coarse-grained computations are used for the detailed reproduction of the surface microstructure nut highly increase the computational requirements. An example is the homoepitaxial growth of Ag on Ag (111) and the diffusion of Ag monolayer islands on Ag (111) reported by Latz *et al*. (2012); in this model, the detailed crystallographic structure of Ag along with interactions among second nearest neighbors is used to perform on the fly simulations for the reproduction of the exact Ag (111) growth. This type of simulations yields an almost hundredfold increase of the computational requirements and self-learning models are applied to reduce the high computational cost (Latz *et al*., 2012).

The applied nanoscale algorithm has been validated by Cheimarios *et al*. (2011) and Cheimarios (2012) for the epitaxial growth of Si(001). In these works, it has been shown that the formation of dimer structures and the different dimers orientation depending on the deposition rate can be predicted by the kMC model as observed experimentally by Hamers *et al*. (1989).

3.2.2. The kinetic Monte Carlo (kMC) algorithm

The surface events simulated by the kMC algorithm are modelled as Markov processes by transition probabilities per unit time (Berg, 2004). The adsorption rate, i.e., the probability of an impinging atom to stick to the surface upon collision is given by the kinetic theory of ideal gases (Lam and Vlachos, 2001):

$$R_{ads} = \frac{s_0 P_p}{C_{tot}\sqrt{2\pi M k_B T_s}}. \tag{3.29}$$

Here R_{ads} is the adsorption rate, s_0 is the sticking coefficient (explained in the next section), P_p is the partial pressure, C_{tot} is the concentration of free sites where adsorption events occur and T_s is the surface temperature. The surface density of adsorption sites is taken 10^{19} sites/m^2 (Vlachos, 1997) and the partial pressure is calculated based on the mass fractions of the species contributing to deposition (e.g. precursors) provided by the macroscale (see §3.3.). It is noted at this point, that species which reach the surface and contribute to the deposition of solid Al and Fe, are totally converted to the corresponding solid atoms.

The desorption rate depends on the local activation energy and the first-nearest neighbor interactions. The desorption rate is given by

$$R_{des}(n) = \nu_0 \exp\left(-\frac{nE}{k_B T_s}\right), \tag{3.30}$$

with E being the single bond energy, ν_0 the frequency factor, $n = 1,2,\ldots,5$ the number of nearest neighbors and $R_{des}(n)$ the desorption rate depending on this number. The desorption energies used for the simulations of Al and Fe surfaces are taken from the literature and are presented in the corresponding chapters.

Surface migration (or diffusion) is modelled as desorption followed by re-adsorption and its transition probability is given by:

$$R_{mig}(n) = \nu_0 \nu_1 \exp\left(-\frac{nE}{k_B T_s}\right), \tag{3.31}$$

where $\nu_1 = \exp\left(\frac{E - E_{mig}}{k_B T_s}\right)$ is a factor associated with the energy difference that a surface adatom has to overcome in order to migrate from one lattice site to an adjacent one in the zero adsorbate concentration limit. E_{mig} is its migration energy. Since the initial flat surface is covered quickly by the corresponding solid adatoms, only the migration energy corresponding to the diffusion of Al on Al and of Fe on Fe is considered (Chapters 4 & 5). This energy accounts for both in-plane (intralayer) and across step edges (interlayer) diffusion that is the Schwoebel-Elrich (ES) barrier is taken equal to 0 (Chapters 4 & 5).

The time step used is given by:

$$\Delta t = -\frac{\ln \xi}{R_{tot}}, \tag{3.32}$$

where ξ is a random number in the interval $(0,1)$ and R_{tot} is the total transition probability per unit time which is expressed as:

$$R_{tot} = R_{ads} N_T + \nu_0 [1+\nu_1] \sum_{n=1}^{5} N_n \exp\left(-\frac{nE}{k_B T_s}\right), \tag{3.33}$$

with N_T being the total number of active atoms on the surface of the simulated lattice and N_n the number of atoms having n nearest neighbors.

It should be noted that among R-quantities, only adsorption is fitted to the experimental data through the sticking coefficient (see §3.2.3.); migration and desorption are not. Their relative importance in the overall simulation of the surface events and the calculation of the roughness are discussed in the corresponding chapters.

The surface is initially flat and it is updated after every adsorption, desorption, or migration event. For simulations, periodic boundary conditions are used, i.e., each atom which moves out of the boundary of the domain, is replaced by an atom which enters the domain from the opposite boundary. Since the adsorption probability is site independent, the surface atoms are grouped into classes according to their number of nearest neighbors. The total probability for a given class is provided by Eq. (3.33). The transition probabilities are calculated *a priory* and every kMC trial leads to the realization of an event. After each event, time evolution is performed in a continuous way based on the duration of the event.

The structure of the classes in the kMC algorithm is presented in Figure 3.7. The algorithm starts by selecting a random number. Based on its magnitude, a nanoscopic event (adsorption, desorption, migration) and a class are selected. Subsequently, a site is randomly picked from the class and the surface event finally occurs. After each event, the classes are updated and the transition probabilities are re-calculated.

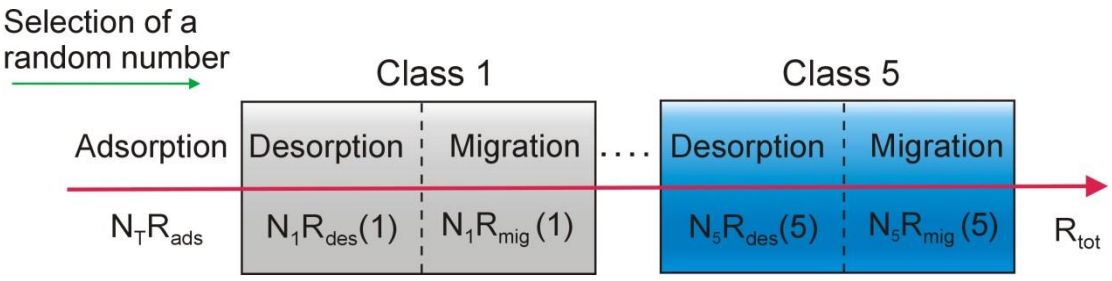

Figure 3.7: Selection of a class to perform a nanoscopic event and a class. A class consists of a group of surface atoms according to the number of their first-nearest neighbors. Grouping the surface atoms into classes reduces the computational cost.

Since this update is computationally expensive, it is performed locally, around the nearest neighbors of the atom, avoiding the screening of the entire lattice. The local updating of the algorithm results in important savings in computational time, since it is practically independent of the lattice size (Reese *et al*., 2001).

The deposition rate (DR) is given by the difference between adsorption and desorption rates:

$$DR = R_{ads} - R_{des}. \tag{3.34}$$

In order to calculate the two rates accurately and to reduce noise effects, the events-counting method is applied (Lam and Vlachos, 2001), e.g., for the calculation of the adsorption rate, the events which lead to the adsorption of atoms on the surface are counted and this number is divided by the time period within which adsorption events are performed. Then, the surface roughness is determined using the following formula of the root mean square (RMS) roughness:

$$RMS = \frac{\sqrt{\sum_{i,j=1}^{N_{lat}} \left[h_{i+1,j} - h_{i,j}\right]^2 + \left[h_{i-1,j} - h_{i,j}\right]^2 + \left[h_{i,j+1} - h_{i,j}\right]^2 + \left[h_{i,j-1} - h_{i,j}\right]^2}}{N_x N_y}, \tag{3.35}$$

where $N_{lat} = N_x N_y$ is the lattice size and $h_{i,j}$ is the thickness of the film at each lattice site. The lattice size used for the kMC model consists of $N_x = 120$ and $N_y = 120$ cells and it is sufficiently high, since the results do not change for denser lattices.

3.2.3. The sticking coefficient

The kMC algorithm used here does not explicitly include chemical reactions and this is done on purpose; indeed, the chemical information is incorporated in the sticking coefficient (s_0 in Eq. 3.29) through a fitting process that correlates this coefficient with T_s. By fitting s_0 to T_s through the macroscopic deposition rate of Al or Fe films, all the steps involved in the chemical reactions (precursor/intermediate species adsorption/desorption, decomposition, products adsorption/desorption, inhibition of the surface by a product) are "absorbed" in a so-called "effective s_0".

The fitting procedure is based on the macroscopic, experimentally measured deposition rate which for each T_s and each position of the substrate on the susceptor is compared to the corresponding computed one. This comparison provides polynomial relations between s_0 and T_s (Chapters 4 & 5) which are applied for the kMC simulations. The fitting is performed with the Matlab software by using a polyfit function procedure.

The sticking coefficient is treated as a "technical term" in order to illustrate the efficiency of CVD processes towards film growth; it depends on all process parameters (e.g.,

temperature, pressure, chemistry) and varies as a function of operating conditions (Vahlas and Blanquet, 1998). The implementation of such type of relations for s_0 provides a correlation of this quantity with the operating temperature while implicitly integrating chemical reactions in the nanoscopic model. Thus, fast and accurate simulations are performed for the MOCVD of Al and Fe by implementing a procedure which appears as a purely physical one; i.e., involving single Al or Fe atomic events only. The incorporation of an effective sticking coefficient in kMC algorithms for an insight into the chemistry has been reported in Frenklach (1992).

3.3. Multiscale modeling: Linking macroscale with nanoscale

The methodology of linking the macroscale of a MOCVD reactor with the nano-morphology of a thin film on an initially flat surface is presented schematically in Figure 3.8. The term "linking" is used instead of "coupling" since the communication between the two scales is one-way and the effect of microscopic features on macroscopic phenomena is not a matter of investigation in this thesis. The linking is based on the assumption that the deposition rate remains unchanged, i.e., it is independent of the simulated scale (Masi *et al*., 2000).

At first, the computational problem is solved at the macroscopic level, as previously described, in order to calculate the mass fraction of the species, at the boundary cells of the surface. Upon convergence, the mass fractions are fed to the kMC model for the calculation of the adsorption probability of the atoms on the surface. Termination of the nanoscale simulations is signalled when the morphology of the surface, expressed by the RMS roughness, does not change with time as shown in Figure 3.9.

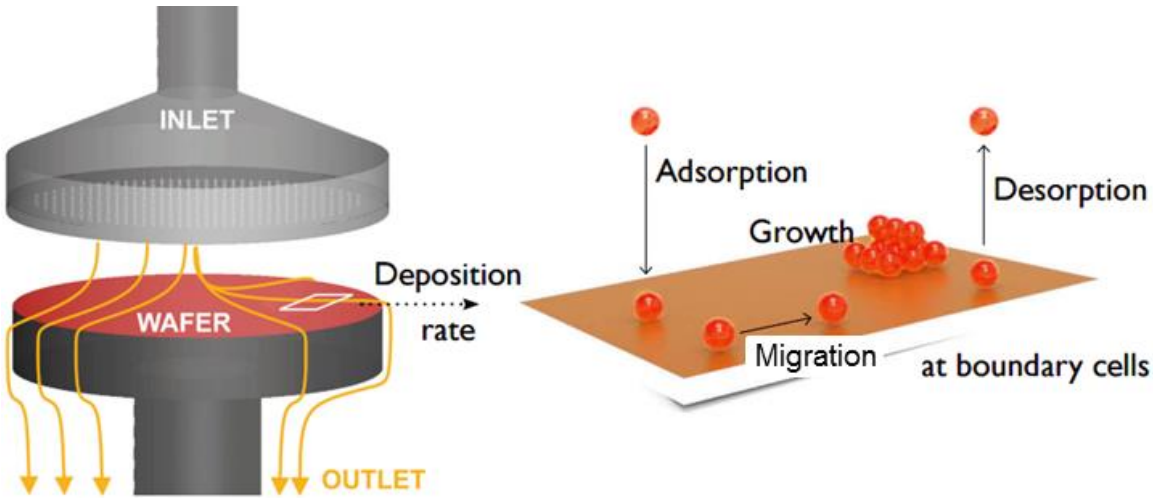

Figure 3.8: Schematic description of the multiscale framework: The reactor scale (macroscale) applies the experimental operating conditions to simulate the transport phenomena and feeds the kMC model with the mass fractions of species contributing in the deposition which are calculated at the boundary cells of the surface (nanoscale). The deposition rate remains unchanged regardless the simulated scale.

The multiscale framework results in accurate and fast simulations as presented in the next sections (Chapters 4 & 5), due to the coarse-grain assumption for the computational lattice of the nanoscopic model and the bypass of the chemistry through the fitting procedure of the sticking coefficient. The implementation of more detailed models accounting for the actual crystalline structures and orientations of the simulated surfaces and the explicit inclusion of chemical processes occurring at the surface level, will certainly lead to much higher computational requirements, possibly fifty times higher CPU time.

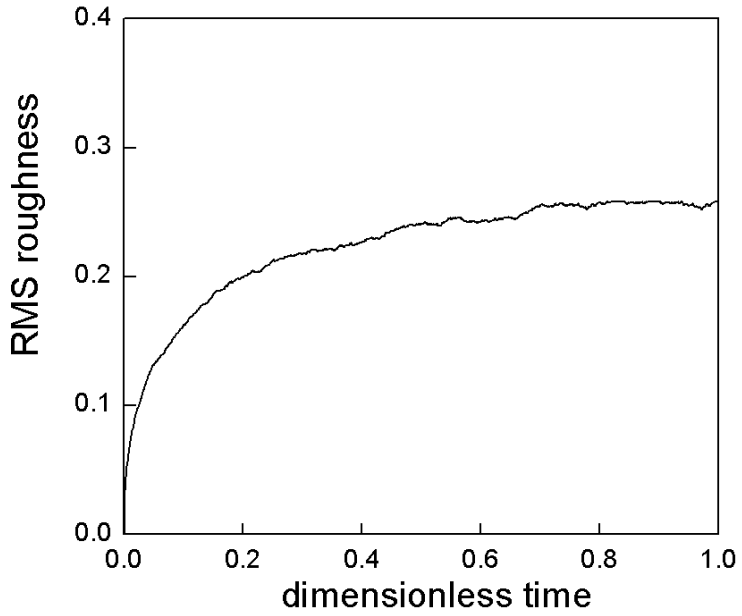

Figure 3.9: The RMS roughness as a function of the time frame set to the stochastic kMC algorithm. RMS stabilizes at a dimensionless time of 0.75 and thus, the simulation may terminated.

3.4. Techinical aspects of the simulations

The macroscale as well as the multiscale simulations are performed in two computer clusters, Pegasus (Pegasus, 2012; Cheimarios, 2012) and Andromeda (Andromeda, 2012; Cheimarios, 2012), located in the School of Chemical Engineering of NTUA. In particular, the 3D macroscopic computations are performed with parallel processing.

Pegasus is composed of 16 nodes each consisting of 2 Xeon (3 GHz and 2 GB ram) processors (32 processors/threads in total). The communication of the nodes is performed by a Gigabit Ethernet and a faster Myrinet networks. The latter is based on MPI libraries for the message exchange. The operating system of Pegasus is the free software Rocks 4.1. Andromeda is a hybrid, shared memory cluster consisting of 4 nodes with 2, 6-cores, Xeon X5660 (2.80 GHz and 16 GB ram) processors (48 threads in total). The communication among the nodes is achieved with a Gigabit Ethernet network and the operating system is the free software Rocks 5.4.

Summary-Conclusions

A macroscale model is developed for the simulation, at steady state, of the simultaneous transport and chemical reaction phenomena in the bulk of a CVD reactor. The governing equations are discretized and solved within the finite volume method in 2D and 3D domains. The macroscopic simulations will be used for analysing the MOCVD of Al and Fe in the following chapters.

At the nanoscale, the evolution of the surface of the films is investigated. The nanoscale model is based on a kMC algorithm which simulates adsorption, desorption and surface events. The computational lattice is chosen to be a coarse one, different from the actual crystalline structures of the films in order to reduce the computational effort. The required chemical information at the surface level is incorporated in the sticking coefficient through a temperature dependent function.

Finally, it is the multiscale model resulting by the linking of the two different scales which enables simulations at the surface levels and the calculation of the surface roughness of the deposited Al and Fe films. The linking is based on the assumption that the deposition rate remains unchanged regardless the scale of simulation and it is realized by feeding the stochastic kMC model with the output of the macroscopic model. Multiscale as well as macroscale simulations of the CVD process provide information for the chemical mechanisms and the surface microstructure, thus, ultimately allowing the control and optimization of the process.

Chapter 4: Investigation of the MOCVD of Al from DMEAA: Experiments and simulations

In this chapter, the MOCVD of aluminum is presented from an experimental and a computational point of view. Experimentally, depositions are carried out in a temperature range to determine the Arrhenius plot of the process and characterizations of the films are performed by means of SEM and interferometry to observe the microstructure of the films and to measure the surface roughness. The modeling of the process at the macroscopic and the surface level is based on the experimental data for the investigation of the mechanisms and kinetics involved in the process as well as at the simulation of the surface nanomorphology and the calculation of the roughness. The experimentally and computationally combined investigation of the MOCVD of Al aims at the creation of a robust process with fully defined parameters for its application to the co-deposition and sequential deposition with Fe.

4.1. Experimental aspects

Deposition of Al films from DMEAA is performed in the reactor described in Chapter 2 (see §2.1.1.). The aim of this study is to investigate the evolution of the deposition rate as a function of the temperature. The determination of the deposition rate at the different temperature regimes allows choosing the proper operating windows for the co-deposition and/or the sequential deposition of Al with Fe which is the ultimate goal of this work. At the same time we aim at getting insight in the microstructural characteristics of the films and in their evolution within the investigated temperature range, which strongly affect the final properties of the film.

DMEAA is synthesized and supplied by Nanomeps. It is maintained with a cryostatic regulator at 3^oC permanently, i.e., below the freezing point of the compound (5^oC), thus enhancing its stability and strongly limiting its degradation (Matsuhashi *et al.*, 1999). It is worth recalling that vapor pressure increases with time, indicating departure of ligands and degradation of the precursor. During the deposition experiments the precursor is regulated at 7^oC. At this temperature, the vapor pressure of DMEAA is 0.7 Torr, according to Eq. (1.1) (see §1.4.2. & §2.1.1.5.):

20 x 10 x 1 mm^3 Si(100) flat coupons are used as substrates. They are prepared according to the protocol described previously (see §2.1.2.). In each experiment, three substrates are placed at different radial positions of the susceptor, as presented in Figure 4.1, with the aim to study the homogeneity of the films along the susceptor, in terms of thickness and surface roughness; the two latter being simulated in the modeling of the process.

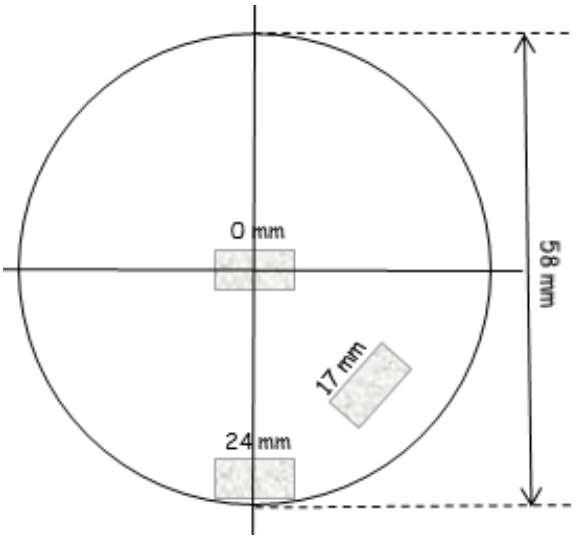

Figure 4.1: A schematic presentation of the location of the Si substrates on the susceptor.

Independent experiments are performed at eight different substrate temperatures, T_s, in the range 139^oC – 241^oC (surface temperature is calibrated with a thermocouple attached to the surface in deposition conditions – see §2.1.1.2.). The total pressure of the reactor, $P_{reactor}$, is fixed at 10 Torr. The lines and the walls of the reactor are thermally regulated at

T_{lines} = 100°C and T_{walls} = 75°C, respectively. Pure nitrogen (N_2, 99.998%, Air products) is fed in the reactor chamber through a dilution line and a carrier line passing through the precursor; both flow rates are regulated by mass flow controllers (see §2.1.1.4.) at $Q_{N_2,dilution}$ = 305 sccm and $Q_{N_2,carrier}$ = 25 sccm, respectively, resulting in a total flow rate of N_2 equal to Q_{N_2} = 330 sccm.

The maximum inflow rate of the precursor, Q_{prec}, in the reactor chamber is calculated by the formula proposed by Hersee and Ballingal (1990) (see Eq. 2.1 – §2.1.1.5.). According to this relation, for a saturated vapor pressure of DMEAA at 7°C of 0.7 Torr, the maximum inflow rate of DMEAA in the process chamber equals 2 sccm. Experiments are processed in the above fixed conditions, at the T_s reported in Table 4.1.

Table 4.1: Experimental conditions adopted for the CVD of Al from DMEAA.

#Experiment	Exp1	Exp2	Exp3	Exp4	Exp5	Exp6	Exp7	Exp8
T_s (°C)	139	151	167	185	198	212	227	241
Fixed conditions	T_{walls}=75°C, T_{lines}=100°C, $P_{reactor}$=10 Torr, Q_{N_2} =330 sccm, Q_{prec} = 2 sccm, Duration = 1h							

The deposition duration for all experiments is 1 h, including the time required for the initiation of the deposition to take place at each T_s. This incubation time is assumed to be the time needed for the surface color to change. It embeds nucleation and first steps of growth that they cannot be observed *in situ* in the used experimental setup. Hence, it is evaluated by visual observation of the substrate surface through the windows of the reactor. In view of the observed time scale (min) such observation allows convenient and rather precise determination of the incubation time. The determination of incubation time provides the net deposition rate. The latter is calculated by the mass gain over the effective deposition duration, namely 1 h minus the incubation time. It is worth mentioning that the same incubation time for all three substrates is considered, regardless their radial position on the susceptor. This assumption holds true for the higher T_s, where the change of the color is fast but it is less valid for the lowest T_s, where films seem to form more quickly on the substrate which is at the central position (0 mm).

For the determination of the incubation time, we observe a sharp color transition from reflecting grey (Si surface) to diffuse white (Al surface). Figure 4.2 shows the evolution of the incubation time as a function of T_s (Aviziotis *et al.*, 2015). A significant delay is observed at low T_s (139°C), where the incubation time equals 310 s. It decreases almost linearly to 48 s at 241°C where it stabilizes. The observed continuous decrease of the incubation time with increasing the deposition temperature in the low to moderate temperature range, followed by stabilization at high deposition temperature has been reported in the literature for the deposition of Al from DMEAA on Si and SiO_2 substrates (Simmonds *et al.*, 1993). The same behavior has also been observed in the case of the CVD of Si (Kajikawa and Noda, 2005) and Cu (Aviziotis *et al.*, 2013).

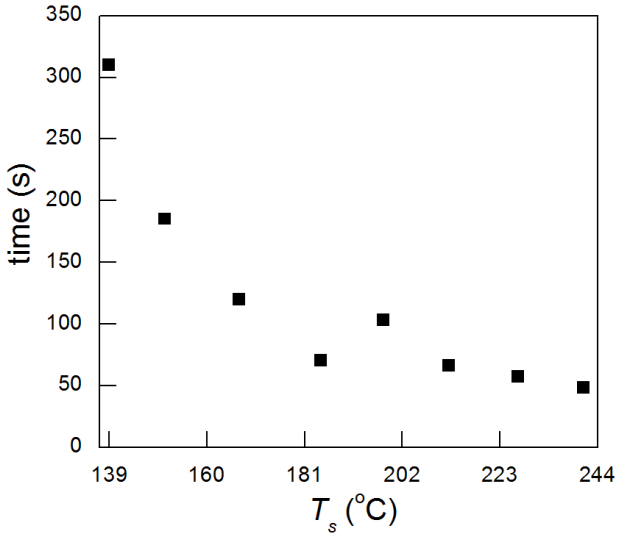

Figure 4.2: The incubation time as a function of the substrate temperature, T_s.

It can attributed either to the evolution of the sticking coefficient of the precursor on the substrate with varying T_s, or to accelerated desorption of the adsorbents at higher temperatures. The fact that it stabilizes above a temperature threshold shows that sticking coefficient, desorption, or other surface phenomena become negligible with respect to the high reaction rate.

The incubation time is activated by temperature, it depends on the precursor's partial pressure and it can be modulated by controlling the reactivity of the substrate. Investigating nucleation mechanisms is beyond the scope of this work. Hence, the incubation time is only used here to determine the net experimental deposition duration. However, such estimation could lead to the overestimation of the deposition rate, since what it is assumed to be incubation is actually the upper limit of the incubation time. We include this overestimation in the measurements of the deposition rate by increasing the downside of the error bars (see Figure 4.3).

Figure 4.3 is the Arrhenius plot of the process. Although it is difficult to distinguish the reaction-limited regime from the transport-limited regime (Jang *et al.*, 1998), the increment of the deposition rate as the temperature increases up to 185°C implies a kinetically limited regime. The definition of the limits between the reaction and the diffusion-limited regimes is close to the range of previously reported data, where the maximum deposition rates are obtained at about 150°C-160°C (Kim *et al.*, 1996; Yang *et al.*, 1998; Yun *et al.*, 1998a). The difference of 20°C-30°C can be attributed to the different setup of the reactor in Kim *et al.* (1996) and Yun *et al.* (1998a), the distance between the susceptor and the shower plate is 3 cm) and in the lower mass inflow rate of DMEAA in the reactor (0.01-1 sccm). The non-discrete distinguishing between the two regimes reveals the high sensitivity of the precursor to the reaction temperature and significant impact of the both the surface and the gas-phase reactions to the deposition of Al, in the entire investigated temperature range.

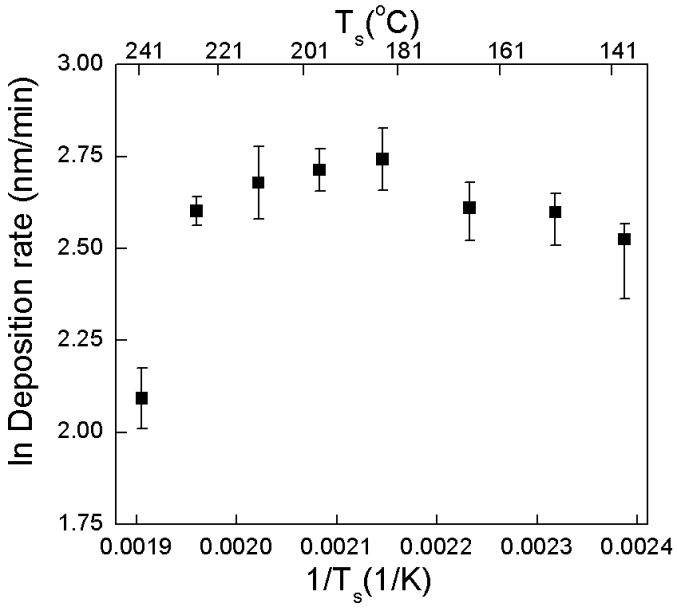

Figure 4.3: The Arrhenius plot of the MOCVD of Al from DMEAA. The deposition rate increases with T_s to a maximum value at T_s=185°C and then, is continuously decreasing.

Above 185°C, the deposition rate presents a light decrease, prior to a steep reduction at the highest investigated temperature that is, above 230°C. This abrupt change is assumed to be due to competitive gas phase processes such as the high gas phase decomposition rate of the precursor (Xenidou *et al.*, 2010). The activation energy of the surface reaction is 19.682 kJ/mol, as it is estimated from the slope of the Arrhenius plot in the reaction-limited regime. This value is in adequate agreement with the value of 22.192 kJ/mol reported in (Jang *et al*., 1998) for the same process.

The overall behavior of the deposition rate as well as the chemical mechanisms involved in the deposition of Al from DMEAA are investigated in terms of macroscopic modeling, in the next paragraph.

The microstructure of the Al films deposited in this temperature range is observed by SEM in the secondary electrons mode (see §2.2.1.). It is presented in Figure 4.4 (Aviziotis *et al.*, 2015), where surface and cross-sectional micrographs are shown for 139°C, 198°C and 227°C. Deposition at the lowest T_s (Figure 4.4a and b) show scattered grains on the surface and form rough morphologies with poor uniformity and no continuity. As opposed to this case, by increasing T_s (Figures 4.4c and d, and then e and f) the density of the film increases because grains coalesced. Measurement of the mass gain, assuming Al bulk density, gives an estimation of thickness of 907 nm (±90 nm) and 833 nm (±90 nm) for 198°C and 227°C, respectively, to be compared with SEM measurements of 873 nm (±50 nm) and 804 nm (±50 nm), respectively. Comparison of film thicknesses estimated by mass difference and measured on SEM cross sections reveals that, except for low T_s, the results are similar. This is because at these T_s, films present low porosity, despite the observed surface roughness.

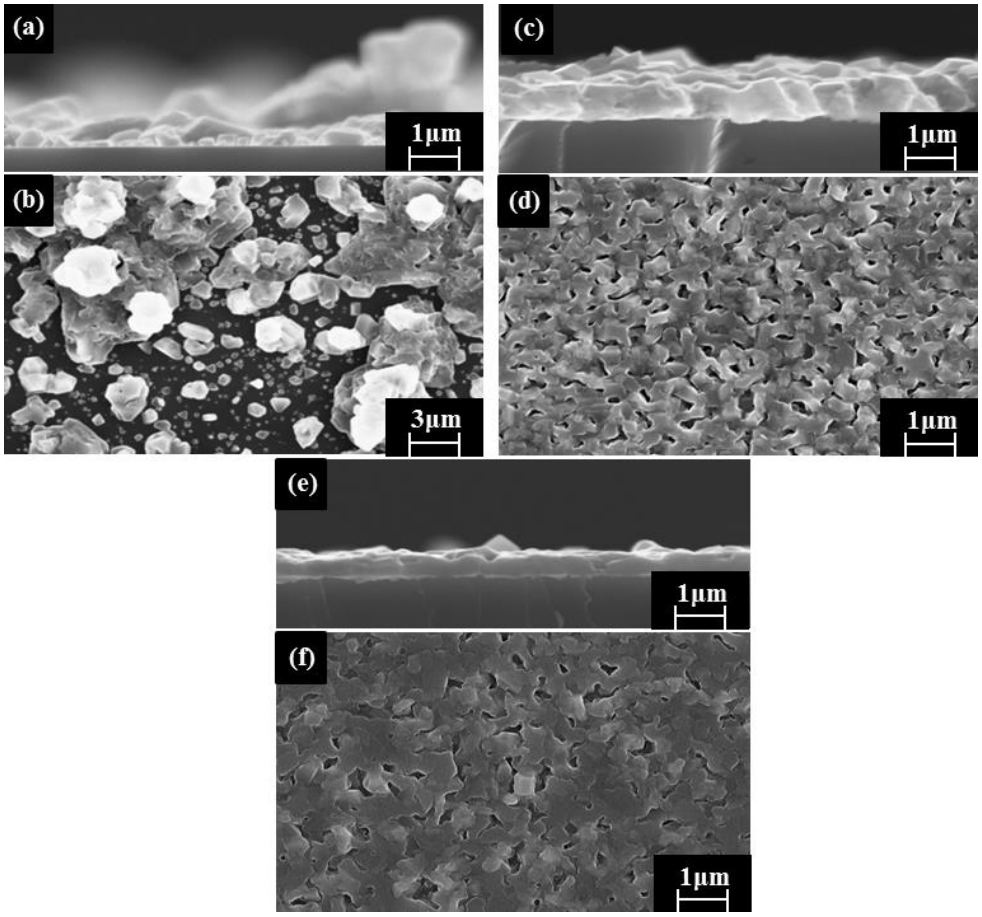

Figure 4.4: Surface and cross-sectional SEM micrographs of Al films deposited at 139°C (a,b), 198°C (c,d) and 227°C (e,f).

Contamination (mainly O, due to the oxophilic nature of Al) and qualitative composition of the films deposited at T_s=139°C and T_s=198°C are determined by EDX analysis (see §2.2.1.). The diagrams obtained for the different temperatures are shown in Figure 4.5. Figure 4.5a is the EDX plot that corresponds to an Al film deposited at 139°C. It is pure, with no oxygen or nitrogen contamination. The low coverage of the surface and the non-uniformity of this film are confirmed by the detection of Si from the bare substrate surface. The film deposited at 198°C (Figure 4.5b) also consists of pure Al without any contamination. Si detection from the substrate is very low, in agreement with the continuous, uniform and thicker films in these temperature conditions.

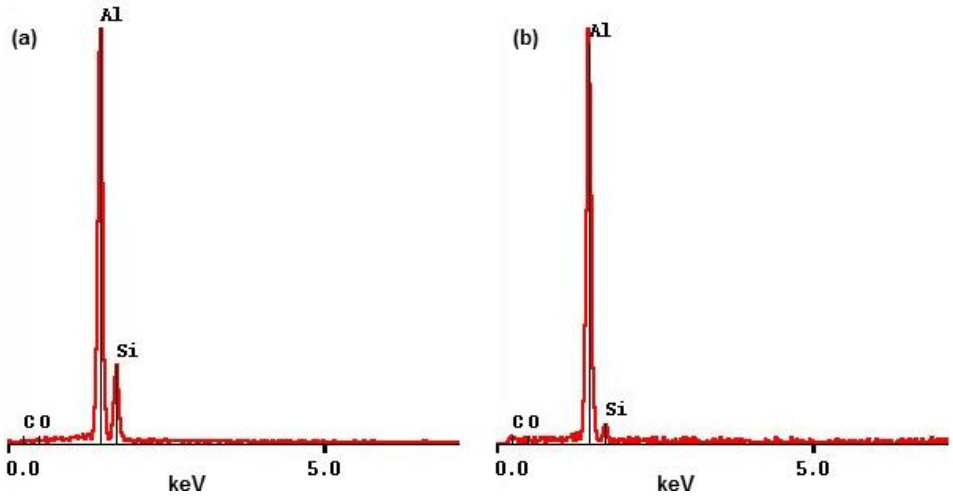

Figure 4.5: EDX elementary qualitative analysis of Al films obtained at the conditions corresponding to (a) T_s=139°C and (b) T_s=198°C.

Visual inspection of the cross-section SEM micrographs of Figure 4.4 reveals that, there is a change of the morphology, and likely a decrease of surface roughness with increasing T_s. Then, interferometry measurements (see §2.2.8) are used for the quantification of the roughness. Five independent measurements are performed at different points on each film and an average of the RMS value is reported. 1.4 x 1.4 mm^2 interferograms of the Al surfaces are presented in Figure 4.6 for T_s=139°C (a) and T_s=227°C (b).

Comparison of the difference between the maximum and the minimum heights for the Al films processed at the lowest T_s (Figure 4.6a) with that observed at the highest T_s (Figure 4.6b) shows that the surface at 139°C is rough and that roughness decreases as T_s increases. This specific topography of the surface is compatible with the previously reported conclusions from the visual observation of the films roughness from the SEM micrographs of Figure 4.4. The roughness of Al films is high, especially at low T_s, and may be problematic if not tailored properly. Therefore, the full data of the RMS roughness along with its behavior as a function of the temperature are presented in the dedicated study of §4.3.3.

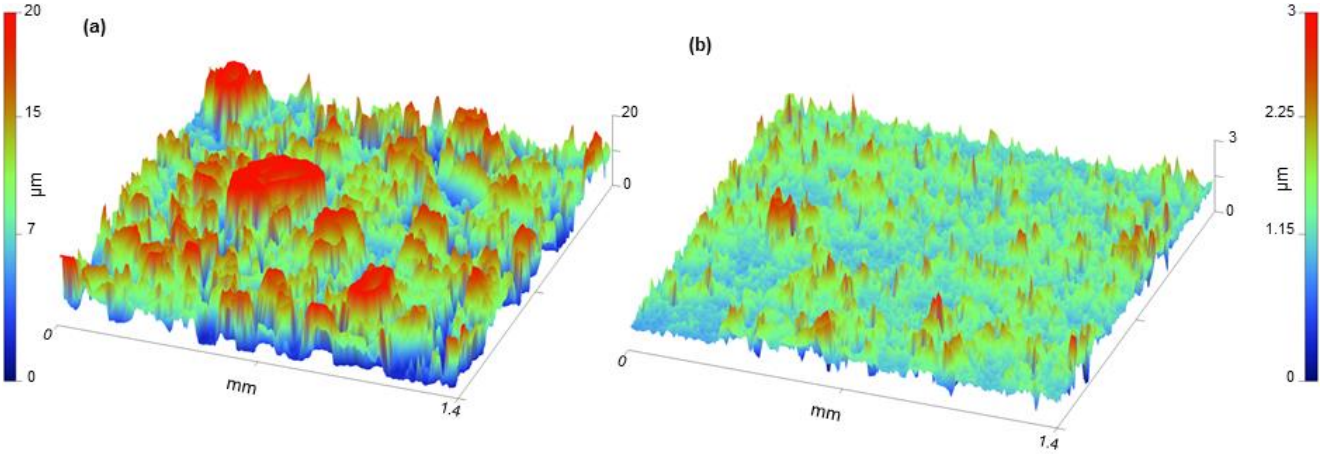

Figure 4.6: Al surfaces as obtained from the interferometer showing the surface microstructure at (a) T_s=139°C and (b) T_s=227°C. The height values presented within the labels in µm are exported from the interferometer.

4.2. Macroscopic modeling of the process

Aiming at investigating the kinetic mechanisms prevailing during the growth of Al films and at determining the corresponding kinetic parameters, a three-dimensional model (3D) of the MOCVD reactor is built, based on the governing equations describing the transport phenomena and the chemical reactions inside the reactor: The continuity, the momentum, the energy and the species transport equations augmented with realistic boundary conditions (Cheimarios *et al*., 2010; Deen, 1998) are discretized in 3D and solved with Fluent CFD code (Ansys 12.1/Fluent Documentation, 2009). The set of the governing transport equations is described in detail previously (see §3.1.3).

A constant mass inflow rate of 6.4332 x 10^{-6} kg/s is imposed at the inlet of the reactor, calculated from the total flow rate (332 sccm) of the gas phase. No-slip condition is imposed at all the walls of the reactor. At the outlet, a standard outflow boundary condition is used and an overall mass balance correction is imposed (Ansys 12.1/Fluent Documentation, 2009). The values of the temperature are set as provided after its calibration on the surface of the substrate, while the temperature at the walls and the inlet of the reactor are set equal to 348 K (75^oC) and 373 K (100^oC), respectively, following the experimental setup. The pressure of the reactor is set at 1333 Pa (10 Torr). Mass fractions of the species entering the reactor are $y_{DMEAA} = 0.02023$ and $y_{N_2} = 0.97977$. These values correspond to the actual mass inflow rate of the precursor in the reactor, which equals to 1.85 sccm (see below). Mesh dependency study has been performed in order for our results to be mesh independent (Chapter 3 – see §3.1.2).

The Lennard-Jones (LJ) parameters, namely σ and ε / k, are the parameters of the LJ potential which are needed for the estimation of the properties of the gas phase mixture in the MOCVD reactor, such as viscosity, mass diffusivity, thermal diffusion coefficient, etc. σ is the radius of the molecules and ε / k is the energy LJ parameter which is equivalent to the attraction strength between molecules. For the unknown species, DMEAA, DMEA and AlH_3, these values are calculated with group contribution methods (Fedors, 1982; Joback and Reid, 1987; Poling *et al*., 2001) and are presented in Table 4.2. The LJ parameters needed for the rest of the species of the mixture participating in the reactions (H_2, N_2) are already implemented in Fluent libraries (Ansys 12.1/Fluent Documentation, 2009).

Table 4.2: The LJ parameters of DMEAA, DMEA and AlH_3.

species	σ (Å)	ε / k (K)
DMEAA	6.39	294.36
DMEA	5.67	268.51
AlH_3	4.39	355.17

4.2.1. Gas phase reactions and kinetics

The decomposition scheme of DMEAA which is examined (see §1.4.3) includes the gas-phase and the surface dissociation of the Al precursor for the deposition of metallic Al.

Experiments for the CVD of Al from DMEAA with the use of in situ FTIR analysis (Yun *et al*., 1998b) have shown that the homogeneous gas phase decomposition of DMEAA yields the production of dimethylethylamine (DMEA – $[(CH_3)_2C_2H_5]N$) and alane (AlH_3) as described by the following reaction:

$$DMEAA_{(g)} \rightarrow AlH_{3(g)} + \mathrm{DMEA}_{(g)}. \quad (4.1)$$

For the volumetric reaction 4.1, the Arrhenius law applied by Fluent (see Eq. 3.14 – §3.1.4) is modified so as to account for a first order Arrhenius type kinetics, expressed by the following equation (Aviziotis *et al*., 2015):

$$R_{gas} = k_{0,gas} \exp(-\frac{E_{a,gas}}{RT_{gas}}) \mathrm{C}_{\mathrm{DMEAA,gas}}. \quad (4.2)$$

$\mathrm{R}_{\mathrm{gas}}$ is the total gas phase reaction rate in kmol/m^{3}s and $\mathrm{T}_{\mathrm{gas}}$, $\mathrm{C}_{\mathrm{DMEAA,gas}}$ are the temperature and the concentration of the precursor in K and kmol/m^3, respectively, in the bulk of the CVD reactor. The activation energy of this reaction is determined as $\mathrm{E}_{\mathrm{a,gas}} = 40\mathrm{kJ/mol}$ (Yun *et al*., 1998b). The pre-exponential factor is fitted based on the experimental data to $\mathrm{k}_{0,\mathrm{gas}} = 7.39 \times 10^5\ \mathrm{s}^{-1}$ (Aviziotis *et al*., 2015). For the fitting of $\mathrm{k}_{0,\mathrm{gas}}$, the process is simulated at higher temperatures, i.e., at the diffusion-limited regime where diffusion dominates and the volumetric reaction occurs at higher rates. At this regime, a pre-exponential factor is defined which is then applied for the simulation of the process at the reaction-limited regime for the fine tuning of the $\mathrm{k}_{0,\mathrm{gas}}$ value.

4.2.2. Surface reactions and kinetics

Several surface reaction pathways have been proposed for the surface decomposition of DMEAA. According to Han *et al*. (1994) and Kim *et al*. (1996), its dissociation on the surface follows that of TMAA, that is, first it produces an intermediate AlH_3 adsorbed compound and then, it further decomposes to solid Al. The successive reaction steps of the surface decomposition of DMEAA can be condensed in the following overall reaction (Kim *et al*., 1996; Xenidou *et al*., 2010):

$$\mathrm{DMEAA}_{(g)} \rightarrow \mathrm{Al}_{(s)} + \mathrm{DMEA}_{(g)} + \frac{3}{2}\mathrm{H}_{2(g)}. \quad (4.3)$$

In the case of the surface reaction (4.3), the DMEA is rapidly desorbed from the surface, as well as molecular hydrogen, i.e., we assume no inhibition of the surface from the by-products of the surface dissociation of the precursor. The kinetics of the surface reaction which is implemented in the macroscopic modeling is a first order Arrhenius kinetics, as for the case of the gas phase reaction, expressed from the following equation (Aviziotis *et al*., 2015):

$$R_{sur} = k_{0,sur} \exp(-\frac{E_{a,sur}}{RT_{sur}}) C_{DMEAA,sur} . \quad (4.4)$$

R_{sur} is the total gas phase reaction rate in kmol/m^{2}s and T_{sur}, $C_{DMEAA,sur}$ denote the temperature and the concentration of the precursor in K and kmol/m^3, respectively, at the boundary cells of the surface. The activation energy $E_{a,sur}$ equals 19.682 kJ/mol, as determined from the slope of the deposition curve in the reaction-limited regime of the Arrhenius plot (see Figure 4.3). Based on the experimentally measured deposition rates along the susceptor radius for each temperature, the pre-exponential factor is fitted to $k_{0,sur} = 5.8579$ m/s (Aviziotis *et al.*, 2015). For the determination of $k_{0,sur}$, the process is first simulated at low temperatures (reaction-limited regime), where the surface reaction is the controlling mechanism for the deposition of Al. Upon the definition of $k_{0,sur}$ value at this regime, simulations are performed at higher temperatures for the final fitting of the pre-exponential factor. It has to be noted at this point, that considering the units of the surface reaction rate and the concentration of the precursor provided by Fluent software, $k_{0,sur}$ is expressed in m/s for consistency reasons. Thus, for the case of the surface reaction this parameter is an apparent pre-exponential factor rather than a real vibrational frequency.

4.2.3. The Arrhenius plot of the process

The implementation of the described chemistry model, along with the imposition of the boundary conditions in the designed 3D reactor (see §3.1.1.) enable the simulation of the Al deposition in the investigated temperature range. Figure 4.7 presents the Arrhenius plot of the process reinforced with two additional lines corresponding to the predictions obtained with the implementation of the model. Two different values for the mass inflow rate of the precursor, namely 2 sccm (full line) and 1.85 sccm (dashed line) are shown in Figure 4.7. The first value is estimated by entering our operating conditions in the formula proposed by Hersee and Balingal (1990) (see Eq. 2.1 – §2.1.1.5.) (Aviziotis *et al.*, 2015). This value has been obtained by assuming that vaporization of the precursor in the bubbler proceeds at thermodynamic equilibrium and that the conductance of the lines connecting the bubbler to the deposition zone is infinite. Thus, this value corresponds to the upper limit of the precursor flow rate in the reaction chamber. Consideration of this value within the modeling of the process yields overestimated deposition rate in the reaction-limited regime.

For this reason, lower mass inflow rates of the precursor are examined as inputs at the model, ranging from 1.5 sccm – 1.95 sccm. In all of the cases, fitting of the pre-exponential factors of the gas-phase and the surface reactions is performed so as to be adapted to the various values of the precursor's input quantity. In the investigated mass inflow rates range and after the fitting of pre-exponential factors, the best match between calculations and experiments is obtained for an inflow rate value slightly lower than the upper limit, *ca.* 1.85

sccm. As it can be seen in Figure 4.7, the computational predictions made with this value improves the match of the deposition rate at low temperatures, while they maintain it close to the low limit of the deposition rate at higher temperatures (Aviziotis *et al*., 2015). That is, the change of the precursor's inflow rate has a greater impact on the behavior of the deposition rate at the kinetically-limited regime rather than at the diffusion-limited regime.

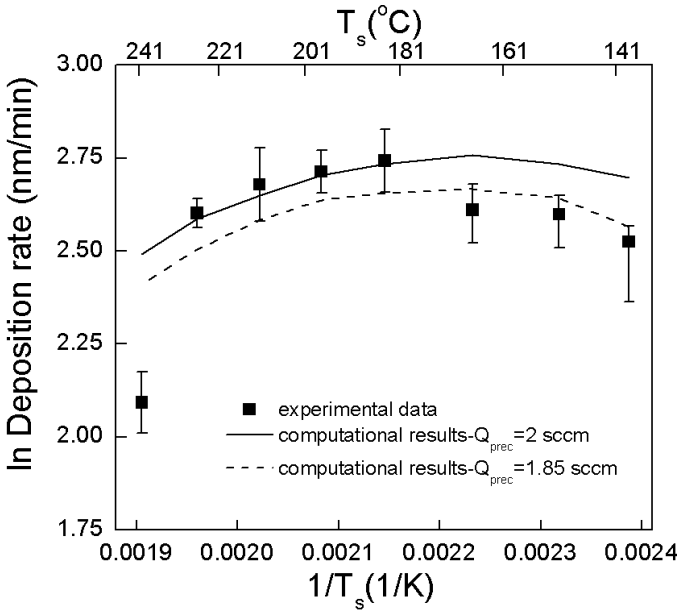

Figure 4.7: The Arrhenius plot of the CVD of Al. Experimental measurements (squares) and computational results for two different precursor inflow rates (lines) are shown.

The change of the mass inflow rate of DMEAA is associated with the quantity of the precursor which reaches the surface and is available for the surface reaction. It is well known that in the kinetically-limited regime the deposition rate is controlled by the surface reaction, regardless the quantity of the precursor that reaches the surface, provided the feeding rate is higher than the consumption rate for the deposition. Thus, in the investigated case, one would expect that the change in the inflow rate of the precursor would influence more the transport-limited regime.

In order to examine this fact, simulations are performed at a temperature of the reaction-limited regime using two different values for the mass inflow rate: (a) 2 sccm, which is the theoretical upper limit of the precursor's input quantity and (b) 1.85 sccm, which provides the best comparison between experiments and computational predictions in the Arrhenius plot. These simulations aim at the investigation of the phenomena occurring at the bulk of the reactor which yield lower deposition rates at the reaction-limited regime, when the inflow rate decreases. Figure 4.8 shows the distribution of the mass fraction of the DMEAA for the two different mass inflow rates applied in the model, at T_s=151^{o}C. It can be observed that the slight decrease from 2 to 1.85 sccm in the initial flow rate of DMEAA which enters the reactor leads to an important reduction, of the order of 17%, of its mass fraction that reaches the surface and this reduction yields the decrease of the deposition rate.

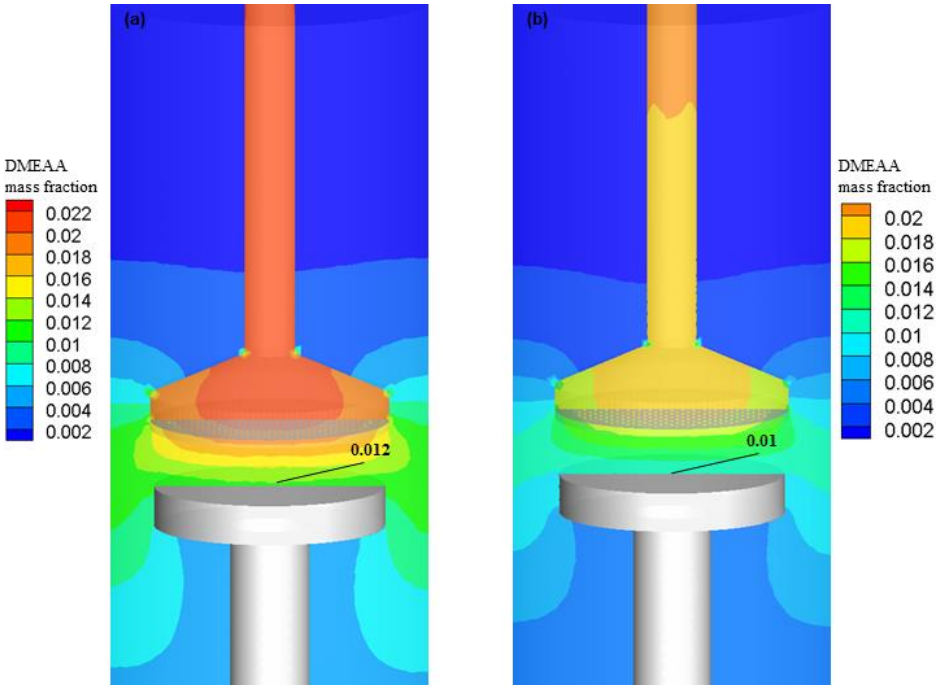

Figure 4.8: The distribution of the mass fraction of DMMEAA in the reactor when T_s=151^{o}C, and the applied precursor's mass inflow rate is (a) 2 sccm and (b) 1.85 sccm.

Despite the fact that at 151^{o}C the process proceeds at the reaction-limited regime, where the surface reaction rate does not depend on the inflow rate of the precursor, it should be considered that the applied chemistry model includes also a gas phase reaction, which may consume an important quantity of the precursor even if low temperatures are set. Figure 4.9, shows the temperature field (Figure 4.9a) and the rate of the volumetric reaction (Figure 4.9b) inside the reactor, for T_s=151^{o}C. Indeed, the volumetric reaction occurs already at 151^{o}C and at even lower temperatures inside the reactor. It is concluded that the volumetric reaction rate is such that consumes the precursor in the gas phase, preventing it to reach the wafer and participate to the surface reaction. This behavior is quantitatively illustrated in Figure 4.10a, which presents the evolution of the mass fraction of DMEAA as a function of the temperature profile and the volumetric reaction rate along the distance between the inlet of the reactor and the susceptor denoted by the green line in Figure 4.10b.

In particular, it can be seen from Figure 4.9 that at the inlet of the reactor where the temperature is 100^{o}C, the volumetric reaction has already taken place. As the mixture travels within the tube the rate slightly decreases, since the temperature at that domain is lower, but when the mixture approaches the susceptor, the rate increases and reaches its maximum. This behavior of the gas phase reaction rate has a direct impact on the mass fraction of DMEAA. In Figure 4.10, it is observed that the precursor mass fraction diminishes slowly until the mixture gets close to the susceptor. There, the temperature is higher, and as consequence the volumetric reaction rate increases abruptly and the DMEAA mass fraction drops steeply.

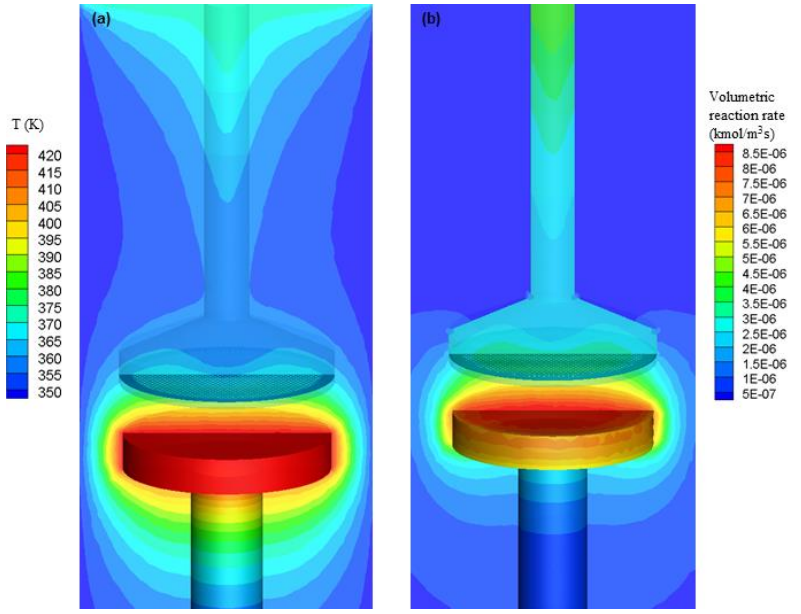

Figure 4.9: (a) The temperature distribution field and (b) the volumetric reaction rate influenced by the temperature field, when the applied surface temperature equals 151°C.

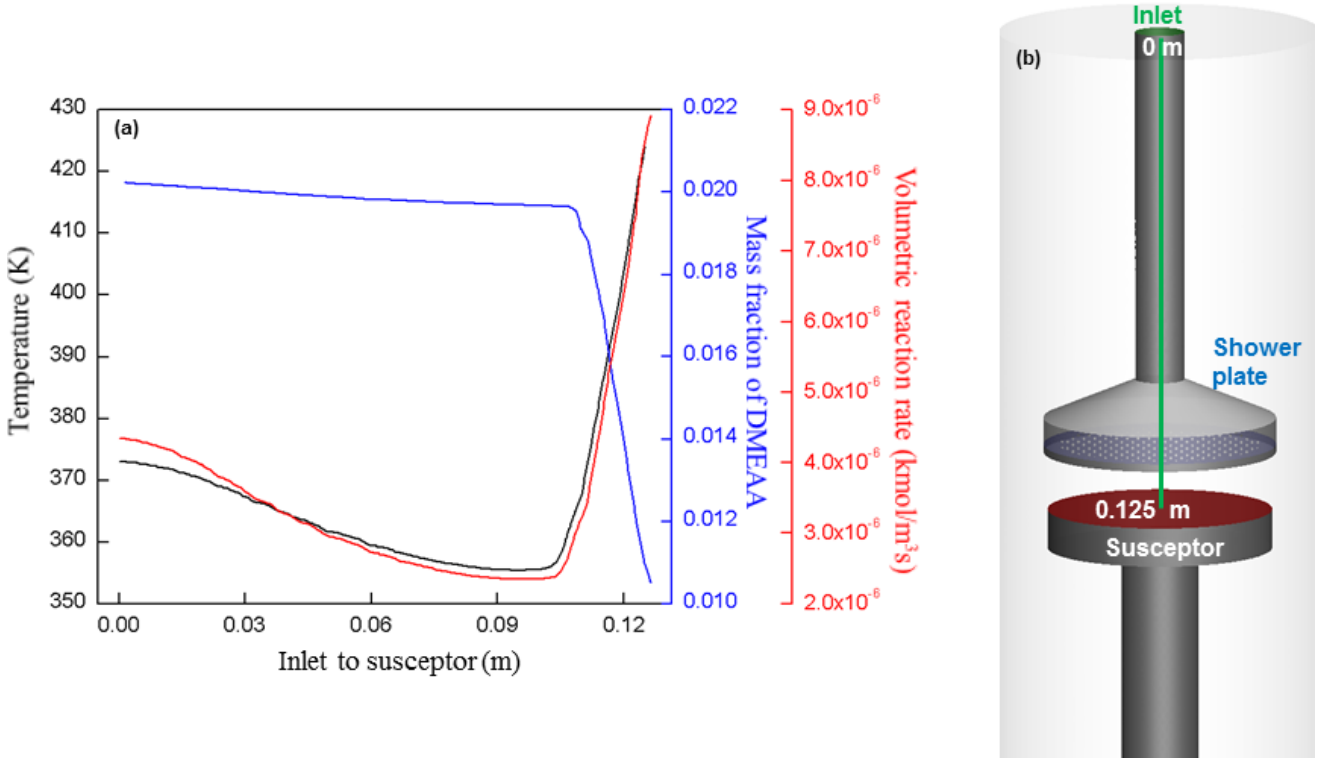

Figure 4.10: (a) The dependence of the DMEAA mass fraction (blue line) from the volumetric reaction (red line), according to the temperature profile (black line). (b) This dependence of the precursor's mass fraction is considered along the distance between the inlet of the reactor and its susceptor, as denoted by the green line. The process temperature is 151°C.

In Figure 4.11, the computed deposition rates along the susceptor radius are compared with the experimental measurements for T_s=139°C (Figure 4.11a) and T_s=151°C (Figure 4.11b). The computed deposition rate in Figure 4.11a is slightly overestimated compared with the experimental results. Since the deposition rate was low at this temperature, the color

change was gradual and therefore difficult to observe. Hence, there is a large uncertainty for this particular T_s. For T_s=151^{o}C the computed deposition rate is in satisfactory agreement with experiments in both the Arrhenius plot (Figure 4.7) and along the susceptor's radius (Figure 4.11b) as it lies within deviation intervals.

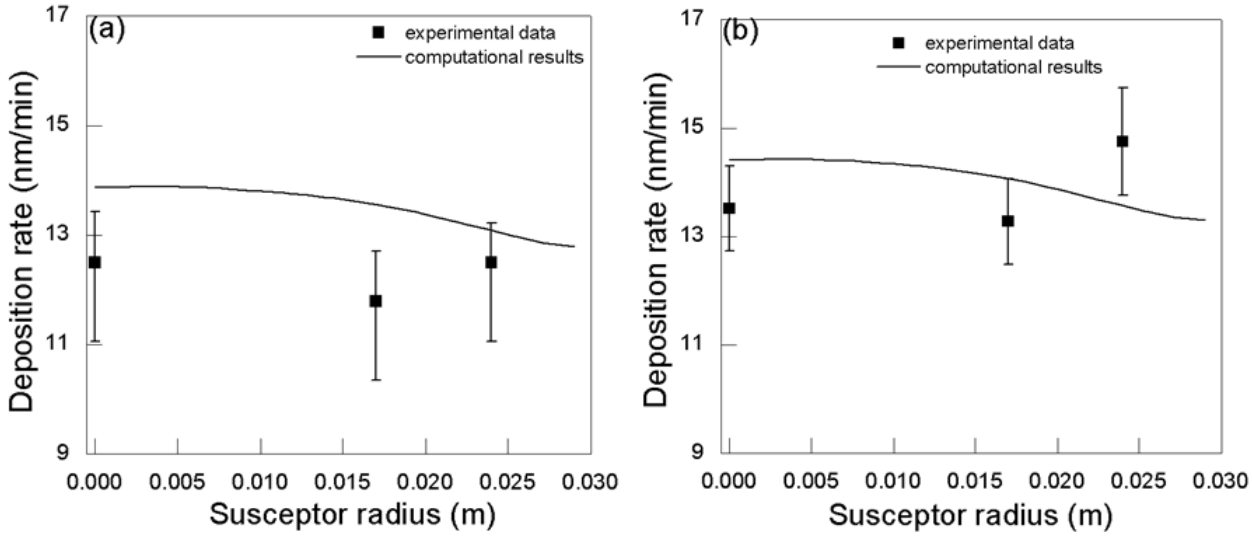

Figure 4.11: Deposition rate along the susceptor radius for (a) T_s=139^{o}C and (b) T_s=151^{o}C. Experimental measurements (squares) and computational predictions (lines) are shown.

In Figure 4.12, the deposition rate along the susceptor radius is presented for two temperatures of the diffusion-limited regime, i.e., 198^{o}C and 241^{o}C. In Figure 4.12a the applied computational model predicts sufficiently reliably the experimental deposition rate in terms of the measured order of magnitude. However, at 241^{o}C (Figure 4.12b), the model fails to predict the deposition rate distributed along the susceptor. This is not surprising since it does not predict the abrupt drop observed in the Arrhenius plot as well.

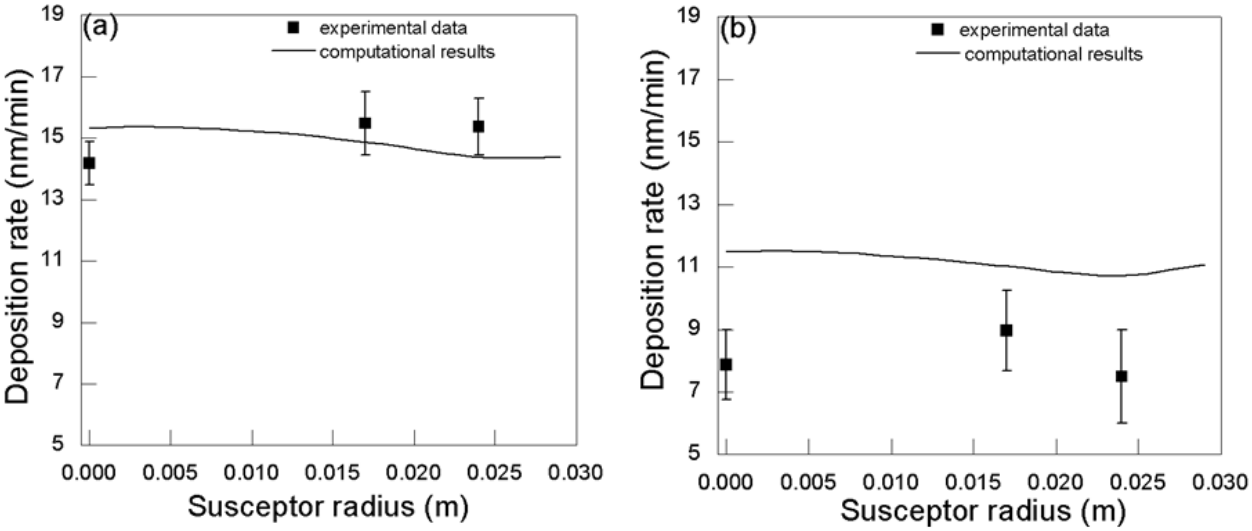

Figure 4.12: Deposition rate along the susceptor radius for (a) T_s=198^{o}C and (b) T_s=241^{o}C. Experimental measurements (squares) and computational predictions (lines) are shown.

The most common explanation is that the degradation rate of the precursor in the gas phase is high and thus, less precursor reaches the substrate (Xenidou *et al*., 2010). Other important reasons may be secondary competitive processes such as recombination of AlH_3 molecules to form dimer or polymer intermediates (Yun *et al*., 1998b) and the recombinative desorption of H_2 from the monohydride H_{ads} surface state which occurs at high temperatures on Si(100) (Nakajima *et al*., 2003; Robinson and Rodgers, 2000). The reaction mechanisms along with the global first order Arrhenius kinetics that are implemented in the described macroscopic model can incorporate none of these effects and consequently cannot predict abrupt changes in the deposition rate at high temperatures.

In both Figures 4.11 and 4.12, the trend of the distribution of the deposition rate as predicted by the model is opposite comparing to the experimental measurements. This is attributed to the computed distribution of the mass fraction of the precursor which is presented in Figure 4.13 for T_s=151^{o}C (Figure 4.13a) and T_s=198^{o}C (Figure 4.13b). In this figure, we can observe that moving from the center of the susceptor to its edge the mass fraction of the precursor decreases. Thus, less quantity is available for the surface reaction and consequently the deposition rate presents a slight decrease. However, at T_s=198^{o}C the mass fraction shows a slight decrease at the edge of the susceptor, which is also depicted in the behavior of the deposition rate at this temperature (Figure 4.12a). It is obvious that for the experimental results the opposite behavior of the precursor's mass fraction holds true; i.e., the quantity of the precursor which reaches the edge is more comparing to its concentration at the center of the susceptor. This discrepancy is due to the applied chemistry model which is not describing in full detail the decomposition path of DMEAA.

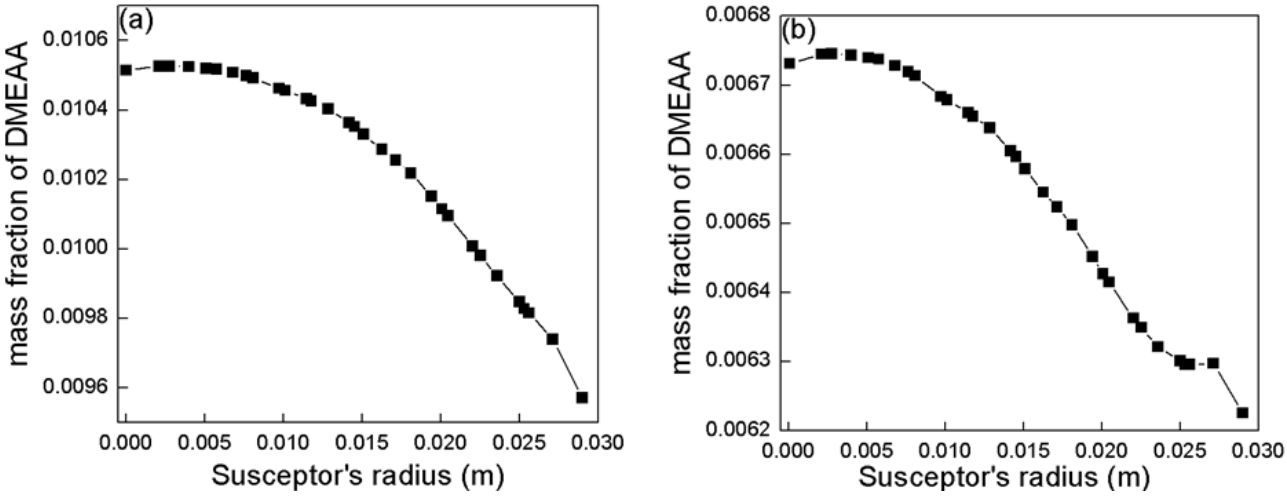

Figure 4.13: The distribution of the mass fraction of DMEAA along the susceptor as predicted by the model for (a) T_s=151^{o}C and (b) T_s=198^{o}C.

Different order kinetics might capture this trend as well as the steep reduction of the deposition rate at high temperatures. The extraction of such kinetics can be performed from feature scale simulations on complex surfaces (e.g. inside trenches) where the deposition rate can be calculated locally (e.g. at the bottom or the sidewall of the trench) and compared to

experimental deposition rates (Kokkoris *et al*., 2013). A different approach lies in the implementation of a more complicated chemistry model including a fully detailed reaction scheme for the decomposition of DMEAA and additional gas-phase reactions with their corresponding kinetic expressions. The two approaches might be complementary to each other; the detailed chemistry is investigated macroscopically for its accuracy and a primary fitting of the required parameters is performed. Feature scale simulations are carried out for the improvement of the fitting.

Still, the macroscopic approximation with the simple reaction pathway obtained by the literature and the implementation of the first order Arrhenius type kinetics presented so far it is not offset the reality and predicts with sufficient accuracy the experimentally measured deposition rates in the temperature range 139^{o}C-227^{o}C. In the latter range, common operating windows for the co-deposition process with elements such as Cu and Fe are located. Furthermore, this simple to be applied kinetics can be used as a reliable source for the simulation of the surface evolution comprising surface roughness by performing multiscale simulations.

4.3. Multiscale modeling of the process

The multiscale computational modeling presented here consists in a framework that links the macroscale level described in §3.1 and §4.2 with the nanoscale model presented in §3.2. The investigation is focused on the surface evolution and more precisely on the calculation of the surface roughness of an Al CVD film on an initially flat surface. Upon convergence of the macroscopic simulations, the mass fraction of the precursor is fed to the stochastic kMC algorithm and the simulation of the surface evolution starts.

4.3.1. Multiscale computations with the simple cubic lattice

As described in §3.2, the simple cubic lattice includes interactions among the five first neighbors of the examined atom – one below and 4 at the same layer – and the investigated surface is initially flat as shown in Figure 3.6. A parameter of crucial importance for the calculation of the adsorption rate (see Eq. 3.29 – §3.2.2.) is the sticking coefficient, s_0. For its calculation, a fitting procedure is adopted (Aviziotis *et al*., 2016); the computed deposition rate is compared with the corresponding experimental one, which remains unchanged regardless the simulated scale (see §3.2.3.), for each T_s and at each position of the substrates on the susceptor. This comparison provides a 4th degree polynomial relation between s_0 and T_s, presented in Eq. 4.5 and used during microscopic simulations. The fitting is performed within the Matlab software with a polyfit function procedure.

$$s_0 = -3.7316\times10^{-8}\times T_s^4 + 6.7438\times10^{-5}\times T_s^3 - 4.5612\times10^{-2}\times T_s^2 + 13.69\times T_s - 1538.6 \quad (4.5)$$

The sticking coefficient is a technical term which is used in previous literature works to illustrate the efficiency of the process towards film growth; it depends on all process

parameters (e.g., temperature, pressure, chemistry) and varies as a function of operating conditions (Vahlas and Blanquet, 1998). Thus, the implementation of such a relation for s_0 in the present model provides a correlation of this technical parameter with the operating temperature while implicitly integrating chemical reactions in our kMC algorithm. In other words, we simulate the CVD process by performing physical vapor deposition microscopic calculations.

The given dependence of s_0 on T_s is valid only for the temperature range used in this work, as the fitting is based only on experimental results obtained in this range. From Eq. 4.5, it comes out that the increase of the temperature results in the increase of the sticking probability according to a relation illustrated in Figure 4.14.

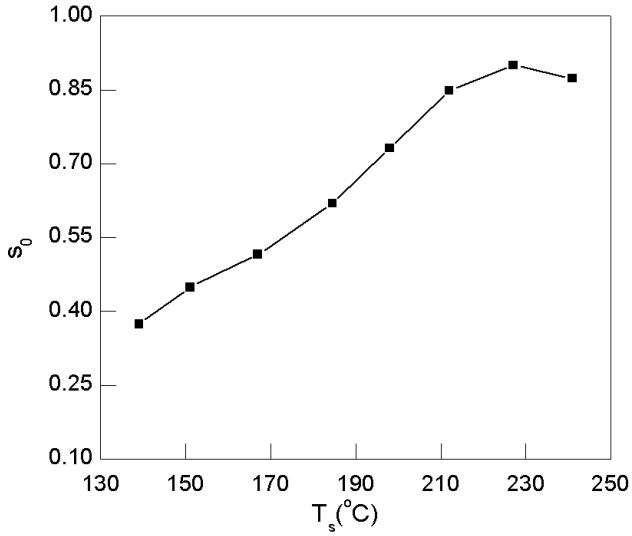

Figure 4.14: The dependence of s_0 on T_s , within the investigated temperature range.

This correlation has already been observed in the literature (Kim *et al*., 1991; Matsuda *et al*., 1990; Raupp and Cale, 1989; Yanguas-Gil *et al*., 2009) and can be explained by the low pressure (flux-limited regime) (Yanguas-Gil *et al*., 2009), by the positive apparent activation energy of the process (Raupp and Cale, 1989) and by the absence of a secondary species which would operate as an inhibitor for the reaction (Yanguas-Gil *et al*., 2009). It is also reported in Somorjai and Li (2010), that when molecules must dissociate in order to adsorb on a surface, s_0 may increase with increasing temperature, indicating that there is an activation energy for adsorption. This is suitable to the Al case presented in this work, where we assume that the sticking coefficient includes the dissociation of the precursor molecule and its adsorbed state and thus, it increases with increasing temperature.

The single bond energy, E, and the frequency factor, ν_0, needed for the calculation of the desorption probability are taken equal to 77.19 kJ/mol (Stumpf and Scheffler, 1996) and 10^{12} s^{-1} (Albao *et al*., 2013), respectively. For the definition of the migration energy, E_m, we implicitly assume that the initial Si surface is covered quickly by Al adatoms, thus, the migration energy corresponds to the diffusion of Al on Al and equals 6.465 kJ/mol

(Papanicolaou *et al*., 2001). Within the model, this migration energy accounts for both in-plane (intralayer) and across step edges (interlayer) diffusion. In such a way, it is implicitly assumed an Ehrlich-Schwoebel (ES) barrier equal to 0 (Aviziotis *et al*., 2016). The zero ES value is adopted also in previous works (Huang *et al*., 1998; Liu *et al*., 2002), where an atomistic simulator for the 3D growth of Al is applied and where a small effect has been observed for crossing Al (111) steps, except for very low temperatures. In the present study, the simulations performed between 139^{o}C and 241^{o}C, indicate that the number of surface migration events is negligible compared to adsorption events, especially at the lowest temperatures of this range (see Figure 4.16 below), thus validating the ES=0 assumption. However, in agreement with results reported for Al growth (Liu *et al*., 2002; Stumpf and Scheffler, 1996) and for Ag and Fe growth (Evans *et al*., 2006), at lower temperatures the rougher growth is attributed to the existence of a small ES barrier. The parameters applied to the stochastic algorithm are summarised in Table 4.3.

Table 4.3: Parameters applied for the kMC stochastic algorithm.

P_{total} (Pa)	1333.22
T_s (^{o}C)	139 – 241
Concentration of surface sites, C_{tot} (sites/m^2)	10^{19}
Single bond energy, E (kJ/mol)	77.19
Migration energy, E_m (kJ/mol)	6.465
Frequency factor, ν_0 (s^{-1})	10^{12}

4.3.2. Surface evolution and RMS roughness

The experimental deposition rates are used to fit the s_0 needed in the adsorption rate expression of the stochastic algorithm. The main purpose of the multiscale framework is the tailoring of the surface roughness through operating parameters of the reactor scale and in particular the T_s (the operating pressure could also be considered as a parameter that influences the roughness). Figure 4.15 presents the dependence of the RMS roughness on the temperature for both experimental measurements and computational predictions (Aviziotis *et al*., 2016). The RMS roughness of Al films deposited at the lower T_s (139^{o}C) is high (0.6 μm). RMS decreases with increasing temperature and shows a minimum value of 0.15 μm at *ca.* 198^{o}C. Above this temperature RMS seems stable. It has been reported that above 200^{o}C the RMS slightly increases (Yun *et al*., 1998a) but in our case such slight increase would lie within deviation intervals. Surface roughness is closely related to the change of the microstructure of the film. At a surface temperature below 150^{o}C, the Al deposit is not continuous and is composed of grains with a broad size distribution, resulting in high roughness. On the other hand, increasing T_s from 150^{o}C up to 227^{o}C results in smoother surface morphology with coalesced grains and decreasing open porosity with increasing deposition temperature. The computational model is close to the experimental data, since all the predicted RMS values, except for T_s=198^{o}C, lie within the intervals of deviations. Although a plateau is observed above 210^{o}C in the experimental data, the trend of the computational predictions is purely monotonous.

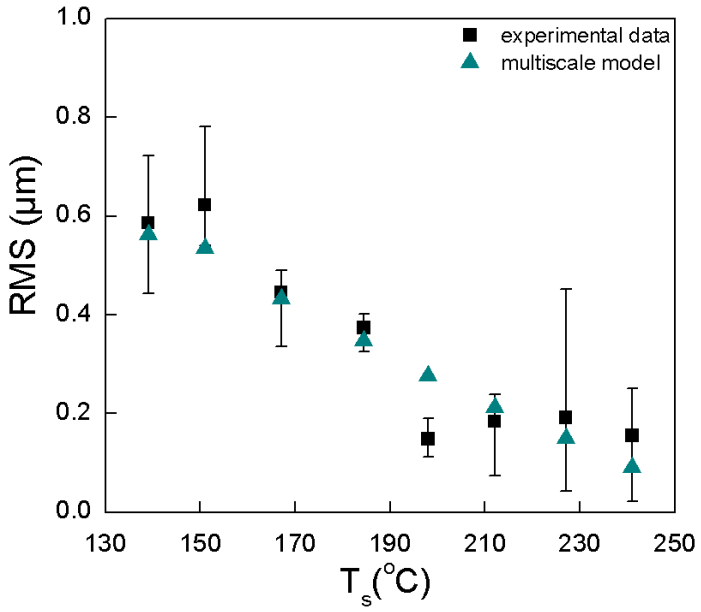

Figure 4.15: Evolution of RMS roughness with surface temperature, T_s. Experimental data (black squares) and multiscale predictions (cyan triangles) are shown. Error bars correspond to deviations from minimum and maximum experimental values.

In order to further understand these discrepancies, we analyze the occurrence of the mechanisms implemented in the kMC algorithm, i.e., adsorption, migration and desorption. Figure 4.16 shows the number of surface events – directly correlated with R-quantities (see Eq. 3.33 – §3.2.2.) – as a function of T_s (Aviziotis *et al.*, 2016). We observe that in all the temperature range, adsorption dominates the process, since the number of adsorption events is much higher than the corresponding number of migration and desorption events. Migration and desorption increase as temperature increases in conjunction with a steep decrease of adsorption.

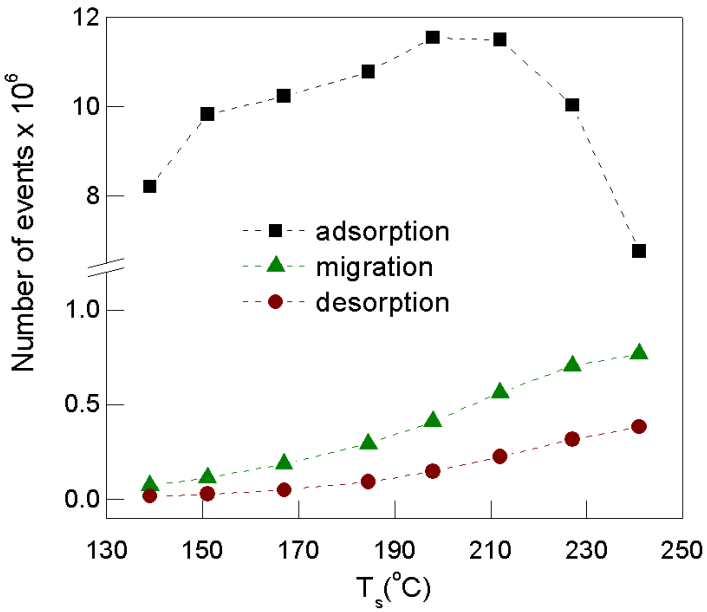

Figure 4.16: The number of surface events as a function of T_s. Adsorption, migration and desorption are illustrated by black squares, green triangles and brown circles, respectively.

Despite the predominance of adsorption, the impact of the migration on the RMS roughness is significant. In particular, it can be seen that as the number of migration events increases, the surface roughness decreases. This trend is monotonous, as opposed to the experimental data of Figure 4.15 which show a plateau. We suppose that after 210^{o}C, when the order of magnitude for migration and adsorption approach each other, migration is no longer negligible, hence the ES=0 assumption becomes questionable. The plateau in the experimental data of Figure 4.15 indicates that the smoothening of the surface is not effective, whereas it apparently occurs in the multiscale model. With a non-zero ES barrier, migration would not lead to such an efficient smoothening but rather to some aggregation at step edges, concurring to the increase of the simulated RMS. Then, the match between experimental and predicted RMS would improve.

The main impact of desorption is on the deposition rate; at high temperatures where it is observed that desorption events are increased, the Al deposition rate is reduced (Aviziotis *et al*., 2015; Xenidou *et al*., 2010).

Figure 4.17 shows the topography of the simulated surfaces (6a, 6b) and of the corresponding experimental surfaces (6c, 6d) characterized by interferometry (Aviziotis *et al*., 2016). The surfaces are processed at 151^{o}C (6a, 6c) and 227^{o}C (6b, 6d) and the surface heights are shown for each temperature.

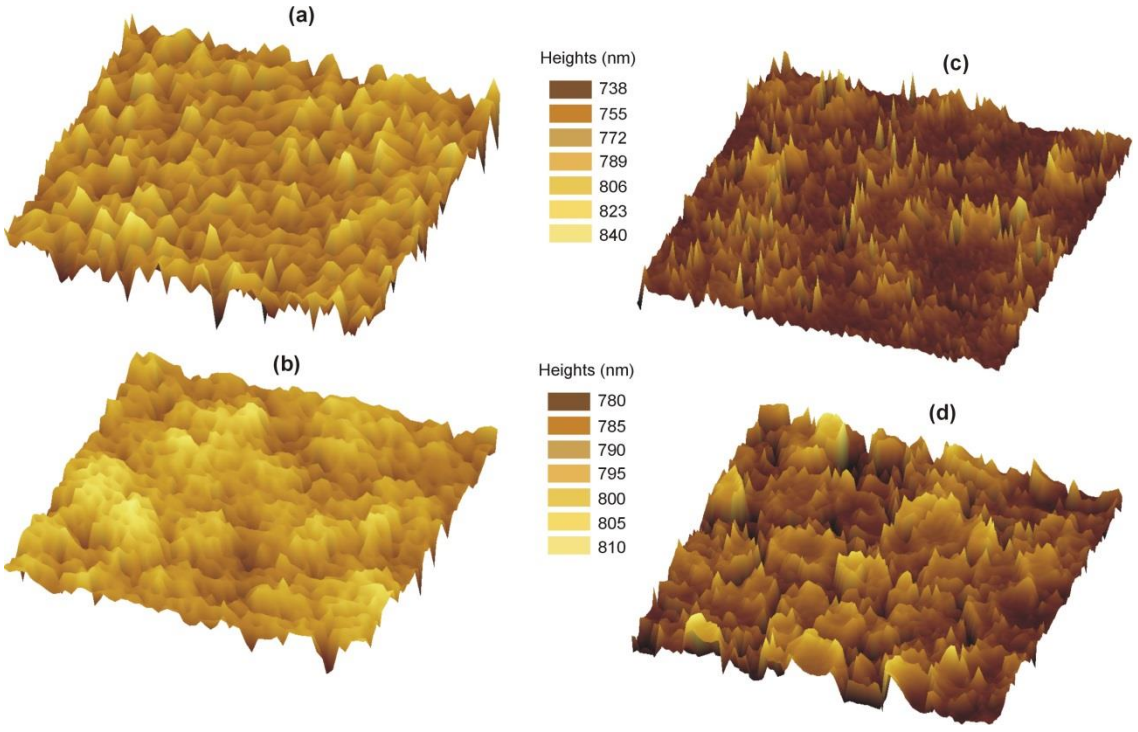

Figure 4.17: The morphology of the surface as predicted by the multiscale computational framework (a,b) and as obtained by optical interferometry (c,d) for 151^{o}C and 227^{o}C, respectively. Color scale is the same for both experimental and computational results which are at the same T_s.

Although we are performing coarse-grained and not atomistic simulations at the nanoscale level, we observe that there are similarities among the simulated and experimental

surfaces, such as spiky peaks at low temperatures and block-like configurations at higher temperatures. Indeed, at the low T_s both the experimental and the computed surfaces seem homogeneous with, however a significant difference between the minimum and the maximum heights resulting in high RMS values. On the other hand, at high T_s the surface seems rougher at a large scale but the small differences among the surface heights yield lower RMS values for both the experimental and the computed surfaces.

The accurate simulation of the surface microstructure and the control of RMS roughness through the variation of the operating conditions of the reactor open a new avenue for the control of the properties of the final film. In the next section an example is introduced with the tentative calculation of the electrical resistivity.

4.3.3. Estimation of the electrical resistivity

For the estimation of electrical resistivity, the extended Fuchs-Sondheimer model (FS model) (Timalshina *et al*., 2015) is applied which is described by the following equation:

$$\rho_0 = \rho_{bulk} \frac{3}{8} \frac{\lambda}{d} (1-p)(1+\alpha\omega^{\beta}), \tag{4.6}$$

where where $\rho_{bulk} = 2.7\ \mu\Omega.cm$ (Giancoli, 1995) is the resistivity of sheet Al, $\lambda = 5\ nm$ (Kanter, 1970) is the electron mean free path in Al films, d is the thickness of the film and p is the specularity parameter ranging from 0 (completely diffuse) to 1 (specular scattering) (Timalshina *et al*., 2015). The effect of RMS roughness is denoted by ω ($\omega = \sqrt{RMS}$) and α, β are additional empirical parameters that can be adjusted to fit the data (Timalshina *et al*., 2015). The FS model is has been tested to calculate accurately the resistivity for film thicknesses in the range 20 nm – 500 nm (Timalshina *et al*., 2015). Despite the high film thickness (*ca.* > 500 nm) of the Al films, this particular model is chosen because it takes into account the RMS roughness explicitly.

Figure 4.18 presents the measured (red spheres) and the computed (black spheres) electrical resistivity (Aviziotis *et al*., 2016). The arrow on the (x,y) plane corresponds to a perfect match between experimental and simulated RMS and points towards the increase of the roughness. The red and black points are projections on the (y,z) plane and along with the blue curve are guides to the eye for the evolution of the electrical resistivity with increasing roughness. It can be seen that electrical resistivity increases with increasing roughness from 10 μΩ.cm at RMS 0.15 μm to *ca.* 80 μΩ.cm at RMS 0.6 μm. These values and the observed evolution of the electrical resistivity are attributed to the increased scattering of the rough surfaces and to their significant contribution to the resistivity (Machlin, 2006). Moreover, the propagation of conduction electrons is inhibited by grain boundaries, therefore, the latter may contribute a significant excess resistivity in polycrystalline Al films (Francombe, 1988). Finally, O contamination within the film can lead to higher resistivity values. Such

dependence of the electrical resistivity on the RMS roughness has also been reported for other materials (Tang *et al*., 2003; Timalshina *et al*., 2015).

As previously mentioned, the extended FS model (Eq. 4.8) is applied to estimate the electrical resistivity of Al films, while the thickness and the RMS roughness are provided by multiscale simulations. Concerning the specularity parameter, we assume a completely diffuse scattering from both the top and bottom surfaces of the Al film, that is $p = 0$, a statement that holds true for surfaces with high roughness (Kanter, 1970). Finally, by fitting the estimated resistivity to the experimental data, we find $a = 30, \beta = 5.6$. The physical meaning of these parameters is not clear (Timalshina *et al*., 2015) and their fit may not be unique. However, we privilege the accuracy of the computed RMS values in order to have a reliable estimation of the electrical resistivity. The estimation of the electrical resistivity with the extended FS model appears to be fairly good with regard to the corresponding experimental measurements and both datasets present the same trend. As roughness decreases, the discrepancy between experimental data and results provided by the multiscale model increases. This is attributed to the fact that in our estimations we do not incorporate any information for grain boundaries or contamination which may become predominant.

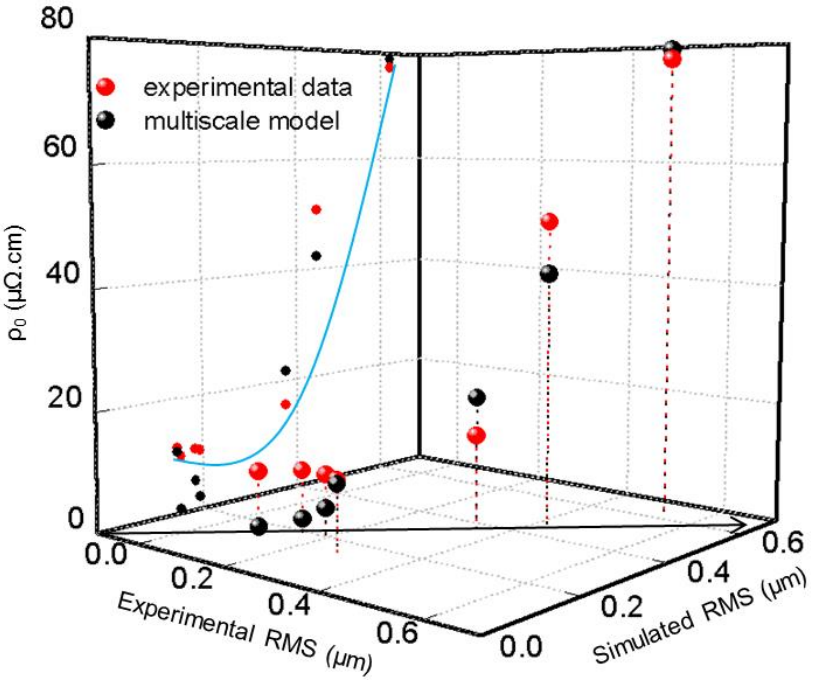

Figure 4.18: The measured (red spheres) and estimated with the multiscale model (black spheres) electrical resistivity of Al films as a function of the experimental and the simulated RMS roughness.

These results about electrical resistivity illustrate the importance of controlling the surface roughness of a developed film, since it impacts the final properties. In this case and by assuming that roughness of crystalline materials often corresponds to the existence of grain boundaries, it may account for the increase in electrical resistivity through grain boundaries scattering of the electrons.

Summary-Conclusions

The CVD of Al from DMEAA is experimentally and a computationally investigated with the aim to correlate the evolution of both the deposition rate and the microstructure of the films with the deposition temperature within the investigated temperature range between 139^{o}C – 241^{o}C. The obtained insight and correlation allow the tuning of the operating conditions for the co-deposition and the sequential deposition of Al with Fe.

Deposition from DMEAA results in pure Al films without any heteroatoms contamination such as C and N which are part of the precursor molecule, or O from the residual partial pressure in high vacuum. Increase of the deposition temperature results in Al films with increased density and decreased surface roughness. It also results in films with higher uniformity and better surface coverage. The incubation time which is taken into account for the determination of the net deposition rate, is high (*ca.* 310 s) at the lowest deposition temperature and it linearly decreases to 48 s at the highest temperature. This behavior of the initiation of the deposition process may be attributed to the different sticking coefficient of the precursor on the substrate and to accelerated desorption of the adsorbents at higher temperatures.

The Arrhenius plot of the process can be divided in three regimes. The first one lies within the temperature range 139^{o}C – 185^{o}C and contains a reaction-limited component where the surface reaction impacts the process and where the deposition rate increases with increasing temperature. Above 185^{o}C and up to 227^{o}C, the process is controlled by the diffusion of the reactants through the boundary layer to the surface. In the diffusion-limited regime, Al deposition rate has a maximum value of *ca.* 15.5 nm/min at 185^{o}C and then remains relatively stable, with a slight decrease to *ca.* 13.5 nm/min at 227^{o}C. Finally, above 227^{o}C the deposition rate of Al abruptly decreases, attributed to the high decomposition rate of the precursor in the gas phase which prevents the reactants to reach the surface.

A computational model based on the continuum mechanics is built for the macroscopic simulation of the process in order to investigate the various phenomena occurring in the CVD reactor. For the gas phase and the surface chemical reactions, first order Arrhenius kinetics are implemented which are based on the obtained experimental results. In particular, the activation energy of the surface reaction is taken from the slope of the reaction-limited regime of the experimental Arrhenius plot, whereas the two pre-exponential factors required in the kinetics expressions are fitted on the experimental results. The activation energy for the gas phase reaction is provided by the literature. Two different mass inflow rates of the precursor are used, that is, the upper limit value corresponding to the thermodynamic equilibrium in the bubbler and infinite conductance of the gas lines and a lower value provided by the realistic assumptions that the gas – liquid interactions in DMEAA bubbler are not fully efficient, part of the precursor is degraded in the lines before entering the reactor, and that the conductance of the gas lines is not infinite.

The results from the computational analysis show satisfactory agreement compared to the experiments, especially within the range 139^{o}C – 227^{o}C. We observe that the decrease of the precursor mass inflow rate improves the deposition rates obtained at the reaction-limited regime, despite the fact that at this temperature range the surface reaction dominates the process. Hence, it should be independent on the quantity of reactants.. However, the applied chemistry model also includes a gas phase reaction which consumes an important quantity of the precursor even at low temperatures. Indeed, the dependence of the gas phase reaction rate on the temperature is presented and it is illustrated that even at 100^{o}C the volumetric reaction occurs. Thus, by considering also that the temperature increases as the surface of substrate is approached, the reaction rate of the gas phase reaction becomes important in the reaction-limited regime, the quantity of the precursor on the surface reduces and the deposition rate decreases, approaching better the experimental one.

On the other hand, above 227^{o}C the model fails to predict the experimental deposition rate and a large discrepancy between the model and the experiments is shown. The main reason for this failure is the high gas phase degradation rate of the precursor molecule. The global chemical reactions and the first order Arrhenius kinetics implemented in the macroscopic model cannot incorporate additional effects such as the formation of intermediate species and, consequently, the model fails to capture the abrupt decrease of the deposition rate at high temperatures. Further investigation is needed in order to develop a more accurate model which will be valid in the whole temperature range. This investigation can be done by applying a more detailed chemistry pathway and by performing microscopic simulations on complex surfaces for the local calculation of the deposition rate. This research is currently under investigation. However, the presented macroscopic framework is valid in the temperature range 139^{o}C – 227^{o}C, where co-deposition requirements can be met.

Upon the computational analysis at the macroscopic level, a multiscale framework is developed for the simulation of the surface evolution and more specifically the calculation of the RMS roughness and the electrical resistivity of Al films produced by the CVD process. In particular, for the two parameters the values obtained by performing multiscale computations are compared with those provided from experiments. Multiscale computations allow fetching from the surface of the growing film the information needed to compute the aforementioned properties.

The multiscale framework links the macroscopic 3D model of the reactor with a stochastic kinetic Monte Carlo algorithm through the mass fractions of the precursor on the vicinity of the substrate and with the assumption that the deposition rate remains unchanged regardless the scale of simulation. The outcome from the macroscopic model is fed to the nanoscale model which simulates the evolution of the film and calculates its surface roughness and through the latter, its electrical resistivity. The chemical information for any reactions of the precursor such as its decomposition on the surface, are incorporated in the sticking coefficient. For the latter, a temperature dependent function is implemented by fitting

experimental deposition rates at various temperatures and at various positions on the susceptor.

The obtained results from the multiscale model are compared with the corresponding experimental values of Al films processed in the same conditions. The RMS roughness decreases with increasing the process temperature from 0.6 μm at 139^{o}C to 0.15 μm at 198^{o}C. The calculated RMS values lie within the deviations of experimental measurements resulting in a very good agreement between the experiments and the predictions obtained by multiscale simulations.

However, above 210^{o}C the experimental RMS shows a plateau which is not captured by the multiscale framework. The latter presents a monotonous decrease of the roughness with increasing temperature. Within all the temperature range, adsorption dominates the process, while desorption and migration events are few. Temperatures increase results in the increase of migration, which despite the predominance of the adsorption has a great impact on the RMS. This effect is due to the fact that as temperature increases above 210^{o}C, migration is no longer negligible and the ES=0 assumption becomes controversial. Incorporating a non-zero ES barrier in the multiscale simulations, migration would lead to a possible aggregation at step edges with a successive increase of the RMS, rather than to a smoothening of the surface which is observed by the presented results of multiscale modeling.

The electrical resistivity of the films increases with increasing surface roughness from 10 μΩ.cm at RMS 0.15 μm to *ca.* 80 μΩ.cm at RMS 0.6 μm, mainly due to the increased scattering caused by rough surfaces and to higher grain boundaries density which results in the entrapment of electrons. The behavior of the electrical resistivity is quantitatively reproduced when the calculated resistivity is correlated with the simulated RMS of the films.

The developed multiscale computational framework can be implemented to perform computational analysis for the simulation of similar surface phenomena taking into consideration the formation of more complex structures, such as the formation of dimers and trimmers. The incorporation of chemical reactions at the nanoscale and the consideration of the exact physical crystallographic structure (*fcc* for Al) of the developed material within the nanoscale algorithm is expected to enable simulation of more complex processes and surface features such as island formation and grain boundaries.

Chapter 5: Investigation of the MOCVD of Fe from $Fe(CO)_5$: Experiments and simulations

In this chapter, the MOCVD of iron is presented from an experimental and a computational point of view. Experimentally, depositions are carried out on Si substrates, in a given temperature range to determine the Arrhenius plot of the process. Characterizations of the films are performed by means of SEM, EPMA, XRD and mechanical profilometry to determine the structure and the composition of the Fe films, their microstructure and their roughness. The modeling of the process at the macroscopic and the surface level is based on the experimental MOCVD process and aims at the investigation of the mechanisms and kinetics involved as well as at the simulation of the surface nanomorphology and the calculation of the roughness. The combined experimental and computational investigation of the MOCVD of Fe aims at the establishing of a robust process with fully defined parameters for its application to the co-deposition and sequential deposition with Al.

5.1. Experimental aspects

Deposition of Fe films from $Fe(CO)_5$ is performed in the reactor described in Chapter 2 (see §2.1.1.). The aim of this study is to investigate the evolution of the deposition rate as a function of operating conditions, such as temperature, pressure, and deposition duration. The determination of the deposition rate in the different temperature regimes combined with the corresponding investigation of the MOCVD of Al, allows identifying the proper operating windows for the co-deposition and/or the sequential deposition of the two metals which is the central goal of this work. At the same time, we aim at getting insight in the microstructural characteristics of the films and in their evolution within the investigated temperature range, which strongly affect the final properties of the film.

$Fe(CO)_5$ is supplied by Sigma-Aldrich and Fischer Scientific and is used as received. It is maintained with a cryostatic regulator at -18^{o}C permanently, i.e., close to the freezing point of the compound (-20^{o}C), where its degradation is limited. It is worth recalling that vapor pressure increases with time, indicating degradation of the precursor through release of CO ligands. The temperature of -18^{o}C during the deposition experiments corresponds to a $Fe(CO)_5$ vapor pressure of 1.88 Torr, according to Eq. (1.2) (see §1.5.2. & §2.1.1.5.).

10 x 10 x 1 mm^3 Si(100) flat coupons are used as substrates. They are prepared according to the protocol described previously (see §2.1.2.). In each experiment, five substrates are placed at different radial positions of the susceptor, as presented in Figure 5.1. The aim is to observe the variations of the deposition rate at different radial positions.

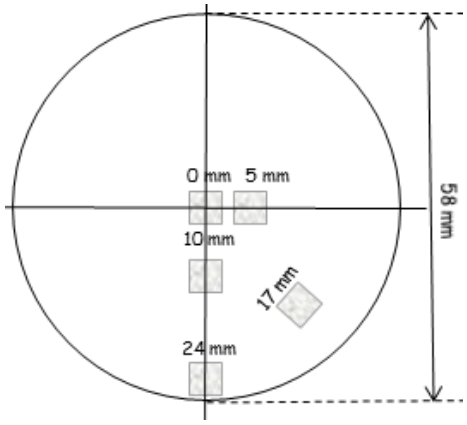

Figure 5.1: A schematic presentation of the location of the Si substrates on the susceptor during the MOCVD of Fe from $Fe(CO)_5$.

Independent experiments are performed at 13 different substrate temperatures, T_s, in the range 130^{o}C – 250^{o}C (surface temperature is calibrated with a thermocouple attached to the surface in deposition conditions – see §2.1.1.2.). For the investigation of the dependence of the deposition rate on T_s the total pressure of the reactor, $P_{reactor}$, is fixed at 10 Torr. The lines and the walls of the reactor are maintained at room temperature. Pure nitrogen (N_2, 99.998%, Air products) is fed in the reactor chamber through a dilution line and a carrier line

passing through the precursor; both flow rates are regulated by mass flow controllers (see §2.1.1.4.) at $Q_{N_2,dilution}$ =302 sccm and $Q_{N_2,carrier}$ =3 sccm, respectively, resulting in a total flow rate of N_2 equal to Q_{N_2} =305 sccm.

The maximum inflow rate of the precursor, Q_{prec}, in the reactor chamber is calculated by the formula proposed by Hersee and Ballingal (1990) (see Eq. 2.1 – §2.1.1.5.). According to this formula, for a saturated vapor pressure of $Fe(CO)_5$ of 1.88 Torr at -18^{o}C, the maximum inflow rate of the precursor in the process chamber, equals 0.69 sccm. Experiments are carried out in the above fixed conditions, at the T_s reported in Table 5.1.

Table 5.1: Experimental conditions adopted for the CVD of Al from DMEAA.

#Experiment	Exp1	Exp2	Exp3	Exp4	Exp5	Exp6	Exp7	Exp8
T_s (^{o}C)	130	140	150	160	170	180	190	200
Fixed conditions	T_{walls}=25^{o}C, T_{lines}=25^{o}C, $P_{reactor}$=10 Torr, Q_{N_2} =305 sccm, Q_{prec} = 0.69 sccm, Duration = 1h							

Table 5.1 (cont'd): Experimental conditions adopted for the CVD of Al from DMEAA.

#Experiment	Exp9	Exp10	Exp11	Exp12	Exp13
T_s (^{o}C)	215	223	232	240	250
Fixed conditions	T_{walls}=25^{o}C, T_{lines}=25^{o}C, $P_{reactor}$=10 Torr, Q_{N_2} =305 sccm, Q_{prec} = 0.69 sccm, Duration = 1h				

The deposition duration for all experiments is 1 h, including the incubation time. The incubation time is estimated by visual observation of the substrate surface through the windows of the reactor. The color transition in this case is from reflecting grey (Si surface) to diffuse grey or black (Fe surface). Figure 4.2 shows the evolution of the incubation time as a function of T_s. A significant delay is observed at the lowest T_s (130^{o}C), where the incubation time equals 1800 s. It seems that, at this T_s, the energy provided from the heating to the substrate is not enough to start the nucleation of the film. The net deposition duration is 30 min and as it will be shown the deposition rate is much less comparing to other temperatures.

The incubation time steeply decreases from 1800 s at T_s=130^{o}C to 300 s at T_s=140^{o}C. It further decreases to 150 s for T_s up to 160^{o}C. From T_s=170^{o}C and above, the incubation time is almost negligible, as it remains below 50 s. The observed decrease of the incubation time with increasing the deposition temperature in the low to moderate temperature range, i.e. up to 160^{o}C, followed by stabilization at high deposition temperatures is in agreement with the trend observed in the MOCVD of Al (see Chapter 4) and with observations reported in the literature, discussed therein. It is recalled at this point that the incubation time is only used here to determine the net experimental deposition duration. The rough optical estimation of this parameter may lead to the overestimation of the deposition rate, since what it is assumed to be incubation is actually the upper limit of the incubation time. Such overestimations in the measurements of the deposition rate are included in the error bars (see next Figure 5.3).

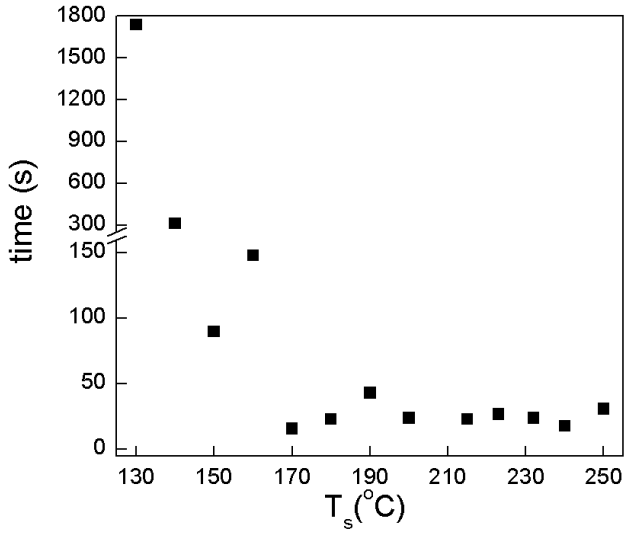

Figure 5.2: The incubation time as a function of the substrate temperature, T_s.

Figure 5.3 is the Arrhenius plot of the process. The different regimes of the plot are easily distinguishable. The deposition rate is continuously increasing with increasing T_s up to T_s=180°C, implying a kinetically-limited regime. A transition regime is observed in the range 180°C – 200°C, where both surface processes and transport phenomena impact the process. In this range, the deposition rate reaches a plateau and a maximum value at 200°C. At higher T_s, transport phenomena dominate the process and the deposition rate decreases. The Arrhenius plot is in agreement with results presented in Carlton and Oxley (1965), where it is reported that below 200°C the deposition rate is very sensitive to temperature and it increases with increasing T_s. It is also reported that above this temperature the rate remains relatively unaffected. In more recent works (Lane and Wright, 1999; Lane *et al*., 1997; Senocq *et al*., 2006; Zhang *et al*., 2016), it is reported that above T_s=200°C the Fe deposition rate is strongly decreasing, similar to our observations. In Lane *et al*. (1997) and Lane and Wright (1999), the sharp decrease is attributed to an etching reaction of the film caused by the CO ligands which are liberated from the thermal decomposition of the $Fe(CO)_5$ precursor. Additionally to that, the sharp decrease of the deposition rate can be also attributed to the increased homogeneous gas phase reactions of the reactants (Senocq *et al*., 2006). However, as shown in Zhang *et al*. (2016) the etching reaction is thermodynamically unfavorable under the low pressure CVD conditions. Thus, the drop of the deposition rate is attributed to the poisoning of the surface from the CO ligand.

In absolute values, the Fe deposition rate is in agreement with the results reported in Lane *et al*. (1997) and Lane and Wright (1999), where same deposition conditions are applied. Comparing to the work of Zhang *et al*. (2016), the thickness of Fe films presents a threefold increase due to the longer duration of the deposition experiments (60 min comparing to 10 min in Zhang *et al*. (2016)) and to the lower temperatures. The same dependence of the deposition rate on the surface temperature is observed during the MOCVD of Ni from $Ni(CO)_4$ (Fau-Canillac and Maury, 1994; Lane *et al*., 1997), which belongs to the same family of carbonyl precursors as the $Fe(CO)_5$.

The activation energy of the surface process is 27.9 kJ/mol, as estimated from the slope of the Arrhenius plot in the reaction-limited regime. This value is in good agreement with the value of 26±2 kJ/mol which is reported in Jackman and Foord (1989) for the complete dissociation of the $Fe(CO)_5$ molecule on Si substrates.

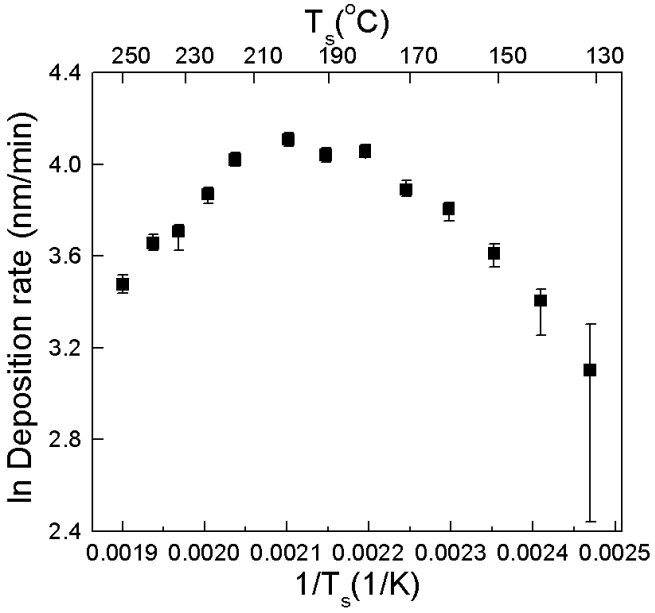

Figure 5.3: The Arrhenius plot of the MOCVD of Fe from $Fe(CO)_5$ on Si substrates. The deposition rate increases with T_s to a maximum value at T_s=200°C and then, is continuously decreasing.

From the comparison between the Arrhenius plot of Fe and Al, it can be seen that the deposition rate of Fe is higher (see Figure 4.3 in §4.1.) within the investigated temperature range. This may result in an *a priori* difficulty for the co-deposition and the sequential process, since an Al-rich film is required for the formation of the targeted $Al_{13}Fe_4$ approximant phase. For this reason, we experimentally investigate the effect of operating conditions other than temperature, such as the pressure and the deposition duration, which may result in the reduction of the Fe deposition rate. The effect of $P_{reactor}$ and deposition duration on the deposition rate are examined at constant T_s=180°C. This particular temperature is chosen as it lies at the vicinity between the reaction-limited and the diffusion-limited regimes, where diffusion phenomena are affected by the change of the pressure.

The results of this investigation are presented in Figure 5.4. Figure 5.4a shows an eightfold decrease of the deposition rate from 58 nm/min to 7 nm/min when $P_{reactor}$ is increased from 10 Torr to 40 Torr. This behavior can be explained by the reduced diffusion of the gas phase to the surface, since the mass diffusion coefficient decreases with increasing pressure (see Eq. 3.7 - §3.1.3.) and to the elevated decomposition rate of the precursor in the gas phase. The latter not only reduces the concentration of the precursor which is available for the surface reaction but also leads to contamination of the films by the liberated CO ligands which reduces the free surface sites. A similar trend has been observed in Zhang *et al*. (2016), where the increase of the pressure is achieved by adding CO in the input gas mixture and in Fau-Canillac and Maury (1994) for the deposition of Ni from $Ni(CO)_4$.

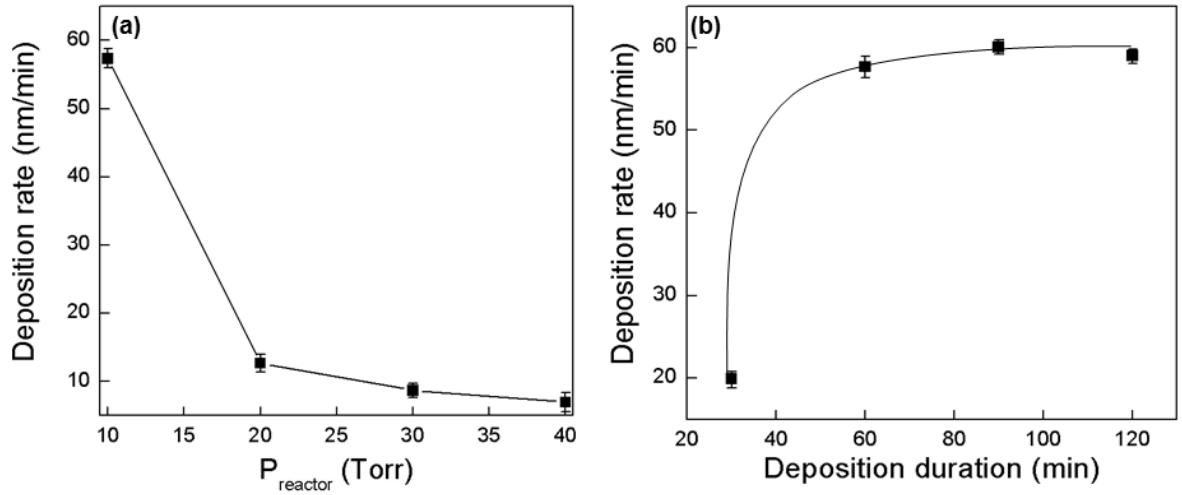

Figure 5.4: The dependence of Fe deposition rate on pressure and deposition duration. The lines show the trend of the deposition rate.

Figure 5.4b shows the deposition rate as a function of the deposition duration. It can be observed that at low deposition times of 30 min the deposition rate is low, 20 nm/min, and it abruptly increases, in an almost threefold manner, to *ca.* 58 nm/min when the duration is doubled. Further increase of the deposition duration shows no effects on the deposition rate, as it is stabilized at 60 nm/min. The increase of the CO concentration could be a possible explanation for this. As the duration of the deposition increases, the CO ligands produced by the decomposition of the $Fe(CO)_5$ increase and poison the surface in such a way that after a given time the surface saturates and the deposition rate reaches a limited value. This fact can be confirmed by similar results reported in Zhang *et al*. (2016).

The overall behavior of the deposition rate as a function of the temperature and the pressure, as well as the chemical reactions involved in the deposition of Fe from the pentacarbonyl compound are modeled at the macroscopic level, below (see §5.2).

The microstructure of the Fe films deposited in this temperature range is observed by SEM in the secondary electrons mode (see §2.2.1.). It is presented in Figure 5.5, where surface micrographs are shown for 130^{o}C, 150^{o}C, 170^{o}C, 190^{o}C, 200^{o}C and 240^{o}C and cross sections are shown for T_s=190^{o}C and 200^{o}C. Deposition at the lowest T_s (Figure 5.5a) show scattered grains on the surface and form films with poor uniformity and no continuity. As opposed to this case, at T_s=150^{o}C (Figure 5.5b) faceted Fe grains start to form and the density of the film increases because of grains coalescence. The size of the grains varies, as it is shown in Figure 5.5b, where some larger grains emerge (bright contrast). When the temperature is increased to 170^{o}C and then to 190^{o}C (Figures 5.5c and d), angular and sharply-faceted grains are formed with apparently homogeneous size. The high density of the film and the sharply-faceted grain morphology are confirmed from the cross section of Figure 5.5g. However, at T_s=200^{o}C (Figure 5.5e) the angular and faceted grain is attenuated, as it is gradually replaced by an acicular morphology with further increasing temperature, to e.g. T_s=240^{o}C (Figure 5.5f). The acicular morphology may result in the increase of the film

porosity, especially for temperatures higher than 200°C but on the other hand, roughness decreases (see §5.4.2.).

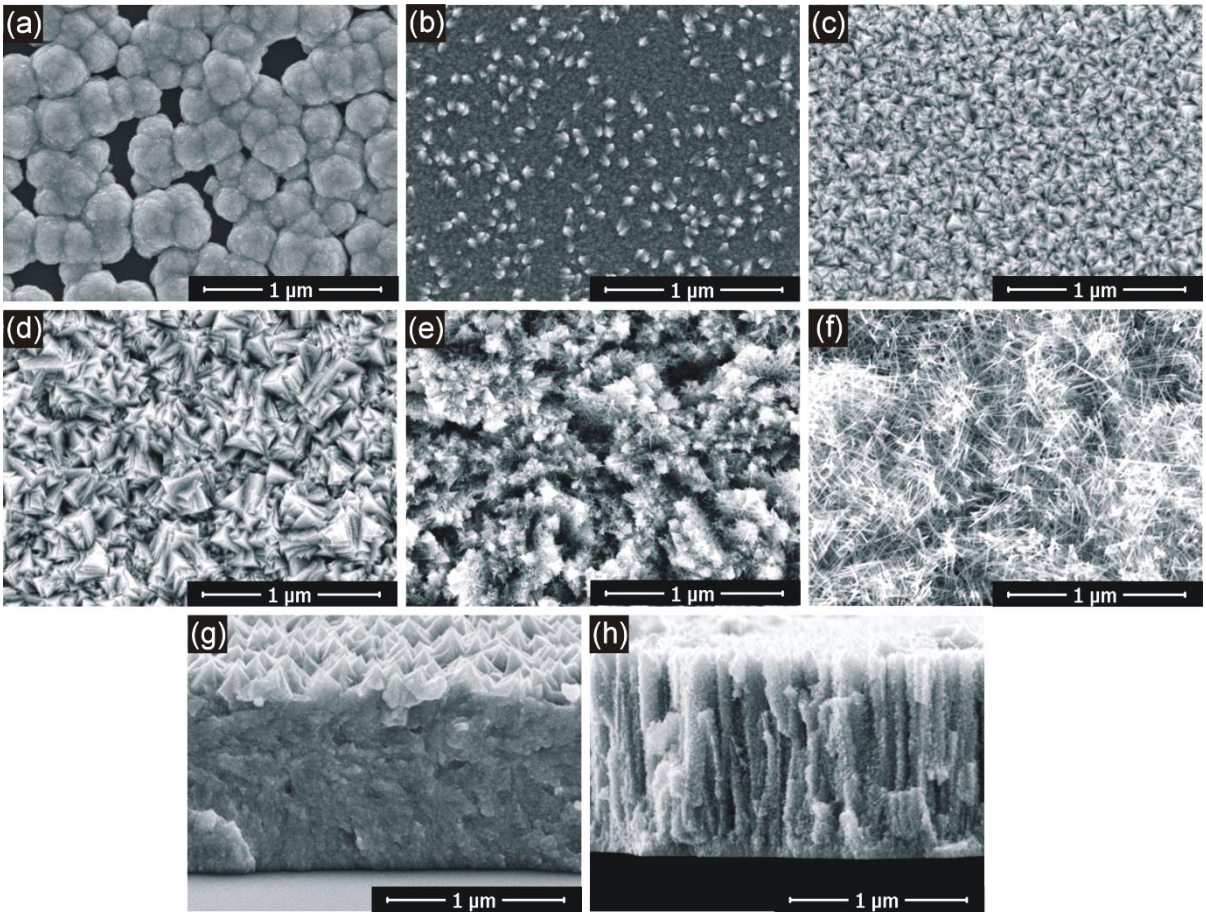

Figure 5.5: Surface SEM micrographs of Fe films deposited at 130°C (a), 150°C (b), 170°C (c), 190°C (d), 200°C (e) and 240°C (f). Additional cross sections images are shown for T_s=190°C (g) and 200°C (h).

The cross section of Figure 5.5h at T_s=200°C, shows a detached film, with columnar morphology and reduced faceting. Cross sections above 200°C are not observed, since we tend to define the common operating window for the co-deposition of Fe with Al in the range 130°C – 200°C (see also Chapters 4 &6). However, to complete the SEM analysis, we cite previous works (Delsol *et al*., 2005; Zhang *et al*., 2016), where it is reported that films deposited above 200°C or at higher temperatures may present a smooth and lamellar morphology.

Measurement of the mass gain, assuming Fe bulk density, gives an estimation of thickness of 3.4 μm (±0.1 μm) and 3.7 μm (±0.1 μm) for 190°C and 200°C, respectively, to be compared with SEM measurements of 3.5 μm (±0.05 μm) and 4.0 μm (±0.05 μm, respectively. Comparison of the film thickness estimated by mass difference and measured on the SEM cross section reveals that, the results are similar, for the case of a conformal and dense film (Figure 5.5d) while they present small discrepancies for the film of the lower density (Figure 5.5f). This can be explained by Figure 5.6 which presents SEM surface micrographs at higher magnifications for films processed at 190°C and 200°C. It can be seen

that at 190°C (Figure 5.6a) films present reduced porosity, whereas at 200°C (Figure 5.6b) the trend for porosity is opposite.

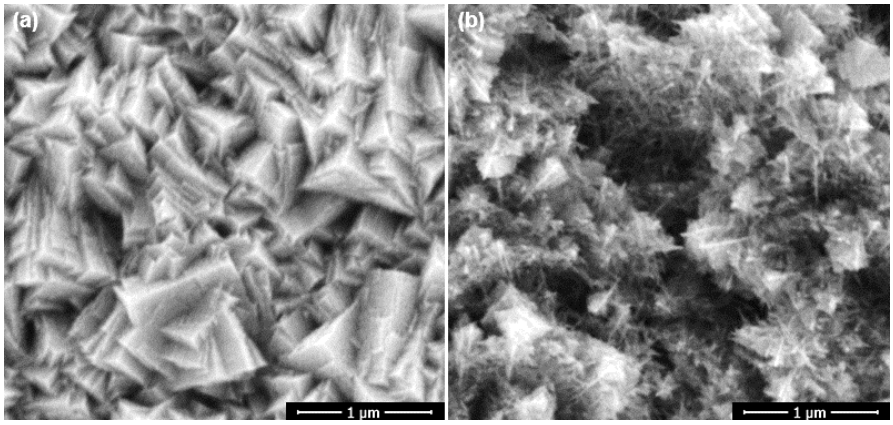

Figure 5.6: Magnified surface micrographs of Fe films deposited at (a) T_s=190°C and (b) T_s=200°C.

Roughness measurements are performed with mechanical profilometry (see § 2.2.8). Profilometry is applied instead of interferometry, since the reflectance of Fe surfaces is limited and leads to detection issues. For each film, a single measurement is performed and reported for the RMS across a 1 mm line on the surface. Results are presented in Figure 5.7. We observe that the RMS initially increases up to 150°C, from *ca.* 0.67 μm to *ca.* 0.75 μm. Above this temperature and up to 190°C, a monotonous decrease observed, from *ca.* 0.75 μm to *ca.* 0.48 μm. The film at 160°C (4th point from the left) peeled off during the scratching of the surface and for this reason it is probably off the trend. Beyond 200°C, the RMS decreases and tends to stabilize at 0.16 μm in the range 230°C – 250°C.

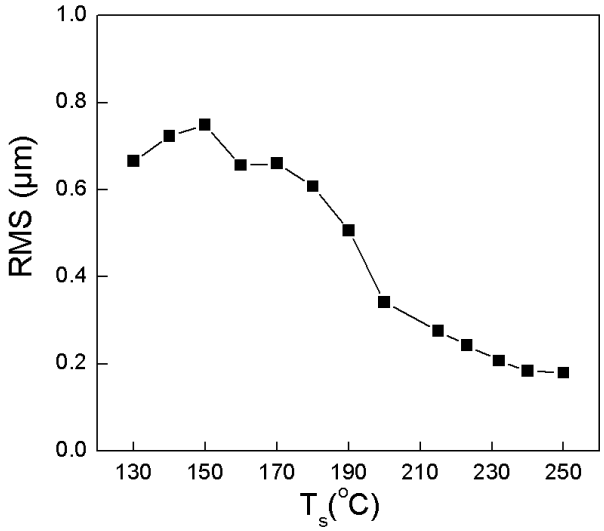

Figure 5.7: Evolution of RMS roughness with surface temperature, T_s, as measured by mechanical profilometry.

The behavior of the RMS roughness can be directly correlated to the change of the microstructure. As shown in Figure 5.5, at the lowest temperature the coverage of the surface is poor and no faceted crystals are observed. The increase of the temperature up to 150°C results in the enhanced surface coverage and in angular crystals which are sharply faceted.

However, the variation among the size of the crystals leads to higher differences between the maximum and the minimum surface heights and to the increase of the RMS. In the temperature range 160°C – 190°C, the size of the angular crystals is more homogeneous, resulting in a monotonous decrease of the roughness. Above 200°C the change of the crystal structure from angular and faceted to acicular results first, to the sharp decrease of the RMS and then to its stabilization. The modeling of RMS as a function of T_s is performed in § 5.3.2.

The composition of the films is investigated with EPMA for films deposited at T_s=160°C, 200°C and 240°C. The results are summarized in Table 5.2. At 160°C, Fe is 90% as O and C heteroatoms are up to 4% and 6%, respectively (at%). The C content may come from the deposition temperature being relatively low, which could lead to incomplete decomposition of the precursor, and its subsequent incorporation into the film. At 200°C, the Fe and O contents are slightly increased to *ca.* 93% and 5.5%, respectively, whereas C is significantly decreased to *ca.* 1.5%. The increased O contamination can be correlated with the increase of the decomposition rate of the reactants in the gas phase which subsequently leads to O incorporation in the films. The decomposition rate becomes even higher at more elevated temperatures (240°C) and as a result the O contamination of the film is further increasing to *ca.* 9% while Fe and C remain relatively stable (90-91% and 1-2%, respectively). The same behavior of the atomic composition has also been observed in Senocq *et al*. (2006). The relatively low O and C contamination at 200°C is compatible with literature results (Jackman and Foord, 1989) where it is reported that the thermal MOCVD of Fe from $Fe(CO)_5$ results in relatively pure films in which the O and C concentrations are a few at%.

Table 5.2: EPMA analyses for Fe films deposited on Si substrates at T_s=160°C, 200°C and 240°C.

T_s	Fe at%	O at%	C at%
160°C	90	4	6
200°C	93	5.5	1-2
240°C	90-91	8	1-2

Figure 5.8 presents the XRD analyses performed on films deposited at 160°C, 200°C and 240°C. All peaks detected at T_s=160°C can be attributed to *bcc* Fe (JCPDS no. 87-0722), as shown in Figure 5.8a. The Fe peaks are even more intense at 200°C and 240°C, indicating the *bcc* Fe is obtained in the investigated temperatures range. No crystalized graphitic carbon is detected. Some small peaks at lower 2θ angles such as at 28°, 34° and 38° for higher temperatures has been reported to correspond to Fe_3C in the literature (Delsol *et al*., 2005; Senocq *et al*., 2006), but these observations cannot be confirmed in the examined case.

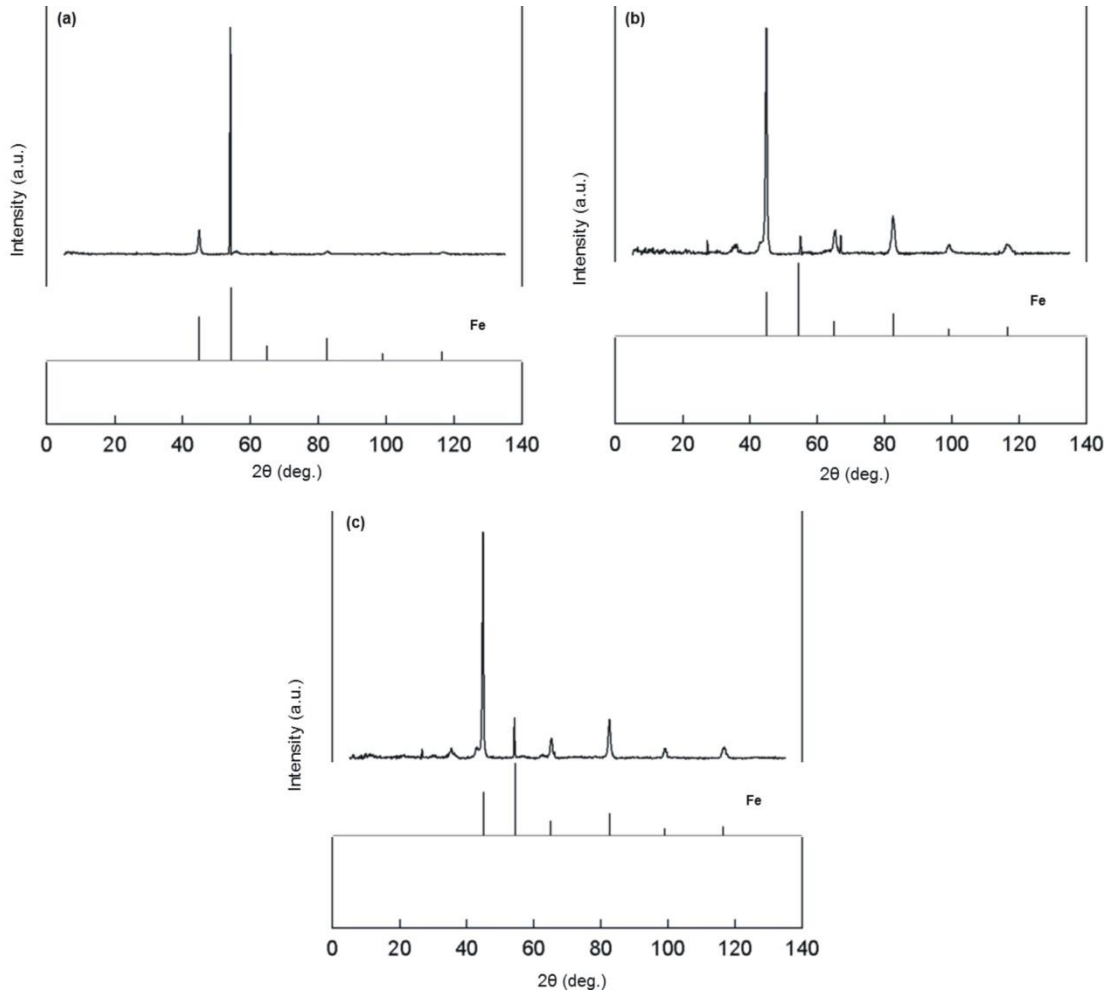

Figure 5.8: XRD analyses of Fe films deposited at (a) T_s=160°C, (b) 200°C and (c) 240°C.

5.2. Macroscopic modeling of the process

Aiming at investigating the kinetic mechanisms prevailing during the growth of Fe films and at determining the corresponding kinetic parameters, a three-dimensional model (3D) of the MOCVD reactor is built, based on the governing equations describing the transport phenomena and the chemical reactions inside the reactor: the continuity, the momentum, the energy and the species transport equations augmented with realistic boundary conditions (Cheimarios *et al.*, 2010; Deen, 1998) are discretized in 3D and solved with Ansys/Fluent (Ansys 12.1/Fluent Documentation, 2009). The set of the governing transport equations is described in detail previously (see § 3.1.3).

A constant mass inflow rate of 5.9177 x 10^{-6} kg/s is imposed at the inlet of the reactor, calculated from the total flow rate (305.69 sccm) of the gas phase. No-slip condition is imposed on the reactor walls. At the outlet, a standard outflow boundary condition is used and an overall mass balance correction is imposed (Ansys 12.1/Fluent Documentation, 2009). The values of the temperature are set as measured after its calibration on the surface of the substrate, while the temperature at the walls and the inlet of the reactor are set equal to room temperature (set at 25°C with an air conditioner for the entire duration of the experiments)

following the experimental setup. For the investigation of the dependence of the deposition rate on temperature, the pressure of the reactor is set to 1333 Pa (10 Torr), corresponding to the experimental setup of the Arrhenius plot of Figure 5.3. Mass fractions of the species entering the reactor are $y_{Fe(CO)_5} = 0.01558$ and $y_{N_2} = 0.98442$. These values correspond to the mass inflow rate of the precursor in the reactor, which equals 0.69 sccm. Mesh independency of the results is ensured, as for the Al case (Chapter 3 – § 3.1.2).

The Lennard-Jones (LJ) parameters (see Chapter 4), required for the estimation of the properties of the gas phase mixture are calculated with group contribution methods (Fedors, 1982; Joback and Reid, 1987; Poling *et al*., 2001) for the unknown species $Fe(CO)_5$, $Fe(CO)_4$, $Fe(CO)_3$, $Fe(CO)_2$ and Fe(CO), and they are summarized in Table 5.3. The LJ parameters needed for the rest of the species participating in the reactions (CO, N_2) are already implemented in Fluent libraries (Ansys 12.1/Fluent Documentation, 2009).

Table 5.3: The LJ parameters of $Fe(CO)_5$, $Fe(CO)_4$, $Fe(CO)_3$, $Fe(CO)_2$ and Fe(CO).

species	σ (Å)	ε / k (K)
$Fe(CO)_5$	3.91	432.38
$Fe(CO)_4$	3.87	283.13
$Fe(CO)_3$	3.71	254.97
$Fe(CO)_2$	3.62	248.77
Fe(CO)	3.52	192.21

5.2.1. Gas phase reactions and kinetics

Several reaction pathways have been proposed for the decomposition of $Fe(CO)_5$ including both gas phase and surface reactions (Barnes *et al*., 1991; Dateo *et al*., 2002; Gonzáles-Blanco and Branchadell, 1999; Lewis *et al*., 1984; Seder *et al*., 1986; Xu and Zaera, 1994; Zaera, 1991). The gas phase scheme consists of successive decarbonylation steps of the pentacarbonyl precursor and recombination of the liberated CO ligands with carbonyl intermediates.

The first step describes the break of the bond between Fe and one CO ligand for the production of the intermediate $Fe(CO)_4$. The first decarbonylation step is found to be more difficult than the other steps: the energy required equals 166.7 kJ/mol, as measured experimentally (Lewis *et al*., 1984) and validated by DFT calculations (Gonzáles-Blanco and Branchadell, 1999). This value is relatively high for the present simulations and for this reason the lower value of 136.7 kJ/mol is adopted instead, by fitting this energy to the obtained experimental data. The difference between the two values may be attributed to the different experiments performed for the determination of the activation energy, namely photo-dissociation of the precursor's molecule (Lewis *et al*., 1984) and thermal heating as energy source, in the present case.

The dissociation process of $Fe(CO)_5$ further proceeds through the loss of another CO group from the $Fe(CO)_4$, resulting in the formation of the $Fe(CO)_3$ species. The activation energy for this step is lower than previously and equals 79.9 kJ/mol (Sunderlin *et al*., 1992).

The intermediate ligands continue undergoing decarbonylations for the successive formation of $Fe(CO)_2$ and Fe(CO). The energy required for the removal of one CO from the tricarbonyl intermediate is determined to be 97.5 kJ/mol, while the corresponding for the loss of CO from $Fe(CO)_2$ 139.1 kJ/mol (Gonzáles-Blanco and Branchadell, 1999; Sunderlin *et al*., 1992). It seems that the linear structure of $Fe(CO)_2$ renders the intermediate more stable than the tricarbonyl and the tetracarbonyl intermediates and higher energy is required for the abstraction of the CO group.

Besides decomposition reactions, the iron carbonyl intermediates can also recombine with CO ligands. The energies required for the recombination reactions are taken from Seder *et al*. (1986). In particular, the recombination of $Fe(CO)_4$ with CO for the formation of $Fe(CO)_5$ occurs with an activation energy of 10.5 kJ/mol. Recombination of $Fe(CO)_2$ and $Fe(CO)_3$ with CO to form $Fe(CO)_3$ and $Fe(CO)_4$, respectively, require 9.5 kJ/mol. The lower activation energies of these two reactions indicate that they occur easier than the recombination reaction of $Fe(CO)_4$ with CO, due to the fact that the latter is spin forbidden (Seder *et al*., 1986). Recombination reactions for the Fe(CO) ligand are not reported in the literature. The gas phase reactions with their corresponding energies are summarized in Table 5.4.

For the gas phase reactions G1-G4 and G1′-G3′, we modify the Arrhenius law implemented in Fluent (see Eq. 3.14 – § 3.1.4) to account for the stoichiometry of the reactions. The two Arrhenius reactions rates used for the forward and the inverse reactions are expressed by Eq. (5.1) and Eq. (5.2), respectively:

$$R_{G_i} = k_{0,G_i} \exp\left(-\frac{E_{\mathrm{a},G_i}}{RT_{gas}}\right) \mathrm{C}_{Fe(CO)_i,gas}, \tag{5.1}$$

$$R_{G_i'} = k_{0,G_i'} \exp\left(-\frac{E_{\mathrm{a},G_i'}}{RT_{gas}}\right) \mathrm{C}_{\mathrm{Fe(CO)_i},gas} \mathrm{C}_{\mathrm{CO,gas}}, \tag{5.2}$$

where R_{G_i} and $R_{G_i'}$ denote the identity of reactions, $\mathrm{C}_{Fe(CO)_i,gas}$ and $\mathrm{C}_{\mathrm{CO,gas}}$ are the gas phase concentrations of each carbonyl species and CO, respectively, E_{a,G_i} and $E_{\mathrm{a},G_i'}$ are the activation energies of the forward and the reverse reactions, respectively, and T_{gas} is the temperature of the gas phase in the reactor. The values of the pre-exponential factors of the reverse reactions, $k_{0,G_i'}$, are taken from Seder *et al*. (1986). The pre-exponential factors of the forward reactions, k_{0,G_i}, are fitted to the experimental data. As for the Al case, in order to fit the unknown pre-exponential factors of the gas-phase reactions, the process is simulated at the high-temperature regime, where the reaction rates are high and diffusion becomes dominant for the deposition process. The fitting of these parameters is facilitated by the fact that not all the reactions have the same impact on the behavior of the deposition rate (see 5.2.3.). The pre-exponential factors fitted in the diffusion-limited regime are applied for the

simulation of the process in the whole temperature range for a fine tuning. Values of the pre-exponential factors for each reaction are summarized in Table 5.4.

Table 5.4: Details of the gas phase chemistry model. The Arrhenius rate expressions are given by Eq. (5.1) and Eq. (5.2). Activation energies are given in kJ/mol. The pre-exponential factors of the forward reactions are in s^{-1} units where for the reverse reactions in m^3/kmol.s units.

ID	Reaction	Pre-exponential factors	Activation energies
G1	$Fe(CO)_5 \rightarrow Fe(CO)_4 + CO$	$9.65x10^{12}$	136.7
G2	$Fe(CO)_4 \rightarrow Fe(CO)_3 + CO$	$8.96x10^{12}$	79.9
G3	$Fe(CO)_3 \rightarrow Fe(CO)_2 + CO$	$1.25x10^{11}$	97.5
G4	$Fe(CO)_2 \rightarrow FeCO + CO$	$3.96x10^{11}$	139.1
G1′	$Fe(CO)_4 + CO \rightarrow Fe(CO)_5$	$3.5x10^{7}$	10.5
G2′	$Fe(CO)_3 + CO \rightarrow Fe(CO)_4$	$1.3x10^{10}$	9.5
G3′	$Fe(CO)_2 + CO \rightarrow Fe(CO)_3$	$1.8x10^{10}$	9.5

5.2.2. Surface reactions and kinetics

The deposition of Fe from $Fe(CO)_5$ can be attributed either to the complete surface dissociation of the precursor (Carlton and Oxley, 1965; Jackman and Foord, 1989; Zaera, 1991) or to the surface dissociation of the $Fe(CO)_3$ (Xu and Zaera, 1994; Zaera, 1991) and the Fe(CO) (Dateo *et al*., 2002; Ricca 2001) intermediate compounds. In particular, the complete surface decomposition of the precursor to Fe and 5 CO ligands is reported in Carlton and Oxley (1965) and Jackman and Foord (1989). Moreover, a Langmuir-Hinshelwood type kinetic equation is proposed (Carlton and Oxley, 1965) to express the poisoning of the surface from the released CO. On the other hand, during the thermal decomposition of $Fe(CO)_5$, evidences for the existence of surface tetracarbonyl and tricarbonyl intermediates are observed by performing TPD and XPS experiments (Xu and Zaera, 1994; Zaera, 1991). The authors propose that the precursor adsorbs on the surface and decomposes to Fe and to $Fe(CO)_4$ and $Fe(CO)_3$ intermediates. The $Fe(CO)_3$ can lose the three CO with a relatively low activation energy so as to contribute to Fe deposition. The dissociation of Fe(CO) to Fe and CO has been proposed to occur during the formation of Fe catalytic particles (Dateo *et al*., 2002).

The surface reaction pathway that we propose combines the works reported in the literature. The $Fe(CO)_5$ which does not undergo gas phase dissociation, reaches the heated surface and reacts completely for the formation of Fe and five CO groups. For the activation of this reaction, the activation energy of 27.9 kJ/mol is used, estimated by the slope of the Arrhenius plot in the reaction-limited regime which is in good agreement with the value of 26±2 kJ/mol obtained in Jackman and Foord (1989). Then, we consider that the gas phase $Fe(CO)_3$ which does not decompose, reaches the surface and decomposes to Fe and three CO ligands with an activation energy of 75.3 kJ/mol (Xu and Zaera, 1994). Finally, the FeCO produced by the successive, gas phase decarbonylations of the pentacarbonyl precursor may contribute to the surface deposition of Fe. The activation energy for its bond dissociation

equals 19.3 kJ/mol. The surface reactions with their corresponding activation energies are summarized in Table 5.5.

In the above proposed scheme for the surface reactions, we do not consider the exact surface pathway for deposition from $Fe(CO)_3$, which includes first, the adsorption of $Fe(CO)_5$ on the surface and then its decomposition to $Fe(CO)_4$, $Fe(CO)_3$ and Fe. Instead, we neglect the adsorption of $Fe(CO)_5$ and we use the gas phase $Fe(CO)_3$ which reaches the surface, as a source of Fe. In this way, we incorporate its effect on the process and at the same time, we keep the model as simple as possible. It has to be noted that the implementation of a 10-reactions chemistry model (Tables 5.4 & 5.5) with their corresponding kinetic rate equations (Eqs. 5.1, 5.2 & 5.3) results in the fitting of 8 parameters (pre-exponential factors) which is a time consuming task. Thus, we choose to examine the accuracy of this realistic model with regard to experimental results.

As we briefly discussed in §5.1, the steep reduction of the deposition rate at high temperatures can be attributed to high gas phase decomposition rate of the precursor and to the poisoning of the surface by CO ligand. Since no adsorption states of the precursor, its intermediate products or the CO ligands are incorporated in the model, the effect of CO on the deposition rate can be investigated by applying a Langmuir-Hinshelwood type kinetic expression, which is given by the following equation:

$$R_{S_i} = \frac{k_{S_i} \exp(-\frac{E_{a,S_i}}{RT_s}) C_{Fe(CO)_i,sur}}{1 + k_{CO} \exp(-\frac{E_{a,CO}}{RT_s}) P_{CO,sur}}, \quad (5.3)$$

where R_{S_i} is the reaction rate of each surface reaction, $C_{Fe(CO)_i,sur}$ is the concentration of the $Fe(CO)_5$, $Fe(CO)_3$ and FeCO species at the surface, T_s is the surface temperature, E_{a,S_i} is the activation energy of each surface reaction and k_{S_i} is the pre-exponential factor of the reaction S_i, which is fitted to the experimental data. For the fitting of these parameters, the process is first simulated at the reaction-limited regime where surface reactions are more important than gas phase reactions or diffusion mechanisms. Then, simulations are performed in the whole temperature range for the better fitting of the pre-exponential factors. The denominator of Eq. (5.3), which is referred as S4 in Table 5.5, expresses the inhibition of the deposition process by the adsorption of CO. $E_{a,CO}$ is the adsorption energy of CO which is taken to be 89.9 kJ/mol (Carlton and Oxley, 1965), $P_{CO,sur}$ is the partial pressure of CO at the boundary of the surface and k_{CO} is the pre-exponential factor of this process. The latter is fitted to the experimental data as described before, by starting from the diffusion-limited regime, where inhibition by CO is more likely to occur. The values of the pre-exponential factors for each reaction are summarized in Table 5.5. Since Fluent uses Arrhenius kinetics by default for the

reaction rates (see §3.3.4.), we insert the Langmuir-Hinshelwood expression through a UDF file written in C language (see §3.3.4.).

Table 5.5: Details of the surface chemistry model. Reaction rates are given by the Langmuir-Hinshelwood type expression of Eq. (5.3). Activation energies are given in kJ/mol. The pre-exponential factors of reactions S1-S3 are in m/s units, while that of S4 is given in $Torr^{-1}$, for consistency with the units of Fluent.

ID	Reaction	Pre-exponential factors	Activation energies
S1	$Fe(CO)_5 \rightarrow Fe_{(s)} + 5CO_{(ads)} \rightarrow Fe_{(s)} + 5CO_{(g)}$	$2.4x10^7$	27.9
S2	$Fe(CO)_3 \rightarrow Fe_{(s)} + 3CO_{(ads)} \rightarrow Fe_{(s)} + 3CO_{(g)}$	$5.3x10^7$	75.3
S3	$FeCO \rightarrow Fe_{(s)} + CO_{(ads)} \rightarrow Fe_{(s)} + CO_{(g)}$	$3.7x10^{10}$	19.3
S4	CO adsorption	$3.8x10^8$	89.9

5.2.3. The Arrhenius plot of the process

Figure 5.9 presents the Arrhenius plot of the process. The computational predictions are in very good agreement with experimental data and the model is able to predict the behavior of the deposition rate over the entire temperature range. In particular, in the low temperature regime, the predicted deposition rate approaches very well the corresponding experimental data and lies within the deviations for the lowest T_s. It is reminded here that the large deviation shown for this experimental point comes from a possible overestimation of the incubation time. As temperature increases, and up to 215°C, the model continues to predict accurately the measured deposition rates. Above this temperature, the computational model follows the experimental trend that is, a steep reduction. However, the predicted deposition rates are slightly underestimated.

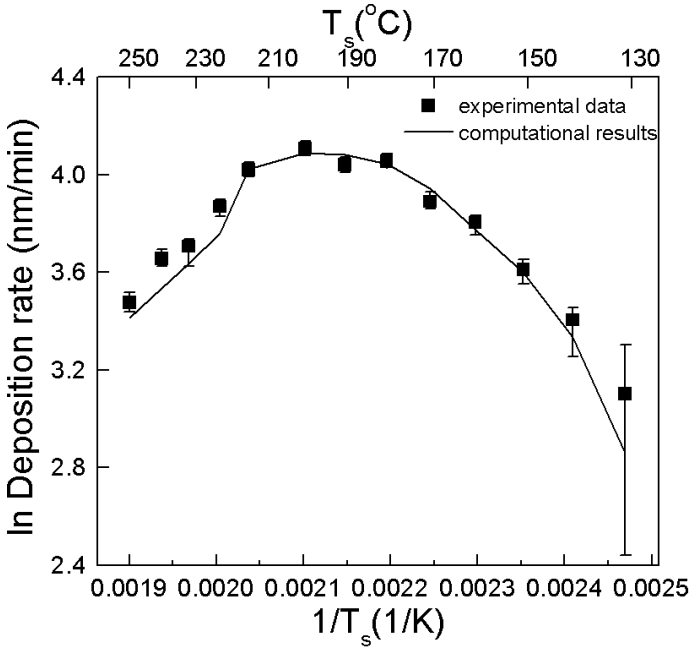

Figure 5.9: The Arrhenius plot of the CVD of Fe from $Fe(CO)_5$. Experimental measurements (squares) and computational results (line) are shown. Error bars correspond to the minimum and the maximum deviations of the deposition rate and include possible overestimations due to large incubation times.

We now further explore the successful prediction of the behavior of the deposition rate. First, we compare the volumetric reaction rates and the mass fractions of the species which contribute to the deposition rate, in the range 215°C – 223°C, where the steep reduction of the deposition occurs. Then, we compare these results with those obtained at T_s=140°C, i.e., in the reaction-limited regime, to investigate the occurrence of gas phase reactions in this regime. It is recalled, that the goal is the co-deposition or the sequential deposition of Fe with Al, thus, the latter step aims at showing if homogeneous reactions may affect these two processes in the reaction-limited regime.

Figure 5.10 shows the volumetric reaction rates at T_s=223°C (Figure 5.10a) and T_s=215°C (Figure 5.10b), at a horizontal line 1 mm above the susceptor. Therefore it shows the radial distribution from the center of the susceptor (0 m in the x-abscissa). Reactions which are not shown yield zero reaction rate and are excluded from this investigation.

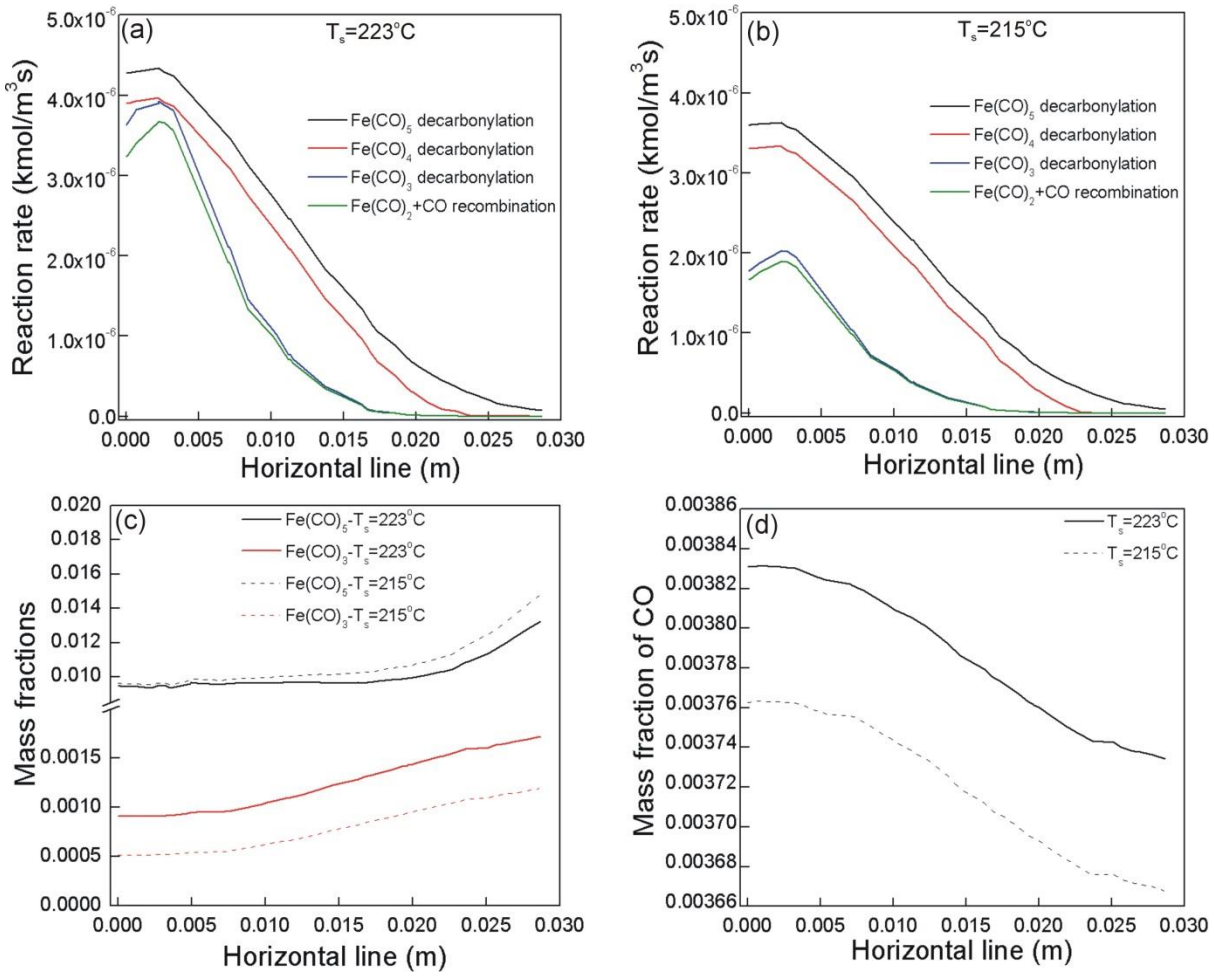

Figure 5.10: The volumetric reaction rates at (a) T_s=223°C and (b) T_s=215°C. For both figures the black lines correspond to $Fe(CO)_5$ decarbonylation, the red lines to $Fe(CO)_4$ decarbonylation, the blue lines to $Fe(CO)_3$ decarbonylation and the green lines to $Fe(CO)_2$+CO recombination. Other reactions give zero rates. (c) The mass fractions of $Fe(CO)_5$ (black lines) and $Fe(CO)_3$ (red lines) at T_s=223°C (solid lines) and T_s=215°C (dashed lines). (d) The mass fraction of CO T_s=223°C (solid line) and T_s=215°C (dashed line). All the quantities are calculated along a horizontal line 1 mm above the susceptor.

It can be seen that at the higher T_s the decomposition rates of the precursor and the tetracarbonyl and tricarbonyl intermediates are higher than the corresponding rates at T_s=215°C, resulting in the decrease of the precursor available for Fe deposition. Interestingly enough, the rate of recombination of $Fe(CO)_2$ with CO (green lines) is almost the same as the decomposition rate of $Fe(CO)_3$ (green lines). As a result, the $Fe(CO)_2$ decomposition (G4) and consequently the FeCO decomposition (S3) do not occur, since all $Fe(CO)_2$ intermediates are consumed in the recombination with CO to form $Fe(CO)_3$. The recombination of $Fe(CO)_4$ with CO yields zero rates, consistent to the literature reports (Seder *et al*., 1986), whereas the recombination of $Fe(CO)_3$ with CO occurs at negligible rates (of the order of 10^{-9} kmol/m^{3}s), due to the consumption of the tricarbonyl by the surface reaction (S2).

Figure 5.10c shows the mass fractions of $Fe(CO)_5$ and $Fe(CO)_3$ at T_s=223°C (black and red solid lines, respectively) and T_s=215°C (black and red dashed lines, respectively), still 1 mm above the susceptor. The mass fractions of the other carbonyl species are zero. Following the trend of $Fe(CO)_5$ decarbonylation for these two temperatures, the $Fe(CO)_5$ which is available for the surface reaction decreases at T_s=223°C. On the other hand, $Fe(CO)_3$ increases as a result of the increased decomposition of $Fe(CO)_5$. This trend becomes more intense as approaching the susceptor where the temperature increases and eventually, this combination leads to the decrease of the deposition rate. As shown in Figure 5.10d, the CO mass fraction is higher at T_s=223°C contributing to the reduction of the deposition rate (Eq. 5.3), which means that the surface process is inhibited by CO. Thus, the model validates the two main reasons for the reduction of the deposition rate at high temperatures that is, increased decomposition rate of the precursor (Senocq *et al*., 2006) and poisoning of the surface by CO (Zhang *et al*., 2016).

Figure 5.11 shows the non-zero volumetric reaction rates of G1, G2, G3 and G3′ along with the mass fractions of $Fe(CO)_5$, $Fe(CO)_3$ and CO, at T_s=140°C, on a horizontal line located 1 mm above the susceptor.

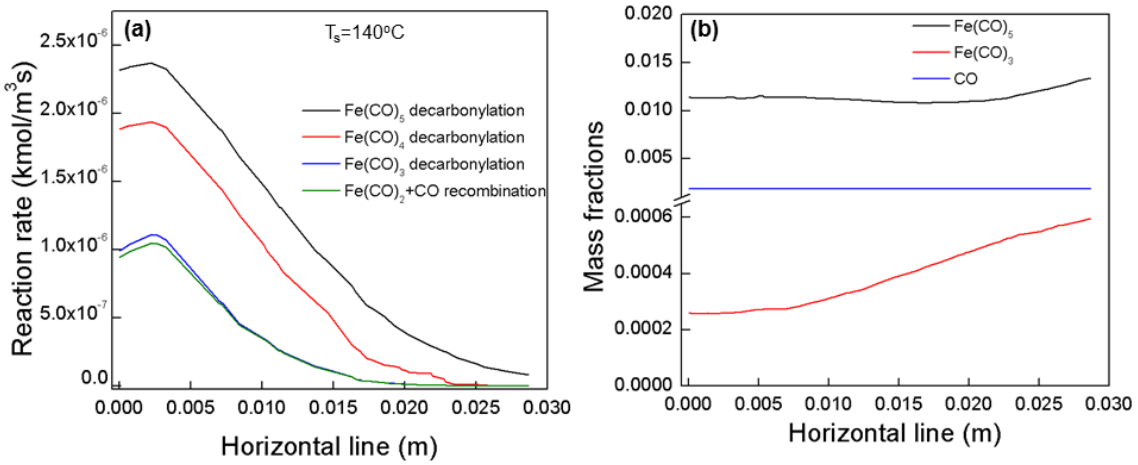

Figure 5.11: (a) The reaction rates of $Fe(CO)_5$ decarbonylation (black lines), $Fe(CO)_4$ decarbonylation (red lines), $Fe(CO)_3$ decarbonylation (blue lines) and $Fe(CO)_2$ +Co recombination (green lines) at T_s=140°C. (b) The mass fractions of $Fe(CO)_5$ (black line), $Fe(CO)_3$ (red lines) and CO (blue line) at the same T_s. All the quantities are calculated along a horizontal line 1 mm above the susceptor.

It can be seen that even at this low temperature the decomposition reactions occur, although with lower rates than in 215°C and 223°C. The lower decomposition rates results in a higher $Fe(CO)_5$ mass fraction and at the same time in reduced $Fe(CO)_3$ and CO mass fractions (Figure 5.11b).

We now focus on the surface (the abscissa is now confounded with the susceptor). In Figure 5.12, the computed deposition rates along the susceptor radius are compared with the experimental measurements at T_s=140°C (Figure 5.12a), T_s=200°C (Figure 5.12b) and T_s=240°C (Figure 5.12c). The experimental data show that in all cases the deposition rate increases when moving from the center of the susceptor to the edge. Although, there is a fairly good agreement between measurements and predictions, the model does not capture the experimental trend. At T_s=140°C, the predicted rate is maximum at the center of the susceptor and decreases to the edge. At T_s=200°C and T_s=240°C, the predicted rate at the center of the susceptor is overestimated, then, it reaches a minimum value and finally, increases again at the edge.

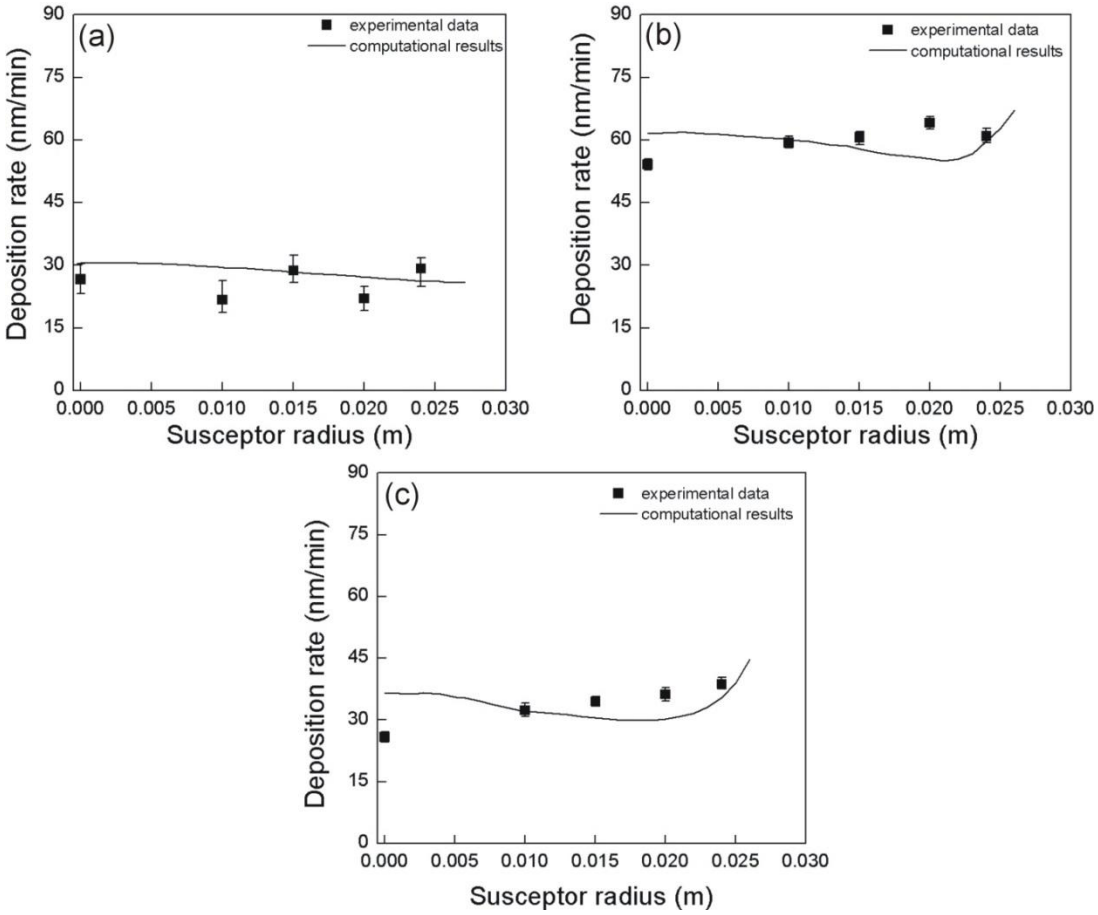

Figure 5.12: Deposition rate along the susceptor radius for (a) T_s=140°C, (b) T_s=200°C and (c) T_s=240°C. Experimental measurements (squares) and computational predictions (lines) are shown.

Figure 5.13 shows the mass fractions of $Fe(CO)_5$ and CO along the susceptor radius at T_s=140°C (Figure 5.13a) and T_s=200°C (Figure 5.13b). At the low temperature, a continuous decrease of $Fe(CO)_5$ and $Fe(CO)_3$ along the susceptor can be observed and at the same time

the CO mass fraction slightly increases. This trend is similar to that of the deposition rate, as shown in Figure 5.12a. At T_s=200°C, the mass fraction of $Fe(CO)_5$ increases after 0.02 m from the center of the susceptor while the mass fraction of $Fe(CO)_3$ follows the opposite trend and CO shows a small increase. The deposition rate at this T_s (Figure 5.12b) follows the trend of the $Fe(CO)_5$ mass fraction but the curvature at the minimum value is more intense due to the decrease of $Fe(CO)_3$ and the increase of CO.

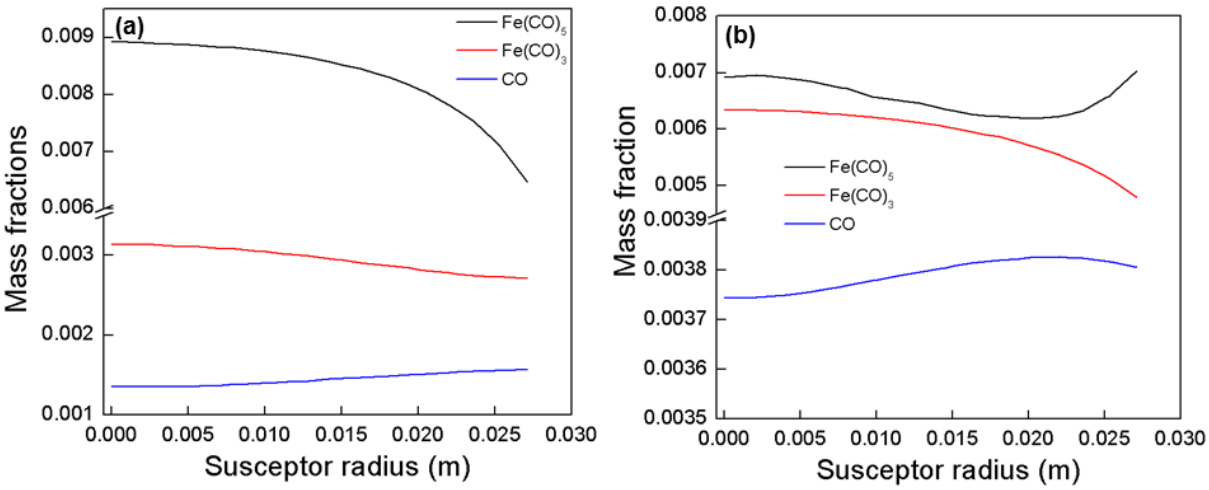

Figure 5.13: Mass fraction of $Fe(CO)_5$ (black lines), $Fe(CO)_3$ (red lines) and CO (blue lines) along the susceptor at (a) T_s=140°C and (b) T_s=200°C.

The discrepancies between the model predictions and experimental data can attributed to the approximation applied for the participation of the $Fe(CO)_3$ in the Fe growth. A more precise surface pathway which will include the site adsorption of the precursor and its further decomposition to $Fe(CO)_4$, $Fe(CO)_3$ and Fe may palliate these discrepancies.

We now investigate the predictive capability of the model concerning the effect of the pressure on the deposition rate and we present these results in the diagram of the deposition rate as a function of the process pressure of Figure 5.14. It is recalled that for this investigation the temperature is fixed at T_s=180°C. In the discussion of Figure 5.4a, and by using input from literature, we have speculated that the decrease of the deposition rate is due to the higher decomposition rate of the precursor and to the decrease of the mass diffusion coefficient. The computational predictions capture the decrease of the deposition rate and show very good agreement against the experimental data.

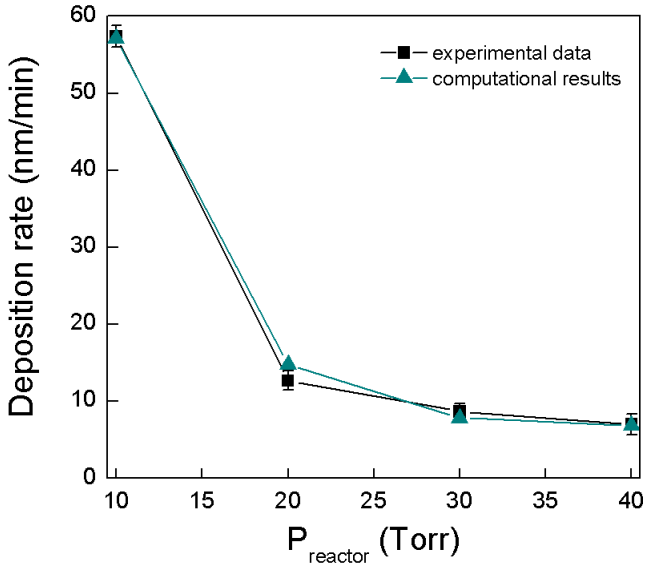

Figure 5.14: The dependence of the deposition rate on $P_{reactor}$ for both experiments (black squares with black trendline) and computational predictions (cyan tringles with cyan trendline).

In Figure 5.15, we present the decomposition rates of $Fe(CO)_5$ (G1) and $Fe(CO)_3$ (G3) (Figure 5.15a) and the mass diffusion coefficient (Figure 5.15b, see Eq. 3.7 – §3.1.3.) of these two species to support our assumption. The results are shown for $P_{reactor}$=10 Torr and $P_{reactor}$=40 Torr and at a horizontal line located 1 mm above the susceptor. It can be seen that increasing the pressure the decomposition rates of $Fe(CO)_5$ and $Fe(CO)_3$ are increased and this results in the reduction of the deposition rate. Figure 5.15b confirms that the increase of the pressure leads to the decrease of the mass diffusion coefficients of the species. Consequently, the concentration of $Fe(CO)_5$ and $Fe(CO)_3$ at the susceptor are lower and the deposition rate is decreased.

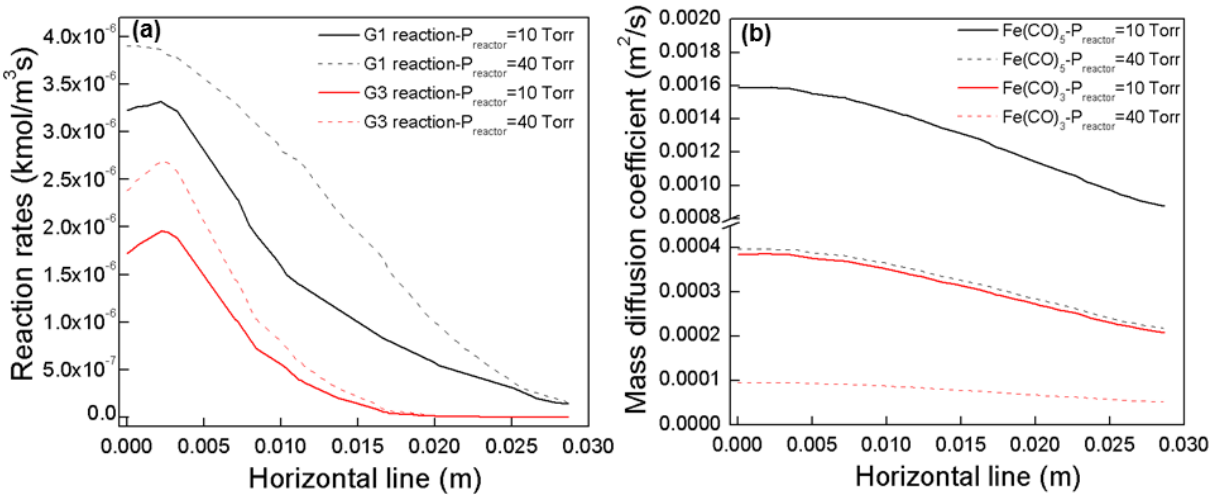

Figure 5.15: (a) The decomposition rates of G1 (black lines) and G3 (red lines) reactions and (b) the mass diffusion coefficients of $Fe(CO)_5$ (black lines) and $Fe(CO)_3$ (red lines) for $P_{reactor}$ =10 Torr (solid lines) and 40 Torr (dashed lines). The temperature is fixed at T_s=180°C.

The macroscopic modeling predicts the behavior of the Fe deposition rate for temperature and pressure variations, in the investigated temperature range 130°C – 250°C.

Less accuracy is observed in the predictions of the deposition rate along the susceptor radius. The model can be improved in order to capture this trend also, by adding the surface decomposition scheme of $Fe(CO)_5$ proposed by Xu and Zaera (1994). However, our results give an insight to the chemical pathways of the decomposition of $Fe(CO)_5$, and help to define the operating conditions for the co-deposition and the sequential deposition of Al with Fe.

5.3. Multiscale modeling of the process

Our multiscale computational modeling is a framework that links the macroscale level described in §3.1 and §5.2 with the nanoscale model presented in §3.2. The investigation is focused on the surface evolution and more precisely on the calculation of the surface roughness of a Fe CVD film grown on an initially flat surface. Upon convergence of the macroscopic simulations, the mass fraction of the species contributing to the deposition rate is fed to the stochastic kMC algorithm and the simulation of the surface evolution starts.

5.3.1. Multiscale computations with the simple cubic lattice

As performed in the multiscale modeling of Al growth, the simple cubic lattice is used which includes interactions among the five first nearest neighbors of the examined atom. The investigated surface is initially flat as shown in Figure 3.6. The sticking coefficient, s_0, is fitted by comparing the computed deposition rate with the corresponding experimental one, which remains unchanged regardless the simulated scale (see §3.2.3.), for each T_s and at each position of the substrates on the susceptor. The 4^{th} degree polynomial relation between s_0 and T_s, provided by this fitting procedure is presented in Eq. 5.4 and used during microscopic simulations. The fitting is performed within the Matlab software with a polyfit function procedure.

$$s_0 = 1.2157\times10^{-8}\times T_s^4 - 2.2791\times10^{-5}\times T_s^3 + 1.5913\times10^{-2}\times T_s^2 - 4.9018\times T_s + 562.26 \qquad (5.4)$$

The implementation of such a relation for s_0 in the present model provides a correlation of this parameter with the operating temperature while implicitly integrating chemical reactions in the nanoscale algorithm. Thus, we simulate the CVD growth of Fe by performing physical vapor deposition multiscale calculations.

The given dependence of s_0 on T_s is valid only for the temperature range used in this work, as the fitting is based only on experimental results obtained in this range. From Eq. 5.4, it comes out that the increase of the temperature results in the increase of the sticking probability up to a maximum value and then to its decrease, according to a relation illustrated in Figure 5.16.

The behavior of s_0 as a function of T_s follows the trend of the deposition rate, shown in Figures 5.3 and 5.8: a direct consequence of fitting. It is recalled that by fitting s_0 to the experimental deposition rates, we implicitly incorporate in it, the chemical behavior of the precursor or intermediate molecules on the surface. For the case of the MOCVD of Fe from

$Fe(CO)_5$, this information may concern the adsorption of molecules on the surface, their surface dissociation or the poisoning of the surface by CO. Thus, the linear increase of s_0 up to 200°C can be attributed the dissociation of $Fe(CO)_5$ and $Fe(CO)_3$ in order to adsorb on the surface and the continuous decrease beyond 200°C to the poisoning of the surface from the released CO which occupies surface sites and inhibits the adsorption of $Fe(CO)_5$ and $Fe(CO)_3$ molecules.

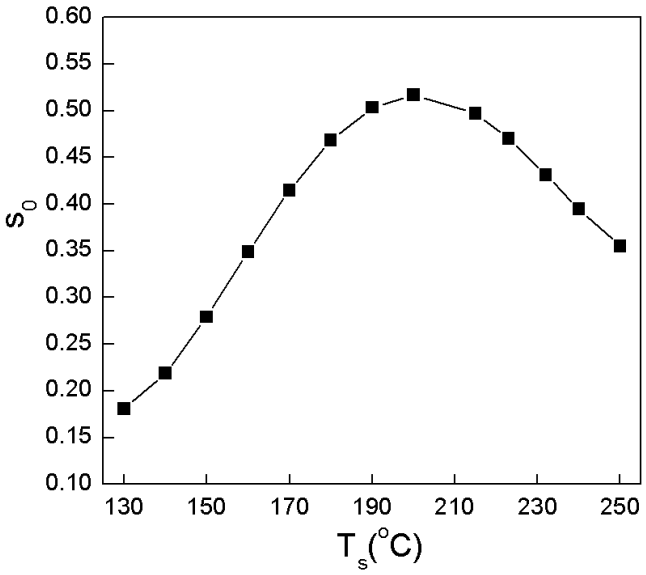

Figure 5.16: The dependence of s_0 on T_s, within the investigated temperature range.

The single bond energy, E, and the frequency factor, ν_0, needed for the calculation of the desorption probability are taken equal to 57.89 kJ/mol (Amar and Family, 1995b; Bartelt and Evans, 1995; Stroscio and Pierce, 1994) and 10^{12} s^{-1} (Evans *et al*., 2006), respectively. For the definition of the migration energy, E_m, we implicitly assume that the initial Si surface is covered quickly by Fe adatoms, thus, the migration energy corresponds to the diffusion of Fe on Fe(100) and equals 43.42 kJ/mol (Amar and Family, 1995a; Evans *et al*., 2006;). As for the Al case, this migration energy accounts for both in-plane (intralayer) and across step edges (interlayer) diffusion. That is, we assume an Ehrlich-Schwoebel (ES) barrier equal to 0. The ES value lies in the range 2.89-5.79 kJ/mol, as determined by the comparison of simulations with scanning tunnelling microscopy (STM) experiments (Amar and Family, 1995a) and it is much lower than that of migration energy, by an order of magnitude. A finite non-zero ES barrier has been found to improve the simulations results with regard to STM experiments at room temperature, whereas the implementation of both a zero and a small positive ES value in the range 180°C – 250°C yield the same reflexion high energy electron diffraction (RHEED) results, indicating that the effect of interlayer diffusion is much less noticeable at these temperatures (Amar and Family, 1995a). In the present study, the simulations are performed between 130°C and 250°C, thus assuming a zero ES barrier is correct as a first approach. By neglecting the interlayer diffusion, we do not sacrifice the accuracy of the model in the calculation of the roughness (See Figure 5.16) but surface

features such as the formation of mounts cannot be captured. The parameters applied to the stochastic algorithm are summarized in Table 5.3.

Table 5.3: Parameters applied in the kMC stochastic algorithm.

P_{total} (Pa)	1333.22
T_s (^{o}C)	130 – 250
Concentration of surface sites, C_{tot} (sites/m^2)	10^{19}
Single bond energy, E (kJ/mol)	57.89
Migration energy, E_m (kJ/mol)	43.42
Frequency factor, ν_0 (s^{-1})	10^{12}

5.3.2. Calculation of the RMS roughness

The experimental deposition rates are used to fit the s_0 needed in the adsorption rate expression of the stochastic algorithm. The main purpose of the multiscale framework is the tailoring of the surface roughness through operating parameters of the reactor scale and in particular the T_s (the operating pressure could also be considered as a parameter that influences the roughness). Figure 5.17 presents the dependence of the RMS roughness on the temperature for both experimental measurements and computational predictions. It can be seen that the multiscale framework predicts with sufficient accuracy the general behavior of the RMS in the investigated temperature range. However, discrepancies exist at particular T_s. We have seen from the experimental results (Figure 5.7) that at the lowest T_s the coverage of the surface is poor. This feature can lead to an underestimation of the roughness during measurements. Additionally, neglecting the uncovered Si surface in the calculations may cause errors at this temperature. Up to 160^{o}C, the model predicts the small changes in RMS quite well, except for the measurement at 130^{o}C, where the surface of the film lacks conformal coverage.

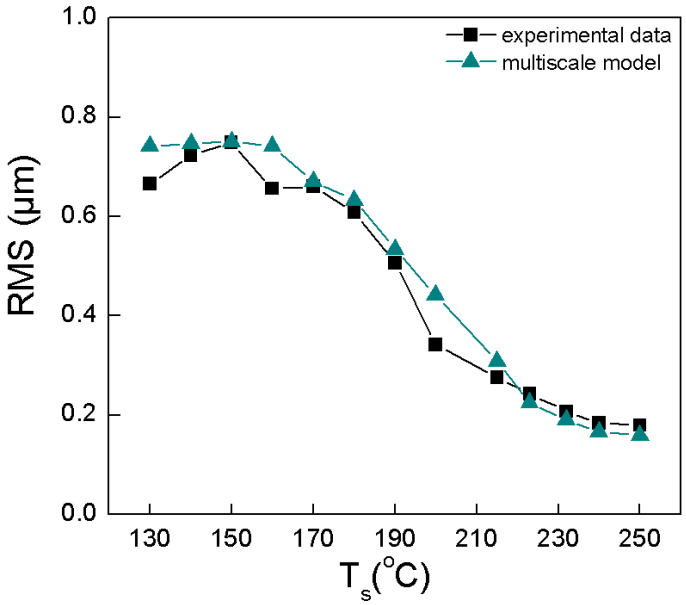

Figure 5.17: Evolution of RMS roughness with surface temperature, T_s. Experimental data (black squares and trendline) and multiscale predictions (cyan triangles and trendline) are shown.

It is recalled that the experimental point at 160°C is off range. Moving at higher T_s and until 190°C, the experimental RMS decreases and the computational predictions follow this trend. However, the step between 190°C and 200°C indicates an abrupt reduction of the roughness which cannot be captured by the model. As discussed in Figures 5.5 and 5.7, this reduction is attributed to the change of the crystals morphology from sharp-faceted to acicular. The multiscale framework does not contain any information about the morphology of the crystals and as a consequence, a smoother decrease of the RMS between these two T_s is predicted. At higher temperatures, computational predictions are in agreement with experimental data. At this point, the measured RMS appears to stabilize and the computed RMS captures this trend.

We now analyze the occurrence of the kMC algorithm events, i.e., adsorption, migration and desorption. Figure 5.18 shows the number of surface events – directly correlated with R-quantities (see Eq. 3.33 – §3.2.2.) – as a function of T_s. We observe that in the entire temperature range, the number of adsorption events is much higher than the corresponding number of migration and desorption events, and consequently adsorption dominates the process. The trend of adsorption events seems to follow the behavior of the deposition rate and of s_0 in the investigated temperature range, i.e., it increases up to a maximum value at T_s=200°C, and then it decreases. This is expected since the adsorption rate incorporates s_0, and it expresses the chemical information incorporated in the sticking coefficient.

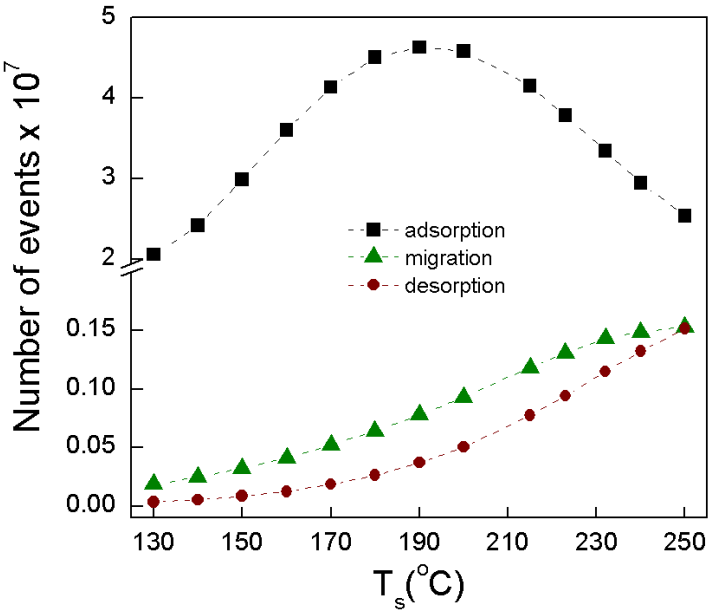

Figure 5.18: The number of surface events as a function of T_s. Adsorption, migration and desorption are illustrated by black squares, green triangles and brown circles, respectively.

Despite the predominance of adsorption, the impact of the migration, which is not fitted, on the RMS roughness is significant. In particular, it can be seen that as the number of migration events increases, the surface roughness decreases. At higher temperatures in the range 230°C – 250°C, the number of migration events stabilizes explaining the plateau which is observed for RMS in Figure 5.17. The number of desorption events slightly increases up to 200°C and

increases faster up to 250°C, where they become equal to migration events. It is noted that during the simulations we have observed desorption of Fe atoms with one neighbor, exclusively, in consistence with literature where it is reported that at temperatures up to 250°C the probability to detach an atom with more than one neighbors is negligible (Amar and Family, 1995b).

The accurate simulation of the surface microstructure and the control of RMS roughness through the variation of the operating conditions of the reactor, such as T_s, may allow the control of the properties of the final film, as shown for the Al case. More importantly, the combination of these results with the previous experimental and computational analyses opens the window for the co-deposition and the sequential deposition processes.

Summary-Conclusions

The CVD of Fe from $Fe(CO)_5$ is experimentally and computationally investigated with the aim to understand and control the behavior of the deposition rate as a function of the temperature in the range 130°C – 250°C and the operating pressure at *ca.* 10 to 40 Torr. Moreover, the evolution of the roughness is correlated with the deposition temperature within the investigated temperature range.

Deposition from $Fe(CO)_5$ results in *bcc* Fe films. The films contain a few percent of O and C heteroatoms which are part of the precursor molecule. The incubation time which is taken into account for the determination of the net deposition rate, is high (*ca.* 1800 s) at the lowest deposition temperature, it decreases to 100-150 s in the range 140°C – 160°C and then it further decreases and stabilizes at less than 50 s, for higher temperatures. This behavior at the initiation of the deposition process may be attributed to the different sticking coefficient of the precursor on the substrate and to accelerated desorption of the adsorbents at higher temperatures.

The surface morphology varies with increasing temperature and these variations can be correlated with the final surface roughness. In particular, at 130°C the surface coverage is low and the uniformity of the films is poor. As a consequence, the roughness is high (*ca.* 0.65 μm) but it might be underestimated because the initial flat Si surface is still measured. As temperature increases to 150°C, faceted grains with varying size are formed and this results to denser films with higher RMS values (*ca.* 0.75 μm). Up to 190°C, RMS decreases to 0.53 μm due to a finest size distribution of the crystals which remain angular and faceted. However, in the range 190°C – 200°C a transition from sharply-faceted to acicular is observed; the acicular character becomes preponderant at higher temperatures. The new morphology results in the steep decrease of RMS to 0.34 μm at 200°C and its stabilization to 0.18μm at 250°C.

The Arrhenius plot of the process can be divided in three regimes. The first one lies within the temperature range 130°C – 180°C; it is surface reaction-limited and the deposition

rate increases with increasing temperature. Between 180°C – 200°C, both surface reactions and transport phenomena impact the process. In this range, the Fe deposition rate has a maximum value of *ca.* 60 nm/min at 200°C. Beyond this temperature, the process is controlled by the diffusion of the reactants through the mass boundary layer to the surface. The deposition rate of Fe abruptly decreases, which is attributed to the high gas phase decomposition rates of the species contributing to the Fe deposition and to the inhibition of the surface from the CO ligand which is produced by the gas phase decomposition reactions. By investigating the effect of the deposition duration on the deposition rate, we see that for durations lower than 60 min the deposition rate increase. Above 60 min it remains unchanged.

A computational model based on continuum mechanics is built for the macroscopic simulation of the process in order to investigate the various phenomena occurring in the CVD reactor. The implemented chemistry model is set up by combining literature data, and includes 7 gas phase and 3 surface reactions. The gas phase reactions describe decarbonylation steps of $Fe(CO)_5$ and recombination reactions of the intermediate species $Fe(CO)_x$, x=2,3,4, with CO. For gas phase reaction Arrhenius type kinetics are implemented with an order dictated by the stoichiometry of the reactions. The surface reactions express the contribution of $Fe(CO)_5$, $Fe(CO)_3$ and FeCO in the Fe deposition. For surface reactions, Langmuir-Hinshelwood type expressions are used to describe the poisoning of the surface by CO. The activation energy of the surface decomposition of $Fe(CO)_5$ is taken from the slope of the experimental Arrhenius plot and it is consistent with previous works reported in the literature. The activation energies for the other reactions are taken from the literature with a slight adjustment to the experimental data of this work. Pre-exponential factors are fitted in order to match the experimental data, except for the recombination gas phase reactions for which pre-exponential factors are found in the literature.

The macroscopic computational model predicts with high accuracy the behavior of the deposition rate in the examined temperature range and it confirms that the steep reduction of the deposition rate at high temperatures is due to the increased gas phase decomposition rate of $Fe(CO)_5$ and $Fe(CO)_3$ which yields less species available for deposition at the susceptor surface. It further confirms that the concentration of CO at the susceptor increases with increasing temperature and this implies inhibition of the surface. The computational analysis shows that gas phase reactions occur also at the reaction-limited regime, but with lower rates. Concerning the dependence of the deposition rate on the operating pressure, the combined experimental and computational investigation shows that as pressure increases the gas phase decomposition rates increase and the diffusion coefficients of $Fe(CO)_5$ and $Fe(CO)_3$ decrease. As a result the concentration of these species at the deposition surface decreases and consequently, the deposition rate decreases. Results from the computational model along the susceptor radius are in relatively good agreement with experimental measurements but the experimental trend cannot be fully predicted. A more detailed

chemistry path proposes the adsorption of $Fe(CO)_5$ on the surface and its subsequent surface decomposition. Such a model may account for different surface sites along the deposition surface and may improve the predictive capability in the radial direction.

Following the macroscopic computational analysis, a multiscale framework is developed for the simulation of the surface evolution and more specifically the evolution of the RMS roughness with temperature. In particular, the values of RMS calculated by performing multiscale computations are compared with those provided from experiments. The multiscale framework links the macroscopic 3D model of the reactor with a stochastic kinetic Monte Carlo algorithm through the mass fractions of the species contributing to the Fe deposition rate at the boundary of the surface and with the assumption that the deposition rate remains unchanged regardless the scale of simulation. As for the Al case, any chemical information is included in the sticking coefficient. This parameter is fitted to the experimental deposition rates and a temperature dependent function is obtained. The graphical representation of this function shows that the sticking coefficient decreases above 200^oC, thus accounting for the poisoning of the surface by CO and for the reduced surface decomposition rates of $Fe(CO)_5$ and $Fe(CO)_3$.

Results from the multiscale model are compared with the corresponding experimental values of Fe films processed in the same conditions. The framework predicts the RMS measurements with sufficient accuracy but discrepancies exist. The most important lies in the range 190^oC – 200^oC. In this range, the model shows a monotonous decrease of RMS whereas experimental data show a steep reduction. This discrepancy is attributed to the fact that no information is incorporated in the model concerning the morphology of the crystals and thus, the alteration of the microstructure in this range cannot be predicted. Finally, multiscale simulations at higher temperatures follow the experimental trend, i.e. the stabilization of RMS, in correlation with the number of migration events that reach a plateau.

The developed multiscale computational framework can be implemented to perform simulations for more detailed systems. The incorporation of chemical reactions at the nanoscale and the consideration of the exact physical crystallographic structure (*bcc* for Fe) of the developed material within the nanoscale algorithm may allow the simulation of more surface features such as island formation during the Fe growth.

Chapter 6: MOCVD of Al with Fe: Formation of the $Al_{13}Fe_4$ intermetallic structure

Chapter 6 presents the co-deposition and the sequential deposition processes of aluminum with iron for the formation of the intermetallic $Al_{13}Fe_4$ approximant phase. The co-deposition is first investigated as the most straightforward approach. Then the sequential deposition, eventually followed by thermal annealing is applied due to problems arising from the co-deposition process. The applied operating conditions of these MOCVD processes are deduced from the unary depositions of Al and Fe presented in the previous chapters. A series of characterization measurements are used for the definition of the chemical composition of the films as well as for the observation of their structure and microstructure. The development of the targeted $Al_{13}Fe_4$ approximant phase is described and discussed in details.

6.1. The phase diagram of the binary Al-Fe system

The phase diagram of the Al-Fe binary system is presented in Figure 6.1 (Massalski, 1990), with the aim to show the region of this diagram where the $Al_{13}Fe_4$ approximant phase is located and to explain from the beginning the rational which is followed for the co-deposition and the sequential deposition processes. In this phase diagram, the targeted $Al_{13}Fe_4$ phase is referred as Al_3Fe, a formula which has also been reported in the literature from other authors (Black, 1955; Ellner, 1995; Grin *et al*., 1994).

It can be observed that in Fe-rich part of the phase diagram the first phases after the solid solution (αFe) are $AlFe_3$ and AlFe, at temperatures between 400°C-600°C (in this work, we cannot apply temperatures higher than 660°C, since the latter is the melting point of Al). Moving to the Al-rich part of the phase diagram, first the Al_2Fe and the Al_5Fe_2 phases are formed in a narrow composition range and for temperatures up to *ca.* 1160°C. When the Al content reaches values in the range 75-77%, the $Al_{13}Fe_4$ (Al_3Fe) phase can be formed in the same temperature range. That is, by processing Al-Fe films, either by co-deposition or by sequential deposition, Al(75)Fe(25) should be targeted. The final composition of the Al-Fe films can be initially approached either by the ratio of the precursors in the input mixture or by the thickness of each metal in the final film. The validity of both approximations is presented in detail in the following sections.

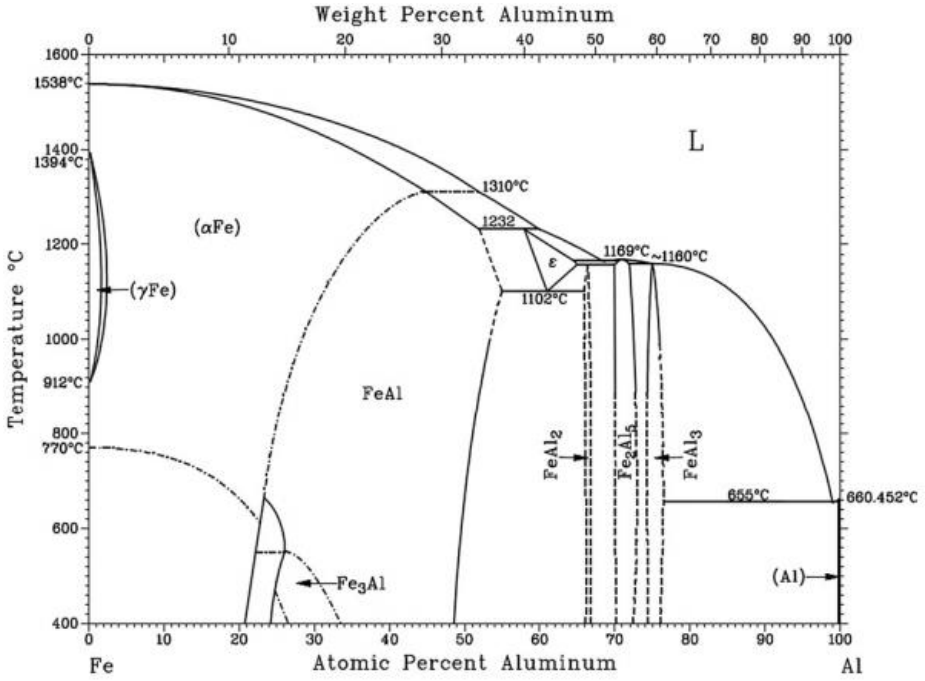

Figure 6.1: The phase diagram of the Al-Fe binary system from Massalski (1990).

It is recalled from previous chapters that depositions are performed at $T_s < 250^oC$ and for this reason a post deposition annealing is applied after the sequential deposition. In the next sections, the operating conditions which result to the desired Al-Fe composition within the films are thoroughly presented and discussed. Also, the annealing conditions which lead

to the formation of the targeted approximant phase are defined through a sequence of experiments, and they are discussed with regard to the homogenization of the film.

6.2. The co-deposition of Al and Fe

The investigation of the CVD of unary of Al and Fe films allows defining appropriate operating conditions in terms of deposition rate in order to proceed to the co-deposition of the two metals in accordance with the $Al_{13}Fe_4$ composition. This statement holds if purity and smooth microstructures are ensured in the CVD of unary Al and Fe. While this is the case for purity (both Al and Fe films are practically heteroatoms free as presented in the previous 2 chapters), the question of their microstructure and of the impact of both microstructures on the Al-Fe film processed by co-deposition remains an open question which will be discussed at the end of this chapter in view of the results.

Another concern with the co-deposition process is the possible interaction among the two precursors, their ligands and/or the by-products resulting from the partial or total thermal decomposition, either in the gas phase or on the growing surface. In this perspective, and since there is a lack of data for these interactions, knowledge of the temperature limits for the reaction and the transport limited regimes for Al and Fe growth is a useful parameter to drive the process, e.g. in a solely reaction limited regime (to reduce the impact of homogeneous gas phase phenomena) or in a temperature range where deposition is controlled by the surface reaction for one film and by diffusion phenomena for the other (to allow a supplementary degree of freedom so as to obtain films with the appropriate elemental ratios).

Whatever the phenomena which control the co-deposition process, the Arrhenius plots of unary Al and Fe films presented in the previous 2 chapters are valuable tools to make progress towards the one-step deposition of the $Al_{13}Fe_4$ approximant phase. Figure 6.2 presents these Arrhenius diagrams in a single plot in order to compare deposition rates and temperature ranges corresponding to reaction and transport limited regimes for both metals. It is recalled at this point that, for the deposition of Al films (black squares) the flow rate of the precursor is 2 sccm (Chapter 4) and for the Fe films (green squares) the precursor's flow rate equals 0.7 sccm, whereas the operating pressure for both processes is 10 Torr.

Figure 6.2 shows that the deposition rate of Fe is 50% higher than that of Al, almost at every deposition temperature in the investigated range. It is questioning though because the initial DMEAA/$Fe(CO)_5$ ratio in the input gas equals to 2.9. Whereas the conditions for the transport of the two precursors from their vessels to the deposition zone are technically the most favorable to maximize the Al/Fe ratio, the latter remains far from the targeted $Al_{13}Fe_4$ composition. Therefore, the superposition of the two Arrhenius plots reveals an inherent major difficulty for the processing of $Al_{13}Fe_4$ films by co-deposition. Despite this drawback, the co-deposition of Al with Fe is performed in order to explore the possibility to obtain Al-Fe intermetallics with a straightforward, one-step process.

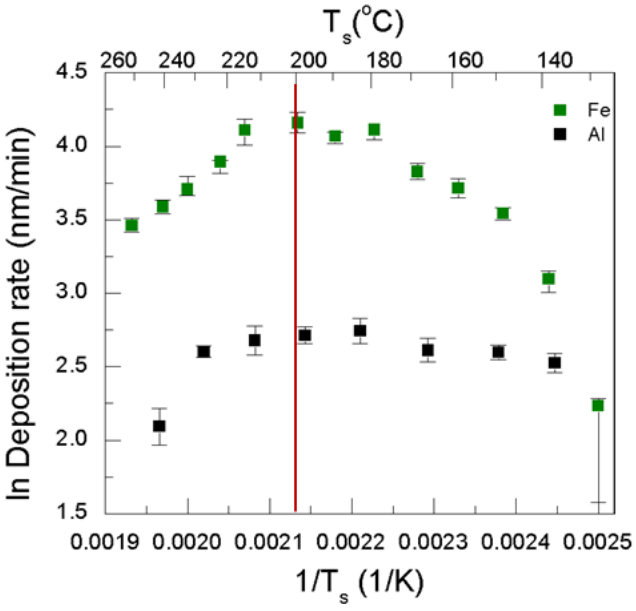

Figure 6.2: The two Arrhenius plots of the CVD of unary Al films (black squares) and Fe films (green squares) performed at $P_{reactor}$=10 Torr. The vertical red line corresponds to T_s selected for the co-deposition (see description below).

6.2.1. Experimental process

Al-Fe co-depositions are performed in the MOCVD reactor described in Chapter 2. 10 x 10 x 1 mm^3 Si flat coupons are used as substrates (from Si(100) silicon wafers, Sil'tronix). Cleaning is performed according to the protocol presented previously (see §2.1.2.). In each co-deposition experiment, three substrates are put at radial positions on the susceptor corresponding to a distance from the center equal to 0, 17 and 24 mm and illustrated in Figure 6.3. In this way, possible changes in the elemental composition of the films along the distance from the center can be monitored.

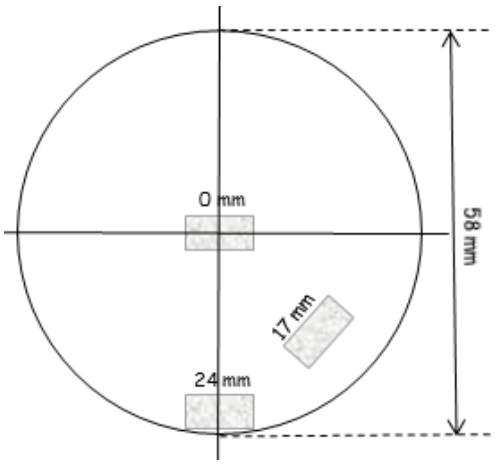

Figure 6.3: Schematic illustration of the positions of Si substrates on the susceptor during the co-deposition of Al with Fe. Numbers in [mm] correspond to the radial position of the center of the coupons to the center of the susceptor.

Co-deposition experiments are performed at fixed pressure and temperature, namely $P_{reactor}$=10 Torr T_s=200°C. Within the prerequisites set for the co-deposition process (see

Chapter 1), it is mentioned that during a co-deposition process it is preferable to operate at low temperatures, i.e., in the reaction-limited regime, so as to have only surface reactions and to avoid more complex gas phase reactions. However, as it is shown for both Al and Fe systems investigated at the present case (see Chapters 4 & 5), homogeneous reactions occur even at the low temperature range of the reaction-limited regime, and their presence is inevitable in the co-deposition process. Thus, by choosing to work at this particular T_s we are trying to limit the effect of the gas phase reactions, since Fe is processed in the limits of the reaction-limited regime and Al at a low temperature of the transport-limited regime where the decomposition of the precursor occurs with a moderate rate. Additionally, at this temperature, the deposition rate of Al is maximum, which is required to approach the targeted Al-rich composition of $Al_{13}Fe_4$. In terms of microstructure this T_s is the optimum for Al deposition since the RMS of the films is minimum and their density is high. Concerning Fe films at this T_s, their deposition rates is also maximum and their microstructure in terms of morphology is less preferable although the roughness is decreased.

The gas lines and the walls of the reactor remain at room temperature (i.e., 25^{o}C) in order to avoid increased gas phase decompositions or reactions between the precursors. The DMEAA and the $Fe(CO)_5$ precursors are evaporated from the bubbler as described in §2.1.1.5., and their mass flow rates in the input gas entering the reactor correspond to 2 sccm and 0.7 sccm, respectively. Considering that each molecule of the precursors contains one atom of metal, these flow rates correspond to an Al:Fe atomic ratio in the input gas equal to 13:4.6, to be compared with the targeted 13:4 atomic ratio in the films. It was not possible to further approach the latter atomic ratio in the input gas in the adopted configuration, due to the significant difference in the saturated vapor pressures of the two precursors and to subsequent technical constraints. H_2 (99.995% Air Products) is added in the input gas mixture with the aim to reduce the O-containing species produced by the decomposition of $Fe(CO)_5$ and thus decrease the potential contamination of the films and the oxidation of the Al layer. The total flow rate is fixed at 325 sccm and is composed of 25 sccm of N_2 carrier gas bubbling through DMEAA, 10 sccm of N_2 carrier gas bubbling through the $Fe(CO)_5$, the rest being N_2 dilution gas in the range 260-290 sccm and H_2 in the range 0-30 sccm. Finally, the duration of all co-depositions is 30 min. The co-deposition conditions for the 8 experiments are summarized in Table 1.

Table 6.1: Operating conditions for the co-deposition of Al with Fe.

#Experiment	1 (Al-Fe)	2 (Al-Fe)	3 (Al-Fe)	4 (Al-Fe)	5 (Al-Fe)	6 (Al-Fe)
Q_{N_2} (sccm)	290	285	275	270	265	260
Q_{H_2} (sccm)	0	5	15	20	25	30
Fixed conditions	T_s=200^{o}C, T_{walls}=25^{o}C, T_{lines}=25^{o}C, $P_{reactor}$=10 Torr, Q_{prec} = 2/0.7 sccm, Duration = 30 min					

6.2.2. Surface morphology and elemental composition of the Al-Fe films

Figure 6.4a shows a surface SEM micrograph of an Al-Fe film obtained by co-deposition at 200°C without H_2 gas (Table 6.1, Exp. #1). The morphology of the surface does not present any changes when H_2 gas is added in the input gas mixture (Table 6.1, Exp. #2 to #6). The film has a loose microstructure with open porosity and high roughness. It is compared to SEM micrographs of unary Al (Figure 6.4b) and Fe (Figure 6.4c) films. Both Al and Fe unary depositions result in porous films at this T_s. It appears that the co-deposited film at this T_s presents a similar morphology with the Fe, and no similarities with Al. The grains are not faceted and show the acicular morphology of the sole Fe film (see Figure 5.5 in Chapter 5).

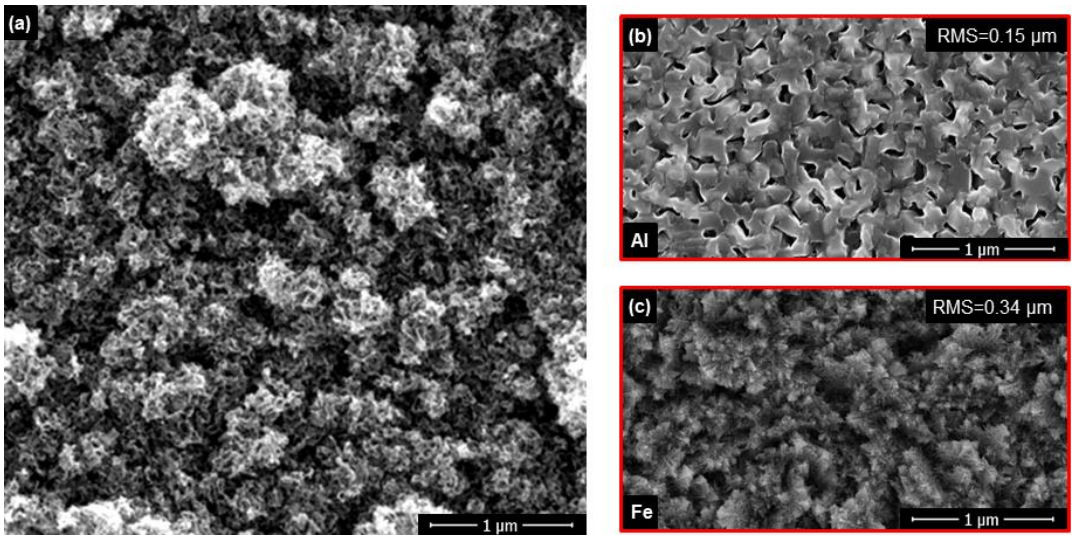

Figure 6.4: (a) A SEM micrograph of an Al-Fe co-deposited film obtained at the conditions of Exp. #1 showing a loose microstructure with porosity and roughness. (b) Al and (c) Fe obtained in the same conditions.

For the surface presented in Figure 6.4, EPMA measurements show that the film consists of 61 % Al, 9 % Fe, 5 % C and 23 % O (at.%). The amount of Fe is low, and the metal composition corresponds to an Al:Fe atomic ratio of 13:1.3 which is way off the targeted $Al_{13}Fe_4$ phase composition. This result is unexpected, since from the Arrhenius plot of Figure 6.1 one would expect to have more Fe in the film. However, we do not have an insight in the interactions between the two precursors. Thus, we assume that the $Fe(CO)_5$ molecule undergoes a high gas phase decomposition with the synergetic effect of the DMEAA precursor and for this reason much less Fe attains the surface. The relatively low C-content of the films is compatible with the clean decomposition of $Fe(CO)_5$ to provide Fe in a unary CVD process. On the other hand, the elemental O contribution is high and can be attributed to the oxophilic nature of Al which combines with the O coming from the gas phase decomposition of $Fe(CO)_5$ and prevents the formation of intermetallics phases to the benefit of oxides. Hence, the addition of H_2 in the input gas in Exp. #2-6 is tested, in order to investigate its impact on the decrease of O content.

Fig. 6.5 shows the mass gain rate along with the atomic elemental composition of the films, determined by EPMA analysis, as a function of the H_2 flow rate. Other processing conditions remain unchanged, as summarized in Table 6.1. As shown in Figure 6.5a, the mass gain rate increases as the flow rate of H_2 increases, before reaching a plateau at 25 sccm. In these conditions, the gain of the deposition rate corresponds to a twofold increase compared with the one obtained without H_2. Beside its potential function as a reducing agent of O atoms, H_2 also operates as a factor which shifts the equilibrium of Eq. (4.3) so as the Al deposition is unfavorable, in a similar way as in the case of the co-deposition of Al with Cu (Prud'homme *et al.*, 2013). Additionally, it seems that there is a simultaneous acceleration of the $Fe(CO)_5$ decomposition and hence, the increase of the mass gain is attributed to the increase of the Fe content.

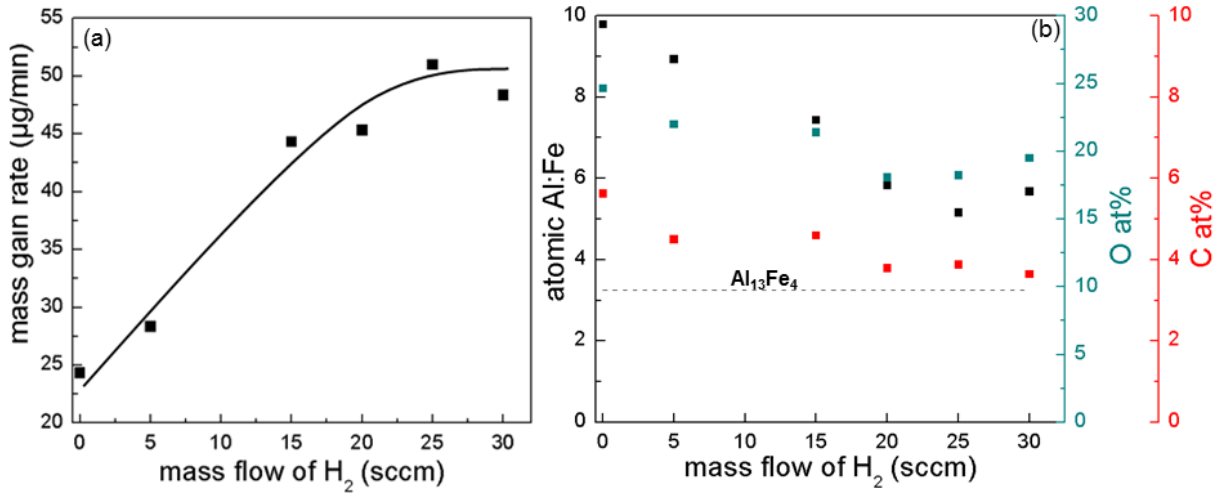

Figure 6.5: (a) Mass gain rate of the film and (b) Al:Fe ratio and heteroatoms composition (at%) as a function of the flow rate of H_2 in the input gas mixture.

This fact is confirmed by the atomic Al:Fe atomic ratio in the films as shown in Figure 6.5b, which presents marginal variations in the range 5 to 10. The Al:Fe composition corresponds at the best to an atomic ratio of 13:2.5, which approaches, but still remains far from the targeted $Al_{13}Fe_4$ one. The increase of H_2 flow rate does but slightly impacts the heteroatoms (C, O) content of the films. The carbon content remains in the range 4-6 at.%, while the oxygen content is significantly higher, in the range 18-25 at.%, that is no reducing effect of H_2 is observed. Yet, for a flow rate of H_2 equal or higher than 25 sccm it slightly decreases to *ca.* 18 at.% but remains constant for higher H_2 flow rates. It is concluded that the addition of H_2 in the input gas has an impact to the deposition of Al, since it favors the reverse of Eq. (4.3) over the formation of Al. At the same time H_2 seems to affect also the decomposition of the $Fe(CO)_5$, yielding the deposition of more Fe and the twofold increase of the mass gain rate; this impact is also illustrated by the Al:Fe ratio of the films which decreases with increasing H_2 flow rate, but still remains far from the targeted value. However, H_2 seems that it does not act as a reducing agent since it does not present a major cleaning and/or reducing effect allowing obtain pure metallic films.

Figure 6.6 presents the mass gain rate as well as the atomic elemental composition of the films, determined by EPMA analysis, along the susceptor's radius, for 25 sccm H_2 mass flow rate in the input gas mixture (Exp. #5). As shown in Figure 6.6a, there is an important variation of the mass gain rate along the susceptor, ranging from 34 μg/min at the center to 51 μg/min, which is the maximum rate, determined at the intermediate position. At the same time, the Al:Fe ratio presents variations in the range 5 to 8 (Figure 6.6b). The best atomic ratio of 13:2.5 is observed for the sample located at the edge of the susceptor, but remains far from the targeted composition. This particular sample presents also the lowest at% of heteroatoms contamination, that is, 18 % of O and 3.8% of C. Thus, the investigation of the possibility to form the $Al_{13}Fe_4$ approximant phase by co-deposition is limited to the sample placed at the edge of the susceptor in these particular operating conditions, with reserves yet concerning the O content.

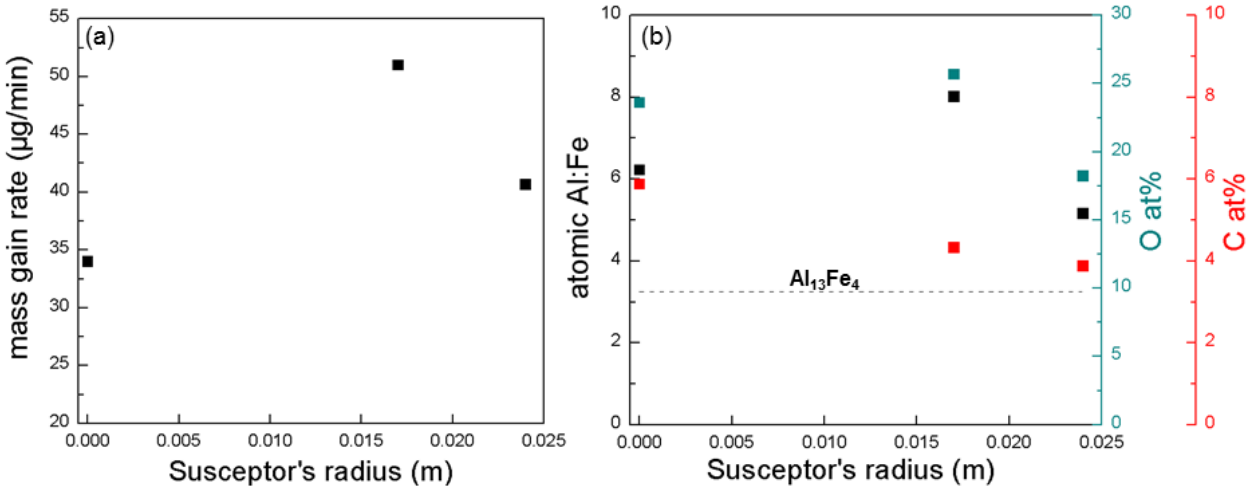

Figure 6.6: Mass gain rate (a) and Al:Fe ratio and heteroatoms composition (at% - b) along the susceptor's radius, at 25 sccm H_2 flow rate.

6.2.3. Structural characteristics

Fig. 6.7 presents the XRD pattern of a film processed with 25 sccm H_2 flow rate (Exp. #5) and located at the edge of the susceptor. All peaks of this diffractogram can be attributed to either *fcc* Al or *bcc* Fe (JCPDS card no. 04-0787 and 87-0722, respectively). In particular, no peaks are obtained at low 2θ angles where complex intermetallic structures diffract (Armbrüster *et al*., 2012; Ellner, 1995; Grin *et al*., 1994; Haidara *et al*., 2012).

All the XRD patterns obtained for lower, and down to zero H_2 flow rates as well as for the highest H_2 flow rate show the same peaks. Therefore, coatings obtained by co-deposition are made of *fcc* Al + *bcc* Fe + oxides and C which do not diffract (amorphous or nanocrystalline). No intermetallic phases are formed.

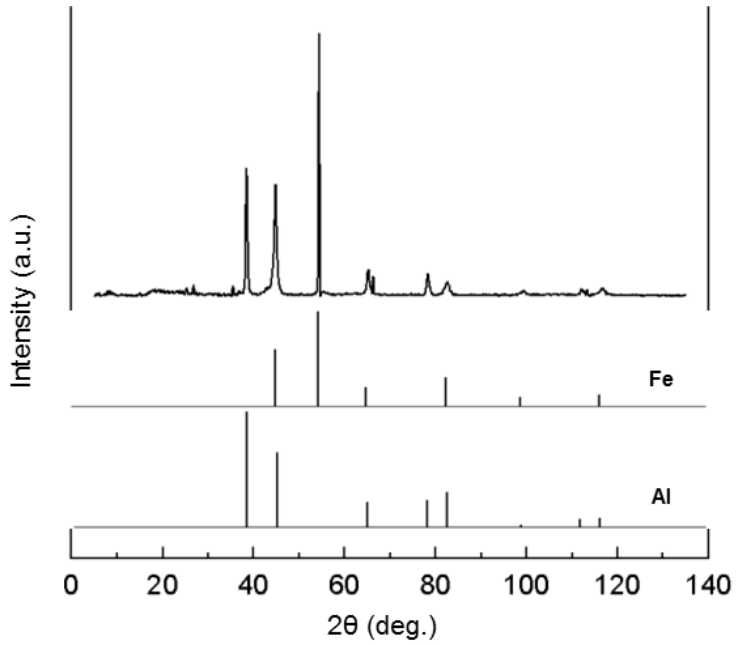

Figure 6.7: XRD diagram of the films obtained by the co-deposition of Al and Fe corresponding to the conditions of Exp. #5 (25 sccm H_2 flow rate) for a substrate located at the edge of the susceptor. The Al and Fe patterns are shown at the bottom of the figure (JCPDS card no. 04-0787 and 87-0722, respectively).

The co-deposition process has inherent difficulties concerning mainly the interactions of the two precursors in the reactor chamber. The main concern is the presence of O in the $Fe(CO)_5$ molecule which leads to the contamination of the co-deposited films. For this reason we have tested the impact of H_2 on the reduction of O heteroatoms during the co-deposition. It seems that the major impact of H_2 is on the surface reaction of Al where the equilibrium shifts to unfavorize the Al formation and on the acceleration of the decomposition of the $Fe(CO)_5$ on the surface. Indeed, addition of H_2 in the input gas mixture results in a twofold increase of the mass gain of the films with a simultaneous decrease of the Al:Fe ratio that is, increased Fe content of the films. The same impact of H_2 has been reported in the co-deposition of Al with Cu (Prud'homme *et al.*, 2013), where the increase of Cu concentration results in the formation of the γ-Al_4Cu_9 approximant phase. In the present case, the addition of H_2 has limited effect on the reduction of O contamination which benefits to the formation of oxides over intermetallic phases. For this reason, the combination of these precursors is abandoned for co-deposition. In order to bypass the interactions between the two precursors, a sequential deposition process is applied where the two precursors are never in contact in the reactor chamber.

6.3. Sequential deposition of Al/Fe layers

Sequential deposition is a two-step process involving the successive deposition of the two metals, so as to eliminate any interactions caused by the simultaneous presence of the two precursors in the reactor chamber. Annealing is often necessary after the sequential deposition, since the thermal budget available during the deposition of the second element is probably not enough, at such low T_s. Thus, additional energy is required to activate the

reactive diffusion and to stabilize the targeted phases. Sequential deposition allows choosing different operating conditions for the deposition of each element. That is, in the Arrhenius plots presented in Figure 6.2 different deposition conditions can be applied for Al and Fe for the *a priori* approach of the desired Al:Fe ratio.

The sequential deposition of the two metals is presented in two parts; first, the deposition is performed on Si substrates and the elemental composition as well as structural and microstructural characteristics are presented and discussed. Then, the deposition process is performed on glass and SiO_2 substrates and the formation of the targeted $Al_{13}Fe_4$ intermetallic phase is presented. The primary choice of Si as substrate lies in the fact that it provides facility of analysis over glass and the SiO_2 substrates. For example, glass provokes charging effects during SEM that are detrimental to the SEM imaging, while the O layer of SiO_2 may re-deposit within the films during FIB cutting. It is important to note here, that no silicides are formed in both unary depositions of Al and Fe and in co-deposition of the two metals. However, in these processes no high temperature annealing was applied which might enhance the formation of silicides. For this reason, glass or SiO_2 substrates are used when thermal annealing is required. We first used glass substrates since they were available when the sequential deposition process was set. Subsequently we have used thermal SiO_2 on Si because it is easy to break and crush into powder for the subsequent catalytic tests.

6.3.1. Deposition on silicon substrates

Al/Fe sequential depositions are performed in the MOCVD reactor described in Chapter 2. As for the case of co-deposition, 10 x 10 x 1 mm^3 Si flat coupons are used as substrates (cut from silicon wafers Si(100) Sil'tronix), upon their preparation according to the protocol presented previously (see §2.1.2.). In each sequential deposition experiment, three substrates are put at different radial positions on the susceptor presented in Figure 6.3 as in the case of the co-deposition.

The MOCVD of Al is performed at $P_{reactor}$=10 Torr and T_s=180^{o}C, while the temperature of the lines and the walls of the reactor is maintained at 25^{o}C. The flow rates during MOCVD of Al are as described before (see §4.1.).

The deposition of the Fe layer Fe is performed by using the DLI system, because DLI provides a better control of the precursor quantity in the input gas mixture as previously described (see §2.1.1.5.). Hence, the flow rate conditions during the MOCVD of the Fe layer correspond to 325 sccm of dilution N_2 which is injected with a frequency of 3 Hz. The conditions set to the liquid injector, namely frequency of 1 Hz and 2 ms opening time of the injector, yield a volumetric flow rate of the precursor equal to 0.02 mL/min (see §2.1.1.5.). The pressure and the temperature are set to $P_{reactor}$=10 Torr and T_s=140^{o}C, respectively and the temperature of the lines and the walls is kept at 25^{o}C. The experimental conditions are summarized in Table 6.2.

Table 6.2: Operating conditions for the Al/Fe sequential deposition on Si substrates.

#Experiment	1 (Al/Fe)	2 (Al/Fe)	3 (Al/Fe)
No of layers	4 – Al/Fe/Al/Fe	3 – Al/Fe/Al	2 – Al/Fe
Duration (min)	30/20/30/20	60/20/60	60/20
Fixed conditions for Al	T_s=180°C, T_{walls}=25°C, T_{lines}=25°C, $P_{reactor}$=10 Torr, Q_{prec} = 2 sccm Q_{N_2} = 325 sccm		
Fixed conditions for Fe	T_s=140°C, T_{walls}=25°C, T_{lines}=25°C, $P_{reactor}$=10 Torr, Q_{prec} = 0.02 ml/min Q_{N_2} = 325 sccm		

Three independent sequential depositions are performed by depositing different number of layers during each one of them. Thus, the first experiment includes the deposition of 4 layers (Al/Fe/Al/Fe), the second deposition consists of 3 layers (Al/Fe/Al) and the third of 2 layers (Al/Fe). For all 3 experiments, the duration of Fe deposition is 20 min while for Al layer it ranges from 30 min for the 1st experiment to 1 h for the 2nd and the 3rd experiments. In all cases, the first layer to be deposited is the Al in order to avoid any potential formation of interfacial Fe silicides. The reactive diffusion between Fe and Si may occur even at the low deposition temperatures of the Fe layer (Novet and Jonshon, 1991; Walser and Bené, 1976), although from the deposition of unary Fe films (Chapter 5) we do not observe any indication in this direction.

6.3.1.1. Elemental composition

Films obtained by sequential deposition on Si substrates consist of Al, Fe, O and C. The EPMA results are presented in Table 6.3. From these results it can be seen that when Fe is the last deposited layer (Exp. #1 and #3) its concentration is too high, in the order of 90% – 95%.

Table 6.3: EPMA measurements for the Al/Fe sequential deposition on Si substrates.

#Experiment	No of layers	Al at%	Fe at%	O at%	C at%
1 (Al/Fe)	4 – Al/Fe/Al/Fe	0	91	4.5	4.5
2 (Al/Fe)	3 – Al/Fe/Al	78	10	10	2
3 (Al/Fe)	2 – Al/Fe	0	95	2.5	2.5

Additionally, no Al detected in Exp. #1 and #3 because at a beam energy of 15 keV, the focused electron beam only penetrates up to 1 μm in Fe. The thickness of the Fe layers deposited in these cases are estimated at 2 μm from SEM cross sections (§6.3.2.3), thus, absorbing the majority of the signal. Nevertheless, the amount of atomic O is drastically reduced compared to the case of co-deposition from 20% to less than 5%. This steep reduction is due to the fact that during sequential deposition the two precursors never come in contact in the reaction chamber. As a consequence, we avoid any interactions among them and the deposition of each layer seems more likely to the decomposition schemes of each precursor presented in Chapters 4 & 5. The concentration of atomic C is systematically low and at the same levels as in the co-deposition process.

In the case where Al is the last deposited layer (Exp. #2), there is again limited detection. The penetrating capability of EPMA is limited to a maximum of 2.5 μm when Al is concerned. In the present case, the thickness of the Al layer is estimated at 6 μm. The Al

thickness is much higher comparing to the films investigated in Chapter 4. This is attributed to the fact that in this case the top Al layer is deposited on Fe which enhances the growth rate (see discussion in the next session). Thus, we cannot rely on the estimated 13:1.7 hypothetical ratio provided by the elemental analysis, since the Fe layer is poorly detected. On the other hand, we observe higher concentration of atomic O comparing to Exp. #1 and Exp. #3 cases. It is recalled at this point that after the deposition of the Fe layer, N_2 flow is used to carry out of the reactor chamber the leftovers of the $Fe(CO)_5$ decomposition. Then, the N_2 stops and the chamber is evacuated by applying primary vacuum (see §2.1.2.). It seems that the evacuation process is not that efficient to remove all of the $Fe(CO)_5$ by-products. Consequently, the oxophilic Al is partially oxidized by O residues which have not been evacuated from the reactor and the concentration of O in the film is shown to be higher. Porosity of the film further accentuates the oxidation.

EPMA is not very well suited for the high thickness of our films. Thus, the elemental composition down to the interface with the substrate cannot be defined properly. However, it provides useful information for the elemental composition of the top layer of the sequentially deposited films. That is, the O levels are in the range 5%-10%, lower comparing to the case of the co-deposition. O contamination is even less when Fe is the last deposited layer (e.g. Exp. #3) due to the absence of direct contact between Al and any O residues.

6.3.1.2. Structural characteristics

Fig. 6.8 presents the XRD pattern of a film processed in the conditions of Exp. #2 (Table 6.3). XRD patterns of Exp. #1 and #3 shows peaks at the same 2θ angles as the presented pattern. All peaks of the diffractogram can be attributed to either *fcc* Al or *bcc* Fe (JCPDS card no. 04-0787 and 87-0722, respectively) and there is an indication of iron silicides formation of the type FeSi (JCPDS card no. 38-1397). In particular, the large intensity peak at 44° is in agreement with the corresponding peak of the FeSi pattern. Moreover, the small peak at 27° can be attributed only to FeSi, as well as the shoulder of the small peak at 70°. Despite the separation of Si and Fe by an Al layer, the diffusion of Fe through Al and the reactivity between Si and Fe even at low temperatures results in the formation of FeSi (Novet and Jonshon, 1991; Walser and Bené, 1976), as the first phase in the Fe-Si system (Kolel-Veetil and Keller, 2010). This fact is illustrated in the next section, where the microstructure of the films is presented. Still, no peaks are observed at low 2θ angles where complex intermetallic structures diffract (Armbrüster *et al*., 2012; Haidara *et al*., 2012). We apply a thermal annealing process (see §6.3.2. & §6.3.3.), after the deposition of the Fe (last) layer, to favor the formation of intermetallics over silicides.

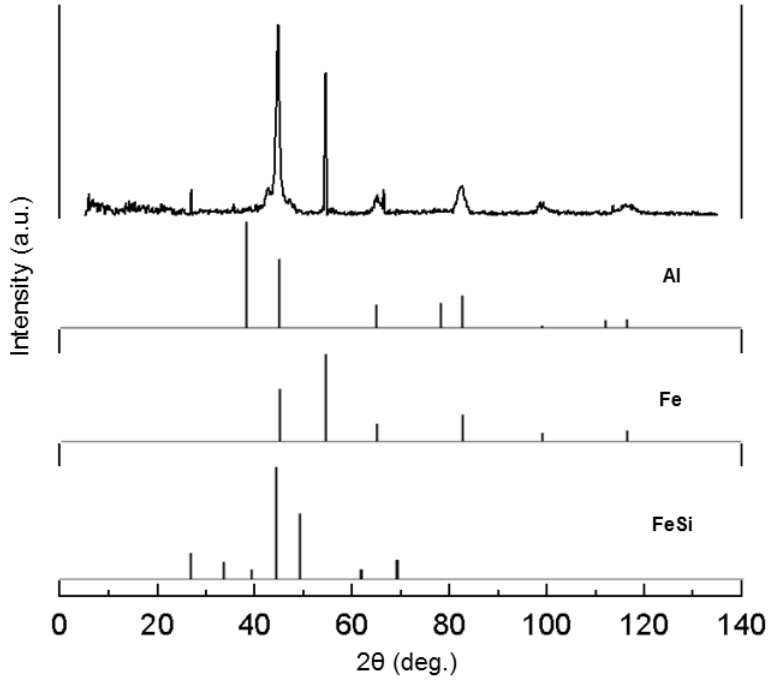

Figure 6.8: XRD spectrum of the films obtained by the sequential deposition of Al and Fe in the conditions corresponding to Exp. #2.

6.3.1.3. Microstructural characterization

Figure 6.9 presents a SEM micrograph of a cross section made on an Al/Fe/Al sample (Exp. #2), taken in secondary electron mode (Figure 6.9a) and in backscattered electron mode (Figure 6.9b). The thickness of the Fe layer is estimated to be 2 μm and the total thickness of the film equals 11 μm. Differences are observed in the morphology of the layers; the middle Fe layer is dense and uniform whereas the top and bottom Al layers are porous and rough. Discrepancies are also observed between the bottom Al layer and the top Al layer. These differences can be attributed to the different substrate, i.e., the bottom layer is deposited on Si, while the top layer is deposited on Fe. In Jang *et al.* (1998), it is reported that the MOCVD of Al from DMEAA results in films of different microstructure and thickness with regard to the substrate material. In particular, the morphology of an Al film deposited on TiN substrates is rougher than on Si substrates. This is attributed to the fast and homogeneous nucleation on the TiN substrate which accelerates the uptake of the upward growth rate to the expense of the coalescence rate of Al grains. This is assumed to result in an almost twofold increase of the growth rate of Al films deposited on TiN substrates at T_s=190^{o}C.

The same trend for the Al thickness is observed in our case, where Al layers are deposited at T_s=180^{o}C. More specifically, the first Al layer, deposited on Si, is estimated to be 3 μm, while the second Al layer, deposited on Fe, equals 6 μm. It is recalled that both Al layers are deposited in the exact same conditions, thus it is assumed that the nucleation on Fe occurs instantaneously, rendering higher deposition rates comparing to the deposition of Al on Si.

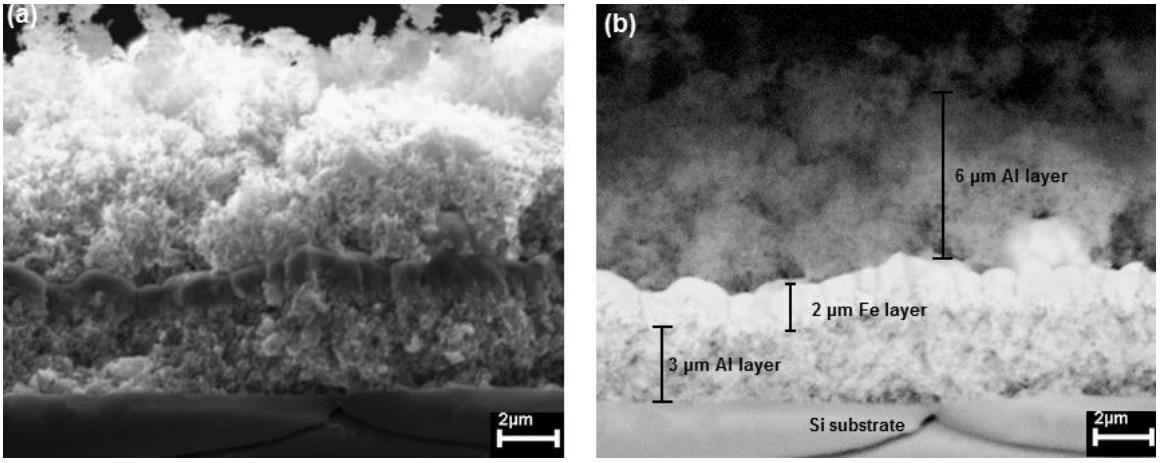

Figure 6.9: SEM micrographs of a cross section of an Al/Fe/Al film of Exp. #2, taken in (a) secondary electron mode and (b) backscattered electron mode.

Although the three deposited layers in Figure 6.9 are distinguishable from each other, we need to see if Fe interdiffuses through the Al layer, at this low process temperature (180^{o}C) and without any thermal annealing. In Figure 6.10b we perform a qualitative EDX elemental analysis for the sample corresponding to Exp. #2. We focus on the elemental analysis close to the interface with the substrate as indicated by the red circle. Fe is present although only Al is deposited on the Si surface.

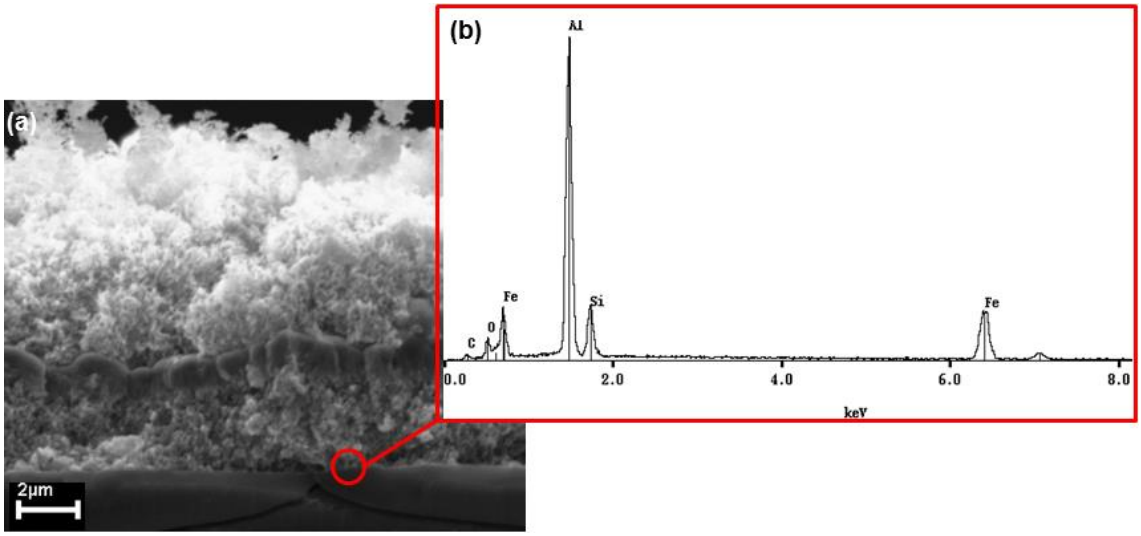

Figure 6.10: (a) A SEM micrograph of a film deposited in the conditions of Exp. #2 and (b) qualitative EDX elemental analysis at the area indicated by the red circle.

Thus, it can be assumed that even at the low temperature of 180^{o}C where the deposition of the second Al layer proceeds, the Fe already starts interdiffusing through Al to the substrate. This result can also explain the XRD pattern of the film (Figure 6.7), where indications for the formation of the FeSi phase are shown.

It is deduced that coatings obtained by the sequential deposition of Al/Fe on Si substrates in the applied operating conditions consist of *fcc* Al + *bcc* Fe + an Fe-Si phase, eventually. No Al-Fe intermetallic phases are formed. Therefore, to prevent the formation of

Fe silicides the sequential deposition on Si substrates is abandoned and alternative substrates are used.

6.3.2. Deposition on glass substrates – The $Al_{13}Fe_4$ phase

In this section a series of sequential depositions of Al/Fe on 10 x 10 x 2 mm^3 glass substrates is presented. Glass is an amorphous solid, kinetically trapped in a non-equilibrium state. It is a multicomponent system, based on SiO_2 but also containing oxides of many other elements including B, Ca, Na, Mg, K, Fe, Al or S. The choice of the glass as a substrate in order to avoid the formation of FeSi during the sequential deposition of Al/Fe lies in the presence of SiO_2 on the surface of the substrate which acts as a barrier to prevent the diffusion of ions from the substrate to the film deposited on it and vice versa. It is recalled at this point that, glass substrates are used prior SiO_2 ones, due to their availability at the time when these sequential depositions were performed. The substrates are prepared as designated by the protocol (Chapter 2) and they are placed on the susceptor as described in the previous sections.

Four independent sequential depositions are performed by depositing 2 layers, one of each metal as in the Exp. #3 of the previous section. Aiming at decreasing the Fe content and at the same time increasing the Al content in the film, we decrease the deposition temperature of Fe to T_s=140^{o}C while the deposition temperature of Al remains at 180^{o}C. In addition, we decrease the operating pressure to $P_{reactor}$=5 Torr for the Al layer and we increase it to $P_{reactor}$=40 Torr for the Fe layer. At these pressures, we have shown the Fe deposition rate decreases (see Chapter 5) while the corresponding of Al is expected to increase by assuming that the same trend holds for the DMEAA precursor. The total flow rate of the input gas mixture as well as the flow rates of the two precursors remains the same as for the case presented in the previous section, i.e., 325 sccm of N_2 gas and 2 sccm of DMEAA during the MOCVD of the Al layer. For the MOCVD of the Fe layer, the 325 sccm of N_2 are injected with a frequency of 3 Hz, while the 0.02 ml/min of the $Fe(CO)_5$, precursor are injected with a frequency and an opening time of 1 Hz and 2 ms, respectively. In all cases the walls of the reactor and the lines are maintained at room temperature.

Figure 6.11 recalls Arrhenius plots of the MOCVD of Al and Fe deposited at $P_{reactor}$=10 Torr, with the addition of a crucial single point which is represented by the red triangle and corresponds to the MOCVD of Fe with $P_{reactor}$=40 Torr and T_s=180^{o}C. We have already shown in Chapter 5 (see Figure 5.4 and 5.13) that a fourfold increase of the process pressure yields an eightfold decrease of the Fe deposition rate, from 58 nm/min to 7 nm/min. At this pressure, the Fe deposition rate becomes lower than that of Al, making possible the formation of the Al-rich phase.

Thus, by increasing the process pressure of Fe, its thickness can be controlled with regard to the targeted 13:4 ratio. For the MOCVD of Al there are no similar experimental results. However, we have shown computationally (see Figure 4.14 in §4.2.3.) that a decrease

of the operating pressure results in the increase of the Al deposition rate, in the range 139°C – 215°C where the computational model predicts the experimental data with sufficient accuracy. Thus, by following modeling results, we decrease the pressure for the deposition of the Al layer to increase its deposition rate.

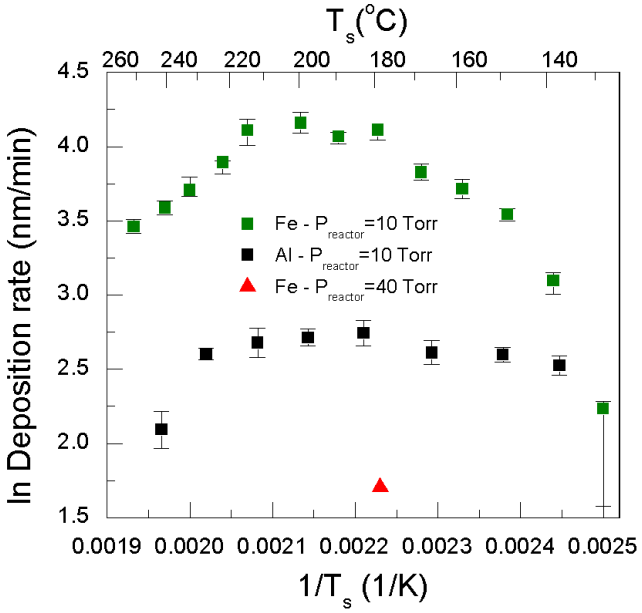

Figure 6.11: The Arrhenius plots of Al (black squares) and Fe (green squares) deposited at 10 Torr and a single measurement of a Fe film deposited at 40 Torr (red triangle).

After sequential deposition, an *in situ* thermal annealing is performed. We have seen so far that, during the co-deposition and the sequential depositions on Si, oxides and silicides are formed, respectively, instead of intermetallics. Thus, a process is required to enhance the reactivity between Al and Fe and to favor the formation of intermetallic phases. Thermal annealing which follows sequential deposition proven its efficiency in this perspective (Aloui *et al.*, 2012; Haidara *et al.*, 2012; Teixeira *et al.*, 1989). We choose annealing temperature from the Al-Fe binary phase diagram (Figure 6.1) and from literature results (Haidara *et al.*, 2012). Thermal annealings are thus performed at T_{anneal}=500°C and T_{anneal}=575°C for 1 h. The annealing process is performed in situ, in the reactor chamber in order to avoid exposing the film to air which may lead to its O contamination. The Fe deposition time is 5 min in all cases except for Exp. #1 (10 min). The Al deposition time is 60 min in all cases except for Exp. #4 (90 min). All the process conditions applied for the sequential deposition on glass substrates are presented in Table 6.4.

Table 6.4: Operating conditions during the sequential deposition of Al/Fe on glass substrates.

#Experiment	1 (Al/Fe)	2 (Al/Fe)	3 (Al/Fe)	4 (Al/Fe)
$P_{reactor}$ (Torr)	10/10	10/10	5/40	5/40
Duration (min)	60/10	60/5	60/5	90/5
T_{anneal} (°C)	500	500	575	575
Thermal annealing duration (min)	60	60	60	60
Fixed conditions for Al	T_s=180°C, T_{walls}=25°C, T_{lines}=25°C, Q_{prec} = 2 sccm Q_{N_2} = 325 sccm			
Fixed conditions for Fe	T_s=140°C, T_{walls}=25°C, T_{lines}=25°C, Q_{prec} = 0.02 ml/min Q_{N_2} = 325 sccm			

The results following in the next sections are presented first for Exp. #1 and #2 and then, for Exp. #3 and #4 in order present the effect of the pressure, time and annealing conditions on the films.

6.3.2.1. Elemental composition

Since EPMA provides limited information within the depth of the films, the elemental composition is defined indirectly through the thickness of each layer. To define this thickness the following procedure is adopted. All the samples are weighted before and after deposition and their mass gain is measured. The thickness of the Fe layer is defined by performing XRF measurements and it is converted to mass by using the surface area of deposition and the density of the solid Fe. Al is not detectable with XRF (Chapter 2 – §2.2.3.) and for this reason, the mass of Fe is subtracted from the total mass gain of the film to provide the mass corresponding to the Al layer. The latter is then converted to thickness with the use of the Al density. Considering the microstructure of the Al-Fe films which reveals significant porosity (see §6.3.2.3.), this assumption is very rough for thickness estimation. But, it is a useful tool which provides a primary estimation for the elemental composition of the films that, unlike thickness, relies on mass. Complementary techniques such as STEM/EDX and XPS analysis are used for the determination of the chemical composition.

The atomic composition is estimated from mass gain measurements, with the assumption that no heteroatoms are included in the layer. Figure 6.12 presents the calculated Al:Fe ratios for Exp. #1 to #4, as a function of the operating pressure (Figure 6.12a) and the process time (Figure 6.12b). That is, by increasing the pressure and reducing the duration if the deposition of the Fe layer and at the same time by decreasing the pressure and increasing the duration of the deposition of the Al layer the Al:Fe ratio is not only enhanced with regard to the targeted one, but also approaches the 13:4, when the conditions of Exp. #4 are applied.

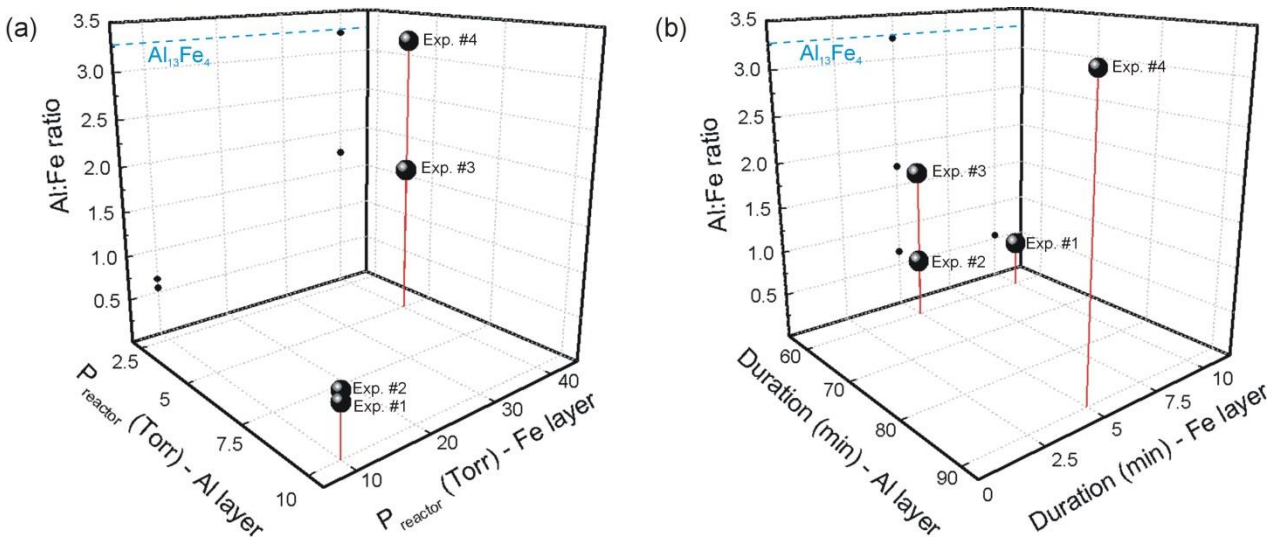

Figure 6.12: The calculated atomic Al:Fe ratio as a function of (a) the operating pressure and (b) the time duration applied for the deposition of each layer. Black circles are projections of the measurements on the YZ plane (Al:Fe ratio axis). The dashed blue line corresponds to the $Al_{13}Fe_4$ composition.

For this particular sample (Exp. #4), a GD-OES analysis is performed and presented in Figure 6.13 which gives the qualitative elemental composition profiles through the film thickness. Although not quantitative the GD-OES analysis provides some useful information. The continuity of the Al and Fe profiles through the film thickness reveal that they have intermixed during the *in situ* annealing. However, such intermixing does not result in homogeneous composition along the thickness. A chemical composition gradient along the depth is observed. The Fe concentration monotonously increases from the surface of the film to the interface with the substrate, despite the fact that it is deposited on the external part of the bilayer, on the surface of the Al film. Consequently, the Al:Fe ratio decreases from the area close to the surface and as the substrate is approached (Figure 6.13a).

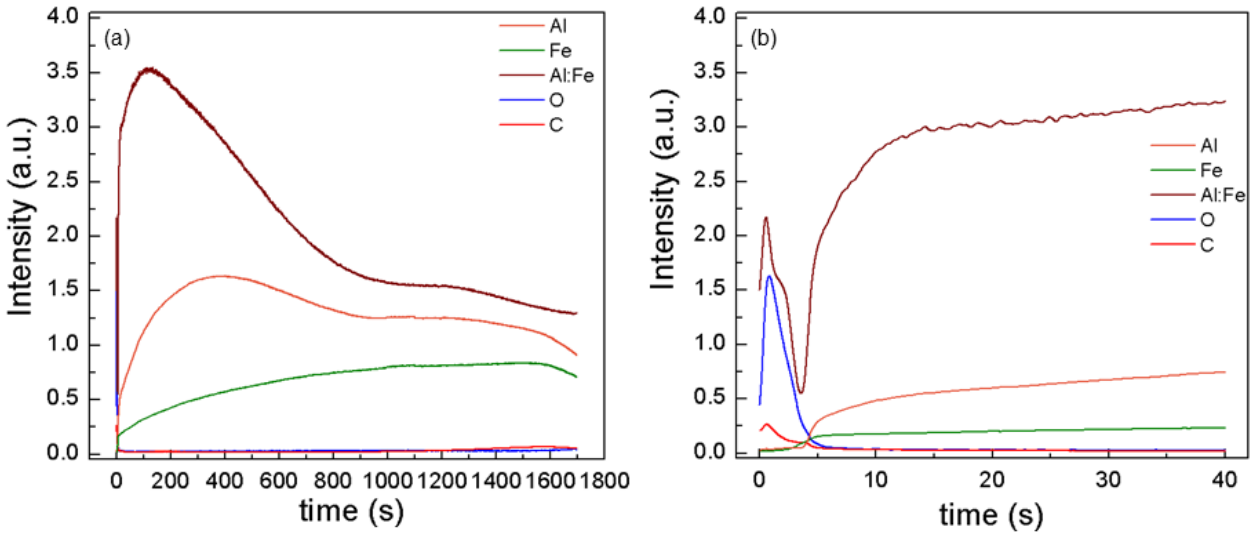

Figure 6.13: Qualitative depth profiles obtained by GD-OES analysis of the film of Exp. #4, (a) through the whole depth of the film and (b) closer to the surface level (t<40 s).

This observation is in agreement with results reported in the literature (Kajihara, 2006; Naoi and Kajihara, 2007), where it has been shown that in the range 550°C-640°C the formation of stable intermetallic phases in the binary Al-Fe system occurs at the interface. The decrease of the Al:Fe ratio through the film is further confirmed from the TEM and STEM/EDX analyses presented in section 6.3.2.3. Furthermore, the O and C contamination remains low within the film. Indeed, by zooming in at the surface level (Figure 6.13b – t < 40 s), it can be observed that O and C heteroatoms cause a superficial contamination. The absence of O through the thickness of the film is discussed in the following XPS results.

XPS is now used for the characterization of the surface of the sample Exp. #4 and for the quantitative composition at the surface level. A 100 nm top layer is etched in order to recover a fresh metallic surface. Due to the fact that the vacuum in our XPS chamber is relatively high (10^{-8} mbar), a continuous oxidation of the surface is observed, in the form of alumina. For this reason atomic O is excluded from the elemental composition of the Al-Fe film. The Al:Fe ratio equals 13:4.3, i.e., very close to the desired 13:4 ratio. Figure 6.14 shows the Fe 2p and the Al 2p XPS spectra of this surface. The Fe 2p spectra (Figure 6.14a)

reveals only one peak attributed to an Al-Fe alloy with a small chemical shift (0.22 eV) with regard to the Fe 2p peak of the reference Fe sheet. This difference is characteristic of the altered electronic structure in intermetallic compounds with transition metals and has also been observed in the Pd-Ga system (Konvir *et al.*, 2009).

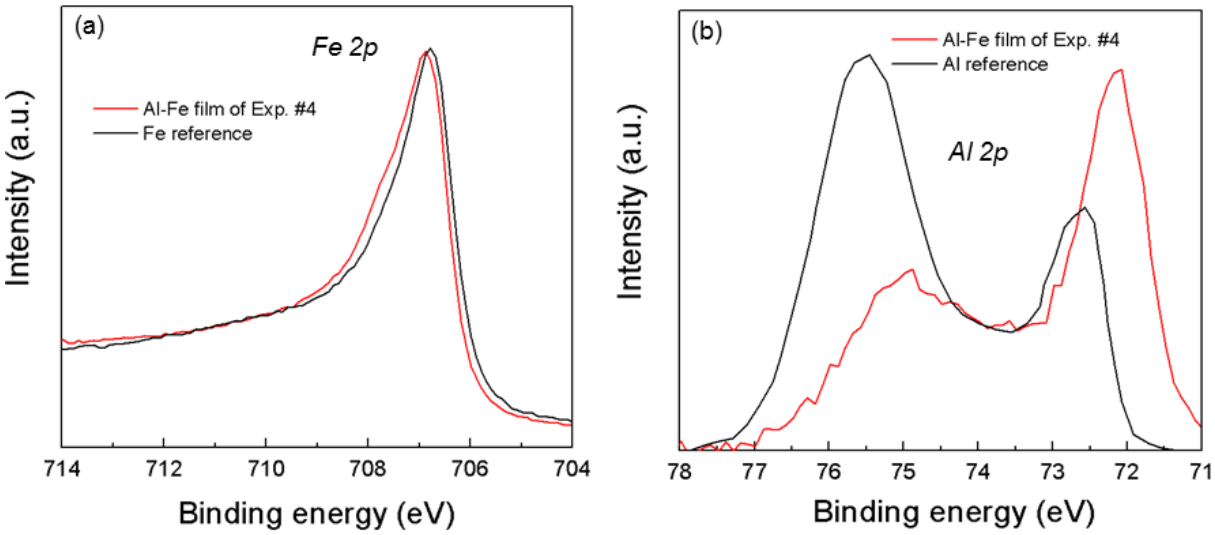

Figure 6.14: The XPS spectra of the Al-Fe film of Exp. #4. (a) Fe 2p XPS spectra in comparison with a Fe reference. (b) Al 2p XPS spectra in comparison with an Al reference.

The contribution at 72.2 eV in the Al 2p spectra (Figure 6.15b) corresponds to metallic Al, while the second signal at *ca.* 74.6–75.6 eV corresponds to oxidized Al. The oxide contribution decreases with increasing depth before it stabilizes at the level of Figure 6.14b. This confirms the superficial O contamination observed in GD-OES (Figure 6.13) and reveals the formation of a surface Al oxide which cannot be avoided completely because of the important open porosity of the films exposing extended surface areas to ambient air and the relatively high pressure in the XPS chamber. These results are in good agreement with the same XPS characterizations performed on the surface of a bulk $Al_{13}Fe_4$ sample (Armbrüster *et al.*, 2012), where the Fe 2p core-level spectra has fine differences such as small shift, decreased half-width and reduced asymmetry, from the elemental iron and the Al 2p spectra has an Al contribution at 72.5 eV and an Al_2O_3 contribution at 75.5 eV. Overall, it is assumed that the surface is composed of a thin alumina layer formed by the preferential segregation of Al to the surface, but limited enough to prevent the dissolution of the Al-Fe alloy underneath.

6.3.2.2. Structural characteristics

Figure 6.15 presents the XRD pattern of the film obtained in Exp. #1. All peaks of this diffractogram can be attributed to either *fcc* Al (JCPDS card no. 04-0787) or *bcc* Fe (JCPDS card no. 87-0722) and no peaks are obtained at low 2θ angles where complex intermetallic structures diffract. Thus, the applied conditions for Exp. #1 and #2, including 1 h of thermal annealing at 500°C, are not the proper for the formation of intermetallic Al-Fe alloys. A similar pattern is obtained for the film of Exp. #2.

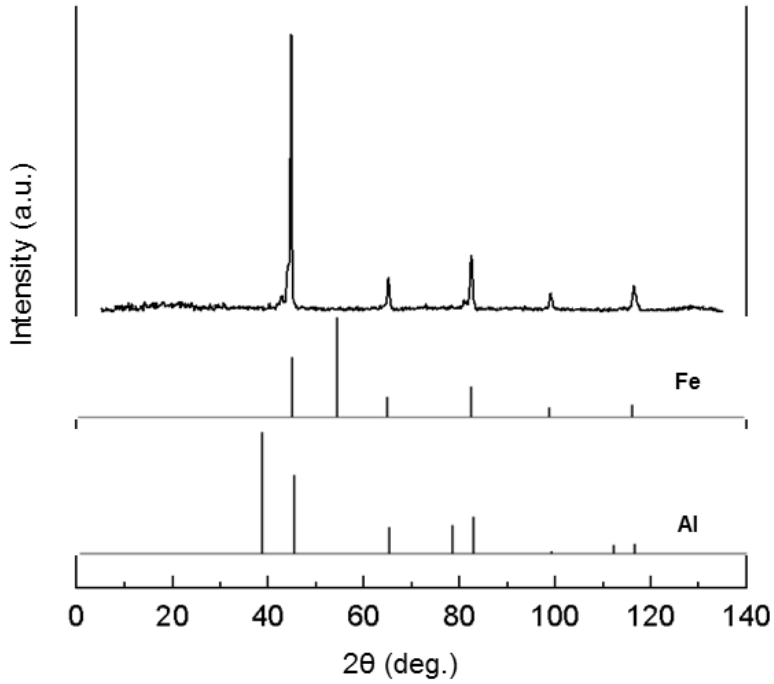

Figure 6.15: XRD spectrum of the films obtained in the conditions of Exp. #1 and #2.

Figure 6.16 shows the XRD pattern of the film obtained in Exp. #3. It is recalled at this point that between Exp. #2 and #3 the operating pressure during the deposition of Al and Fe layers changes as well as the annealing temperature. This figure is the first evidence for the existence of intermetallic phases.

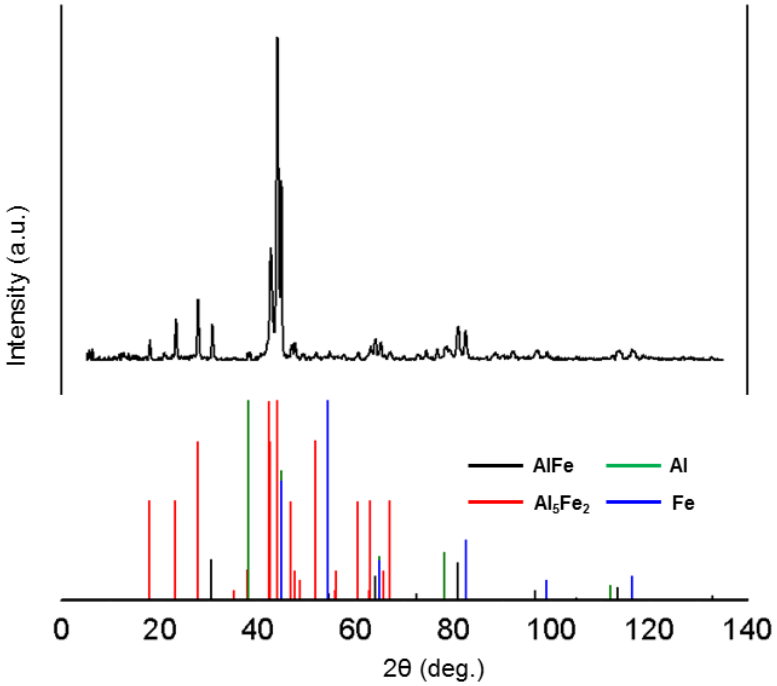

Figure 6.16: XRD spectrum of the film obtained at Exp. #3. The JCPDS of the intermetallic phases AlFe and Al_5Fe_2 as well as of the crystalline Al and Fe are also depicted.

In particular, the AlFe (JCPDS card no. 33-0020) and the Al_5Fe_2 (JCPDS card no. 29-0043) intermetallic phases are observed. The peaks at the low angles 18°, 23°, 28° and 39° are

attributed to the Al_5Fe_2 phase, as well as the two large peaks at 43° and 44°. There are also some smaller peaks at 47°, 61° and 63° which correspond also to the same phase. On the other hand, the peaks at 31°, 81°, 97° and 114° match well the pattern of the AlFe intermetallic phase. The remaining peaks which do not match any of the two intermetallic patterns, are attributed to unreacted *fcc* Al (peaks at 65°, 78° and 116°, JCPDS card no. 04-0787) and *bcc* Fe (peaks at 65°, 83°, 100° and 117°, JCPDS card no. 87-0722). The AlFe phase is located mostly in the Fe-rich part of the Al-Fe phase diagram. To the contrary, the Al_5Fe_2 phase is located at the Al-rich part of the Al-Fe phase diagram but still before the $Al_{13}Fe_4$ phase (Figure 6.1). We can deduce that the amount of Fe is above the targeted $Al_{13}Fe_4$ phase composition. Thus, the time duration of the deposition of the Al layer is increased (Exp. #4) to increase the Al content in the final film.

Figure 6.17 presents the XRD pattern of the Al-Fe film obtained at the conditions of Exp. #4. The spectrum is compared with the $Al_{13}Fe_4$ XRD pattern reported in Ellner (1995) and Grin *et al*. (1994). The comparison of the pattern is not performed with the JCPDS cards of the $Al_{13}Fe_4$ phase (no. 29-0042 and 65-1257), since the latter show peaks up to 60°, only.

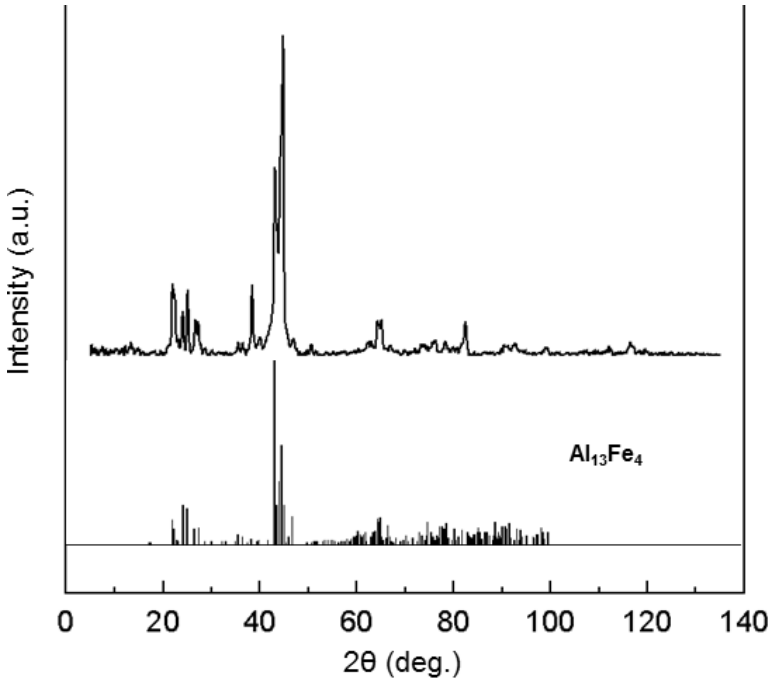

Figure 6.17: XRD spectrum of an Al-Fe intermetallic film of Exp. #4 (top) compared with the $Al_{13}Fe_4$ pattern (bottom) calculated in Ellner (1995) and Grin *et al*. (1994).

A good match between the XRD spectrum and the two literature patterns is observed confirming the formation of the $Al_{13}Fe_4$ intermetallic structure. In particular, peaks at low 2θ angles, *ca.* 20°-30° as well as the large peaks between 40°-50° and some smaller peaks at higher 2θ angles are characteristics of the existence of the approximant monoclinic m-$Al_{13}Fe_4$. However, in the presented XRD pattern, there are a few peaks that do not match the $Al_{13}Fe_4$ diffractogram of the literature and reveal that other phases co-exist. Specifically, the peak at 38°-39° can be attributed to the Al_5Fe_2 phase and to pure Al (JCPDS card no. 29-

0043 and 04-0787, respectively) and the peak at 50° to the Al_5Fe_2 phase. The intensity of the peak at around 45° implies that within the film there exists unreacted Fe (JCPDS card no. 87-0722). The peak at 82° matches very well the *fcc* Al and the *bcc* Fe crystalline structures whereas the two last peaks at *ca.* 112° and 117° correspond to *fcc* Al. The $AlFe_3$, which is the most stable Fe aluminide, is not observed in the XRD pattern (JCPDS card no. 06-0695). From this analysis, it can be deduced that apart from the presence of the secondary Al_5Fe_2 approximant phase, there is an excess of unreacted Al in the film. The latter conclusion is in agreement with the phase equilibria in the Al-Fe binary system, indicating that pure *fcc* Al is in equilibrium with the $Al_{13}Fe_4$ phase (Black, 1955; Massalski, 1990). It also reveals that annealing time (60 min) is not long enough to homogenize the composition within the film (see also the discussion of the TEM results).

Consecutively, SEM and STEM/EDX are used to monitor the composition uniformity, to further confirm the formation of m-$Al_{13}Fe_4$ and to identify secondary phases, and finally to get a better insight into the film microstructure.

6.3.2.3. Microstructural characterization

Figure 6.18 presents a SEM micrograph of a cross section of the Al-Fe film #4, prepared by FIB. It is recalled that the Pt layer is deposited on top of the film in order to avoid the oxidation of the film during the FIB cutting. Observation at low magnification (Figure 6.18a) shows a 15 μm thick film with significant surface roughness and porosity. A higher magnification of a region in the center of the film pointed by the red circle (Figure 6.18b) and an elemental mapping of this region (Figures 6.18c and d) reveals intermixing of the two elements as. The elemental mapping shows also detection of O and especially around the pores. The O may re-deposit from the glass substrate during the cross-section.

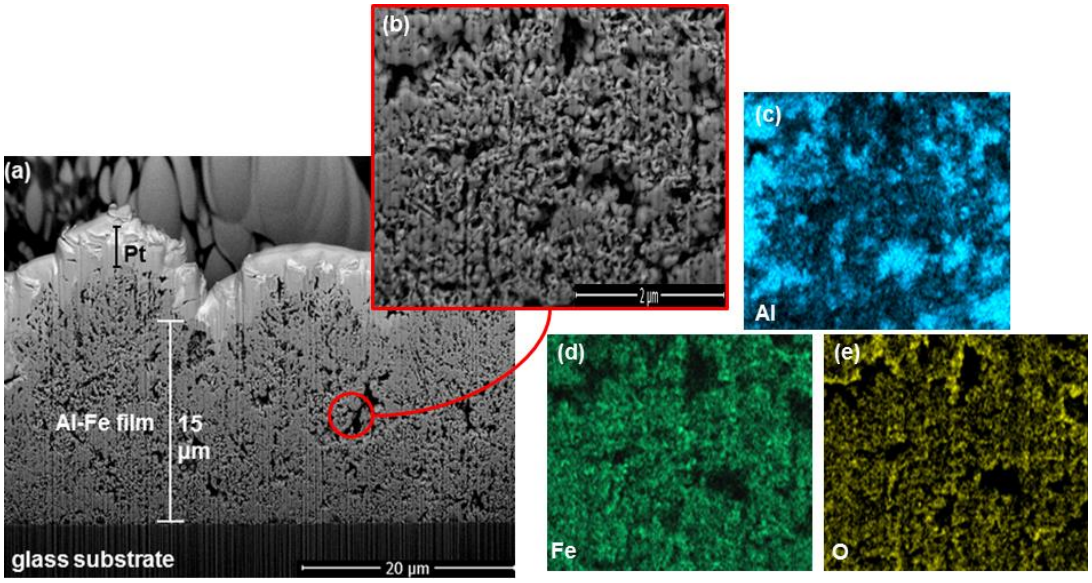

Figure 6.18: (a) A FIB-SEM cross section showing a 15 μm thick Al-Fe film. (b) A higher magnification shows that Al (c) and Fe (d) are intermixed as it can be confirmed from the elemental mapping at this point. (e) Oxygen is also detected within the film.

A TEM lamella is prepared by FIB (Figure 6.19a) from the cross section of the previous figure (sample Exp. #4). A 1.2 µm thick layer is etched from the two sides of the lamella, due to its high initial thickness that renders it inappropriate for TEM. The etching process increases the porosity and finally, a fragile lamella is created with a thickness of 85 nm in the z direction. In the SEM micrograph of the lamella (Figure 6.19a), no pure Al regions are observed, meaning that alloying is effective across the whole coating. However, a composition gradient still exists: the Fe concentration is higher at the interface and decreases up to the surface. For instance, it is observed in Figure 6.19b that more than 50 vol. % of the bottom part of the lamella is composed of Fe-rich grains (e.g. Al(25)Fe(75) or Al(15)Fe(85) measured by STEM/EDX). In the upward direction (to the right in Figure 6.19a), the fraction of Fe-rich grains decreases until the top 2-3 µm-thick layer where the composition is homogeneous.

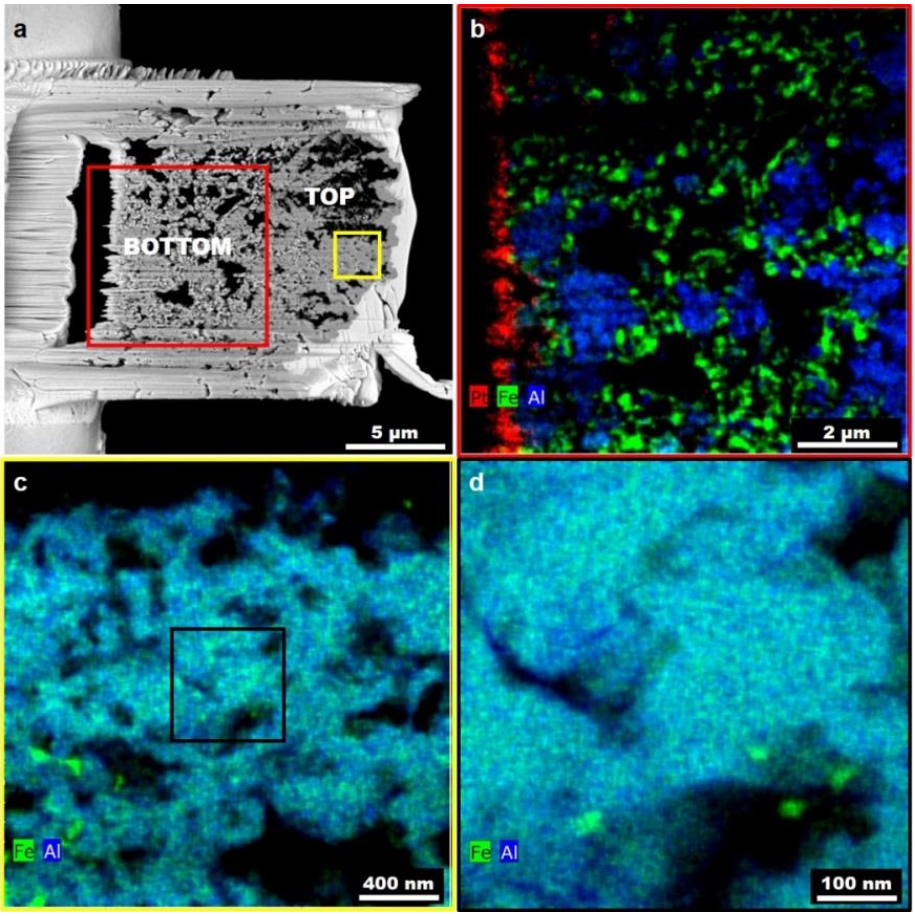

Figure 6.19: (a) Lamella of the sample Exp. #4 prepared by FIB. STEM-EDX mapping of (b) the bottom (red) square and of (c) the top (yellow) square. (d) A higher resolution STEM-EDX map within the black square in c.

Figure 6.19c shows the mapping of the chemical composition in the top region. Except for some Fe-rich inclusions at the bottom (left of the image), we observe a homogeneous Al(75)Fe(25) matrix, corresponding to the m-$Al_{13}Fe_4$ composition. A higher resolution map corresponding to the black square is shown in Figure 6.19d. A few 20-40 nm wide Al(53)Fe(47) inclusions (bright green contrast) are found. At the edges of the matrix,

and surrounding pores, a slightly higher Al content than in the matrix is found (Al(79)Fe(21)). This Al enrichment is correlated with the presence of O. Al preferential oxidation is common in Al-transition metal alloys, and this is in good agreement with the formation of Al oxide at free surfaces that is confirmed in XPS measurements (Figure 6.14). It cannot be assessed, though, if this oxidation occurs during the film formation or *ex situ* during the lamella preparation/transfer (from Toulouse, France to Julich, Germany).

It is further observed that Fe diffuses towards the interface with glass, readily at its MOCVD deposition temperature (140^{o}C). When temperature is increased for *in situ* annealing (575^{o}C), it is assumed that Al-Fe phases first form in the vicinity of the interface. This is corroborated by the STEM/EDX observations made on the lamella, where Fe-rich grains concentrate in the vicinity of the interface. Since the microstructure exhibits a high concentration of defects - in the form of grain boundaries and porosity - Fe diffusion may be facilitated.

The sequential deposition of Al/Fe on glass substrates, in the operating conditions of Exp. #4 including an in situ annealing at 575^{o}C for 1 h, yield the formation of the $Al_{13}Fe_4$ intermetallic phase. The sequential deposition is repeated in the conditions where the $Al_{13}Fe_4$ film is obtained, for its deposition on thermally oxidized Si wafers, hereafter named SiO_2 for convenience.

6.3.3. Deposition on SiO_2 substrates

A series of 6 sequential depositions is performed on SiO_2, substrates for the production of $Al_{13}Fe_4$ of total mass 185 mg to be used for the catalytic tests, as demanded by the catalytic institute of IRCELYON. Three silicon wafers, with a radius of 5 cm, are treated under O_2 atmosphere at 1100^{o}C for 50 min and under Ar atmosphere for 10 min. This treatment provides the SiO_2 substrates with an O_2 layer of 100±10 nm thickness. The wafers are then cut into 40 x 40 mm^2 and 10 x 10 mm^2 squares to be used as substrates for the sequential deposition. Prior deposition experiments the substrates are prepared according to the protocol (Chapter 2). In each experiment, a large and a smaller substrate are used and they are placed on the susceptor, at its center and its edge, respectively. The bigger sample to be deposited is used for the catalytic tests, whereas the smaller one is used for the various analyses of the obtained films. The operating conditions applied in this case are the same as for the deposition on glass substrates and they are described in detail in the previous section.

6.3.3.1. Elemental composition

The definition of the elemental composition is performed in the same way as described in §6.3.2.1. with the exploitation of the thickness and the mass of each deposited layer. In this way and by applying the conditions of Exp. #4, the elemental composition of Al and Fe within the obtained films varies slightly in the range 74-77 at% and 23-26 at%, respectively. The reproducibility of the results shows that the sequential deposition process

for the development for the $Al_{13}Fe_4$ approximant phase as set in the framework of this thesis is a robust process.

The heteroatoms contained in the film are qualitatively estimated through EDX analysis providing the elemental mapping on a cross section created by FIB on the film at a random point and they are presented in Figure 6.20. As shown in Figure 6.20, C contamination of the film seems to be very low. From the O and Si images we distinguish the SiO_2 substrate containing the Si and the oxide layer on top of it. O and Si are detected within the film. In particular, it seems that these two elements exist in appreciable levels and especially, within the pores of the film. However, it is believed that this trend is observed due to the re-deposition of O and Si during the FIB cross section and thus, their detection is not a matter of concern. The Al and the Fe are completely intermixed since the Fe layer which is deposited on top of the film is detected through the whole depth of the film. The only region that Fe is not traced is within the large pores. At these regions only the oxophilic Al exists and this fact explains the apparent high concentration of O at the same regions. The higher concentration of Fe at the interface with the SiO_2 substrate has been already observed in the case of the glass substrate and it is presented also in a next section where high resolution TEM/EDX analysis is performed.

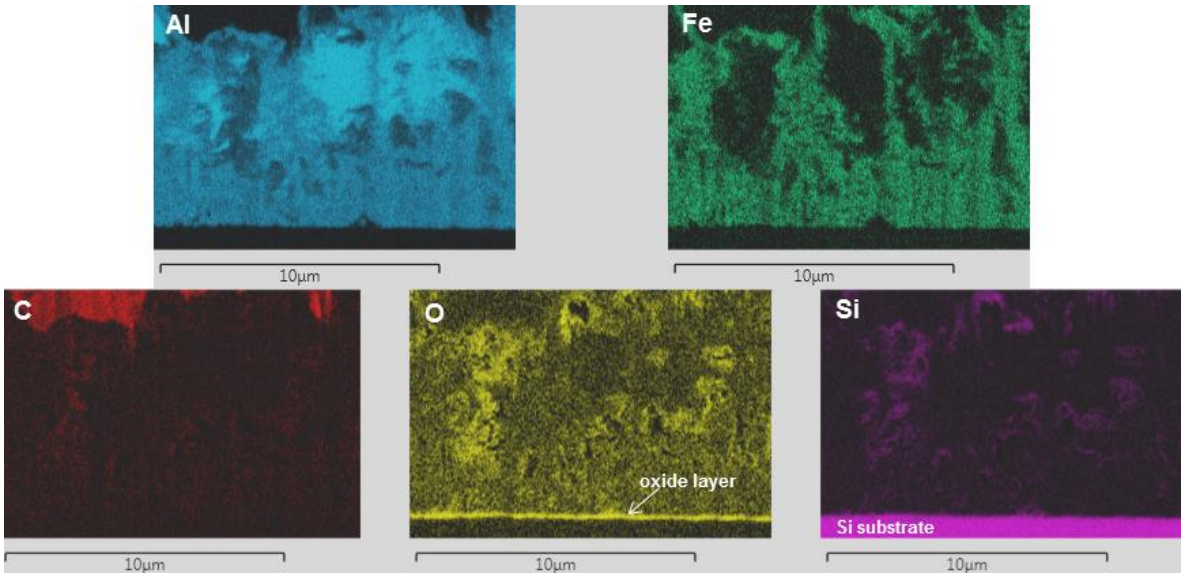

Figure 6.20: EDX qualitative analysis for the elemental mapping along a cross section of an Al-Fe film deposited on a SiO_2 substrate in the conditions of Exp. #4 (Table 6.4).

6.3.3.2. Structural characteristics

Figure 6.21 is the XRD spectrum of films deposited on SiO_2 substrates. As for the case of glass substrates, the obtained spectrum is compared with the $Al_{13}Fe_4$ XRD pattern reported in Ellner (1995) and Grin *et al*. (1994). A good agreement between the two patterns is observed further confirming the formation of the $Al_{13}Fe_4$ intermetallic structure and thus, validating the reproducibility of the process.

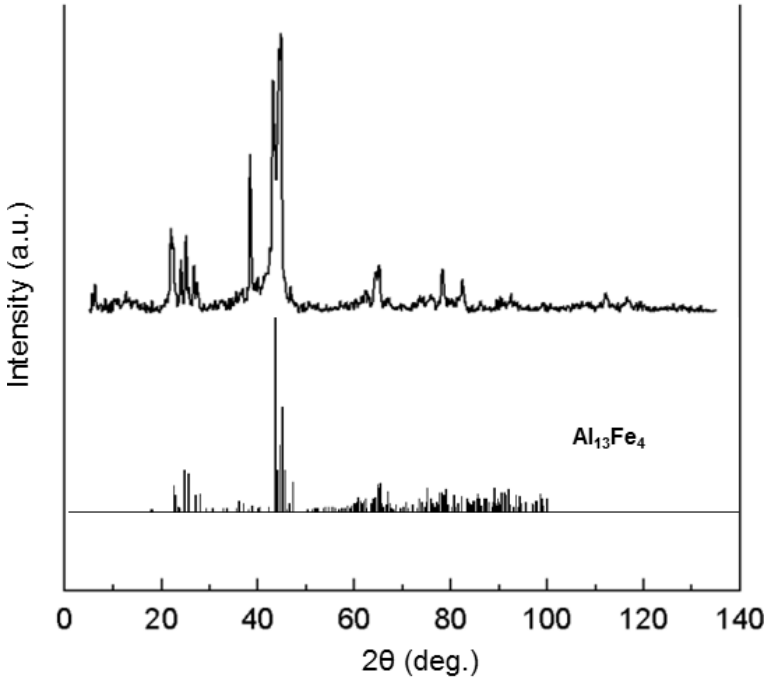

Figure 6.21: XRD spectrum of an Al-Fe intermetallic film deposited on a SiO_2 substrate in the conditions of Exp. #4 (Table 6.4) (top) with the $Al_{13}Fe_4$ pattern (bottom) calculated in Ellner (1995) and Grin *et al*., (1994).

As in the case of glass substrates, there exist remaining discrepancies which are attributed to the potential formation of secondary Al-Fe phases. The peaks at low 2θ angles, *ca.* 20°-30° as well as the large peaks between 40°-50° and some smaller peaks at higher 2θ angles are characteristics of the existence of the approximant $Al_{13}Fe_4$. The large peak at 39° is attributed to the Al_5Fe_2 phase and to pure Al (JCPDS card no. 29-0043 and 04-0787, respectively). The intensity of the peak at around 45° implies that within the film there exists unreacted Fe (JCPDS card no. 87-0722). The peak at 82° matches very well the *fcc* Al and the *bcc* Fe crystalline structures whereas the two last peaks at *ca.* 112° and 117° correspond to *fcc* Al. Thus, it can be deduced that during the sequential deposition of Al and Fe on SiO2 substrates the formed $Al_{13}Fe_4$ approximant phase coexists with the secondary Al_5Fe_2 approximant phase and an excess of unreacted Al.

For the definition of the film thickness and porosity SEM observations are performed. Further investigation of the composition uniformity, the microstructure of the film and the crystallographic structures is performed by high resolution TEM analysis.

6.3.3.3. Microstructural characterization

Figure 6.22 presents the SEM cross section prepared by FIB, at a random position of the substrate. Figure 6.22a shows a 14 to 17 μm Al-Fe film with significant porosity across its depth and high surface roughness. The higher magnification image (6.22b) focuses on a pore where the different grey scales reveal the formation of various phases. In particular, an $Al_{13}Fe_4$ phase is formed which is in equilibrium with pure *fcc* Al indicated by darker grey tone, in the area around the pore. Inside the pore, a higher O amount is detected, as

mentioned also in Figure 6.20, which leads to the formation of Al oxide indicated by the brighter grey scale.

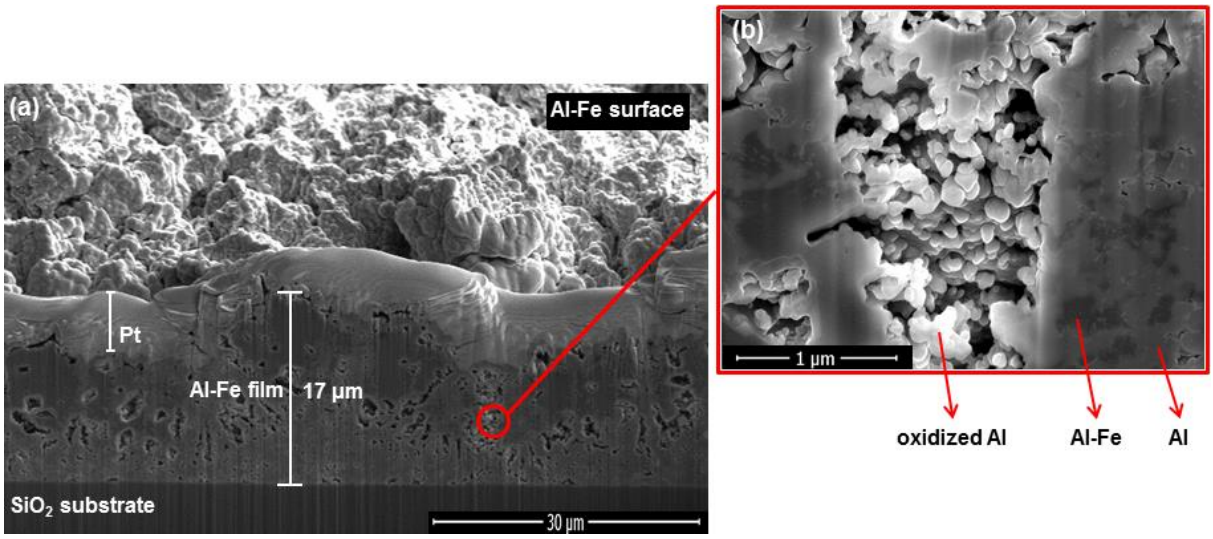

Figure 6.22: (a) A FIB-SEM cross section showing a 14 to 17 μm thick Al-Fe film deposited on a SiO_2 substrate in the conditions of Exp. #4 (Table 6.4), in which various phases exist as indicated by the different scales in (b).

Al-Fe films deposited on SiO_2 substrates have similarities with the corresponding films deposited on glass substrates. The thickness of the film is in the range of 15-17 μm and the porosity in both cases is high, leaving open pores within the films. Oxidation during FIB cutting may enhance Al segregation in these regions.

Figure 6.23 shows the TEM analysis of an Al-Fe coating, deposited on SiO_2. The bottom half of the coating is fully intermixed whereas the top half presents alternating pure Al and Al-Fe stripes which are perpendicular to the substrate (Figure 6.23a). Therefore, this region is partially alloyed; a result that could not be caught with the macroscopic techniques for elemental composition as GD-OES or by the performed calculation of the at% Al and Fe. A closer look at the interface between an Al-Fe and an Al stripe (white circle in Fig. 6.23a) is illustrated in Figure 6.23b. We observe an Al-Fe grain that grew laterally into the Al region, in the form of a 180 nm-thick rectangle. A high-resolution TEM image of this crystal is shown in Fig. 6.23c. A fast Fourier transformation (Fig. 6.23d) of the atomically resolved image is performed in order to determine crystallographic parameters. The indexation of the spots and the zone axis confirm the formation of the monoclinic m-$Al_{13}Fe_4$ phase (the analogous m-$Al_{13}Fe_4$ phase of Villars and Calvert (1998) is used) with the following parameters a=15.49Å, b=8.08Å, c=12.48Å, β=107.75°, which are in very good agreement with the corresponding parameters reported in previous works (Ellner, 1994; Grin *et al.*, 1995).

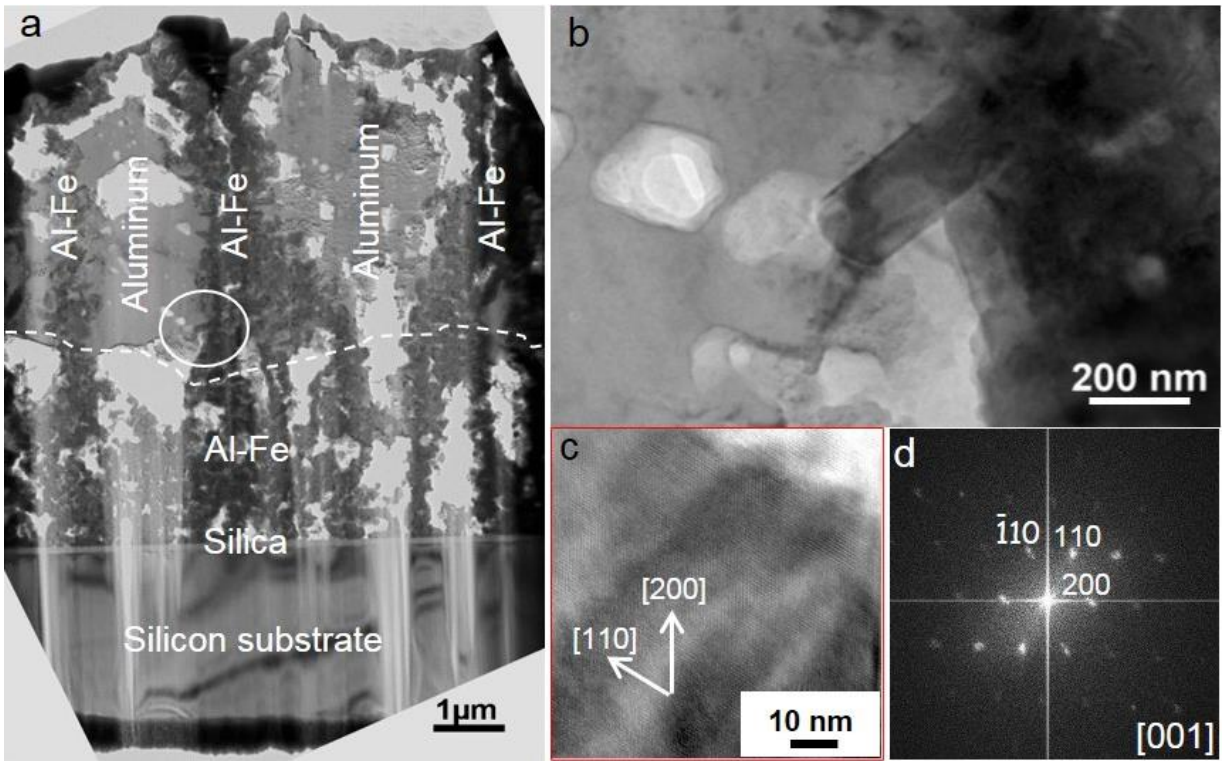

Figure 6.23: (a) TEM cross section of an Al-Fe film deposited on a SiO_2 substrate in the conditions of Exp. #4 (Table 6.4). (b) Zoom in the white circle: $Al_{13}Fe_4$ crystallite. (c) High-resolution TEM image showing the atomic plane arrangement in Al-Fe nanocrystal of (b). (d) Indexed fast Fourier transform of image (c) confirming the formation of m-$Al_{13}Fe_4$ along [001] zone axis.

From all the presented results, we can deduce that Fe diffuses towards the interface with SiO_2 or glass, readily at its deposition temperature (140°C). When temperature is increased for *in situ* annealing, the Al-Fe phases first form in the vicinity of the interface, and this is why the lamella obtained from the SiO_2 substrate (Fig. 6.24) exhibits pure Al stripes on top of an Al-Fe layer. Since the microstructure exhibits a high concentration of defects - in the form of grain boundaries and porosity - Fe diffusion may be facilitated.

The differences between the glass and SiO_2 lamellas microstructure and composition do not originate from temperature differences (the surface temperature has been calibrated on glass and on oxidized Si as described in §2.1.1.2.). A likely explanation is that two very localized regions of large and numerous samples are observed, and that these two cases are two possible microstructures obtained in these conditions. Therefore, globally, it shows that annealing time (60 min) is not long enough to homogenize the composition of all the coatings, but that forming a pure m-$Al_{13}Fe_4$ surface layer is feasible. In Mengucci *et al.* (2003), 4 h of annealing were required for the complete formation of the FeAl B2 phase and further annealing only increases the structural order of this phase. In Naoi and Kajihara (2007), the system of Al/Fe/Al layers was annealed for 9 h for the homogeneous formation of the Al_5Fe_2 intermetallic compound.

6.3.3.4. Catalytic tests of the semi-hydrogenation of acetylene with $Al_{13}Fe_4$ films formed by MOCVD

For the complete of the research of the $Al_{13}Fe_4$ approximant phase formed by the applied MOCVD framework, the catalytic properties of this structure are tested at IRCELYON (§2.2.10) and the results are presented in this section. Figure 6.24a shows the activity and the selectivity of the $Al_{13}Fe_4$ film. The results correspond to conditions of the first setup (§2.2.10), i.e., C_2H_2:H_2:He=2:10:88 at 50ml/min and 200°C, and without pretreatment of the film. The catalyst shows from the beginning a weak activity of 8% and a high selectivity of 80%. There is no evidence for the formation of ethane or C_4 compounds, since only ethylene is formed. The selectivity remains unchanged with increasing time but the catalytic activity decreases to less than 2% after 15 hours on stream. For the restoration of the catalytic activity of $Al_{13}Fe_4$, a reductive treatment is conducted under H_2 at 200°C for 4 h and under O_2 at 200°C for 30 min and tests are performed with C_2H_2:H_2:He=2:10:88 and C_2H_2:H_2:He=0.5:5:94.5, respectively, at 50ml/min and 200°C. The results are presented in Figure 6.24b. It can be seen that the activity of the catalyst remains very low, since only 1% is restored. Concerning the H_2 treatment, the selectivity remains at the same level (80%) while it significantly decreases to ca. 60% after the O_2 treatment.

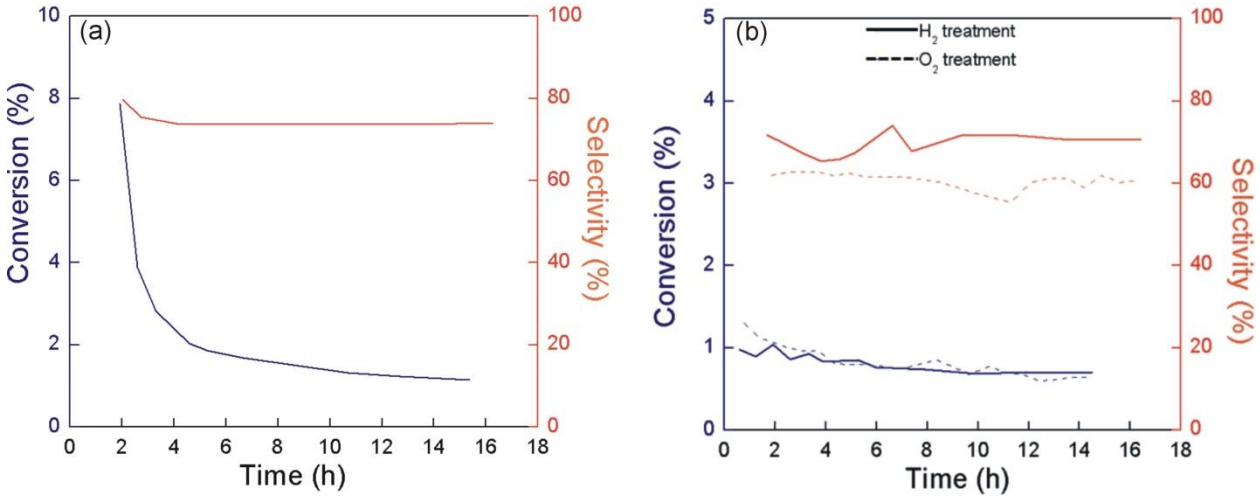

Figure 6.24: Conversion (blue lines) and selectivity (orange lines) of the semi-hydrogenation of acetylene using the $Al_{13}Fe_4$ films (a) without pretreatment and (b) with H_2 (solid lines) and O_2 (dashed lines) treatment.

The most possible explanation for the low activity of the $Al_{13}Fe_4$ films is their extended oxidation which enhances the formation of Al_2O_3 and prevents the catalytic activity. It is recalled that a pre-existed Al_2O_3 surface layer is already observed during the formation of the films. Extended oxidation might be caused during the transfer of the films (from Toulouse to Lyon), during their long residence in a glovebox before the catalytic tests (1 month) and even during the catalytic experiments. More catalytic experiments are required along with improvement of the films, prior to provide conclusive results for the catalytic activity of the supported $Al_{13}Fe_4$ approximant phase formed during CVD.

Summary-Conclusions

The MOCVD process is applied for the deposition of Al-Fe films containing complex intermetallics, with the aim to form the approximant phase m-$Al_{13}Fe_4$. Two deposition pathways are followed: one based on the co-deposition of the two metals, the other on their sequential deposition. In the former, potential interactions between the precursors of the two elements may be inhibiting factors for high deposition rate and purity, and for the formation of the intermetallic phase. This potential drawback is raised in the latter, where process conditions are established to avoid interaction between the two precursors.

The one-step, co-deposition process is performed at T_s=200^{o}C, which lies in the vicinity of the reaction-limited regime of the $Fe(CO)_5$ precursor and at the early stage of the diffusion-limited regime for the DMEAA precursor. As we show from the computational analysis presented in previous chapters, homogeneous reactions for both precursors occur even at low temperatures, although at lower reaction rates. By choosing to perform depositions at this T_s, we intend to limit the effect of the gas phase reactions and the gas phase interactions between the two precursors. At the same time, at T_s=200^{o}C the microstructure of Al presents benefits such as low roughness and high surface density and its deposition rate reaches a maximum value, which is preferable for the targeted $Al_{13}Fe_4$ phase, since it is located at the Al-rich part of the Al-Fe binary phase diagram. On the other hand, Fe deposition at this T_s presents some disadvantages, such as an acicular structure with open porosity. Thus, by choosing to operate at 200^{o}C, it seems that we benefit more the Al deposition.

The co-deposition process results in the formation of Al-rich films with low Fe amounts, corresponding to a hypothetically 13:1.3 ratio, which is off the targeted 13:4 one. Moreover, these films suffer from high O contamination sourcing from the $Fe(CO)_5$ precursor. This contamination prevents the formation of intermetallic phases to the benefit of oxides. The addition of H_2 in the input gas does not result in the decrease of the O contamination. However, it has an important impact on the shifting of the equilibrium of the surface reaction of Al to the benefit of AlH_3 formation and on the Fe deposition kinetics. Thus, the content of Al in the film is reduced and the increase of the growth rate of the film, from 25 μg/min to 50 μg/min, is attributed to the increase of the Fe content in the film. This fact allows the improvement of the Al:Fe to a best 13:2.5 ratio which is although insufficient, with regard to the targeted 13:4 ratio.

Co-deposited films consist of *fcc* Al, *bcc* Fe and possibly of amorphous oxides. No intermetallic phases are detected therein. The large amount of oxygen does not allow space for further investigation of the formation of complex intermetallic phases by e.g. appropriate post-deposition annealing.

A first series of sequential depositions is performed on Si substrates by depositing an Al layer first and a subsequent Fe layer. The process temperature of the Fe layer is reduced

along with its deposition duration and at the same time the duration for the processing of the Al layer increases while the process temperature is slightly decreases. Operating conditions, namely T_s=180^{o}C and 60 min for the Al layer and T_s=140^{o}C and 20 min for the Fe layer are screened with the aim to deposit Al and Fe layers of such thicknesses so as to be close to the 13:4 ratio. The concentration of Fe in the final film is too high with regard to the targeted ratio, however the heteroatoms content is as low as *ca.* 5%. The films are composed of *fcc* Al, *bcc* Fe and Fe silicide with no Al-Fe intermetallic phases. Even at a Fe process temperature as low as 140^{o}C, Fe diffuses through the pre-deposited Al layer towards the interface with the substrate, enhancing the potential formation of Fe silicides.

A second series of sequential deposition experiments is performed on glass substrates in order to prevent the formation of Fe silicides. In this series the process pressure during Fe deposition is increased at $P_{reactor}$=40 Torr and the deposition time is decreased in order to reduce the Fe content in the film. At the same time, the operating pressure of the deposition of Al layers is decreased at $P_{reactor}$=5 Torr and the duration of the process is increased for the increase of the Al content in the film. These actions are screened in order to achieve the elemental composition which corresponds to the 13:4 ratio. After the sequential deposition on glass, a post-deposition thermal annealing is applied to activate the reactive diffusion of Al and Fe and to form intermetallic phases. The annealing is performed at T_{anneal}=575^{o}C, where it has been shown that the formation of the $Al_{13}Fe_4$ phase occurs. The duration of the annealing process is 1 h and the process is performed *in situ*, in the reactor chamber to protect the films from oxidation.

The elemental composition of the films obtained by the deposition on glass substrates is determined indirectly through the mass gain of the coating and the thickness of each deposited layer. It is shown that by varying the process pressure and the deposition duration the 13:4 ratio can be approached. Qualitative GD-OES analysis which is performed on the film with a 13:4.3 ratio reveals that there is a chemical composition gradient through the depth of the film. The Fe concentration increases from the free surface of the film to the interface with the substrate and the Al:Fe ratio follows the opposite trend. The contamination of the coating from heteroatoms is superficial, since O and C are detected only at the surface. The Fe 2p XPS spectra presents a small chemical shift with regard to the Fe 2p peak of the reference Fe sheet, which is attributed to the formation of an Al-Fe intermetallic. On the other hand, the Al 2p spectra reveals two peaks, one corresponding to metallic Al and a second corresponding to oxidized Al. By combining the GD-OES and XPS analysis, it is concluded that the surface of the film is composed of a thin alumina layer limited enough to prevent the dissolution of the intermetallic phase underneath.

Observations of a cross section of this film reveal that it suffers from high porosity and that more than one crystalline phases co-exist. Indeed, the structural analysis shows that the $Al_{13}Fe_4$ approximant phase co-exists with the secondary Al_5Fe_2 phase and an excess of unreacted, *fcc* Al. However, STEM-EDX analysis of a lamella cut within the film reveals

complete alloying across the film with a composition gradient normal to the surface. The Fe concentration is lower close to the surface and it increase when the substrate is approached. Thus, the bottom part of the sample is composed of Fe-rich grains, e.g. Al(25)Fe(75), whereas at the middle of the film a homogeneous Al(75)Fe(25) matrix is observed, which corresponds to the m-$Al_{13}Fe_4$ composition. Higher resolution analysis of the upper part of the film illustrates Al enrichment which is correlated with the presence of O and the preferential Al oxidation.

A final series of Al/Fe sequential deposition is performed on thermally oxidized Si substrates. The choice of this particular substrate lies in the fact that it provides the same barrier properties as glass but it is also easy to crush into powder which is required for the catalytic tests. The optimum conditions of sequential deposition are applied for the MOCVD on SiO_2 substrates. The map of the elemental composition along a cross section of the obtained films shows complete intermixing of the two metals. Furthermore, within the pores of the coating higher concentration of Al is detected. C concentration is low within the film, while O is detected through the whole depth. The important level of O detection is due to its etching from the Si surface during the FIB cutting and the re-deposition within the film and especially in the pores where it is attracted by the Al preferential oxidation. The obtained films contain the intermetallic $Al_{13}Fe_4$ phase, as indicated by their crystallographic XRD pattern. TEM and high resolution analysis reveal that the Al-Fe coating presents two distinct regions, i.e., the bottom half where the two metals are fully intermixed and the top half where alternating pure Al and Al-Fe stripes are observed. Post process fast Fourier transformation of an atomically resolved image provides the parameters a=15.49Å, b=8.08Å, c=12.48Å, β=107.75°, which correspond to the formation of the monoclinic, m-$Al_{13}Fe_4$ phase. The differences in the microstructure of the glass and the SiO_2 coated samples are due to the random choice of the film area from which the lamella is taken. Thus, in order to avoid differences of this kind, an increase of the annealing time will enhance the homogenization of the composition for the whole film.

Catalytic experiments of the semi-hydrogenation of acetylene are performed at IRCELYON, by using crushed $Al_{13}Fe_4$ films as catalysts. The activity of the films is limited since in all cases it provides low conversions. On the other hand, its selectivity is of the order of 80% and it reduces to 60% when the films are treated under O_2. The low performance of the $Al_{13}Fe_4$ films produced by CVD is attributed to their oxidation which favors the formation of Al_2O_3 over the catalytic activity. More catalytic experiments are required as well as improvement of the films so as to limit the formation of Al_2O_3 during the CVD processing of the $Al_{13}Fe_4$ phase and to homogenize its formation across the film.

General summary-conclusions and perspectives

The computational and experimental analyses of the CVD of unary films, namely Al and Fe, have central stage in this thesis. Besides their own worth, they serve the final target of the thesis that is, the formation of multifunctional intermetallic compounds, the case in point being the $Al_{13}Fe_4$ approximant phase. Both unary and intermetallic compounds are formed in thin films grown on the surface of various substrates in CVD reactors.

The main advantages of CVD are the high surface-to-volume ratio of the resulting material and the conformal coverage of complex surfaces. Furthermore, by operating at relatively low to moderate temperatures, CVD can meet strict processing constraints. Complex physical and chemical phenomena are involved in CVD: simultaneous transport phenomena and homogeneous and heterogeneous chemical reactions, in gas phase and on solid surfaces, respectively; they condition the characteristics of the films and subsequently their functional properties. The thorough investigation of the associated mechanisms – from the reactor inlet to the rough film surface – require modeling, computations and experiments at different scales, namely from the macroscopic scale of the bulk of the reactor down to the nanoscopic scale of the film roughness. In the developed multiscale framework, the macroscale modeling is based on the conservation of mass, momentum and energy, and gives way to large computational fluid dynamics (CFD) problems. The nanoscale modeling treats stochastic physical and chemical events at the surface of the film with the kinetic Monte Carlo (kMC) method. The kMC method is coarse-grained since, for the sake of computational cost-effectiveness, it simulates events on a simple cubic lattice instead of the one dictated by the crystallographic structure of Al and Fe. The computational linking of the two scales is implemented by feeding the nanoscale with needed information, namely species mass flux, computed in the macroscale. Such a multiscale analysis framework enables theoretical predictions of the effects of the reactor operating conditions, such as pressure, temperature and inlet flow rate, on the structure of the deposited film and the evolution of its surface roughness. In this thesis, theoretical and experimental analyses are carried out inseparably: the former is triggered, fed and validated by the latter whereas the former's predictions illuminate and advance the latter's findings. The ultimate purpose served by the combined multiscale and experimental analysis is the determination of advantageous operating "windows" and the control and optimization of the CVD processes of concern.

Before the application of a combined co-deposition or sequential deposition of Al-Fe process, the unary Al and Fe CVD processes should be investigated for determining common operating conditions which will allow the formation of the targeted intermetallic phase. The experimental and theoretical investigation of the unary depositions provides useful information concerning potential gas phase and surface interactions during the common process and preferable temperature and pressure conditions.

A vertical, stainless steel MOCVD reactor is designed to process unary and binary Al and Fe coatings from their corresponding precursors; it has been successfully tested for ensuring the possibility to grow metallic and intermetallic films. *Ad hoc* characterizations are

implemented for the determination of the composition, the structure and the microstructure of the films.

For the CVD of Al, DMEAA is chosen as precursor. The choice is dictated by its relatively high vapor pressure at room temperature and by the possibility to perform depositions at low to moderate temperatures. The CVD of Al from DMEAA is experimentally and computationally investigated with the aim to relate the evolution of both the deposition rate and the microstructure of the films with the deposition temperature in the investigated temperature range 139^{o}C – 241^{o}C on one side, and with the electrical resistivity of the films, on the other side.

Deposition of Al results in pure films without any heteroatoms contamination. Increase of the deposition temperature yields increased film density, decreased surface roughness and increased film uniformity with improved substrate surface coverage. The incubation time is high (*ca.* 310 s) at the lowest deposition temperature and it linearly decreases to 48 s at the highest temperature. This behavior of the initiation of the deposition process may be attributed to the variation of the sticking coefficient of the precursor on the substrate and to accelerated desorption of the adsorbents at higher temperatures.

The Arrhenius plot of the process shows that the reaction-limited regime is located in the range 139^{o}C – 185^{o}C, where the deposition rate increases with increasing temperature. In the diffusion-limited regime and between 185^{o}C – 227^{o}C the deposition rate reaches a maximum value of *ca.* 15.5 nm/min at 185^{o}C and then remains relatively constant, with a slight decrease to *ca.* 13.5 nm/min at the last temperature. Above 227^{o}C, a steep reduction of the Al deposition rate is observed. The model applied for the macroscopic simulation of the CVD of Al includes a simplified chemical scheme with a gas phase and a surface decomposition of the precursor. First-order Arrhenius kinetics is implemented for these reactions based on the experimental data. Two different mass inflow rates of the precursor are used for the simulation of the process. The upper limit value, which is dictated by the experimental procedure and corresponds to the thermodynamic equilibrium in the bubbler and infinite conductance of the gas lines, and a lower value provided by the realistic assumptions that the gas – liquid interactions in DMEAA bubbler are not fully efficient; in fact, part of the precursor is degraded in the lines before entering the reactor, and the conductance of the gas lines is finite.

The computational predictions are in satisfactory agreement with experimental measurements, mostly in the range 139^{o}C – 227^{o}C. The decrease of the precursor mass inflow rate improves the prediction of the deposition rates obtained at the reaction-limited regime, despite the fact that at this temperature range the surface reaction dominates the process. Nevertheless, the gas phase reaction consumes an important quantity of the precursor even at low temperatures. Indeed, the dependence of the gas phase reaction rate on the temperature is presented and it is illustrated that even at 100^{o}C the volumetric reaction is on. Thus, given that the temperature increases as the substrate is approached, the gas phase reaction rate

becomes important in the reaction-limited regime, the quantity of the precursor on the surface reduces and the deposition rate decreases, in accordance with experiments.

On the other hand, above 227^{o}C the model fails to predict the experimental deposition rate probably due to the high gas phase degradation rate of the precursor molecule. The global chemical reactions and the first-order Arrhenius kinetics implemented in the macroscopic model cannot incorporate additional effects such as the formation of intermediate species and, consequently, the model does not capture the abrupt decrease of the deposition rate at high temperatures. Investigation is under way for the development of a more accurate model which will be valid in the entire temperature range. This investigation is performed by applying a more detailed chemistry pathway and by performing microscopic simulations on complex surfaces for the local calculation of the deposition rate. However, the presented macroscopic framework is valid in the temperature range 139^{o}C – 227^{o}C, where co-deposition requirements with Fe can be met.

The macroscopic model feeds the nanoscale kMC algorithm with the mass fraction of the precursor at the surface in order to enable multiscale simulations of the Al surface. The chemical information for any reactions of the precursor such as its decomposition on the surface, are incorporated in the sticking coefficient. For the latter, a temperature dependent function is employed by fitting experimental deposition rates at various temperatures and at various positions of the substrates in the CVD reactor.

The obtained results from the multiscale model are compared with the corresponding experimental measurements of Al films. The RMS roughness decreases with increasing the process temperature from 0.6 μm at 139^{o}C to 0.15 μm at 198^{o}C. The calculated RMS values lie within the deviations of experimental measurements resulting in a very good agreement between the experiments and the predictions. However, above 210^{o}C the experimental RMS shows a plateau which is not captured by the multiscale framework. The latter presents a monotonous decrease of the roughness with increasing temperature. Within the entire temperature range, adsorption dominates the process, while desorption and migration events are limited. Temperatures increase results in the increase of migration, which despite the predominance of the adsorption has a significant impact on the RMS. This effect is due to the fact that as temperature increases above 210^{o}C, migration may no longer be negligible and the assumption of the zero Ehrlich-Schwoebel (ES) barrier for migration at step edges becomes controversial. Incorporating a non-zero ES barrier in the multiscale simulations, migration would lead to a possible aggregation at step edges with a successive increase of the RMS, rather than to a smoothening of the surface which is observed by the presented results of multiscale modeling.

The electrical resistivity of the films increases with increasing surface roughness from 10 μΩ.cm at RMS 0.15 μm to *ca.* 80 μΩ.cm at RMS 0.6 μm, mainly due to the increased scattering caused by rough surfaces and to higher grain boundaries density which results from the entrapment of electrons. The behavior of the electrical resistivity is quantitatively

reproduced when the computational predictions of the RMS of the films are considered for its estimation.

The development of a multiscale framework which will account for the exact crystallographic structure of Al and for chemical reactions at the surface level is under way. These modifications may enable the simulation of more complex processes and surface features, such as island formation, grain boundaries and height-height correlations. Regarding the calculation of the porosity evolution within the film, the solid-on-solid (SOS) approximation should be replaced by triangular lattice models which, in contrast to SOS models, can accommodate the formation of vacancies.

For the CVD of Fe, the $Fe(CO)_5$ is chosen as precursor. This choice is dictated by its high vapor pressure at room temperature and by the possibility to perform relatively pure Fe depositions in the same temperature range with Al. The computational and experimental investigation of the CVD of Fe concerns the relation of the deposition rate with temperature in the range 130^oC – 250^oC and pressure in the range 10 – 40 Torr, and the relation of the film roughness with the deposition temperature.

Deposition from $Fe(CO)_5$ results in *bcc* Fe films containing possibly the secondary Fe_3C phase, observed mostly at higher temperatures. The films contain low O and C heteroatoms at the level of 5% and 1.5%, respectively. The morphology of the films depends on the process temperature. Increase of the deposition temperature above a certain limit results in the modification of the surface morphology from sharply-faceted to acicular. It also results in films with higher uniformity and better surface coverage. The surface roughness can be directly correlated with the change of the morphology. In particular, at low temperatures where sharply-faceted grains are formed, the roughness is high and relatively stable with a slight decrease with increasing temperature. On the other hand, when the morphology changes to acicular a sharp decrease of the roughness is observed prior its stabilization.

The incubation time is high (*ca.* 1800 s) at the lowest deposition temperature, it decreases to 100-150 s in the range 140^oC – 160^oC and then it further decreases and stabilizes at less than 50 s, for higher temperatures. This behavior of the initiation of the deposition may be attributed to the different sticking coefficient of the precursor on the substrate and to accelerated desorption of the adsorbents at higher temperatures. By investigating the effect of the deposition duration on the deposition rate, we observe that for duration lower than 60 min the deposition rate increases and then remains unchanged.

The Arrhenius plot of the process shows a reaction-limited regime between 130^oC – 200^oC where the deposition rate increases with increasing temperature. Above 200^oC, the process is diffusion-limited. In the diffusion-limited regime, Fe deposition rate has a maximum value of *ca.* 60 nm/min at 200^oC. Beyond this temperature, the deposition rate of Fe abruptly decreases, which is attributed to the high gas phase decomposition rates of the

species contributing to the Fe deposition and to inhibition of the surface from the CO ligand which is produced by the gas phase decomposition reactions.

The macroscopic computational model for this process incorporates 7 gas phase and 3 surface reactions. The gas phase reactions describe decarbonylation steps of the $Fe(CO)_5$ precursor and recombination reactions of the intermediate species $Fe(CO)_x$, x=2,3,4, with CO. For the gas phase reactions Arrhenius kinetics are implemented with an order dictated by the stoichiometry of the reactions. The surface reactions express the contribution of $Fe(CO)_5$, $Fe(CO)_3$ and FeCO on the Fe deposition. For the surface reactions, Langmuir-Hinshelwood type expressions are used to describe the poisoning of the surface from CO.

Macroscopic simulations with this model accurately predict the behavior of the deposition rate in the examined temperature range. The model confirms that the steep reduction of the deposition rate at high temperatures is due (a) to the increased gas phase decomposition rate of $Fe(CO)_5$ and $Fe(CO)_3$ which results in reduced concentration of these species at the susceptor and (b) to the increased CO concentration which inhibits the surface. The computational analysis shows that gas phase reactions occur also in the reaction-limited regime, but with lower rates. Concerning the dependence of the deposition rate on the operating pressure, the combined experimental and computational investigation shows that as pressure increases the gas phase decomposition rates increase and the diffusion coefficients of $Fe(CO)_5$ and $Fe(CO)_3$ decrease. As a result the concentration of these species at the susceptor decreases and consequently the deposition rate decreases. The model predicts with less accuracy the experimental data along the susceptor. A more precise surface chemistry model might capture this trend by taking into account the adsorbed states of the precursor and intermediates at specific surface sites.

The mass fraction of $Fe(CO)_5$ and $Fe(CO)_3$ at the vicinity of the surface are calculated by the macroscopic model and they are used as an input to the kMC model for the performance of multiscale simulations. Again, any chemical information which describes potential interactions of $Fe(CO)_5$ and $Fe(CO)_3$ with the surface is incorporated in the sticking coefficient.

The multiscale framework predicts RMS roughness which is in good agreement with the corresponding experimental data. In the range 190^oC – 200^oC, the predictions are less accurate due to the fact that the change of the surface microstructure, which is experimentally observed, cannot be captured by the applied multiscale model. At higher temperatures, predictions follow the experimental trend and RMS reaches a plateau, due to small variations of migration events.

The multiscale framework for the surface simulation of Fe growth could be improved in order to account for the exact crystallographic structure of Fe and for chemical reactions at the surface level. The improved framework may enable the multiscale simulation of more

complex processes and surface features, such as 3D growth, island formation and variations of the microstructure.

The detailed investigation of the unary Al and Fe CVD leads to the application of a CVD method for the processing of Al-Fe films containing complex intermetallics, with the aim to form the approximant phase m-$Al_{13}Fe_4$. The first path to this direction is a co-deposition process, which involves the simultaneous deposition of the two metals with potential interactions between the two precursors. An alternative is the sequential deposition where the precursors are not intermixed, at least at the gas phase. This process is applied in order to cope with difficulties during co-deposition due to the interactions between the two precursors.

Co-deposition experiments are performed at 200^{o}C. Regarding the depositions of Al and Fe, this temperature is located at the early stage of the diffusion-limited regime for Al and in the vicinity of the reaction-limited regime for Fe. The study of the unary CVD processes shows that, homogeneous reactions for both precursors occur even at low temperatures. By choosing to perform depositions at this temperature, we intend to limit the effect of the gas phase interactions between the two precursors which most likely occur at higher temperatures. At the same time, at 200^{o}C the microstructure of Al exhibits low roughness and high surface density and its deposition rate reaches a maximum value, which is preferable for the targeted Al-rich, $Al_{13}Fe_4$ phase. On the other hand, Fe deposition presents some disadvantages, such as an acicular structure with open porosity. Thus, it seems that operating at 200^{o}C facilitates Al deposition.

Co-deposition results in the formation of Al-rich films with low Fe amounts, and the elemental composition corresponds to a hypothetical 13:1.3 ratio, which is off the targeted 13:4 one. Moreover, these films suffer from high O contamination coming from the $Fe(CO)_5$ precursor. This contamination prevents the formation of intermetallic phases in favor of oxides. The addition of H_2 in the input gas has a limited impact on the O concentration. However, it significantly shifts the equilibrium of the surface reaction of Al in favor of AlH_3 formation and also of the Fe deposition kinetics, possibly due to the formation of hydrocarbons which removes the CO from the surface. Thus, the content of Al in the film is reduced and the increase of the growth rate of the film, from 25 μg/min to 50 μg/min, is attributed to the increase of the Fe content in the film. This fact allows the improvement of the Al:Fe to a best 13:2.5 ratio, which is still insufficient with regard to the targeted 13:4 one.

Co-deposited films consist of *fcc* Al, *bcc* Fe and possibly of amorphous oxides. No intermetallic phases are detected therein. The large amount of oxygen leaves no space for further investigation of the formation of complex intermetallic phases, e.g. by appropriate post-deposition annealing. However, the co-deposition process at lower temperatures along with thermal annealing should be examined as a possibility to form intermetallic Al-Fe phases. Modeling can support such an investigation. Macroscopic simulations can be performed by incorporating the chemical systems of both precursors and additional

interactions between them, such as the formation of aluminum oxides. Theoretical predictions will include the elemental composition of the films. Then, gas phase reactions will be turned off while surface reactions will be allowed to occur and the surface temperature within the model will be raised so as the model to adapt to the annealing conditions.

Sequential deposition experiments are performed on Si substrates by first depositing an Al layer and then a Fe layer. Compared to co-deposition experiments, the processing temperature of the Fe layer is reduced to T_s=140^{o}C with a simultaneous decrease of the deposition duration to 20 min. On the other hand, the processing temperature of the Al layer is also reduced but to a limited extend, to T_s=180^{o}C, and its deposition duration is increased to 60 min. The particular operating conditions are so chosen to yield Al and Fe layers whose composition is close to the 13:4 ratio. The concentration of Fe in the final film is too high with regard to the targeted ratio, however the heteroatoms content is as low as *ca.* 5%. The films are composed of *fcc* Al, *bcc* Fe and Fe silicide with no Al-Fe intermetallic phases. Even at a Fe process temperature as low as 140^{o}C, Fe diffuses through the pre-deposited Al layer towards the interface with the substrate, favoring the potential formation of Fe silicides.

A second series of sequential deposition experiments is performed on glass substrates in order to prevent the formation of Fe silicides. In this series the processing pressure during Fe deposition is increased at $P_{reactor}$=40 Torr and the deposition time further decreases to 10 min in order to reduce the Fe content in the film. At the same time, the operating pressure of the deposition of Al layers is decreased at $P_{reactor}$=5 Torr and the duration of the process is increased to 90 min for the increase of the Al content in the film. The aim of these actions is the achievement of an elemental composition corresponding to the targeted 13:4 ratio. After the sequential deposition on glass, a post-deposition thermal annealing is applied to activate the reactive diffusion of Al and Fe and to form intermetallic phases. The annealing is performed at T_{anneal}=575^{o}C, where it has been shown that the formation of the $Al_{13}Fe_4$ phase occurs. The duration of the annealing process is 1 h and the process is performed *in situ*, in the reactor chamber to protect the films from oxidation.

The overall elemental composition of the films approaches the targeted 13:4 ratio. Qualitative GD-OES analysis which is performed on the film with a 13:4.3 ratio reveals that there is a chemical composition gradient through the depth of the film. The Fe concentration increases from the surface of the film to the interface with the substrate resulting in an opposite trend for the Al:Fe ratio. The contamination of the coating is limited, since O and C are detected only at the surface. The Fe 2p XPS spectra presents a small chemical shift with regard to the Fe 2p peak of the reference Fe sheet, which is attributed to the formation of an Al-Fe intermetallic. On the other hand, the Al 2p spectra reveals two peaks, one corresponding to metallic Al and a second corresponding to oxidized Al. By combining the GD-OES and XPS analysis, it is concluded that the surface of the film is composed of a thin alumina layer small enough to prevent the dissolution of the intermetallic phase underneath.

Al-Fe films formed by sequential deposition are characterized by high porosity and consist of more than one crystalline phases. The structural analysis shows that the $Al_{13}Fe_4$ approximant phase co-exists with the secondary Al_5Fe_2 phase and an excess of unreacted, *fcc* Al. However, STEM-EDX analysis of a lamella cut within the film reveals complete transverse alloying with a composition gradient normal to the surface. The Fe concentration is lower close to the surface and it increases as the substrate is approached. Thus, the bottom part of the sample is composed of Fe-rich grains, e.g. Al(25)Fe(75), whereas in the middle of the film a homogeneous Al(75)Fe(25) matrix is observed, which corresponds to the m-$Al_{13}Fe_4$ composition. Higher resolution analysis of the upper part of the film illustrates Al enrichment which is related with the presence of O and the preferential Al oxidation.

A final series of Al/Fe sequential deposition is performed on thermally oxidized Si substrates. The particular substrates provide the same barrier properties as glass and they are easy to break and crush into powder for the subsequent catalytic experiments. The operating conditions applied are those used for the formation of the m-$Al_{13}Fe_4$. The films present complete intermixing of the two metals. C concentration is low within the film, while O is detected through the whole depth. The O contamination comes from the SiO_2 surface during the FIB cutting and its re-deposition within the film. The films contain the intermetallic $Al_{13}Fe_4$ phase, as indicated by their crystallographic pattern. High resolution analysis of the films reveal that the Al-Fe coating has two distinct regions, namely the bottom half where the two metals are fully intermixed and the top half where alternating pure Al and Al-Fe stripes are observed. The interatomic parameters determined by this analysis correspond to the formation of the monoclinic, m-$Al_{13}Fe_4$ phase. The differences in the microstructure between the films formed on glass and on SiO_2 are due to the random choice of the film area from which the lamella is taken. Differences of this kind can be alleviated by increasing annealing time, which may improve the homogenization of the film. A better insight in the microstructure of these films and a better control of the porosity can be provided by multiscale simulations which will incorporate the exact crystallographic structure of Al and Fe along with chemical interactions at the surface level.

Catalytic experiments of the semi-hydrogenation of acetylene are performed at IRCELYON, by using crushed $Al_{13}Fe_4$ films as catalysts. Preliminary measurements indicate that the activity of the films is limited; in all cases, it provides low conversions of acetylene to ethylene. Its selectivity is relatively high at 80% and it reduces to 60% when the films are treated under O_2. The oxidation of the films and the formation of Al_2O_3 might be the main cause for the low performance of the $Al_{13}Fe_4$ phase which is produced by the CVD process. The determination of the catalytic properties of the films was performed at the end of the present thesis. A detailed, combined investigation between materials characteristics and catalytic performance is necessary to make progress towards increasing its catalytic activity of its durability.

References

Adam, T.N. UHV/CVD growth techniques, in: Cressler, J.D. (Ed.), *SiGe and Si Strained-Layer Epitaxy for Silicon Heterostructure Devices*, CRC Press, Boka Raton, **2010**.

Albao, M.A., Putungan, D.B., Hsu, C.-H., Chuang, F.-C. 2013. Enhanced nucleation of Al islands on H-dosed Si(100)-2x1 surface: A combined density functional theory and kinetic Monte Carlo study. *Surf. Sci*. **617**, 73-80.

Aloui, L. *Dépôt Chimique en Phase Vapeur d'Al, Cu et Fe en vue d'élaboration de films composés de phases intermétalliques*. Institut National Polytechnique de Toulouse. PhD thesis, **2012**.

Aloui, L., Duguet, T., Haidara, F., Record, M.-C., Samélor, D., Senocq, F., Mangelinck, D., Vahlas, C. 2012. Al-Cu intermetallic coatings processed by sequential metalorganic chemical vapor deposition and post deposition annealing. *Appl. Surf. Sci.* **258**, 73-80.

Amar, J.G. and Family, F. 1995a. Step barrier for interlayer-diffusion in Fe/Fe(100) epitaxial growth. *Phys. Rev. B* **52**, 13801-13804.

Amar, J.G. and Family, F. 1995b. Critical cluster size: Island morphology and size distribution in submonolayer epitaxial growth. *Phys. Rev. Lett.* **74**, 2066-2069.

Amazawa, T. 1998. Very low pressure selective aluminum chemical vapor deposition using dimethylaluminum hydride without H_2 carrier gas. *J. Electrochem. Soc.* **145**, 4327-4332.

Andromeda, 2012: http://febui.chemeng.ntua.gr/andromeda.htm

Ansys/Fluent v12.1sp1. Documentation. Ansys Inc., 2009

Armbrüster, M., Konvir, K., Friedrich, M., Teschner, D., Wowsnick, G., Hahne, M., Gille, P., Szentmiklósi, L., Feuerbacher, M., Heggen, M., Girgsdies, F., Rosenthal, D., Schlögl, R., and Grin, Yu. 2012. $Al_{13}Fe_4$ as a low-cost alternative for palladium in heterogeneous hydrogenation. *Nat. Mater.* **11**, 690-693.

Aviziotis, I.G., Cheimarios, N., Duguet, T., Vahlas, C., and Boudouvis, A.G. 2016. Multiscale modeling and experimental analysis of chemical vapor deposited aluminum films: linking reactor operating conditions with roughness evolution. *Chem. Eng. Sci.* **155**, 449-458.

Aviziotis, I.G., Cheimarios, N., Vahlas, C., and Boudouvis, A.G. 2013. Experimental and computational investigation of chemical vapor deposition of Cu from Cu amidinate. *Surf. Coat. Technol.* **230**, 273-278.

Aviziotis, I.G., Duguet, T., Sussi, K., Kokkoris, G., Cheimarios, N., Vahlas, C., and Boudouvis, A.G. 2015. Investigation of the kinetics of the chemical vapor deposition of aluminum from dimethylethylamine alane: experiments and computations. *Phys. Status Solidi C* **12**, 923-930.

Azem, S., Nechiche, M., Taibi, K. 2011. Development of copper matrix composite reinforced with FeAl particles produced by combustion synthesis. *Powder Technol.* **208**, 515-520.

Barabasi, A.L. and Stanley. H.E. *Fractal concepts in surface growth*, Cambridge University Press, **1995**.

Barbato A., Fiorucci, A., Rondanini, M., Cavallotti, C. 2007. Multiscale investigation of the influence of surface morphology on thin film CVD. *Surf. Coat. Technol.* **201**, 8884-8887.

Barnes, L.A., Rosi, M., and Bauschlicher Jr., C.W. 1991. An ab initio study of $Fe(CO)_n$, n=1,5 and $Cr(CO)_6$. *J. Chem. Phys.* **94**, 2031-2039.

Bartelt, M.C., and Evans, J.W. 1995. Transition to multilayer kinetic roughening for metal (100) homoepitaxy. *Phys. Rev. Lett.* **75**, 4250-4253.

Barton, J., Guillemet C. *Le verre, science et technologie*, EDP Sciences, Parc d'activités de Courtaboeuf, **2005**.

Battaile, C.C., Srolovitz, D.J. 2002. Kinetic Monte Carlo simulation of chemical vapor deposition. *Annu. Rev. Mater. Res.* **32**, 297-319.

Battaile, C.C., Srolovitz, D.J., Butler, J.E. 1998. Atomic-scale simulations of chemical vapor deposition on flat and vicinal diamond substrates. *J. Gryst. Growth* **194**, 353-368.

Baxter, D.V., Chisholm, M.H., Gama, G.J., Hector, A.L., and Parking, I.P. 1995. Low pressure chemical vapor deposition of metallic films of iron, manganese, cobalt, copper, germanium and tin employing bis(trimethyl)silylamido complexes, $M(N(SiMe_3)_2)_n$. *Chem. Vapor Depos.* **1**, 49-51.

Beach, D.B., Blum, S.E., and LeGoues, F.K. 1989. Chemical vapor deposition of aluminum from trimethylamine-alane. *J. Vac. Sci. Technol. A* **7**, 3117-3118.

Bent, B.E., Dubois, L.H., and Nuzzo, R.G. 1989. Aluminum chemical vapor deposition using triisobutylaluminum: mechanism, kinetics, and deposition rates at steady state. *MRS Proceedings* **131**, 327-338.

Berg, B.A. *Markov Chain Monte Carlo simulations and their statistical analysis*, World Scientific, Singapore, **2004**.

Binder, K., and Stoll, E. 1973. Scaling theory for metastable states and their lifetimes. *Phys. Rev. Lett.* **31**, 47-51.

Bird, G.A. *Molecular Gas Dynamics and the Direct Simulation of Gas Flows*, Oxford University Press, **1994**.

Bird, R.B., Stewart W.E., and Lightfoot. E.N. *Transport Phenomena*, second ed. John Wiley and Sons, USA, **2002**.

Black, P.J. 1955. The structure of $FeAl_3$. I. *Acta Cryst.* **8**, 43-48.

Bloomfield, M.O., and Cale, T.S. 2004. Formation and evolution of grain structures in thin films. *Microelectron. Eng.* **76**, 195-204.

Bloomfield, M.O., Richards D.F., and Cale, T.S. 2003. A computational framework for modelling grain-structure evolution in three dimensions. *Philos. Mag.* **83**, 3549-3568.

Bormashenko, E., Stein, T., Whyman, G., Bormashenko, Y., Pogreb, R. 2006. Wetting properties of the multiscaled nanostructured polymer and metallic superhydrophobic surfaces. *Langmuir* **22**, 9982-9985.

Bortz, A.B., Kalos, M.H., Lebowitz, J.L., and Zendejas, M.A. 1974. Time evolution of a quenched binary alloy: Computer simulation of a two-dimensional model system. *Phys. Rev. B* **10**, 535-541.

Boudouvis, A.G. Engineering analysis of chemical vapor deposition processes, in: Belin-Ferré, E. (Ed.), *Surface Properties and Engineering of Complex Intermetallics*. Book Series on Complex Metallic Alloys – vol. 3, World Scientific, Singapore, **2010**.

Braatz, R.D., Alkire, R.C., Seebauer, E., Rusli, E., Gunawan, R., Drews, T.O., Li, X., and He, Y. 2006. Perspectives on the design and control of multiscale systems. *J. Process Contr.* **16**, 193-204.

Braga, D. Grepioni, F., Guy Orpen, A. 1993. Nickel carbonyl [$Ni(CO)_4$] and iron cabonyl [$Fe(CO)_5$]: molecular structures in the solid state. *Organometallics* **12**, 1481-1483.

Bravo, J., Zhai, L., Wu. Z., Cohen, R.E., Rubner, M.F. 2007. Transparent superhydrophobic films based on silica nanoparticles. *Langmuir* **23**, 7293-7298.

Canakci, A., Erdemir, F., Varol, T., Ozkaya, S., 2013. Formation of Fe-Al intermetallic coating on low carbon steel by a novel mechanical alloying technique. *Powder Technol*. **247**, 24-29.

Carlton, H.E. and Oxley, J.H. 1965. Kinetics of the heterogeneous decomposition of iron pentacarbonyl. *AIChE J.* **11**, 79-84.

Cavallotti, C., Barbato, A., Veneroni, A. 2004. A combined three-dimensional kinetic Monte Carlo and quantum chemistry study of the CVD of Si on Si(100) surfaces. *J. Cryst. Growth* **206**, 371-380.

Cavallotti, C., Pantano, E., Veneroni, A., Masi, M. 2005. Multiscale simulation of silicon film growth. *Cryst. Res. Technol.* **40**, 958-963.

Chaterjee, A., Vlachos, D.G. 2007. An overview of spatial microscopic and accelerated kinetic Monte Carlo methods. J. *Comput.-Aided Mater. Des.* **14**, 253-308.

Cheimarios, N. *Multiscale simulation and systemic analysis of chemical vapor deposition processes.* School of Chemical Engineering, National Technical University of Athens, PhD thesis, **2012**.

Cheimarios, N., Garnelis, S., Kokkoris, G., and Boudouvis, A.G. 2011. Linking the operating parameters of chemical vapor deposition reactors with film conformality and surface nano-morphology. *J. Nanosci. Nanotechno.* **11**, 8132-8137.

Cheimarios, N., Kokkoris, G., Boudouvis, A.G. 2010. Multiscale modeling in chemical vapor deposition processes: Coupling reactor scale with feature scale computations. *Chem. Eng. Sci.* **65**, 5018-5028.

Choy, K. L. 2003. Chemical vapour deposition of coatings. *Prog. Mater. Sci.* **48**, 57-170.

Christofides, P. D., Armaou, A., Lou, Y. and Varshney, A. Control and optimization of multiscale process systems, in: Levine, W.S. (Ed.), *Control Engineering Series*, Birkhäuser, Boston, **2008**.

Crose, M., Kwon, J.S.-I., Nayhouse, M., Ni, D., Christofides, P.D. 2015. Multiscale modeling and operation of PECVD of thin film solar cells. *Chem. Eng. Sci.* **136**, 50-61.

Csanády A., Gunter J.R., Barna P.B., Mayer J. 1988. Intermetallic phase formation in aluminium and iron thin film systems. *Thin Solid Films* **167**, 203-216.

Dadbakhsh, S. Hao, L. 2012. In situ formation of particle reinforced Al matrix composite by selective laser melting of Al/Fe_2O_3 powder mixture. *Adv. Eng. Mater.* **14**, 45-48.

Dateo, C., Gökçen, T., and Meyyappan M. 2002. Modeling of the HiPco process for carbon nanotube production. I. Chemical Kinetics. J. Nanosci. Nanotechno. 2, 523-534.

Deen, W.M. *Analysis of transport phenomena*, Oxford University Press, New York, **1998**.

Delmas, M. *Revêtements Al-Pt obtenus par dépôt chimique en phase vapeur pour la protection de l'alliage Ti6242 contre l'oxydation à des températures inférieures à 600C.* Institut National Polytechnique de Toulouse. PhD thesis, **2005**.

Delmas, M., Poquillon, D., Kihn, Y., Vahlas, C. 2005. Al–Pt MOCVD coatings for the protection of Ti6242 alloy against oxidation at elevated temperature. *Surf. Coat. Technol.* **200**, 1413-1417.

Delsol, T., Maury, F., Senocq, F. 2005. Thin films of iron from $Fe(CO)_5$ under atmospheric pressure, in: Devi, A., Fischer, R., Parala, H., Allendorf, M., Hitchman, M. (Eds.) *Fifteenth European Conference on Chemical Vapor Deposition (EUROCVD-15),* Proceedings Volumes 2005-09, The Electrochemical Society, Inc., New Jersey, **2005**.

Drotar, J.T., Zhao, Y.P., Lu, T.M., and Wang, G.C. 2000. Surface roughening in shadowing growth and etching in 2+1 dimensions. *Phys. Rev. B* **62**, 2118-2125.

Dubois, J.-M. An introduction to complex metallic alloys and to the CMA Network of Excellence, in: Belin-Ferré, E. (Ed.), *Basics of Thermodynamics and Phase Transitions in Complex Intermetallics*. Book Series on Complex Metallic Alloys – vol. 1, World Scientific, Singapore, **2008**.

Dubois, L.H., Zegarski, B.R., Gross, M.E., and Nuzzo, R.Z. 1991. Aluminum thin film growth by the thermal decomposition of triethylamine alane, *Surf. Sci.* **44**, 89-95.

Dubois, L.H., Zegarski, B.R., Kao, C.-T., and Nuzzo, R.Z. 1990. The adsorption and thermal decomposition of trimethylamine alane on aluminum and silicon single crystal surfaces: kinetic and mechanistic studies. *Surf. Sci.* **236**, 77-84.

Ehteman Haghighi, Sh., Janghorban, K., Izadi, S. 2010. Structural evolution of Fe-50 at.% Al powders during mechanical alloying and subsequent annealing processing. *J. Alloys Compd.* **495**, 260-264.

Ellner, M. 1995. Polymorphic phase transformation of Fe_4Al_{13} causing multiple twinning with decagonal pseudo-symmetry. *Acta Cryst.* **B51**, 31-36.

Etchepare, P.-L., Vergnes, H., Samélor, D., Sandowski, D., Brasme, C., Caussat, B., Vahlas, C. 2014. Amorphous alumina coatings on glass bottles using direct liquid injection MOCVD for packaging applications. *Adv. Sci. Tech.* **91**, 117-122.

Etchepare, P.-L., Vergnes, H., Samélor, D., Sandowski, D., Caussat, B., Vahlas, C. 2015. Modelling a MOCVD process to apply alumina films on the inner surface of bottles. *Surf. Coat. Technol.* **275**, 167-175.

Evans, J.W., Thiel, P.A., Bartlet, M.C. 2006. Morphological evolution during epitaxial thin film growth: Formation of 2D islands and 3D mounds. *Surf. Sci. Rep.* **61**, 1-128.

Fau-Canillac, F., and Maury, F. 1994. Control of the uniformity of thickness of Ni thin films deposited by low pressure chemical vapor deposition. *Surf. Coat. Technol.* **64**, 21-27.

Fedors, R.F. 1982. A relationship between chemical structure and the critical temperature. *Chem. Eng. Commun.* **16**, 149-151.

Feurer, R., Larhrafi, M., Morancho, R., Calsou, R. 1988. Use of binuclear organometallic compounds in chemical vapour deposition. *Thin Solid Films* **167**, 195-202.

Fosdick, L.D. Monte Carlo computations on the ising lattice, in: Alder, B. (Ed.) *Methods in Computational Physics* – vol. 1, Academic Press, New York, **1963**.

Francombe, M.H. *Physics of thin films: Advances in research and development*, Academic Press, San Diego, **1988**.

Frenkel, D.I., and Smit, B. *Understanding molecular simulation*, Academic Press, Orlando, **2002**.

Frenklach, M. 1992. Monte Carlo simulation of diamond growth by methyl and acetylene reactions. *J. Chem. Phys.* **97**, 5794-5802.

Frigo, D.M., van Eijden, G.J.M., Reuvers, P.J., and Smit, C.J. 1994. Preparation and properties of alane dimethylethylamine, a liquid precursor for MOCVD. *Chem. Mater.* **6**, 190-195.

Froger, V. *Couches minces de chalcogénures de zinc déposées par spray-CVD assisté par rayonnement infrarouge pour des applications photovoltaïques.* École Nationale Supérieure d'Arts et Métiers, PhD thesis, **2012**.

Gambit, Ansys Inc. Documentation. 2006.

Giancoli, D.C. *Physics: Principles with applications*, seventh ed. Pearson Prentice Hall, USA, **2013**.

Gilbert, A.G., and Sulzmann, K.G.P. 1974. The vapor pressure of iron pentacarbonyl. *J. Electrochem. Soc.* **121**, 832-834.

Gille, P., and Bauer, B. 2008. Single crystal growth of $Al_{13}Co_4$ and $Al_{13}Fe_4$ from Al-rich solutions by the Czochralski method. *Cryst. Res. Technol.* **43**, 1161-1167.

Gillespie, D.T. 1977. Exact stochastic simulation of coupled chemical reactions. *J. Phys. Chem.* **81**, 2340-2361.

Gillespie, D.T. 2001. Approximate accelerated stochastic simulation of chemically reacting systems. *J. Chem. Phys.* **115**, 1716-1733.

Gilmer, G.H., Bennema, P. 1972. Simulation of crystal growth with surface diffusion. *J. Appl. Phys.* **43**, 1347-1360.

Gladfelter, W.L., Boyd, D.C., and Jensen, K.F. 1989. Trimethylamine complexes of alane as precursors for the low-pressure chemical vapor deposition of aluminium. *Chem. Mater.* **1**, 339-343.

Glassbrenner, C.J., and Slack, G.A. 1964. Thermal conductivity of silicon and germanium from 3^oK to the melting point. *Phys. Rev.* **134**, A1058-A1069.

Godlewska, E., Szczepanik, S., Mania, R., Krawiarz, J., Koziñski, S. 2003. FeAl materials from intermetallic powders. *Intermetallics* **11**, 307-312.

Goldman, A.I., and Kelton, K.F. 1993. Quasicrystals and crystalline approximants. *Rev. Mod. Phys.* **65**, 213-230.

Gonzáles-Blanco, O. and Branchadell V. 1999. Density functional study of the Fe-CO bond dissociation energies of $Fe(CO)_5$. *J. Chem. Phys.* **110**, 778-783.

Gottlieb-Schoenmeyer, S., Assmus, W., Prud'homme, N., and Vahlas, C. Metallurgy of complex metallic alloys, in: Dubois, J.-M., and Belin-Ferré, E. (Eds.) *Complex Metallic Alloys: Fundamentals and Applications*, Wiley-VCH Verlag GmbH & Co. KGaA, Weinheim, **2010**.

Green, M.L., Levy, R.A., Nuzzo, R.G., and Coleman, E. 1984. Aluminum films prepared by metal-organic low pressure chemical vapor deposition. *Thin Solid Films*, **114**, 367-377.

Grin, J., Burkhardt, U., Ellner, M., and Peters, K. 1994. Refinement of the Fe_4Al_{13} structure and its relationship to the quasihomological homeotypical structures. *Z. Kristallogr.* **209**, 479-487.

Grujicic, M., Lai, S.G. 2000. Multi-length scale modeling of CVD of diamond Part I: A combined reactor-scale/atomic-scale analysis. *J. Mater. Chem.* **35**, 5359-5369.

Haidara, F., Record, M.-C., Duployer, B., Mangelinck, D. 2012. Phase formation in AlFe thin film systems. *Intermetallics* **23**, 143-147.

Hamers, R.J., Kohler, U.K., Demuth, J.E. 1989. Nucleation and growth of epitaxial Silicon on Si(001) and Si(111) surfaces by scanning tunneling microscopy. *Ultramicroscopy* **31**, 10-19.

Han, J., Jensen, K.F., Senzaki, Y., Gladfelter, W.L. 1994. Pyrolytic laser assisted chemical vapor deposition of Al from dimethylethylamine alane: Characterization and a new two-step writing process. *Appl. Phys. Lett.* **64**, 425-427.

Hersee, S.D., Ballingal, J.M. 1990. The operation of metalorganic bubblers at reduced pressure. *J. Vac. Sci. Technol. A* **8**, 800-804.

Huang, H., Gilmer, G.H., de la Rubia, T.D. 1998. An atomistic simulator for thin film deposition in three dimensions. *J. Appl. Phys.* **80**, 3636-3649.

Jackman, R.B., and Foord, J.S. 1989. Thermal and and photochemical vapour deposition of Fe from $Fe(CO)_5$ on Si(100). *Surf. Sci.* **209**, 151-158.

Jang, T.W., Moon, W., Baek, J.T., Ahn, B.T. 1998. Effect of temperature and substrate on the growth behaviors of chemical vapor deposited Al films with dimethylethylamine alane source. *Thin Solid Films* **333**, 137-141.

Joback, K.G., and Reid, R.C. 1987. Estimation of pure-component properties from group-contributions. *Chem. Eng. Commun.* **57**, 233-243.

Jones, A.C., and Hitchman, M.L. *Chemical Vapour Deposition: Precursors, Processes and Applications.* RCS Publishing, Cambridge, **2009**.

Kajikawa, Y. 2008. Roughness evolution during chemical vapor deposition. *Mater. Chem. Phys.* **112**, 311-318.

Kajikawa, Y. Noda, S. 2005. Growth mode during initial stage of chemical vapor deposition. *Appl. Surf. Sci.* **245**, 281-289.

Kanter, H. 1970. Slow-electron mean free paths in aluminum, silver, and gold. *Phys. Rev. B* **1**, 522-536.

Kim, B.-Y., Li, X., Rhee, S.-W. 1996. Microstructure and deposition rate of aluminum thin films from chemical vapor deposition with dimethylethylamine alane. *Appl. Phys. Lett.* **68**, 3567-3569.

Kim, H.J., Egashira, Y., Komiyama, H. 1991. Temperature dependence of the sticking probability and molecular size of the film growth species in an atmospheric chemical vapor deposition process to form AlN from $AlCl_3$ and NH_3. *Appl. Phys. Lett.* **59**, 2521-2523.

Klöwer, J. 1996. High temperature corrosion behaviour of iron aluminides and iron-aluminiumchromium alloys. *Mater. Corros.* **47**, 685-694.

Kobayashi, T., Sekiguchi, A., Hosokawa, N., and Asamaki, T. 1988. Epitaxial growth of Al on Si by gas-temperature-controlled chemical vapor deposition. *Jpn. J. Appl. Phys.* **27**, L1775–L1777.

Kokkoris, G., Brault, P., Thomann, A.-L., Caillard, A., Samélor, D., Boudouvis, A.G., Vahlas, C. 2013. Ballistic and molecular dynamics simulations of aluminum deposition in micro-trenches. *Thin Solid Films* **536**, 115-123.

Kokkoris, G., Constantoudis, V., Angelikopoulos, P., Boulousis, G., Gogolides, E. 2007. Dual nano-scale roughness on Si plasma etched surfaces: The role of etch inhibitors. *Phys. Rev. B* **76**, 193405:1-4.

Kolel-Veetil, M.K., and Keller, T.M. 2010. Organometallic routes into the nanorealms of binary Fe-Si phases. *Materials* **3**, 1049-1088.

Kondoh, E., and Ohta, T. 1995. Chemical vapor deposition of aluminum from dimethylaluminumhydride (DMAH): Characteristics of DMAH vaporization and Al growth kinetics. *J. Vac. Sci. Technol. A* **13**, 2863-2871.

Konvir, K., Armbrüster, M., Teschner, D., Venkov, T.V., Jentoft, F.C., Knop-Gericke, A., Grin, Yu., Schlögl, R. 2007. A new approach to well-defined, stable and site-isolated catalysts. *Sci. Technol. Adv. Mater.* **8**, 420-427.

Konvir, K., Armbrüster, M., Teschner, D., Venkov, T.V., Szentmiklósi, L., Jentoft, F.C., Knop-Gericke, A., Grin, Yu., Schlögl, R. 2009. *In situ* surface characterization of the intermetallic compound PdGa – A highly selective hydrogenation catalyst. *Surf. Sci.* **603**, 1784-1792.

Kovács, A., Schierholz, R., Tillmann, K. 2016. FEI Titan G2 80-200 CREWLEY. *Journal of large-scale research facilities* **2** A43, 1-4.

Krasnowski, M., Kulik, T. 2007. Nanocrystalline FeAl intermetallic produced by mechanical alloying followed by hot-pressing consolidation. *Intermetallics* **15**, 201-205.

Krisyuk, V., Aloui, L., Prud'homme, N., Sysoev, S., Senocq, F., Samélor, D., Vahlas, C. 2011. CVD of pure copper films from amidinate precursor. *Electrochem. Solid St.* **14**, D26-D29.

Krisyuk, V., Gleizes, A.N., Aloui, L., Turgambaeva, A., Sarapata, B., Prud'homme, N., Senocq, F., Samélor, D., Zielinska-Lipiec, A., de Caro, D., and Vahlas, C. 2010. Chemical

vapor deposition of iron, iron carbides and iron nitrides films from amidinate precursors. *J. Electrochem. Soc.* **157**, D454-D461.

Kumar, S., Selvarajan, V., Padmanabhan, P.V.A., Sreekumar, K.P. 2006. Characterization and comparison between ball milled and plasma processed iron-aluminium thermal spray coatings. *Surf. Coat. Technol.* **201**, 1267-1275.

Kuykendall, T., Pauzauskie, P.J., Zhang, Y., Goldberger, J., Sirbuly, D., Denlinger, J., and Yang, P. 2004. Crystallographic alignment of high-density gallium nitride nanowire arrays. *Nat. Mater.* **3**, 524-528.

Lam, R., Vlachos, D.G. 2001. Multiscale model for epitaxial growth of films: Growth mode transition. *Phys. Rev. B* **64**, 035401:1-10.

Lane, P.A., Wright, P.J. 1999. The use of 1,2,3,4,5 pentamethylcyclopentadiene as an in situ growth modifier chemical for the chemical vapour deposition of iron from iron pentacarbonyl. *J. Cryst. Growth* **204**, 298-301.

Lane, P.A., Wright, P.J., Oliver, P.E., Reeves, C.L., Pitt, A.D., Keen, J.M., Ward, M.C., Tilsley, M.E., Smith, N.A., Cockayne, B., and Rex Harris, I. 1997. Growth of iron, nickel, and permalloy thin films by MOCVD for use in magnetoresistive sensors. *Chem. Vapor Depos.* **3**, 97-101.

Langsdorf, A., and Assmus, W. 1999. Crystal growth of large icosahedral Zn-Mg-Y single grains by a liquid encapsulated top seeded solution growth method, *Cryst. Res. Technol.* **34**, 261-265.

Latz, A. Brendel, L. and Wolf, D.E. 2012. A three-dimensional self-learning kinetic Monte Carlo model: application to Ag(111). *J. Phys.: Condens. Matter* **24**, 485005:1-9.

Ledieu, J., Gaudry, É., Serkovich Loli, L.N., Alarcon, S., de Weerd, M.-C., Hahne, M., Gille, P., Grin, Y., Dubois, J.-M., and Fournée, V. Structural investigation of the (010) surface of the $Al_{13}Fe_4$ catalyst. *Phys. Rev. Lett.* **110**, 076102:1-5.

Lee, J.-H., Park, M.-Y., Yun, J.-H., and Rhee, S.-W. 1999. The effect of additives on the viscosity of dimethylaluminum hydride and FTIR diagnostics of the gas-phase reaction. *Thin Solid Films* **348**, 130-133.

Lewis, K.E., Golden, D.M., and Smith, G.P. 1984. Organometallic bond dissociation energies: laser pyrolysis of iron pentacarbonyl, chromium hexacarbonyl, molybdenum hexacarbonyl, and tungsten hexacarbonyl. *J. Am. Chem. Soc.* **106**, 3905-3912.

Li, J., Wang, G., Geng, H., Zhu, H., Zhang, M., Di, Z., Liu, X., Chu, P.K., and Wang, X. 2015. CVD Growth of Graphene on NiTi Alloy for Enhanced Biological Activity. *ACS Appl. Mater. Interfaces* **7**, 19876-19881.

Lim, B.S., Rahtu, A., and Gordon, R. G. 2003. Atomic layer deposition of transition metals. *Nat. Mater.* **2**, 749-754.

Liu, S.J., Huang, H., Woo, C.H. 2002. Schwoebel-Ehrlich barrier: from two to three dimensions. *Appl. Phys. Lett.* **80**, 3295-3297.

Luithardt, W., Benndorf, C. 1996. Fe-C:H-film growth by plasma-assisted CVD from organometallic precursors, *Thin Solid Films* **290-291**, 200-205.

Luo, B., and Gladfelter, W.L. Chemical vapor deposition of metals: W, Al, Cu and Ru, in Jones, A.C., and Hitchman, M.L. (Eds.), *Chemical Vapour Deposition: Precursors, Processes and Applications.* RCS Publishing, Cambridge, **2009**.

Machlin, E.S. *Materials science in microelectronics II: The effects of structure on properties in thin films*, second ed. Elsevier Ltd., Oxford, **2006**.

Madurga, V., Vergara, J., Favieres, C. 2008. Broad UHF ferromagnetic resonance of iron rich-aluminum pulsed laser deposited thin films. *J. Non. Cryst. Solids* **354**, 5198-5200.

Masi, M., Bertani, V., Cavallotti, C., Carra, S. 2000. Towards a multiscale approach to the growth of silicon films by chemical vapor deposition. *Mater. Chem. Phys.* **66**, 229-235.

Massalski, T.B. Binary alloys phase diagrams, in: Massalski, T.B., Okamoto, H., Subramanian, P.R., Kacprzak L. (Eds.), *Desk Handbook: Phase Diagrams for Binary Alloys*, ASM International, Materials Park, **1990**.

Mathey, F. *Transition Metal Organometallic Chemistry*, Springer, Singapore, **2013**.

Matilainen, A., Pussi, K., Diehl, R.D., Hahne, M., Gille, P., Gaudry, É., Serkovic Loli, L.N., Mcguirk, G., de Weerd, M.-C., Fournée, V., Ledieu, J., 2015. Structure of the monoclinic $Al_{13}Fe_4$(010) complex metallic alloy surface determined by low-energy electron diffraction. *Phys. Rev. B* **92**, 014109:1-6.

Matsuda, A., Nomoto, K., Takeuchi, Y., Suzuki, A., Yuuki, A., Perrin, J. 1990. Temperature dependence of the sticking and loss probabilities of silyl radicals on hydrogenated amorphous silicon. *Surf. Sci.* **227**, 50-56.

Matsuhashi, H., Lee, C.-H., Nishimura, T., Masu, K., and Tsubouchi, K. 1999. Superiority of DMAH to DMEAA for al CVD technology. *Mater. Sci. Semicond. Process.* **2**, 303-308.

Maury, F. 1995. Recent trends in the selection of metal-organic precursors for MOCVD. *J. Phys. IV* **05**, C5:449:463.

Mengucci, P., Majni, G., Di Cristoforo, A., Checchetto, R., Miotello, A., Tosello, C., Principi, G., 2003. Structural evolution of Fe–Al multilayers submitted to thermal annealing. *Thin Solid Films* **433**, 205-210.

Michkova, K., Schneider, A., Gerhard, H., Popovska, N., Jipa, I., Hofmann, M., Zenneck, U. 2006. MOCVD of iron with [(arene)(diene)Fe(0)] precursors in a fluidized bed. *Appl. Catal. A-Gen.* **315**, 83-90.

Moon, H., Seong, H., Shin, W.C., Park, W.-T., Kim, M., Lee, S., Bong, J.H., Noh, Y.-Y., Cho, B.J., Yoo, S., and Im, S.G. 2015. Synthesis of ultrathin polymer insulating layers by initiated chemical vapour deposition for low-power soft electronics. *Nat. Mater.* **14**, 628-635.

Naik, M., Guo, T., Chen, L., Mosley, R., and Beinglass, I., 1998. Texture and surface morphology improvement of Al by two-stage chemical vapor deposition and its integration in an Al plug-interconnect scheme for sub 0.25 μm metallization. *J. Vac. Sci. Technol. A* **16**, 1233-1238.

Nakajima, T., Nakatomi, M., Yamashita, K. 2003. Quantum chemical calculations on Al-CVD using DMEAA: surface reaction mechanism of AlH_3 on Al(111). *Mol. Phys.* **101**, 267-276.

Naoi, D., Kajihara, M. 2007. Growth behavior of Fe_2Al_5 during reactive diffusion between Fe and Al at solid-state temperatures. *Mater. Sci. Eng. A Struct. Mater.* **459**, 375-382.

Neo, Y., Niwano, M., Mimura, H., Yokoo, K. 1999. Growth of aluminum on Si using dimethyl-ethyl amine alane. *Appl. Surf. Sci.* **142**, 443-446.

Novet, T., and Johnson, D.C. 1991. New synthetic approach to extended solids: Selective synthesis of iron silicides via the amorphous state. *J. Am. Chem. Soc.* **113**, 3398-3403.

Osswald, J., Konvir, K., Armbrüster, M., Giedigkeit, R., Jentfot, R.E., Wild, U., Grin, Y., Schlögl, R. 2008. Palladium-gallium intermetallic compounds for the selective hydrogenation of acetylene: Part II: Surface characterization and catalytic performance. *J. Catal.* **258**, 219-227.

Papanicolaou, N.I., Papathanakos, V.C., Papageorgiou, D.G. 2001. Self-diffusion on Al(100) and Al(111) surfaces by molecular-dynamics simulation. *Physica B* **296**, 259-263.

Park, S., Lim, S., and Choi, H. 2006. Chemical vapor deposition of iron and iron oxide thin films from Fe(II) dihydride complexes. *Chem. Mater.* **18**, 5150-5152.

Pegasus, 2012: http://febui.chemeng.ntua.gr/pegasus.htm.

Pierson, H.O. *Handbook of Chemical Vapor Deposition (CVD) - Principles, Technology, and Applications*, second ed., Noyes Publications/William Andrew Publishing, LLC, New York, **1999**.

Poling, B.E., Prausnitz, J.M., O'Connell, J.P. *The properties of gases and liquids*, fifth ed. McGraw-Hill, USA, **2001**.

Ponja, S., Sathasivam, S., Chadwick, N., Kafizas, A., Bawaked, S.M., Obaid, A.Y., Al-Thabaiti, S., Basahel, S.N., Parkin, I.P., and Carmalt, C.J. 2013. Aerosol assisted chemical vapour deposition of hydrophobic TiO_2–SnO_2 composite film with novel microstructure and enhanced photocatalytic activity. *J. Mater. Chem. A* **1**, 6271-6278.

Prud'homme, N., Duguet, T., Samélor, D., Senocq, F., Vahlas, C. 2013. Surface-driven, one-step chemical vapor deposition of γ-Al_4Cu_9 compex metallic alloy film. *Appl. Surf. Sci.* **283**, 788-793.

Raimondeau, S., Vlachos, D.G. 2000. Low-dimensional approximations of multiscale epitaxial growth models for microstructure control of materials. *J. Comput. Phys.* **160**, 564-576.

Rapaport, C.D. *The art of molecular dynamics simulation*, second ed. Cambridge University Press, New York, **2004**.

Raupp, G.B., Cale, T.S. 1989. Step coverage prediction in low-pressure chemical vapor deposition. *Chem. Mater.* **1**, 207-214.

Rechendorff, K., Hovgaard, M.B., Foss, M., Zhdanov, V.P., Besenbacher, F. 2006. Enhancement of protein adsorption indeced by surface roughness. *Langmuir* **22**, 10885-10888.

Reese, J.S., Raimondeau, S., Vlachos, D.G. 2001. Monte Carlo algorithms for complex surface reaction mechanisms: Efficiency and accuracy. *J. Comput. Phys.* **173**, 302-321.

Ricca, A. 2001. Heats of formation of $Fe(CO)_n$ (n=1-4). *Chem. Phys. Lett.* **350**, 313-317.

Robinson, D.W., and Rogers, J.W. 2000. Low temperature atomic layer growth of aluminum nitride on Si(100) using dimethylethylamine alane and 1,1-dimethylhydrazine. *Thin Solid Films* **372**, 10-24.

Rodgers, S.T., Jensen, K.F. 1998. Multiscale modeling of chemical vapor deposition. *J. Appl. Phys.* **83**, 524-530.

Samélor, D., Sandowski, D., Senocq, F., Vahlas, C., 2010. Device for measuring the electrical properties of thin films at high temperature. Appl. Number FR10 51074.

Seder, T.A., Ouderkirk, A.J., and Weitz, E. 1986. The wavelength dependence of excimer laser photolysis of $Fe(CO)_5$ in the gas phase. Transient infrared spectroscopy and kinetics of the $Fe(CO)_x$ (x=4,3,2) photofragments. *J. Chem. Phys.* **85**, 1977-1986.

Sekiguchi, A., Kobayashi, T., Hosokawa, N., and Asamaki, T. 1988. Gas-temperature-controlled (GTC) CVD of aluminum and aluminum-silicon alloy film for VLSI processing. *Jpn. J. Appl. Phys.* **27**, L2134–L2136.

Senderowski, C. 2014. Nanocomposite Fe-Al intermetallic coating obtained by gas detonation spraying of milled self-decomposing powder. *J. Therm. Spray Techn.* **23**, 1124-1134.

Senderowski, C., Bojar, Z., Wołczyński, W., Pawłowski, A. 2010. Microstructure characterization of D-gun sprayed Fe-Al intermetallic coatings. *Intermetallics* **18**, 1405-1409.

Senocq, F., Duminica, F.-D., Maury, F., Delsol, T., Vahlas, C. 2006. Iron thin films from $Fe(CO)_5$ and $FeCp_2/H_2O$ under atmospheric pressure. *J. Electrochem. Soc.* **153**, G1025-G1031.

Sherman, A. Chemical vapor deposition for microelectronics: Principles, Technology and Applications, in: Bunshah, R.F., McGuire, G.E. (Eds.), *Materials Science and Process Technology Series*, Noyes Publications, New Jersey, **1987**.

Shishkovsky, I., Missemer, F., Kakovkina, N., Smurov, I. 2013. Intermetallics synthesis in the Fe-Al system via layer by layer 3D laser cladding. *Crystals* **3**, 517-529.

Simmonds, M.G., Gladfelter, W.L., Li, H., and McMurry, P.H. 1993. Particle contamination in low pressure organometallic chemical vapor deposition reactors: Methods of particle detection and causes of particle formation using a liquid alane (AlH_3) precursor. *J. Vac. Sci. Technol. A* **11**, 3026-3033.

Simmonds, M.G., Gladfelter, W.L., Nagaraja, R., Szymanski, W.W., Ahn, K.-H., and McMurry, P.H. 1991. Detection of aluminum particles during the chemical vapor deposition of aluminum films using tertiaryamine complexes of alane (AlH_3). *J. Vac. Sci. Technol. A* **9**, 2782-2784.

Simmonds, M.G., Taupin, I., Gladfelter, W.L. 1994. Selective area chemical vapor deposition of aluminum using dimethylethylamine alane. *Chem. Mater.* **6**, 935-942.

Smits, F.M., 1958. Measurement of sheet resistivities with the four-point probe. *Bell System Technical Journal* **34**, 711-718.

Smy, T., Dew, S.K., and Joshi, R.V. 2001. Efficient modeling of thin film deposition for low sticking using a three-dimensional microstructural simulator. *J. Vac. Sci. Technol. A* **19**, 251-261.

Somorjai, G.A., Li, Y. *Introduction to surface chemistry and catalysis*, second ed. John Wiley & Sons, Inc., New Jersey, **2010**.

Song, B., Dong, S., Coddet, P., Liao, H., Coddet, C. 2012. Fabrication and microstructure characterization of selective laser-melted FeAl intermetallic parts. *Surf. Coat. Technol.* **206**, 4704-4709.

Sovar, M.-M. *Du tri-isopropoxyde aux oxydes d'aluminium par dépôt chimique en phase vapeur: procédé, composition et propriétés des revêtements obtenus.* Institut National Polytechnique de Toulouse et Université Polytechnique de Bucarest, PhD thesis, **2006**.

Srolovitz, D.J., Dandy, D.S., Butler, J.E., Battaile, C.C., Parintosh. 1997. The integrated multiscale modeling of diamond chemical vapor deposition. *JOM* **49** (9), 42-47.

Stassen, I., Styles, M., Grenci, G., Van Gorp, H., Vanderlinden, W., De Feyter, S., Falcaro, P., De Vos, D., Vereecken, P., and Ameloot, R., 2016. Chemical vapour deposition of zeolitic imidazolate framework thin films. *Nat. Mater.* **15**, 304-310.

Stoloff, N.S. 1998. Iron aluminides: present status and future prospects. *Mater. Sci. Eng. A* **258**, 1-14.

Stroscio, J.A., and Pierce, D.T. 1994. Scaling of diffusion-mediated island growth in iron-on-iron homoepitaxy. *Phys. Rev. B* **49**, 8522-8525.

Stumpf, R., Scheffler, M. 1996. Ab initio calculations of energies and self-diffusion on flat and stepped surfaces of Al and their implications on crystal growth. *Phys. Rev. B* **53**, 4958-4973.

Sunderlin, L.S., Wang, D., Squires, R.R. 1992. Metal (iron and nickel) carbonyl bond strengths in Fe(CO)n- and Ni(CO)n-. *J. Am. Chem. Soc.* **114**, 2788-2796.

Sundman, B., Ohnuma, I., Dupin, N., Kattner, U.R., Fries, S.G. 2009. An assessment of the entire Al–Fe system including $D0_3$ ordering. *Acta Mater.* **57**, 2896-2908.

Tang, W., Xu, K., Wang, P., Li, X. 2003. Surface roughness and resistivity of Au film on Si-(111) substrate. *Microelectron Eng.* **66**, 445-450.

Teixeira, S.R., dos Santos, C.A., Dionisio, P.H., Schreiner, W.H., Baumvol, I.J.R. 1987. Interdiffusion and reaction in the FeAl bilayer: III: Phase characterization of furnace-annealed samples. *Mater. Sci. Eng.* **96**, 285-293.

Teixeira, S.R., Freire Jr., F.L., Baumvol, I.J.R. 1989. Interdiffusion, reaction, and stability in a thin film iron-aluminium bilayered system. *Appl. Phys. A* **48**, 481-488.

Thompson, E.J., Warsi, Z.U.A., and Mastin, C.E. *Numerical Grid Generation*, Elsevier North-Holland, Inc., New York, **1985**.

Timalshina, Y.P., Horning, A., Spivey, R.F., Lewis, K.M., Kuan, T.-S., Wang, G.-C., Lu, T.-M. 2015. Effects of nanoscale surface roughness on the resistivity of ultrathin epitaxial copper films. *Nanotechnology* **26**, 075704:1-10.

Tortorelli P.F., and Natesan, K. 1998. Critical factors affecting the high-temperature corrosion performance of iron aluminides. *Mater. Sci. Eng. A* **258**, 115-125.

Tsalikis, D.G., Baig, C., Mavrantzas, V.G., Amanatides, E., Mataras, D. 2013. A hybrid kinetic Monte Carlo method for simulating silicon films grown by plasma-enhanced chemical vapor deposition. *J. Chem. Phys.* **139**, 204706:1-14.

Tsubouchi, K., and Masu, K. 1992. Selective aluminum chemical vapor deposition. *J. Vac. Sci. Technol. A* **10**, 856-862.

Tsubouchi, K., Masu, K., Shigeeda, N., Matano, T., Hiura Y., and Mikoshiba, N. 1990. Complete planarization of via holes with aluminum by selective and nonselective chemical vapor deposition. *Appl. Phys. Lett.* **57**, 1221–1223.

Vahlas, C. Chemical vapor deposition of metals: From unary systems to complex metallic alloys, in: Belin-Ferré, E. (Ed.), *Surface Properties and Engineering of Complex*

Intermetallics. Book Series on Complex Metallic Alloys – vol. 3, World Scientific, Singapore, **2010**.

Vahlas, C., Blanquet, E. Thermochemistry of silicon LPCVD revisited with kinetic data, in: Branz, H.M., Hack, M., Schropp, R., Shimizu, I., Wagner, S. (Eds.), *Amorphous and microcrystalline silicon technology*, Cambridge University Press, **1998**.

Vahlas, C., Caussat, B., Gladfelter, W.L., Senocq, F., Gladfelter, E.J. 2015. Liquid and solid precursor delivery systems in gas phase processes. *Recent Patents on Complex Metallic Alloys* **8**, 91-108.

Versteeg, H. K., and Malalasekera, W. *An introduction to computational fluid dynamics:The finite volume method*, second ed. Pearson Education Limited, Glasgow, **2007**.

Villars, P., Calvert, L.D. *Pearson's Handbook of Crystallographic Data for Intermetallic Phases*, vol. 1, ASM International, Materials Park, **1998**.

Vlachos, D. G. 2005. A review of multiscale analysis: examples from systems biology, materials engineering, and other fluid-surface interacting systems. *Advances in Chemical Engineering* **30** 1-61.

Vlachos, D.G. 1997. Multiscale integration hybrid algorithms for homogeneous-heterogeneous reactors. *AIChE J.* **43**, 3031-3041.

Vlachos, D.G. 2008. Temporal coarse-graining of microscopic-lattice kinetic Monte Carlo simulations via τ leaping. *Phys. Rev. E* **78**, 046713, 1-7.

Vlassiouk, I., Smirnov, S., Regmi, M., Surwade, S.P., Srivastava, N., Feenstra, R., Eres, G., Parish, C., Lavrik, N., Datskos, P., Dai, S., and Fulvio, P. 2013. Graphene nucleation density on copper: Fundamental role of background pressure. *J. Phys. Chem. C* **117**, 18919-18926.

Voigt, A. *Multiscale Modeling in Epitaxial Growth. International Series of Numerical Mathematics* – vol. 149, Birkhäuser Verlag, Germany, **2005**.

Walser, R.M., and Bené, R.W. 1976 First phase nucleation in silicon–transition-metal planar interfaces. *Appl. Phys. Lett.* **28**, 624-625.

Xenidou, T.C., Boudouvis, A.G., Markatos, N.C., Samélor, D., Senocq, F., Prud'homme, N., and Vahlas, C. 2007. An experimental and computational analysis of a MOCVD process for the growth of Al films using DMEAA. *Surf. Coat. Technol.* **201**, 8868-8872.

Xenidou, T.C., Prud'homme, N., Vahlas, C., Markatos, N.C., and Boudouvis, A.G. 2010. Reaction and transport interplay in Al MOCVD investigated through experiments and computational fluid dynamic analysis. *J. Electrochem. Soc.* **157**, D633-D641.

Xu, M., Zaera, F. 1994. Evidence of ligand exchange in iron pentacarbonyl adsorbed on Ni(100) surfaces. *Surf. Sci.* **315**, 40-50.

Yang, G.J., Wang, H.T., Li, C.J., Li, C.X. 2011. Effect of annealing on the microstructure and erosion performance of col-sprayed FeAl intermetallic coatings. *Surf. Coat. Technol.* **205**, 5502-5509.

Yanguas-Gil, A., Yang, Y., Kumar, N., Abelson, J.R. 2009. Highly conformal film growth by chemical vapor deposition. I. A conformal zone diagram based on kinetics. *J. Vac. Sci. Technol. A* **27**, 1235-1243.

Yun, J.-H., Kim, B.-Y., Rhee, S.-W. 1998a. Metal-organic chemical vapor deposition of aluminum from dimethylethylamine alane. *Thin Solid Films* **312**, 259-264.

Yun, J.-H., Park, M.-Y., and Rhee, S.-W. 1998b. Fourier transform infrared diagnostics of gas phase reactions in the metalorganic chemical vapor deposition of aluminum from dimethylethylamine alane. *J. Vac. Sci. Technol. A* **16**, 419-423.

Yun, J.-H., Rhee, S.-W. 1998. Effect of carrier gas on metal-organic chemical vapour deposition of aluminium from dimethylethylamine alane. *J. Mater. Sci.: Mater. Electron.* **9**, 1-4.

Zaera, F. 1991. Mechanism for the decomposition of iron pentacarbonyl on Pt(111): evidence for iron tetracarbonyl and iron tricarbonyl intermediates. *Surf. Sci.* **255**, 280-288.

Zhang, P., Mohimi, E., Talukdar, T.K., Abelson, J.R., Girolami, G.S. 2016. Iron CVD from iron pentacarbonyl: Growth inhibition by CO dissociation and use of ammonia to restore constant growth. *J. Vac. Sci. Technol. A* **34**, 051518:1-7.

Zhang, Y., Hu, G., Orkoulas, G., Christofides, P.D. 2010. Controller and estimator design for regulation of film thickness, surface roughness, and porosity in a multiscale thin film growth process. *Ind. Eng. Chem. Res.* **49**, 7795-7806.

Zhao, L., Zhao, M.J., Li, D.Y., Zhang, J., Xiong, G.Y. 2012. Study on Fe-Al-Si in situ composite coating fabricated by laser cladding. *Appl. Surf. Sci.* **258**, 3368-3372.

Zhdanov, V.P., Rechendorff, K., Hovgaard, M.B., Besenbacher, F. 2008. Deposition at glancing angle, surface roughness, and protein adsorption: Monte Carlo simulations. *J. Phys. Chem. B* **112**, 7267-7272.

Zhu, N., Cacouris, T., Scarmozzino, R., and Osgood Jr., R.M. 1992. Patterned metal growth from dimethylaluminum hydride. *J. Vac. Sci. Technol. B* **10**, 1167-1176.